

***Investigation of Dye-sensitized Photoanodes and  
Tris(2,2'-bipyridine)cobalt Redox Mediators  
Using Scanning Electrochemical Microscopy***

(Untersuchung farbstoffsensibilisierter Fotoanoden und Cobalt-tris-bipyridin-  
Redoxmediatoren mittels elektrochemischer Rastermikroskopie)

Von der Fakultät für Mathematik und Naturwissenschaften  
der Carl von Ossietzky Universität Oldenburg  
zur Erlangung des Grades und Titels eines

Doktors der Naturwissenschaften (Dr. rer. nat.)

angenommene Dissertation

von Frau Ina Schmidt (M.Sc.)  
geboren am 11.11.1983 in Nienburg an der Weser  
Oldenburg, den 07. März 2018

Die vorliegende Arbeit entstand im Zeitraum von Oktober 2011 bis März 2015 in der Arbeitsgruppe von Herrn Professor Gunther Wittstock in der Physikalischen Chemie an der Universität Oldenburg.

Tag der Disputation:	24. Mai 2018
Gutachter:	Prof. Dr. Gunther Wittstock
Zweitgutachter:	Prof. Dr. Rüdiger Beckhaus

*Für meine Eltern*

# Abstract

Photovoltaic (PV) plays an increasingly important role in the field of renewable energies due to the continuous growth of the worldwide energy demand. Dye-sensitized solar cells (DSC) are PV devices of a future generation compared with the commercially available, rooftop-deployed silicon solar cells. In a DSC, the processes of light absorption and charge carrier transport are separated from each other. Therefore, it is possible and reasonable to study both processes independently. In this thesis, scanning electrochemical microscopy (SECM) was employed in feedback (FB) mode to study the kinetics of the dye regeneration in a DSC with tris(2,2'-bipyridine)cobalt(II/III) ( $[\text{Co}(\text{bpy})_3]^{2+/3+}$ ) as redox mediator. Major studies were performed with the triphenylamine-based metal-free dyes D35 and D45 which are environmentally more friendly and cheaper compared to established ruthenium-based dyes such as Z-907. Based on preliminary works, a theoretical model for dye regeneration by a one-electron redox mediator was developed, tested and applied experimentally.  $[\text{Co}(\text{bpy})_3]^{2+/3+}$  was synthesized, characterized and successfully employed in SECM FB mode. The impact of the dye architecture on the kinetics in a DSC was investigated for two structurally similar dyes, D35 and D45, adsorbed onto a nanoporous  $\text{TiO}_2$  film. Herein, SECM was used for the first time to determine the dye regeneration rate constant  $k_{\text{ox}}$  of a photooxidized organic dye by the one-electron redox mediator  $[\text{Co}(\text{bpy})_3]^{2+/3+}$ . Another all-organic dye, V35, structurally comparable to D35 and D45 but with hydrophilic glycolic side chains, was used in combination with  $[\text{Co}(\text{bpy})_3]^{2+/3+}$  in aqueous media.

Nanostructured DSCs fabricated from  $\text{TiO}_2$  and D35 were imaged using shear force distance control SECM (SF-SECM) in FB mode. In FB mode,  $[\text{Co}(\text{bpy})_3]^{2+/3+}$  is reduced at the microelectrode (ME) and re-oxidized at the illuminated photoanode. While it was not possible to resolve the response of individual sensitized  $\text{TiO}_2$  nanoparticles due to their small size compared to the ME, local differences in the performance of screen-printed photoanodes could be resolved. The photoanodes showed signatures in the size regime of 100 – 200  $\mu\text{m}$  in topography and performance which could be related to the mesh used for screen printing. Isolated irregularities in photoanode thickness, barely visible by optical microscopy, also revealed deviation from the average performance of the photoanode. The morphological variations were corroborated by scanning force microscopy and optical phase contrast microscopy.

# Zusammenfassung

Vor dem Hintergrund des weltweit ansteigenden Energiebedarfs ist Fotovoltaik eine immer wichtiger werdende Technologie auf dem Gebiet der erneuerbaren Energien. Farbstoffsensibilisierte Solarzellen (engl.: *dye-sensitized solar cells*, DSC) sind eine Weiterentwicklung der bekannten Siliciumsolarzellen. In einer DSC finden die Prozesse der Lichtabsorption und Ladungstrennung unabhängig voneinander statt. Daher ist es möglich und interessant, beide Prozesse auch unabhängig voneinander zu betrachten. In dieser Arbeit wurde der *Feedback-Modus* (FB) des elektrochemischen Rastersondenmikroskops (engl.: *scanning electrochemical microscope*, SECM) verwendet, um die Kinetik der Farbstoffregeneration als Teilreaktion des Ladungsträgertransports mit Cobalt(II/III)-tris-bipyridin ( $[\text{Co}(\text{bpy})_3]^{2+/3+}$ ) als Redoxmediator zu untersuchen. Ein auf vorhergehenden Arbeiten beruhendes theoretisches Modell der Farbstoffregeneration wurde entwickelt, zunächst mit dem bekannten Ru-Farbstoff Z-907 experimentell getestet und angewendet. Dafür wurde  $[\text{Co}(\text{bpy})_3]^{2+/3+}$  synthetisiert, charakterisiert und erfolgreich im FB-Modus eingesetzt. Der Einfluss der Farbstoffarchitektur auf die kinetischen Prozesse innerhalb einer DSC wurde anhand zweier strukturell sehr ähnlicher Triphenylamin-Farbstoffe, D35 und D45, untersucht. SECM wurde zum ersten Mal mit einem stöchiometrisch korrekten Modell angewendet, um die Farbstoffregeneration mit einem Ein-Elektron-Redoxmediator zu bestimmen. Der Farbstoff V35, dessen Aufbau dem von D35 und D45 ähnelt, jedoch zwei hydrophile Glykolketten statt der Alkoxyketten enthält, wurde verwendet, um  $[\text{Co}(\text{bpy})_3]^{2+/3+}$  in wässrigem Medium zu testen.

Nanostrukturierte DSCs bestehend aus  $\text{TiO}_2$  und D35 wurden mit *shear force* SECM (SF-SECM) im FB-Modus mit  $[\text{Co}(\text{bpy})_3]^{2+/3+}$  als Redoxmediator topographisch und hinsichtlich ihrer elektrochemischen Oberflächenaktivität abgebildet. Im FB-Modus wird  $[\text{Co}(\text{bpy})_3]^{3+}$  an einer Mikroelektrode (ME) reduziert und an der beleuchteten Fotoanode re-oxidiert. Obwohl es aufgrund der Größe der ME im Vergleich zu den  $\text{TiO}_2$ -Partikeln nicht möglich ist, individuelle Informationen zu erhalten, konnten verschiedene Reaktivitäten der per Siebdruck hergestellten, beleuchteten Fotoanode aufgelöst werden. Es wurden Strukturen im Bereich von 100 – 200  $\mu\text{m}$  sichtbar, die auf das beim Siebdruck verwendete Gitter zurückzuführen sind. Unterschiede in der Morphologie wurden mit Rastertkraftmikroskopie sowie optischer Phasenkontrastmikroskopie bestätigt.

# Danksagung

Herzlichen Dank, *Herr Professor Gunther Wittstock*, dafür, dass ich meine Dissertation in Ihrer Arbeitsgruppe anfertigen durfte. Vielen Dank außerdem für das sehr interessante Thema, Ihre freundliche Übernahme des Erstgutachtens sowie für Ihre ständig offene Tür, Ihre Diskussionsbereitschaft und überaus wertvollen Tipps.

*Herr Professor Rüdiger Beckhaus*, ich danke Ihnen herzlich für die Übernahme des Zweitgutachtens. *Herr Professor Michael Wark*, Ihnen danke ich herzlich für Ihre Übernahme der Rolle des Drittprüfers.

*Liebe Wiebke* und *liebe Inka*, danke für das wunderbare und vertrauensvolle Arbeitsklima, das sich schnell zu einer beständigen Freundschaft entwickelt hat.

*Patrick*, vielen Dank für deine Hilfe im Labor sowie für die kleinen Ratschläge und Kniffe, die einiges erleichtert und praktischer gemacht haben.

*Dear Hanna*, thank you for the great cooperation which exceeded work and became a friendship. Thanks for many encouraging words as well as helpful and fruitful discussions about both work and life.

Vielen Dank an die aktuellen und ehemaligen Mitglieder der AG Wittstock, im Besonderen *Frank, Gerd, Iza, Andreas*, meine Azubine *Kristin, Heinz, Carsten* und *Julia*.

Thank you, *Nick*, for responding so quickly to my questions especially during the first time of the thesis.

*Liebe Henrike* und *liebe Wiebke*, vielen Dank dafür, dass ihr euch die Zeit genommen habt, meine Arbeit zu lesen und mir eine Rückmeldung zu geben.

*Meine Freunde*, danke fürs gute Zuspochen, für euer Interesse und für unzählige, unbezahlbare Situationen.

*Tobi*, danke für dein offenes Ohr, dein Verständnis, deine Unterstützung in allen Lebenslagen und dein großes Herz. Ich bin sehr froh und dankbar dafür, dass es dich gibt.

*Meine liebe Familie* und *meine lieben Eltern*, ich danke euch für eure stets liebevolle Unterstützung in allen Lebenslagen. Ohne euer Verständnis, euer Vertrauen und den mir gewährten Freiraum hätte ich das Studium und die Promotion niemals schaffen können. Ich danke euch von ganzem Herzen.

# Contents

<b>1</b>	<b>Introduction.....</b>	<b>1</b>
<b>2</b>	<b>Theory and Application of Photoelectrochemistry .....</b>	<b>4</b>
2.1	Photoelectrochemistry .....	4
2.1.1	Historical Perspective.....	4
2.1.2	Semiconductors .....	5
2.1.3	Titanium Dioxide .....	7
2.1.4	Semiconductor / Redox Electrolyte Interface .....	8
2.2	Solar Cells .....	10
2.2.1	First Generation: Silicon Solar Cells.....	10
2.2.2	Second Generation Solar Cells.....	11
2.2.3	Third Generation Solar Cells.....	11
2.2.4	Classifying DSCs .....	11
2.3	Dye-Sensitized Solar Cells.....	12
2.3.1	Initial Idea of a DSC.....	12
2.3.2	Operation Principle and Kinetics of a DSC .....	14
2.4	Importance of the Dye.....	16
2.4.1	Requirements of Dyes .....	16
2.4.2	Dyes under Investigation.....	17
2.5	Redox Electrolytes .....	22
2.5.1	Different Types of Redox Electrolytes.....	22
2.5.2	Cobalt Complexes as Redox Mediators .....	24
2.5.3	Cobalt Complexes vs. Iodide/triiodide .....	25
2.5.4	Alternative Redox Electrolytes .....	27

<b>3</b>	<b>Fundamentals of Experimental Methods .....</b>	<b>28</b>
3.1	Conventional Characterization Methods of Dye-Sensitized Solar Cells .....	28
3.2	Microelectrodes .....	32
3.3	Scanning Electrochemical Microscopy .....	34
3.3.1	Setup and Techniques.....	34
3.3.2	Feedback Mode for Kinetic Investigations .....	37
3.3.3	Shear Force SECM and Spatially Resolving Techniques .....	41
3.3.4	Further SECM Modes and Scanning Probe Techniques .....	42
3.4	Linear Sweep Voltammetry at a Rotating Disk Electrode .....	42
<b>4</b>	<b>Material and Procedures.....</b>	<b>45</b>
4.1	Overview of Techniques Used .....	45
4.2	Chemicals .....	46
4.3	Instruments .....	49
4.3.1	Potentiostats .....	49
4.3.2	Rotating Disk Electrode Setup .....	50
4.3.3	Confocal Laser Scanning Microscope / Optical Microscope.....	50
4.3.4	UV-Vis Spectrometer .....	50
4.3.5	Nuclear Magnetic Resonance Spectroscopy .....	51
4.4	Preparation and Characterization of Gold and Platinum Microelectrodes.....	52
4.4.1	Preparation .....	52
4.4.2	Characterization .....	53
4.5	Scanning Electrochemical Microscope with Controlled Illumination .....	54
4.6	Light Emitting Diodes .....	58
4.6.1	Setup of the LED Light Source .....	58
4.6.2	Calculating the Photon Flux Density .....	61
4.7	Redox Electrolyte Preparation .....	63

4.7.1	Electrolyte for Experiments with Different Concentrations .....	63
4.7.2	Electrolyte for Experiments with Different Light Intensities and Shear Force Imaging.....	64
4.8	Titanium Dioxide Electrodes .....	64
4.8.1	Preparation of Titanium Dioxide Electrodes.....	64
4.8.2	Dye-sensitization of the Titanium Dioxide Electrodes .....	67
4.9	Cobalt Complexes .....	69
4.9.1	Synthesis.....	69
4.9.2	UV Spectroscopic Characterization .....	71
4.9.3	Nuclear Magnetic Resonance Spectroscopy .....	73
4.9.4	Electrochemical Characterization .....	74
<b>5</b>	<b>Characterization of Cobalt Complexes.....</b>	<b>76</b>
5.1	Electrochemical Characterization .....	76
5.1.1	Linear Sweep Voltammetry at a Rotating Disk Electrode .....	76
5.1.2	Determination of Diffusion Coefficients at a ME.....	80
5.2	Redox Mediator Stability .....	82
5.2.1	Stability towards Light .....	82
5.2.2	Long-Term Stability .....	84
5.3	Choice of Microelectrode Material .....	86
<b>6</b>	<b>Establishing DSC One-Electron Redox Mediators for use in SECM .....</b>	<b>88</b>
6.1	SECM Model for Dye Regeneration by a One-Electron Redox Mediator ....	88
6.2	Probing the Reliability of the New Redox Mediator.....	98
6.2.1	Effect of Increasing Redox Mediator Concentration .....	98
6.2.2	Effect of Different Light Intensities .....	103
6.3	Influence of DSC Components of Different Polarity.....	105

6.3.1	Aqueous Redox Mediator.....	105
6.3.2	Reactions over Pristine Titanium Dioxide Electrodes .....	105
6.3.3	Comparison of Redox Mediators of Different Polarity.....	107
6.3.4	Comparison of a Hydrophilic to a Hydrophobic Dye .....	111
<b>7</b>	<b>Impact of Dye Architecture on Kinetics in Dye-Sensitized Solar Cells .</b>	<b>114</b>
7.1	Method Development .....	114
7.2	SECM Feedback Mode Investigation of D35- and D45-sensitized TiO <sub>2</sub> ...	121
7.3	Determination of Regeneration Rate Constant from SECM Experiments...	124
7.4	Comparison with TAS and EIS Measurements.....	126
<b>8</b>	<b>Spatially Resolved Analysis of Screen Printed Photoanodes by SF-SECM</b>	<b>127</b>
8.1	Methodology .....	127
8.2	Dye Migration .....	130
8.3	SF-SECM Imaging of the Transition between Illuminated and Non-illuminated Areas of D35-Sensitized TiO <sub>2</sub> Electrodes .....	132
8.4	Consideration of Positioning Systems.....	135
8.5	Visualization of Defects Using High Resolution SF-SECM FB Imaging ...	136
8.6	High Resolution Imaging by SF-SECM.....	139
<b>9</b>	<b>Summary and Perspective.....</b>	<b>141</b>
<b>10</b>	<b>Appendix.....</b>	<b>XI</b>
10.1	Microelectrodes Used.....	XI
10.2	Validation of the LED Light Intensity .....	XII
10.3	Abbreviations .....	XV
10.4	Symbols and Units .....	XVIII
<b>11</b>	<b>References.....</b>	<b>XXI</b>
<b>12</b>	<b>Publications .....</b>	<b>XXVII</b>
<b>13</b>	<b>Curriculum vitae.....</b>	<b>XXIX</b>

# I Theory

## 1 Introduction

“..., but coal is not inexhaustible.”<sup>[1]</sup> What Italian photochemist Giacomo Ciamician recognized back in 1912 is nowadays at least as important as during his lifetime more than 100 years ago. The oil crises in 1973 and 1979 intensified the desire and need for energy independence from oil exporting countries. Now, in the 21<sup>st</sup> century, not only does mankind need to deal with the challenge of an increasing energy consumption of a growing population but almost more important is how to do so in a responsible way towards nature and future generations. Renewable energy sources such as wind energy, geothermal energy, hydropower and solar energy are good alternatives to nuclear power and fossil fuels in terms of sustainability, eco-friendliness and availability. The European Commission announced in 2013 that up to the year 2020, at least 20 % of EU’s overall energy should stem from renewable sources, their motivation being the dramatic increase of CO<sub>2</sub> in the atmosphere resulting from fossil fuels. The amount of CO<sub>2</sub>, one of the main greenhouse gases, in air increased significantly and almost doubled since the beginning of the industrialization in the 18<sup>th</sup> century, from 277 ppm in 1750 to 399.4 ppm in 2015.<sup>[2]</sup> To abate CO<sub>2</sub>, the worldwide installation of renewable energies was reinforced and the share of renewable energy sources has grown within the last 15 years from about 4 % in 2000 to over 35 % in 2015, the trend still increasing (Fig. 1.1).

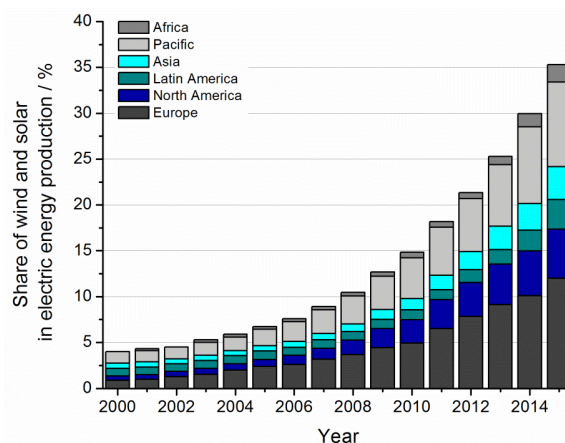


Fig. 1.1 – Development of share of wind and solar in electric energy production worldwide from 2000 to 2015, divided into regions of the world; collected by Enerdata.<sup>[3]</sup>

Following these statistics, in 2015 Europe had a share of wind and solar in electric energy production of about 12 % and is on a good way to reach the goal announced by the EU. The sun is the most abundant source of energy on earth and supplies sufficient energy within one hour to satisfy the worldwide energy needs for a whole year.<sup>[4, 5]</sup> The sun has the potential to play a major role in the future sustainable energy supply. In a scenario of the future energy demand established jointly by the World Meteorological Organization and the United Nations Environment Program, an energy consumption of 27 TW is proposed for the year 2050 (for comparison: 13.5 TW in the year 2001).<sup>[4]</sup> This moderate scenario takes into account continued improvement of technology, meaning a better energy efficiency, as well as population and economic growth, the latter two arguments leading to an increased energy demand.

Photovoltaic (PV) devices are used to convert the light of the sun into electric energy. They are divided into three different generations, the most popular and commercially available one being 1<sup>st</sup> generation solar cells. They consist of highly pure silicon which functions both as light absorber and electron injector. In this thesis, a further generation of solar cells is investigated where, in contrast to silicon solar cells, the processes of light absorption and charge carrier transport are separated. A dye attached onto a semiconductor is photooxidized by the sunlight and injects an electron into the conduction band (CB) of the semiconductor, typically titanium dioxide (TiO<sub>2</sub>). This type of solar cell is called dye-sensitized solar cell (DSC). The first photovoltaic device of this kind was presented by O'Regan and Grätzel<sup>[6]</sup> in 1991 and showed a power conversion efficiency (PCE) of 7.9 % which was considered a breakthrough. In contrast to classic 1<sup>st</sup> generation silicon single crystal solar cells with a PCE of currently 27.6 %<sup>[7]</sup> which requires highly pure silicon, the production of a DSC is low-cost since only low-to-medium purity materials are needed.

The kinetically challenging step of a DSC is the regeneration of the photooxidized dye. It is crucial for the efficiency of the device to know how fast the dye regains an electron which was released before during photooxidation. In this thesis, the one-electron outersphere redox mediator tris(2,2'-bipyridine)cobalt(II/III) ([Co(bpy)<sub>3</sub>]<sup>2+/3+</sup>) was employed for dye regeneration studies. Commonly, the two-electron mediator iodide/triiodide (I<sup>-</sup>/I<sub>3</sub><sup>-</sup>) is applied in DSCs as redox mediator. I<sup>-</sup>/I<sub>3</sub><sup>-</sup> came to dominate the field of DSCs because it shows good solubility, provides a rapid dye regeneration and most of all it shows very slow recombination kinetics with electrons in TiO<sub>2</sub>.<sup>[8]</sup> However, it is far from being

ideal. Due to the relatively large difference between its redox potential and the redox potential of the dye, the DSC voltage is limited. Redox electrolytes based on cobalt complexes as mediators have been considered as alternatives because of different features. They have a lower absorption coefficient and are less corrosive than  $\Gamma/I_3^-$ . Furthermore, the redox potential of cobalt complexes can be varied *via* the design of the ligands, allowing fine tuning of the driving force. The breakthrough of cobalt complexes was achieved by tailoring a combination of a cobalt bipyridine redox couple and an organic dye with bulky donor units.<sup>[9, 10]</sup> At present, the record efficiency of a comparable system is 14.7 %.<sup>[11]</sup>

In this thesis, the reaction of such cobalt bipyridine redox mediators with photooxidized dyes is analyzed using scanning electrochemical microscopy (SECM) approaches. To determine the dye regeneration rate constant  $k_{ox}$ , SECM in feedback (FB) mode using a Au microelectrode (ME) was used. SECM is a versatile tool and has been proven applicable for the determination of heterogeneous reactions of energy producing devices before.<sup>[12-14]</sup> The organometallic dye *cis*-bis(isothiocyanato)(2,2'-bipyridyl-4,4'-dicarboxylato)(4,4'-di-nonyl-2'-bipyridyl)ruthenium(II), called Z-907, which is well-known in DSC research,<sup>[15]</sup> was used for initial experiments in order to verify the applied method which in terms of the  $[Co(bpy)_3]^{3+}$  redox mediator is new in SECM research.  $[Co(bpy)_3]^{3+}$  has been used in combination with SECM before, however using a model based on a stoichiometry for the  $\Gamma/I_3^-$  redox mediator.<sup>[16, 17]</sup> In this thesis, a kinetic model based on the dye regeneration rate law of order 1 with respect to  $[Co(bpy)_3]^{3+}$  was developed and tested (chapter 6.1 to 6.2.2). This development was based on the model for  $\Gamma/I_3^-$ <sup>[18]</sup> which Tefashe *et al.* employed with D149-sensitized zinc oxide (ZnO)<sup>[19, 20]</sup> and N-719-sensitized  $TiO_2$ <sup>[21]</sup>. Using this tailored kinetic model, two structurally very similar triphenylamine dyes, (E)-3-(5-(4-(Bis(2',4'-dibutoxy-[1,1'-biphenyl]-4-yl)amino)phenyl)-thiophene-2-yl)-2-cyanoacrylic acid, known as D35, and (E)-3-(5-(4-(Bis(2',4'-dimethoxy-[1,1'-biphenyl]-4-yl)amino)phenyl)-thiophene-2-yl)-2-cyanoacrylic acid, known as D45, were studied as sensitizers in a DSC with  $[Co(bpy)_3]^{2+/3+}$  (chapter 7). The results were compared to electrochemical impedance spectroscopy (EIS) and transient absorption spectroscopy (TAS) measurements which were performed by a cooperation partner at the University of Uppsala in Sweden. The two dyes D35 and D45 differ in the length of their alkoxy chains but show comparable energy levels. Thus, a difference in the regeneration rate of the dye should be traced back to structural rather than energetic properties of the

dyes. For the kinetic analysis of dye regeneration, the diffusion coefficient ( $D$ ) of  $[\text{Co}(\text{bpy})_3]^{2+/3+}$  was necessary which was obtained by linear sweep voltammetry (LSV) at a rotating disk electrode (RDE) (chapter 5.1.1). Following an approach in literature,<sup>[22]</sup>  $[\text{Co}(\text{bpy})_3]^{3+}$  was applied in aqueous media in combination with the hydrophobic dye D35<sup>[23]</sup> and the more hydrophilic dye V35<sup>[24]</sup> to look for differences in dye regeneration at substrates of different hydrophilicity (chapter 6.3).

Shear force distance control SECM (SF-SECM) was employed to spatially resolve D35-sensitized nanoparticulate  $\text{TiO}_2$  electrodes (chapter 8). Therefore, SECM FB mode was used to systematically explore the options for characterizing local variations of DSC performance with  $[\text{Co}(\text{bpy})_3]^{3+}$  as redox mediator. The electrochemical activity of the surface was matched to the morphology of the sample and afterwards compared to results from scanning force microscopy (SFM) and optical phase contrast microscopy which were performed by colleagues at the University of Oldenburg.

## 2 Theory and Application of Photoelectrochemistry

### 2.1 Photoelectrochemistry

#### 2.1.1 Historical Perspective

In general, the term photoelectrochemistry describes electrochemical reactions which result from the absorption of photons. The principle of photoelectrochemical reactions can be traced back to the French physicist Alexandre Edmond Becquerel who discovered a special case of the photoelectric effect. Later on, two developments achieved high attention for their conversion of sunlight into energy, both based on photoelectrochemical reactions which are a key to use light energy for a sustainable energy supply. The first development was a solar cell which converts photons of the sunlight into another type of energy: electric current. The second development is the photoelectrochemical splitting of water. Products of water splitting reactions are  $\text{O}_2$  and  $\text{H}_2$ , the latter being a storable fuel with a high energy density of 5.6 MJ/l at 700 bar and the highest specific energy of 142 MJ/kg<sup>[25]</sup> among non-

radiative materials. To have a comparison, liquid hydrocarbons have a specific energy of about 56 MJ/kg.<sup>[26]</sup>

When talking about photoelectrochemistry, it is impossible to do so without mentioning the names Giacomo Ciamician,<sup>[1]</sup> Heinz Gerischer,<sup>[27-29]</sup> Akira Fujishima, Kenichi Honda,<sup>[30]</sup> Michael Grätzel,<sup>[6, 31-34]</sup> and Allen J. Bard.<sup>[35-39]</sup> Each one of them dedicated a great deal of his life to the electrochemistry of semiconductors or to the understanding of the importance of photosynthesis and established the base for photoelectrochemical applications such as solar water splitting and DSCs. Moreover, except for Ciamician, they contributed to the understanding of the behavior of semiconductors. Ciamician was a scientist who, more than one hundred years ago, in 1912, suggested in his manuscript “The photochemistry of the future” to switch from fossil energy (coal) to solar energy.<sup>[1]</sup> Fujishima and Honda<sup>[30]</sup> irradiated a TiO<sub>2</sub> electrode immersed in an aqueous electrolyte and demonstrated the possibility to decompose water into its constituent elements H<sub>2</sub> and O<sub>2</sub> by photolysis. Moreover, Fujishima was the first person who used SECM to monitor photocatalytic properties of TiO<sub>2</sub> to split water.<sup>[40, 41]</sup>

### 2.1.2 Semiconductors

Semiconductors are solids which become conductive when exposed to light or heat while they behave in an insulating manner in the dark and at low temperatures. There are two different types of semiconductors: elemental ones such as Si and molecular ones such as TiO<sub>2</sub> or ZnO. In a single molecule, discrete energy levels are described by molecular orbitals. The most important orbitals, because they are involved in chemical reactions, are the highest occupied molecular orbital (HOMO) and the lowest unoccupied molecular orbital (LUMO). In a molecule cluster, each molecule contributes one energy level. Following Hund’s rule, those molecular energy levels are not allowed to occupy the same level. Thus, in a crystal, all energy levels are aggregated to energy bands (Fig. 2.1). Important for the use of semiconductors in electronics and optoelectronics are those two bands close to the energy level of a solid, at which the probability of being occupied by electrons at 0 K is 50 %. This level is called Fermi level  $E_F$ . The two important bands are the valence band (VB) with filled bonding orbitals and the conduction band (CB) with vacant antibonding orbitals. These bands are separated by a band gap, a forbidden region for electrons, de-

scribed by the band gap energy  $E_g$ . This energetic difference strongly influences the electrical and optical properties of a crystalline solid and is a measure of its chemical bond strength. In metals,  $E_g$  can be very small with the possibility that VB and CB overlap, leading to conductive behavior. Another scenario in metals which induces conduction is a partially filled VB in which electrons are free to move (Fig. 2.1A). In an insulator,  $E_g$  is very large ( $E_g > 4.0$  eV) and even by energy supply, an electron promotion from VB to CB is excluded (Fig. 2.1C). Semiconductors are less conductive than metals and more conductive than insulators and the  $E_g$  of semiconductors is situated between that of metals and insulators (Fig. 2.1B).

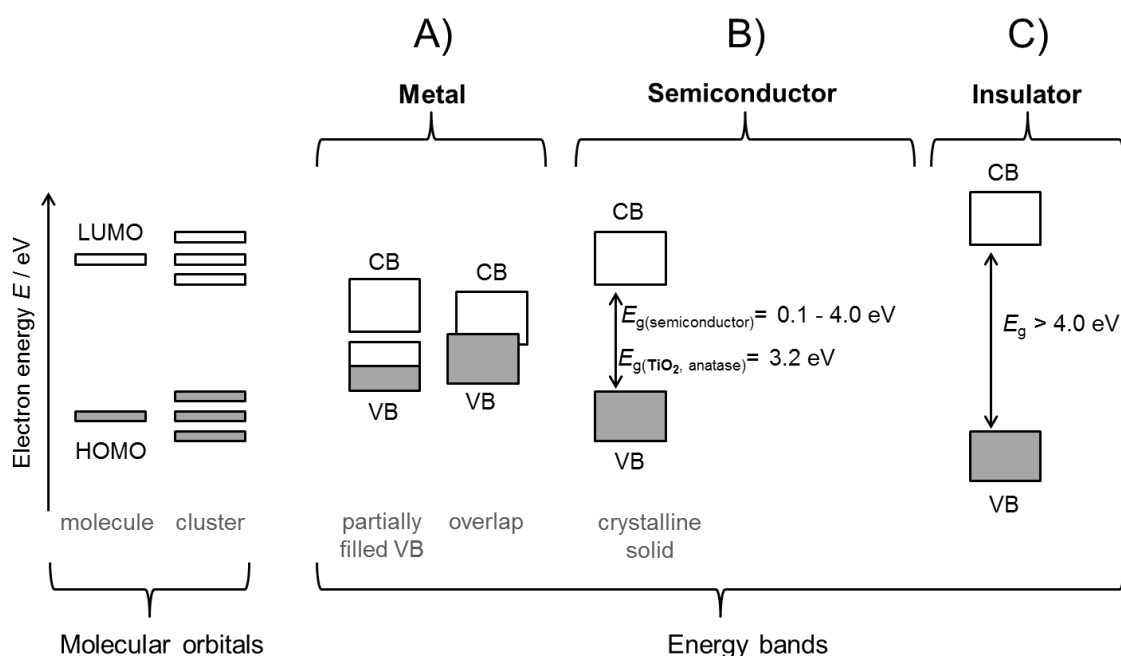


Fig. 2.1 – Energy diagrams of a molecule, a molecule cluster and the aggregation to VB and CB for A) metals, B) semiconductors and C) insulators.  $\text{TiO}_2$  in anatase configuration is classified as a semiconductor with  $E_g = 3.2$  eV. Grey refers to filled bands and white to empty bands.

Semiconductors are divided into intrinsic and extrinsic semiconductors. Pure material semiconductors such as Si and Ge are intrinsic semiconductors with  $E_g = 0.1$  to  $1.5$  eV (e.g. Si:  $E_g = 1.1$  eV, Fig. 2.2). In those materials, thermal energy is sufficient to promote an electron from VB to CB to create conduction. Electrons and holes, called charge carriers, exist in a dynamic equilibrium with equal densities. Extrinsic semiconductors ( $E_g = 1.5$  to  $4.0$  eV) such as  $\text{TiO}_2$  ( $E_g = 3.2$  eV (anatase), Fig. 2.2) are either trivalent or pentavalent

doped materials. These induced impurities create an excess of holes or electrons and thus conductivity.

### 2.1.3 Titanium Dioxide

TiO<sub>2</sub> is a non-toxic, abundant, biocompatible and cheap semiconductor which cannot be decomposed by sunlight. Besides its practical applications as a pigment in white wall paint, tooth paste or in waste water management, it is a common component in photoelectrochemical devices. This is due to the property of TiO<sub>2</sub> being a wide-band-gap semiconductor which creates free charge carriers (e<sup>-</sup> and h<sup>+</sup>) when irradiated with photons of appropriate energy. TiO<sub>2</sub> occurs in different crystalline forms with the most important ones brookite, rutile and anatase. Among those, anatase is the most important one for the use in photoelectrochemical devices because it has a larger bandgap (3.2 eV compared with 3.0 eV for rutile) and a higher conduction band edge energy,  $E_C$ . TiO<sub>2</sub> is usually slightly oxygen-deficient with a sum formula of TiO<sub>2-x</sub> ( $x \approx 0.01$ ). This small oxygen deficiency can be considered as a Ti<sup>3+</sup> impurity which induces an n-type doping to the semiconductor material.

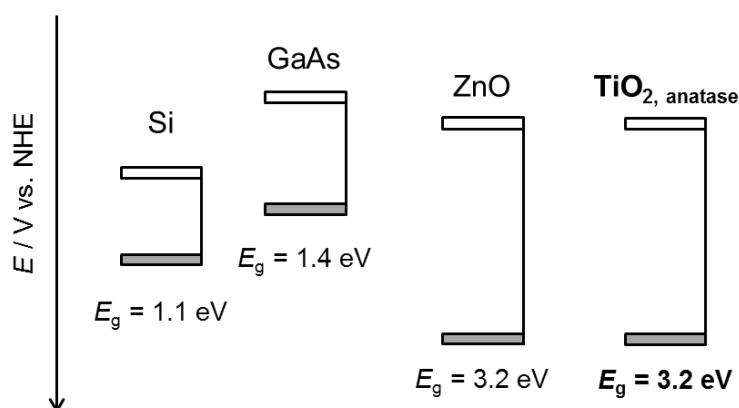


Fig. 2.2 – Scheme of the relative band edges of semiconductors commonly used in solar cell applications with corresponding  $E_g$  with respect to the normal hydrogen electrode (NHE).<sup>[42, 43]</sup>

Compared to conventional semiconductors, such as Si and GaAs, oxidic semiconductors such as TiO<sub>2</sub> show a better stability at the electrode/electrolyte interface. Therefore, oxides in general and TiO<sub>2</sub> in particular are ideally suited for use in electrochemistry and photoelectrochemistry.<sup>[29, 44]</sup> Besides TiO<sub>2</sub>, ZnO is a popular material in the field of electrochemistry and photoelectrochemistry. However, it was demonstrated that only oriented ZnO

nanowires could compete with  $\text{TiO}_2$ .<sup>[45]</sup>  $\text{TiO}_2$  also enables dyes with carboxylic acid groups to bind strongly to  $\text{TiO}_2$ . The resulting good electronic overlap between the  $\text{TiO}_2$  surface and the dye is essential for efficient charge transfer.<sup>[46]</sup>

#### 2.1.4 Semiconductor / Redox Electrolyte Interface

Depending on the nature of the mobile charge carriers, semiconductors are divided into different types: n-type, where majority carriers are electrons and p-type, in which holes are the majority carriers. When an n-type semiconductor such as  $\text{TiO}_2$  is brought into contact with an electrolyte containing oxidized and reduced species, an electron transfer occurs due to the largely different electrochemical potential of both components. The electrochemical potential of a one-electron redox electrolyte is given by the Nernst equation on the energy scale<sup>[47]</sup>

$$E_{\text{redox}} = E_{\text{redox}}^{0'} + k_{\text{B}}T \ln\left(\frac{c_{\text{ox}}}{c_{\text{red}}}\right) \quad (2.1)$$

with  $E_{\text{redox}}^{0'}$  being the formal redox energy,  $k_{\text{B}}$  being Boltzmann's constant  $8.617 \times 10^{-5}$  eV/K,  $T$  being the temperature and  $c_{\text{ox}}$  and  $c_{\text{red}}$  being the concentration of the oxidized or reduced species of the redox couple in the electrolyte, respectively. From equation (2.1) it is evident that varying the ratio of  $c_{\text{ox}}$  to  $c_{\text{red}}$  directly influences  $E_{\text{redox}}$ . As long as  $E_{\text{F}}$  of an insulating semiconductor is greater than  $E_{\text{redox}}$  of an electrolyte,  $e^-$  will move from the semiconductor to the electrolyte to equilibrate the two energy levels (Fig. 2.3). During this electron transfer, the oxidized species of the electrolyte is reduced and  $E_{\text{F}}$  of the semiconductor is lowered. This electron transfer stops when both energy levels have equalized. The result is a space charge layer in the semiconductor where the initial electrons were located before being transferred to the electrolyte (Fig. 2.3B). Since this region is depleted of charge carriers, it is called depletion zone.  $E_{\text{C}}$  and  $E_{\text{V}}$  bend upwards towards the interface (so-called "band bending"). This creates a potential barrier which allows no further  $e^-$  transfer to the electrolyte. On the electrolyte side, a Helmholtz layer is formed containing adsorbed electrolyte ions of the opposite charge to that induced in the semiconductor. In an n-type semiconductor, where a positive charge is induced, anions will form the Helmholtz layer.



## 2.2 Solar Cells

### 2.2.1 First Generation: Silicon Solar Cells

Solar cells are devices which directly convert sunlight, a flow of photons, into an electric current, a flow of electrons. Historically, solar cells can be divided into different generations, depending on the active material, the working principle and the thermodynamics. The well-known rooftop-deployed solar cells, produced from highly pure silicon, are referred to as first generation. In this solid-state semiconductor, an n-type Si crystal (doped with an atom with five valence electrons, usually phosphorous) is brought into contact with a p-type Si crystal (doped with an atom with three valence electrons, usually boron). Once brought into contact, the  $e^-$  strive for equilibrium.  $e^-$  from the n-type semiconductor move to the p-type semiconductor to occupy free spaces ( $h^+$ ). *Via* this equilibration of occupancy, charges are separated. A so-called p-n-junction is formed with a potential barrier. In a Si solar cell, two fundamental processes occur: first, the light absorption, where photons are converted into electron-hole-pairs, and second, the charge separation, where the generated  $e^-$  and  $h^+$  are separated by the internal electric field and the electrons can be fed into the electrical circuit. The underlying mechanism is the photovoltaic effect, which is a special case of the inner photoelectric effect where light is converted into electric energy. Becquerel was the first person to describe this effect during which charge carriers are released from an illuminated metal surface dipped into an electrolyte.

Up to today, first generation solar cells are electronics with the highest PCE commercially available. However, their efficiency is limited by the Shockley-Queisser limit which describes the maximum efficiency achievable by solar cells considering that sunlight undergoes physical processes such as absorption. The Shockley-Queisser limit was calculated to an efficiency of 33% for solar cells with one p-n-junction and a band gap of  $E_g = 1.1$  eV illuminated with unfocussed sunlight.<sup>[50]</sup> To create an electron-hole-pair, the semiconductor only absorbs photons whose energy  $h\nu$  exceeds the energy of the band gap ( $h\nu > E_g$ ). Photons of smaller energy are not absorbed and their energy will be lost. If the photon energy exceeds  $E_g$ , the energy excess will also be lost due to thermalization which solely heats up the solar cells. Thermalization describes a process during which the difference of the energy between  $E_g$  and  $h\nu$  is transferred to the excited electron-hole pair as ki-

netic energy. Within picoseconds, the semiconductor lattice absorbs the surplus energy due to the energy relaxation. As a consequence, the solar cell heats up. The power limit of solar cells depends on  $E_g$  and certain geometrical factors such as, for example, the angle of incidence or the angle subtended by the sun (standard AM 1.5). AM1.5 G refers to the 1.5-fold thickness of the earth's atmosphere through which the sunlight travels before hitting the earth's surface.

### 2.2.2 Second Generation Solar Cells

Silicon solar cells are disadvantageous in terms of the high amount of energy needed for the production of high purity crystalline silicon. Therefore, cheaper alternatives had to be developed. Second generation solar cells are based on low-energy preparation techniques such as vapor deposition and electroplating to achieve thin semiconductor films. During earlier research on second generation solar cells, amorphous silicon was employed. Later, other semiconductor materials, such as copper-indium-gallium-selenide (CIGS), were used.<sup>[51]</sup> Recently, a combination of CIGS solar cells and DSC was constructed with an efficiency of 13 %.<sup>[52]</sup> Both the first and the second generation solar cells are based on single junction devices which are thermodynamically limited by the Shockley-Queisser limit.

### 2.2.3 Third Generation Solar Cells

Third generation solar cells comprise technologies that use multi-junctions as well as cheap and easily producible materials. Moreover, third generation solar cells are devices which are able to circumvent the Shockley-Queisser limit and can obtain theoretical efficiencies up to 86% for an infinite number of layers<sup>[53]</sup> since the energy of the sun provides high-quality energy due to its high temperature.<sup>[54]</sup> Tandem cells (also: multi-junction solar cells),<sup>[55]</sup> quantum-dot cells<sup>[56, 57]</sup> and hot carrier cells<sup>[58]</sup> are examples of third generation solar cells.

### 2.2.4 Classifying DSCs

The technology of a DSC is considered to be in between second and third generation solar cells.<sup>[59]</sup> One could argue that DSCs are third generation because they have two band gaps,

one from the dye and one from the  $\text{TiO}_2$ , classifying them as multi-junctional and thus able to overcome the Shockley-Queisser limit. However, DSCs are partly liquid whereas “traditional” multi-junction solar cells consist of a semiconductor and a solid state multi-junction. The following chapter describes the design and the working principle of a DSC.

### 2.3 Dye-Sensitized Solar Cells

#### 2.3.1 Initial Idea of a DSC

The idea of a DSC is to shift the photo response of  $\text{TiO}_2$  into the visible region by sensitizing it with a dye. A DSC takes nature as role model and mimics the photosynthesis in plants, in which the chlorophyll-containing parts of a plant convert the greenhouse gas  $\text{CO}_2$  and water into glucose and oxygen under the influence of sunlight. In contrast to a Si solar cell, in which physical processes occur, the DSC is a photoelectrochemical cell.

Modern DSCs are based on a concept developed in 1988 in the lab of Michael Grätzel where a polycrystalline  $\text{TiO}_2$  film sensitized with a ruthenium dye was immersed into a  $\text{Br}_2/\text{Br}^-$  redox system and gained an incident-photon-to-electron efficiency (IPCE) of 73 %.<sup>[60]</sup> However, the concept of immersing dye-sensitized semiconductor electrodes into liquid solutions dates back to the 1970s and 1980s.<sup>[47, 61]</sup> The breakthrough DSC of Grätzel from 1991 and his co-workers in Switzerland,<sup>[6]</sup> showed an initial PCE of 7.9 %. This DSC consisted of a 10  $\mu\text{m}$  thick, optically transparent film of  $\text{TiO}_2$  particles a few nanometers in size, coated with a monolayer of the ruthenium complex  $\text{RuL}_2(\mu\text{-(CN)Ru(CN)L}'_2)_2$  with L being 2,2'-bipyridine-4,4'-dicarboxylic acid and L' being 2,2'-bipyridine. The redox electrolyte consisted of 0.5 M tetrapropylammonium iodide and 0.04 M iodine in a mixture of 80 vol% ethylene carbonate in MeCN.

In general, a DSC is built in a sandwich arrangement of a counter electrode (CE) and a photoanode with a distance of a few micrometers. The space between the electrodes is filled with an electrolyte, usually containing a redox mediator, a supporting electrolyte and a solvent (Fig. 2.4). The non-photoactive CE (upper part in Fig. 4.2) consists of conducting glass which is coated with Pt nanoparticles, graphite or various materials under research such as poly-3,4-ethylenedioxythiophene (PEDOT).<sup>[62]</sup> This coating is applied to a transparent conducting oxide (TCO) to accelerate the reaction at the CE and to minimize

overpotentials (and thus internal energy loss) at that interface. The photoanode consists of glass coated with TCO, most often fluorine-doped tin oxide (FTO). Commonly, a compact blocking layer of  $\text{TiO}_2$  is applied between the conducting glass and the nanoparticulate  $\text{TiO}_2$  film to avoid a direct recombination of injected  $e^-$  from the back contact with the oxidized mediator species (rec1 in Fig. 2.5). This behavior was studied by Grätzel and co-workers.<sup>[63]</sup> A second, nanoparticulate and porous  $\text{TiO}_2$  layer is attached on top of the blocking layer. Thereby, the surface area is increased in order to obtain a better sensitizer adsorption and a good electron transport. This porous  $\text{TiO}_2$  layer is sensitized with a dye.

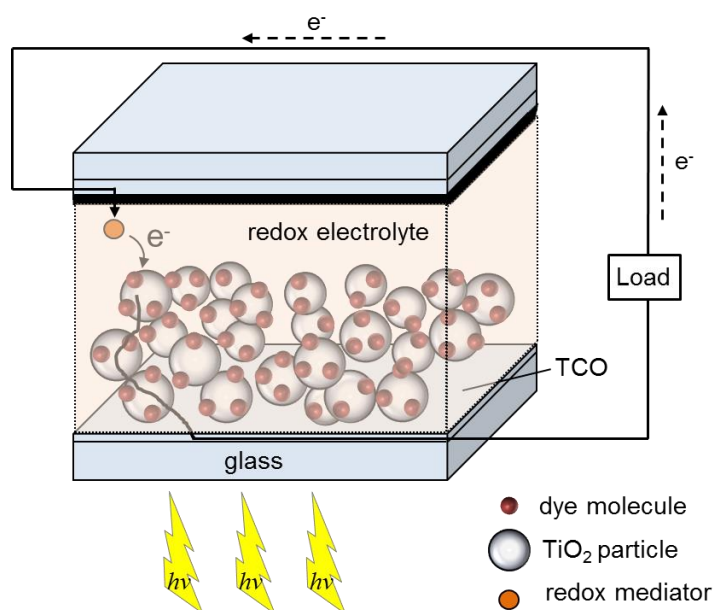


Fig. 2.4 – Schematic structure of a DSC.

For a proper functioning of a DSC it is crucial to match substrate roughness, dye photochemistry, CE kinetics and the redox electrolyte chemistry. Many researchers have taken this statement to heart and developed new dyes and redox mediators and varied parameters such as porosity and layer thickness of the semiconductor material to achieve an optimum electron transport through the semiconductor interface. In a nanocrystalline semiconductor such as the one used for those DSCs investigated in this thesis, the charge separation is mainly determined by electron kinetics at the semiconductor/dye/electrolyte interface, rather than by built-in electric fields (Schottky barriers).<sup>[64]</sup> This thesis aims to contribute to the understanding of semiconductor/redox electrolyte interfacial kinetics.

## 2.3.2 Operation Principle and Kinetics of a DSC

To understand the processes within a DSC, it is necessary to take a look on the operation principle (Fig. 2.5).

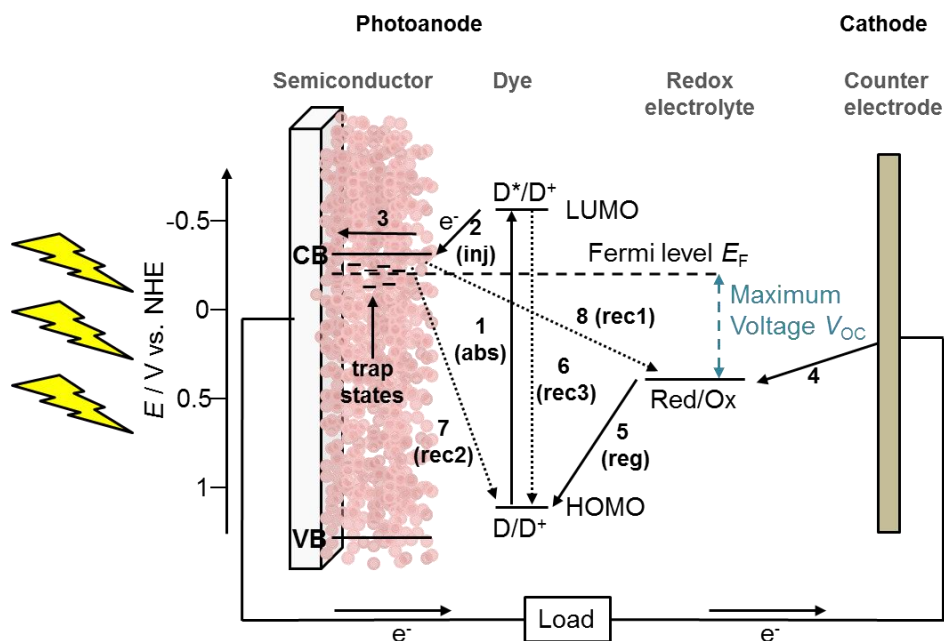


Fig. 2.5 – Detailed scheme of the processes within an illuminated DSC where solid arrows refer to wanted and dotted arrows to unwanted processes, adapted from Grätzel.<sup>[42]</sup>

In contrast to first generation Si solar cells, where photons are converted into electron-hole pairs during light absorption and the charge is separated by the internal electric field, these two fundamental processes are separated in a DSC. When photons of energy  $h\nu$  hit the photoanode (left side in Fig. 2.5), the dye molecule (diameter approx. 1 nm) in its ground state  $D$  absorbs a photon. An electron  $e^-$  is elevated from the HOMO to the LUMO and the dye is excited to  $D^*$  (abs). Then,  $D^*$  injects an  $e^-$  with a certain reaction rate constant  $k_{inj}$  into CB of a semiconductor (inj), usually in the time dimension of  $10^{-14}$  to  $10^{-11}$  s.<sup>[65]</sup> After this process, the dye is left in its oxidized form as  $D^+$ . The electron in the CB diffuses through the dye-sensitized spherical semiconductor nanoparticles (diameter approx. 30 nm). It would be ideal for the efficiency of a DSC, if the electron would diffuse straight through the semiconductor layer to rapidly reach the TCO. However, during the electron transport through the nanoporous  $TiO_2$ , electrons are trapped and detrapped in so-called trap states. Those trap states (illustrated as small lines above and below  $E_F$  in Fig. 2.5) were

extensively studied by Bisquert *et al.*<sup>[66]</sup> and appear to be distributed exponentially with respect to the energy scale. It is possible that some CB electrons remain close to the interface between the semiconductor and electrolyte solution and, under illumination, recombine with Ox (rec1) or with  $D^+$  (rec2) instead of passing through the semiconductor layer. To avoid the latter recombination process, the regeneration of the dye by the redox mediator (reg) needs to be faster than rec2. In the dark, where no  $D^+$  is present, only recombination of the CB electrons with the redox species could occur (rec1). When the electron finally reaches the TCO at the back contact of the photoanode, it is fed into the external circuit. The electron powers a load and follows its way to the CE (cathode side) where the oxidized form of the redox mediator (Ox) accepts this electron and is reduced (Red) (reaction 4). Red is transported by diffusion and migration to the photoanode where it regenerates the photooxidized dye  $D^+$  (reg) by re-reduction and leaves the dye in its original, neutral form D. With this last step, the electrical circuit is closed. During the electron transfer from Red to  $D^+$ , the redox mediator is oxidized to Ox (in this thesis  $[\text{Co}(\text{bpy})_3]^{3+}$ ) with a reaction rate constant  $k_{\text{ox}}$ .

**Advantages and Disadvantages of a DSC.** In terms of its lower cost, its aesthetical appearance and its transparency, a DSC is an attractive alternative to conventional Si solar cells. The setup of a DSC allows the sunlight to enter the cell from various angles with almost no decrease in efficiency because the light is refracted and reflected within the semiconductor layer to harvest the highest amount of light possible. Therefore, DSCs can be employed in diffusive daylight and inside houses, reliably producing energy and outperforming competitive technologies. Bifacial cells even capture light from all angles. Furthermore, the heating of the silicon solar cells due to sunlight reduces their efficiency, whereas DSCs are only slightly influenced by this heating. The devices are lightweight and the production cost is low while the design opportunities, such as transparency and multicoloring, are high. Sufficient material is available to build DSCs which produce energy in the terawatt scale and the energy payback time is less than one year.<sup>[59]</sup> Due to the possibility of producing transparent DSCs by using dyes that absorb radiation in the infrared (IR) and ultraviolet (UV) region, it is possible to integrate DCSs into house facades or windows as building integrated photovoltaics (BIPV). The large variety of dyes comes along with a lot of possible designs and provides a high light harvest. By applying more than one dye,

the absorption spectra can also be extended and varied in an infinite number of ways. A combination of three different cyanine dyes, absorbing in the blue, yellow and red region, respectively, gained higher efficiencies than each dye applied alone.<sup>[67]</sup> Another approach was followed by combining the “black dye”, a Ru complex (also known as N749), with the organic indoline-based dye D131 in a one-pot reaction, which gained an efficiency of 11 %.<sup>[68]</sup>

It cannot be neglected that DSCs have some drawbacks. There is, for example, a dispute regarding the thickness of dye layers. While a monolayer absorbs 1 % of sunlight at best, a thicker dye layer acts as a filter.<sup>[59]</sup> To solve this problem the semiconductor surface was increased by employing a porous film of TiO<sub>2</sub> nanocrystals in order to gain a higher light absorption. Also, to seal liquid electrolyte DSCs for long-term use is still a problem due to the usually aggressive solvents and their high vapor pressure. While designing DSCs, it must be kept in mind that every advantage is a possible disadvantage. For example, a high surface area within the TiO<sub>2</sub> layer is advantageous because the light harvesting is improved due to more dye molecules which can adsorb on a larger TiO<sub>2</sub> surface. On the opposite, a larger surface area is also related to more grain boundaries which increase the possibility of electrons being trapped within the TiO<sub>2</sub> layer. Additionally, a higher number of traps increases the probability of a recombination of the electrons and the oxidized dye.

Solar cells based on perovskites have very recently shown to be a huge competitor to DSCs. Zhou *et al.*<sup>[69]</sup> gained an efficiency of 19.3 % with a perovskite solar cell. However, they are far behind in long-term stability and stability against moisture compared to DSCs. They also contain lead which is environmentally problematic.

## 2.4 Importance of the Dye

### 2.4.1 Requirements of Dyes

As the name of the device suggests, the dye is one of the key components of a DSC. A dye is referred to as a “sensitizer” when it triggers a photochemical process at a reactive surface by transferring absorbed light energy. Interesting reviews on the optimization of

dyes<sup>[70]</sup> and on natural dye photosensitizers for DSCs<sup>[71]</sup> are available. A dye needs to fulfill some prerequisites in order to be employed in a DSC:<sup>[59]</sup>

- A dye needs to have an anchoring group, usually a carboxylic or a phosphoric acid group, allowing for a strong binding to the TiO<sub>2</sub>. A strong binding ensures a high electronic coupling between the dye and the semiconductor. This leads to a fast and efficient electron injection into the CB of TiO<sub>2</sub> and thus a high photo current.
- Furthermore, the dye should be photostable as well as electrochemically and thermally stable.
- In case of an n-type semiconductor, the energy of the LUMO of the dye needs to be sufficiently high to drive an efficient charge injection into TiO<sub>2</sub>. At the same time, the HOMO needs to be energetically low enough to receive electrons from the redox mediator to be reduced (compare Fig. 2.5).
- The electron transfer from the excited dye D\* to TiO<sub>2</sub> needs to be faster than the decay to the energetic ground state of the dye D.<sup>[72]</sup>
- Ideally, a sensitizer in a single junction solar cell should absorb all light below a threshold wavelength of about 920 nm in order to be excited by the sunlight. Herein, the dye architecture is important because a higher  $\pi$ -conjugation increases the extinction coefficient  $\epsilon$  in the visible range.

### 2.4.2 Dyes under Investigation

The electromagnetic spectrum of the sun shows a maximum at a wavelength of 500 nm which corresponds to blue-green light (Fig. 2.6A). To collect and convert as many photons into electrons as possible, dyes which absorb light in this wavelength range are favored. The dyes investigated in this thesis have been chosen accordingly and absorb light in this region as shown by ultraviolet-visible (UV-Vis) spectroscopy (Fig. 2.6B).

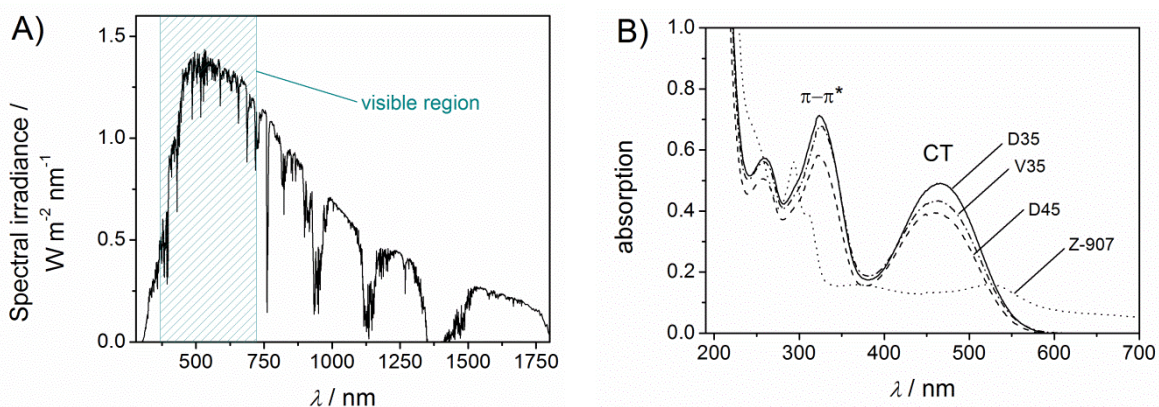


Fig. 2.6 – A) Solar spectrum for AM1.5 irradiation<sup>[73]</sup> with visible region marked. B) UV-Vis spectra ( $\approx 0.2$  mM solutions) of the triphenylamine-based dyes D35 (solid line,  $\lambda_{\text{max}} = 462$  nm), D45 (dashed line,  $\lambda_{\text{max}} = 460$  nm) and V35 (dash-dotted line,  $\lambda_{\text{max}} = 463$  nm) as well as the Ru-based dye Z-907 (dotted line,  $\lambda_{\text{max}} = 369$  and 526 nm), in MeCN. Different absorption intensities result from slightly different concentrations and can be neglected. Due to small particles in the Z-907 solution, the light was scattered and prevented a zero base line.

The three triphenylamine-based dyes D35, D45 and V35 exhibit absorption bands in the visible region of the electromagnetic spectrum which can be attributed to charge transfer (CT) processes resulting from a donor-acceptor transition. The maximum intensities are at  $\lambda_{\text{max,D35}} = 462$  nm,  $\lambda_{\text{max,D45}} = 460$  nm and  $\lambda_{\text{max,V35}} = 463$  nm. The  $\pi-\pi^*$  transition is in the UV range at 323 nm. Z-907 shows both metal-ligand charge transfer (MLCT) transitions ( $4d-\pi^*$ ) at 526 and 369 nm as well as two ligand-centered charge transfer (LCCT) transitions ( $\pi-\pi^*$ ) at 304 and 294 nm. For the studies in this thesis, the dyes were adsorbed onto  $\text{TiO}_2$  films. When D35 adsorbs to  $\text{TiO}_2$ , the absorption peak is red-shifted by about 15 nm.<sup>[74]</sup> This behavior was quite similar for V35 where the red-shift occurred by a few nm.<sup>[24]</sup>

D35 was developed in 2009<sup>[23]</sup> and from that date on used by several groups for sensitization<sup>[10, 75, 76]</sup> and co-sensitization.<sup>[77, 78]</sup> D35 shows good device stability after storing it for at least 1000 h at 85 °C both in the dark and under illumination. As is typical for organic metal-free dyes, D35 as well as the structurally similar D45 do not need co-adsorbents.<sup>[76]</sup> Since the development of DSCs, Ru-based dyes such as Z-907 and N-719 have been and still are of great academic interest. They give high PCE due to their comparably high extinction coefficients which offer the possibility to design a very thin semiconducting film, thereby enhancing the mass transport.<sup>[79]</sup> Also, a closely packed dye mono-

layer is necessary for maximal sensitization effectiveness. However, the world record efficiency of 14.7 % DSCs is currently held by an organic dye.<sup>[11]</sup> Noble metal-containing dyes are expensive though and the aim is to replace them by organic, metal-free dyes. Organic dyes are environmental more friendly, facile to synthesize, also have a high extinction coefficients and their absorption spectral response is tunable from the visible to the near infrared (NIR) region of the solar spectrum.<sup>[79]</sup>

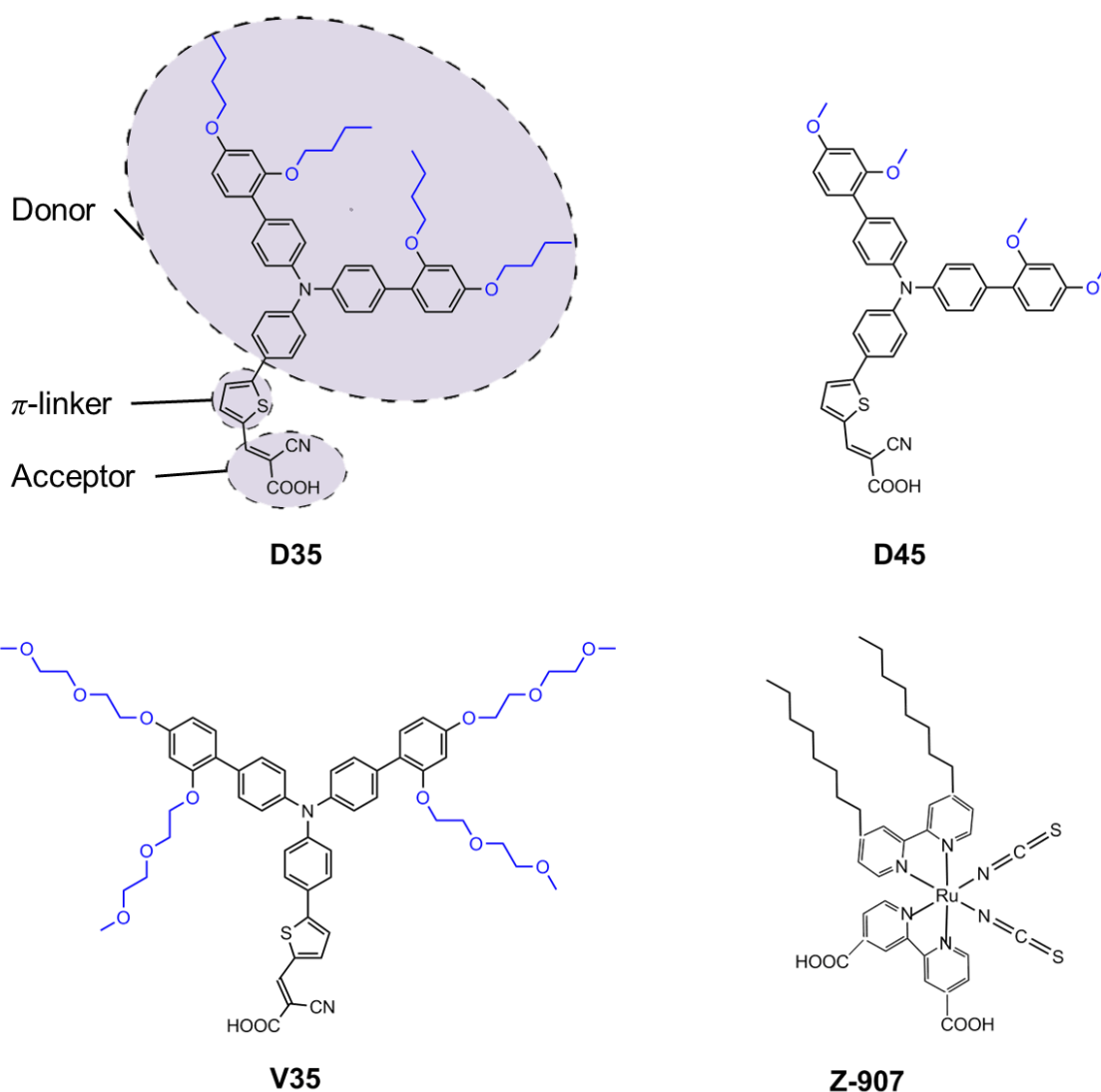


Fig. 2.7 – Dyes used for dye regeneration studies and lateral imaging of photoanodes: triphenylamine-based dyes D35, D45 and V35 as well as the Ru-based dye Z-907.

In this thesis, both metal-containing and all-organic dyes were investigated. The organic and metal-free triphenylamine-based dyes D35<sup>[10]</sup>, D45<sup>[80]</sup> and V35<sup>[24]</sup> as well as the Ru-based dye Z-907 were used (Fig. 2.7). Z-907 as an established high performance dye was

employed to test the new system with  $[\text{Co}(\text{bpy})_3]^{2+/3+}$  for its applicability in SECM measurements. Liu *et al.*<sup>[81]</sup> showed that  $[\text{Co}(\text{bpy})_3]^{2+/3+}$  works in combination with the dye Z-907 and they obtained a PCE of 8.5 % with octadecylphosphonic acid (OPA) as co-adsorbent in the ratio OPA : Z-907 of 1 : 18 under full sunlight. For the SECM measurements performed in this thesis, the co-adsorbent OPA was omitted in order to keep the investigated system as simple as possible.

The three triphenylamine-based dyes D35, D45 and V35 show similarities in their architecture because they belong to a class of dyes called donor-( $\pi$ -linker)-acceptor (D- $\pi$ -A) dyes which represent a famous group of metal-free dyes. Besides the triphenylamine unit, they have the same phenyl thiophene-2-yl-2-cyanoacrylic acid unit which acts as linker to the semiconductor of a DSC. Also, all three dyes have two 1,1'-biphenyl units with electron donating alkoxy chains in 2' and 4' positions. However, these chains differ in length and hydrophilicity. The oligoethylene glycolic chains of V35 are more hydrophilic than the *n*-butoxy chains of D35 and the *n*-methoxy chains of D45, respectively.<sup>[24]</sup> An attractive feature of D- $\pi$ -A dyes is their modular concept (Fig. 2.8) which offers the possibility to control and tune their structural and hence electronic and spectroscopic properties, such as the enhancement of the photovoltaic response. This can be achieved by substitution of each of the three modules to adjust the dye molecule to the properties of the semiconductor and the redox mediator.



Fig. 2.8 – Modular concept of donor -  $\pi$  - acceptor dyes.

The name originates from an electron-rich donor unit (tertiary amine), the  $\pi$ -conjugated linker thiophene, and an electron-deficient acceptor (cyanoacrylic acid).<sup>[82]</sup> The HOMO of the donor and the LUMO of the acceptor are dictating the HOMO-LUMO gap of the dye molecule under the influence of the linker.<sup>[83]</sup> The bridging thiophene unit between the carboxylic anchoring group and the donor is necessary to provide the conjugation of the aromatic system and to increase the extinction coefficient. The electron acceptor group  $\text{C}\equiv\text{N}$  leads to a higher optical response by decreasing the gap between the HOMO and the LUMO, which induces a red-shift. In general, there are three ways for a dye to attach to a semiconductor: monodentate, bidentate and bridging. The dyes employed in this thesis

bind as bidentate ligands to the  $\text{TiO}_2$  via the formation of two O bridges over the acrylic acid unit.

A drawback of the D- $\pi$ -A dyes under investigation, which is a general disadvantage of organic dyes, is the relatively narrow absorption spectrum (see Fig. 2.6) which has been addressed by Gabrielsson *et al.*<sup>[82]</sup> with regard to D35. In Gabrielsson's study, the  $\pi$ -linker unit was modified systematically to enhance the visible light absorption to the red wavelength region, thus achieving a higher IPCE. Phthalocyanines exhibit absorption maxima near 700 nm with high extinction coefficients. However, they show low PCE, probably due to aggregation and a lack of directionality in the excited state.<sup>[84]</sup> Efficient electron transfer from the excited dye to the  $\text{TiO}_2$  CB can be achieved by a good electronic coupling between the LUMO of the dye and the Ti 3d orbital which relies on a well-engineered molecular sensitizer with HOMO and LUMO adjusted to the CB of  $\text{TiO}_2$ . Z-907 exhibits another operating principle and absorbs light in the long-wave visible range. It undergoes a MLCT, leaving the metal center positively charged.

Besides triphenylamine-based dyes, different other organic dye classes are employed in DSCs such as porphyrines,<sup>[85]</sup> coumarine dyes,<sup>[86]</sup> indoline dyes,<sup>[87]</sup> squaraines<sup>[88]</sup> and very recently ullazine-based sensitizers combined with 2,2',7,7'-tetrakis-(N,N-di-4-methoxyphenylamino)-9,9'-spirobifluorene (better known as spiro-MeOTAD) as a hole transport material.<sup>[89]</sup>

Generally, a dye can be structurally tailored in a way that the open-circuit potential  $V_{\text{OC}}$  of a DSC (see Fig. 2.5) is increased due to retardation of the recombination between injected electrons and the oxidized form of the redox mediator (rec1 in Fig. 2.5). Kroeze *et al.*<sup>[90]</sup> also showed the importance and influence of dye architecture with respect to the overall cell performance. They varied the length of the alkyl chains on the basis of the dye Z-907 and observed a significant retardation of the charge recombination of injected electrons with oxidized sensitizers (rec2 in Fig. 2.5) with increasing alkyl chain length from R =  $\text{CH}_3$  to R =  $\text{C}_{13}\text{H}_{27}$ ). Co-sensitization is another approach in which different sensitizers are employed in order to broaden the photocurrent-action spectrum and, in the best case, to cover the entire visible domain which is known as panchromatic sensitization which was successful very recently employing D35 as co-sensitizer and a new organic dye called AP3 with dual donors and dual anchor-acceptors.<sup>[91]</sup> In 2000, Hagfeldt and Grätzel<sup>[92]</sup> presented an account on the molecular engineering of efficient heterogeneous electron-transfer sensi-

tizers and questioned the factors which afford the quantitative charge separation at the dye/semiconductor interface.

## 2.5 Redox Electrolytes

### 2.5.1 Different Types of Redox Electrolytes

Redox electrolytes in DSCs commonly consist of a redox mediator, a supporting electrolyte and in some cases some additives such as *n*-methylbutyl imidazole (NMBI) to push up the TiO<sub>2</sub> CB edge aiming to increase the solar cell potential.<sup>[22]</sup> The redox mediator is especially important for a stable DSC operation since it regenerates the oxidized dye D<sup>+</sup>. Depending on their physical properties and their charge transfer processes, redox electrolytes for DSCs are divided into different categories (Fig. 2.9).

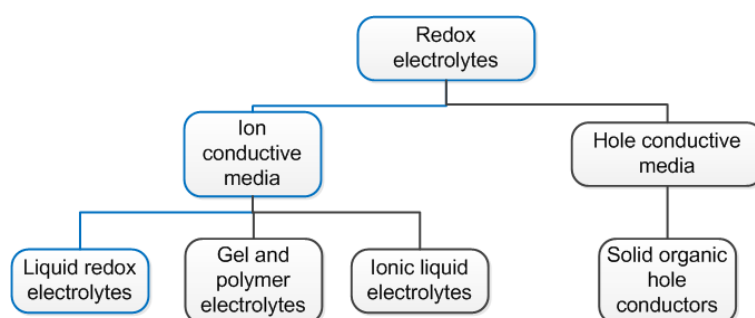


Fig. 2.9 – Classification of redox electrolytes employed in DSCs (whole scheme) and in this thesis (blue frames).<sup>[59]</sup>

In DSC research, different types of electrolytes employing different charge transfer processes are under investigation. A good overview can be found elsewhere.<sup>[59]</sup> In this thesis, [Co(bpy)<sub>3</sub>]<sup>2+/3+</sup> was employed in different solvents as liquid ion conductive electrolyte (framed blue in Fig. 2.9). MeCN was the most often used solvent in this thesis as it shows good solubility towards metal organic complexes such as the employed [Co(bpy)<sub>3</sub>]<sup>2+/3+</sup> complex, building the basis for a good accessibility of the TiO<sub>2</sub> sites by the redox mediator. A disadvantage of MeCN is its high vapor pressure and high volatility which demands good engineering of the sealing materials of the DSCs. Due to its low viscosity, the diffusion coefficient of the active redox mediator is much higher than in an ionic liquid which is more viscous. Tefashe *et al.*<sup>[21]</sup> showed that the dye regeneration rate of dye N-719 was by

two magnitudes higher in MeCN compared to the room temperature ionic liquid 1-ethyl-3-methylimidazolium bis-(trifluoromethylsulfonyl)-imide (EMimTFS). However, ionic liquids are advantageous in terms of non-volatility which is a prerequisite for a long-term stability. Because organic solvents such as MeCN are volatile, flammable and hazardous, attempts were made to use a  $[\text{Co}(\text{bpy})_3]^{2+/3+}$  containing aqueous electrolyte. Xiang *et al.*<sup>[22]</sup> employed  $[\text{Co}(\text{bpy})_3]^{2+/3+}$  in aqueous media with polyethylene glycol 300 (PEG300) added as wetting agent to enable the redox couple to reach a hydrophobic dye-sensitized sample surface and obtained a PCE of 5.1 %.

In contrast to liquid and ionic liquid electrolytes, where charges are transported by redox mediators, in a solid hole conductor a positive charge (“hole”) “hops” between neighboring molecules or moieties. Using hole transport materials (HTM) follows a general trend to build solid-state DSCs that circumvent the problem of electrolyte leaking however with comparably low efficiencies. Spiro-OMeTAD, an established HTM, achieved very good performances in both solid-state DSCs and perovskite cells. However, due to the high synthetic cost of Spiro-OMeTAD, other spiro-structured HTMs were recently developed as environmentally more friendly alternatives. Those showed a PCE of 7.3 % in a solid-state DSC.<sup>[93]</sup>

**Prerequisites of Redox Mediators.** It would be preferable to use thoroughly investigated redox mediator couples such as ferrocenium/ferrocene ( $\text{Fc}^+/\text{Fc}$ ), the standard redox mediator in electrochemistry. However, this particular redox mediator is not suitable for the application in solar cells since the recombination of the oxidized redox species  $\text{Fc}^+$  and the photoinjected electrons is very fast and eliminates the photovoltaic effect.<sup>[94]</sup> In order to be suitable for use in a DSC, a redox mediator must fulfill some prerequisites:<sup>[95]</sup>

- The redox potential of a redox mediator needs to be higher than that of the dye in order to reduce the oxidized dye. The redox potential should enforce a sufficiently high driving force to reduce the dye but still achieve a high  $V_{\text{OC}}$  (see also Fig. 2.11), since  $V_{\text{OC}}$  of a DSC is determined by the difference between the Fermi level under irradiation and the redox potential of the mediator.
- Moreover, the charge recombination should be slow in order to prevent a recombination of the electrons in the  $\text{TiO}_2$  with the oxidized species of the redox couple (compare step 8 in Fig. 2.5).

- Additionally, a high turnover number of the redox shuttle is necessary to build a long-term stable DSC.

### 2.5.2 Cobalt Complexes as Redox Mediators

Cobalt is a transition metal in the seventh transition group of the periodic table of the elements and builds, along with iron and nickel, the iron group. Cobalt shows the stable oxidation state of +2 in salts, in complexes, however, Co(II) is easily oxidizable so that Co(III) complexes are more stable. Co(III) builds characteristically octahedral diamagnetic low-spin complexes in the configuration  $t_{2g}^6$  which are intensively colored. Whether a transition metal ion with a  $d^4$ ,  $d^5$ ,  $d^6$  or  $d^7$  configuration is in a high spin (HS) or low spin (LS) state depends on the difference between the spin pairing energy and the energy difference between the two d-orbitals  $t_{2g}$  and  $e_g$ , the so-called ligand field splitting  $\Delta$ . Due to the splitting of the d-orbitals, an energy gain occurs for the d-electrons in most of the electron configurations. This energy gain is called ligand field stabilization energy (LFSE). The LFSE is high for  $Co^{3+}$ , which is in a  $d^6$  configuration in a low spin state, because only the energetically favorable  $t_{2g}$  level is occupied with 6 electrons.<sup>[96]</sup>

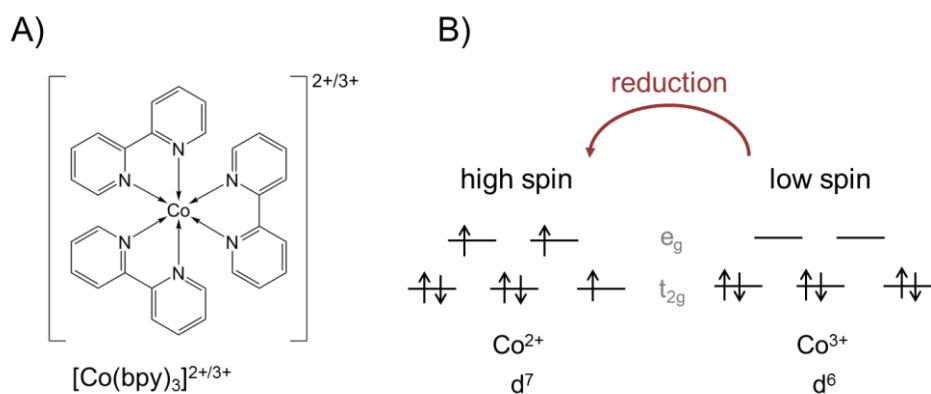


Fig. 2.10 – A) Structure of  $[Co(bpy)_3]^{2+/3+}$  cation of complexes employed in this thesis and B) electron configuration of high spin  $Co^{2+}$  ions and low spin  $Co^{3+}$  ions.

An electron of an occupied molecular orbital that belongs to the metal (for example from an occupied d-orbital) is excited to an energetically higher empty molecular orbital of ligand character such as a  $\pi^*$  orbital of equal symmetry of a bipyridine ligand.  $[Co(bpy)_3]^{2+/3+}$  (Fig. 2.10A) is a one-electron outersphere redox couple which undergoes a spin change

during the reduction from LS in  $\text{Co}^{3+}$  ( $d^6$ ) to HS in  $\text{Co}^{2+}$  ( $d^7$ ) (Fig. 2.10B).  $[\text{Co}(\text{bpy})_3]^{2+}$  is a complex with a  $t_{2g}^5 e_g^2$  ground state which at room temperature is mainly present in its HS state.<sup>[97, 98]</sup>

In  $[\text{Co}(\text{bpy})_3]^{2+/3+}$ , Co is in the first coordination sphere coordinated sixfold by three bidentate 2,2'-bipyridine ligands, building an octahedron. Tris-chelated Co(II/III) complexes such as  $[\text{Co}(\text{bpy})_3]^{2+/3+}$ ,  $[\text{Co}(\text{phen})_3]^{2+/3+}$  and  $[\text{Co}(\text{py-pz})_3]^{2+/3+}$  have provided high DSC efficiencies<sup>[99]</sup> and promising results have been obtained using Co(II/III) redox mediators in combination with organic dyes.<sup>[10, 100-102]</sup> A further and important step towards the applicability of Co complexes was done by Feldt *et al.*<sup>[10]</sup> They employed the organic dye D35 in combination with  $[\text{Co}(\text{bpy})_3]^{2+/3+}$  and reached a PCE of 6.7 %, thus paving the way for further considerations of Co complexes as redox mediators in DSCs. Transition metal complexes with organic ligands are relatively easy to tailor to a certain redox potential and hence to adjust them to the redox potential of nearly every dye.<sup>[9]</sup> The use of  $[\text{Co}(\text{bpy})_3]^{2+/3+}$  in conjunction with  $\text{TiO}_2$  co-sensitized with a D- $\pi$ -A zinc porphyrin dye yielded an efficiency of up to 12.3 %, <sup>[103]</sup> a higher efficiency than the original DSC.<sup>[6]</sup> The world record of DSCs with PCE of 13 % using a panchromatic D- $\pi$ -A porphyrin dye combined with  $[\text{Co}(\text{bpy})_3]^{2+/3+}$ <sup>[85]</sup> was recently increased to a PCE of 14.7 % by a co-sensitization of a silyl-anchor dye and a carboxy-anchor dye employing  $[\text{Co}(\text{phen})_3]^{2+/3+}$  as redox mediator in a lab module.<sup>[11]</sup> As literature states, the key for high PCE can be reached by shifting the distribution of Co(III) ions away from the semiconductor surface.<sup>[99]</sup>

### 2.5.3 Cobalt Complexes vs. Iodide/triiodide

The mediator of choice in DSCs today is  $\text{I}/\text{I}_3^-$  whose major advantage is the slow interception of electrons at the  $\text{TiO}_2$  surface minimizing the recombination losses in a DSC. However,  $\text{I}/\text{I}_3^-$  shows some drawbacks. The redox mechanisms are complex which complicates simulations of the working principle of a DSC implementing  $\text{I}/\text{I}_3^-$ . A huge drawback is the fact that it absorbs light in the visible range where the sun's light has the highest intensity (compare Fig. 2.6A). In general, Co complexes have smaller extinction coefficients than  $\text{I}/\text{I}_3^-$  which is preferred because the dye rather than the redox mediator should absorb as much light as possible. Furthermore,  $\text{I}/\text{I}_3^-$  is corrosive towards metallic electrodes and seal-

ing materials of DSCs<sup>[104-107]</sup> mainly due to  $I_2$  which is a product of the redox process. Another disadvantage of  $I^-/I_3^-$  is its large driving force for the dye regeneration which generates an internal potential loss and leads to a smaller  $V_{OC}$  (Fig. 2.11).  $V_{OC}$  is determined by the difference of the Fermi level  $E_F$  of the semiconductor and the Nernst potential  $E^\circ$  of the redox mediator. The driving force is the potential difference of  $E^\circ$  of the redox mediator and the redox potential of the dye. It is significantly higher for  $I^-/I_3^-$  than for  $[Co(bpy)_3]^{2+/3+}$  (compare both dashed red arrows in Fig. 2.11). With  $[Co(bpy)_3]^{2+/3+}$ , the driving force is lower which directly leads to a higher cell voltage (compare both dotted blue arrows in Fig. 2.11) and consequently a higher efficiency.

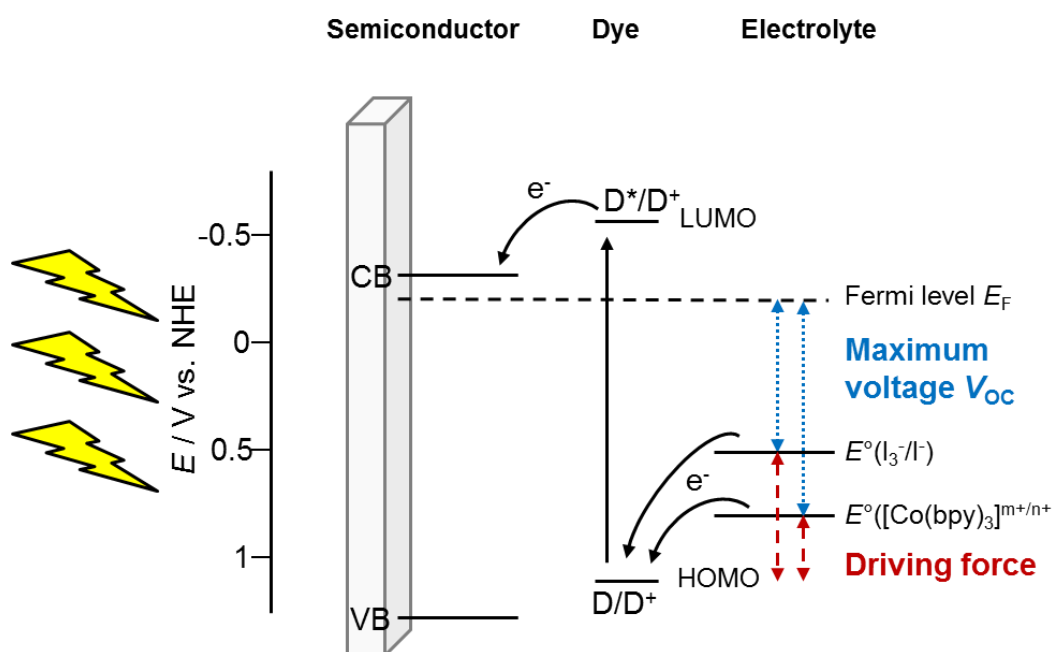


Fig. 2.11 – Comparison of the energetics of the  $I^-/I_3^-$  and the  $[Co(bpy)_3]^{2+/3+}$  with regard to the driving force and the resulting increased maximum cell voltage  $V_{OC}$ , adapted from Boschloo and Hagfeldt.<sup>[8]</sup>

The striving of the mediator to release an electron always needs to be higher than the striving of a dye to accept a CB electron. In other words, the redox electrolyte potential should be large enough to provide a sufficient driving force for fast dye regeneration in order to suppress the unwanted recombination of CB electrons with  $D^+$  (rec2 in Fig. 2.5). On the contrary, the potential should be as close as possible to the HOMO of D to maximize the  $V_{OC}$ . It is possible to tailor the ligands of Co complexes to adjust them to the potential of the dye employed which opens the way for applying a huge number of different dyes. In

order to follow this approach, Feldt *et al.*<sup>[102]</sup> combined the triphenylamine-based dye D35 with a series of  $[\text{Co}(\text{bpy})_3]^{2+/3+}$  and  $[\text{Co}(\text{phen})_3]^{2+/3+}$  redox couples and gained  $V_{\text{OC}}$  values above 1 V. It is necessary to use Co complexes with bulky ligands to prevent a back reaction from CB electrons with the redox mediator (rec1 in Fig. 2.5).<sup>[100]</sup>

Co mediators show some disadvantages as well. The unwanted recombination of electrons in  $\text{TiO}_2$  with the oxidized species of outersphere one-electron redox mediators, such as the Co complex, is much faster compared to  $\text{I}/\text{I}_3^-$ .<sup>[94]</sup> Also, mass transport of Co complexes is slow compared to the  $\text{I}/\text{I}_3^-$  mediator.<sup>[108]</sup> Attempts to increase the mass transport were made by optimizing the pore size as well as the porosity of the semiconductor material. Kim *et al.*<sup>[109]</sup> could substantially improve the mass transport of  $[\text{Co}(\text{bpy})_3]^{2+/3+}$  with a porosity of about 60 % and a pore size of approximately 24 nm. In a study,<sup>[99]</sup> photovoltaic characteristics under 1 sun simulated sunlight ( $100 \text{ mW cm}^{-2}$ ) of different combinations of two ruthenium dyes N-719 and Z-907 gave drastically lower performances for  $[\text{Co}(\text{bpy})_3]^{2+/3+}$  as redox mediator with  $V_{\text{OC}}$  of 578 mV (N-719) to 649 mV (Z-907) compared to the same dyes in conjunction with  $\text{I}/\text{I}_3^-$  of 675 mV (N-719) and 666 mV (Z-907). This shows that an approximately 100 mV  $V_{\text{OC}}$  increase is observed for  $\text{I}/\text{I}_3^-$  compared to  $[\text{Co}(\text{bpy})_3]^{2+/3+}$  in conjunction with N-719 whereas the  $V_{\text{OC}}$  difference in conjunction with Z-907 is negligible.

#### 2.5.4 Alternative Redox Electrolytes

Besides  $\text{I}/\text{I}_3^-$  and Co complexes one can think of many other molecules to use as redox mediators. Pseudohalides such as  $(\text{SeCN})_2/\text{SeCN}^-$ <sup>[110]</sup> as well as bulky ligand transition metal complexes<sup>[10, 102, 111, 112]</sup> and tetrathiafulvalene<sup>[75]</sup> as one-electron redox systems were under investigation, the latter redox mediator in combination with the all-organic dye D35. Other two-electron redox mediators similar to  $\text{I}/\text{I}_3^-$  were investigated as alternatives. Examples are disulfide/thiolate<sup>[113]</sup> which absorbs light of a small wavelength range only and the organic redox couple consisting of 2-mercapto-5-methyl-1,3,4-thiadiazole and a disulfide dimer<sup>[114]</sup> which gave an efficiency of 4.0 %. Still, their complexity in electron transfer is disadvantageous and redox mediators with simpler kinetics may require lower energy expenditure for dye regeneration which is associated with a higher  $V_{\text{OC}}$  of the DSC.<sup>[99]</sup>

Very recently, DSCs employing manganese complexes along with the Ru dye N-719 were built and gave a PCE of 4.4 %.<sup>[115]</sup>

## 3 Fundamentals of Experimental Methods

### 3.1 Conventional Characterization Methods of Dye-Sensitized Solar Cells

Despite many investigations within the last ten to 20 years, the precise working principle of a DSC is not fully understood yet. In general, DSCs are characterized by solar cell performance measurements such as current density-voltage characteristics ( $j$ - $V$ -characteristics) and the resulting fill factors ( $FF$ ) as well as the spectral response, e.g. IPCE. Other interesting parameters are the electron lifetime and the electron transport time which are determined by time-resolved techniques,<sup>[116]</sup> IMVS, IMPS and EIS<sup>[117]</sup> at several  $V_{OC}$ . DSC kinetics are generally analyzed by nano-second TAS<sup>[102]</sup> and photo-induced absorption spectroscopy (PIA).<sup>[118]</sup> The energy level determination of DSCs is usually performed by charge extraction measurements.<sup>[48, 119]</sup> To be able to compare the performance characteristics of different solar cells, the measurements are usually performed at 1 sun ( $1000 \text{ W m}^{-2}$ ) and under AM1.5 G standard conditions. The electron transfer kinetics within DSCs were investigated *via* SECM by the author of this thesis at Carl von Ossietzky University in Oldenburg and *via* TAS,  $j$ - $V$  curves and EIS by Hanna Ellis at Uppsala University.

**Current Density–Voltage Characteristics.** One of the most widely applied and most important characterization techniques of solar cells is the  $j$ - $V$  measurement. A  $j$ - $V$  curve (solid black line in Fig. 3.1) describes the energy conversion capability of a solar cell. Under illumination, the external potential is altered from  $V_{OC}$  to the short-circuit current density ( $j_{SC}$ ), where no external voltage is applied to the cell, to yield the maximum power point  $P_{max}$ , the point at which the solar cell produces the highest amount of power (Fig. 3.1).

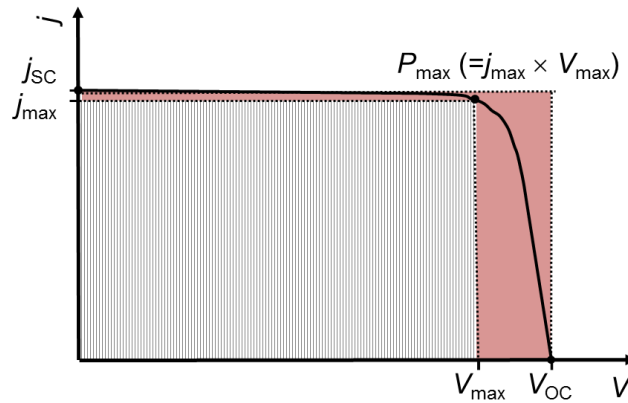


Fig. 3.1 – Schematic  $j$ - $V$  curve of a photovoltaic device.

$FF$  is introduced as the ratio of  $P_{\max}$  and the product of  $j_{sc}$  and  $V_{OC}$ .

$$FF = \frac{j_{max} \times V_{max}}{j_{sc} \times V_{oc}} \quad (3.1)$$

$FF$  is a quality factor of the  $j$ - $V$  curve and describes its squareness, meaning, the degree to which the curve deviates from an ideal  $j$ - $V$  curve (rectangle spanning from  $j_{sc}$  to  $V_{OC}$  in Fig. 3.1). A  $FF$  of unity corresponds to an ideal  $j$ - $V$  curve. In Fig. 3.1, the ratio between the red and grey shaded area yields  $FF$ .<sup>[120]</sup>  $PCE$  is the ratio of the maximum electrical power output  $P_{\max}$  to the incident solar power  $P_{in}$  (3.2) and expresses to which extent the incident power of the sun is converted into useful electrical power output.

$$PCE = \frac{P_{max}}{P_{in}} = \frac{j_{sc} \times V_{oc} \times FF}{P_{in}} \quad (3.2)$$

**Incident Photon-to-Current Conversion Efficiency.** The IPCE gives the efficiency of conversion of incoming photons into electrons for every measured wavelength  $\lambda$ , i.e. the monochromatic quantum efficiency of a device. IPCE is a dimensionless number with values between zero and unity. It is determined by illuminating the solar cell with monochromatic light, wavelength for wavelength, and measuring the photocurrent. The IPCE can be expressed as the product of the light harvesting efficiency (LHE) of the dye  $\eta_{lh}$ , the quantum yield of electron injection  $\eta_{inj}$  and the efficiency of collecting the injected electrons at the transparent back side of the DSC  $\eta_{cc}$  (equation (3.3)).<sup>[121]</sup>

$$IPCE = LHE \times \phi_{inj} \times \eta_{reg} \times \eta_{coll} \quad (3.3)$$

Thus, if the light harvesting of the dye, the charge injection into  $\text{TiO}_2$  or the collection at the back contact of a DSC are inefficient, the resulting IPCE will be low.

**Pump-probe Techniques.** TAS is a pump-probe technique which was performed by a cooperation partner at the University of Uppsala for a study jointly published with the author of this thesis.<sup>[122]</sup> It was performed in the nanosecond regime using a nanosecond laser to pump the dye molecules into an excited state and to probe them with a Xe lamp. The time constants for the following electron transfer kinetic processes were obtained by TAS (see chapter 7.4):

- the recombination of CB electrons of  $\text{TiO}_2$  with the photooxidized dye (rec2 in Fig. 2.5),
- the recombination of CB electrons of  $\text{TiO}_2$  with the electrolyte (rec1 in Fig. 2.5)
- the deactivation of the excited dye  $\text{D}^*$  back to the ground state dye  $\text{D}$  when no electron injection into  $\text{TiO}_2$  occurred (rec3 in Fig. 2.5)
- and the dye regeneration by the electrolyte (reg in Fig. 2.5) which in contrast to the three aforementioned reactions is wanted.

Photo-induced absorption spectroscopy (PIA) is another pump-probe technique exhibiting a lower time resolution compared to the TAS system. In contrast to TAS, PIA was only applied to observe the regeneration and to obtain information of whether the regeneration was taking place or not, without considering the time scale.

**Electrochemical Impedance Spectroscopy.** EIS allows the detection of resistances and losses within a DSC<sup>[123]</sup> and it has been proven to be useful for DSC characterization.<sup>[117, 124, 125]</sup> Using EIS, the resistance of the complete DSC  $R_{\text{tot}}$ , consisting of the series resistance  $R_s$ , the charge transfer resistance at the CE  $R_{\text{CE}}$ , the recombination resistance  $R_{\text{rec}}$  and the diffusion resistance of the electrolyte  $R_D$  can be determined (Fig. 3.2). The Nyquist plot shows four resistance elements which are related to the different resistances in a DSC.  $R_s$  is the sheet resistance of the TCO, for example FTO, the wires and the external contacts. The first semicircle illustrates the resistance of the charge transfer process ( $\text{Co}^{3+}$  to  $\text{Co}^{2+}$ ) at the CE  $R_{\text{CE}}$ . The resistance of the charge transport at the  $\text{TiO}_2$ /dye/electrolyte interface  $R_{\text{rec}}$  gives a resistance in the form of the second semicircle. The third semicircle is related to

$R_D$ .<sup>[126]</sup> For the analysis and interpretation of Nyquist plots, equivalent circuits are designed (Fig. 3.2B) and the obtained data are fitted to models to determine the resistances. Generally important elements of equivalent circuits are resistors  $R$ , Warburg element  $W$  describing the diffusion resistance of the redox species in the electrolyte and capacitors  $C$ . However, when constructing an equivalent circuit for a DSC, constant phase elements (CPE) are used instead of capacitors because the surfaces of the DSC (the working and counter electrodes) are not ideal capacitors.

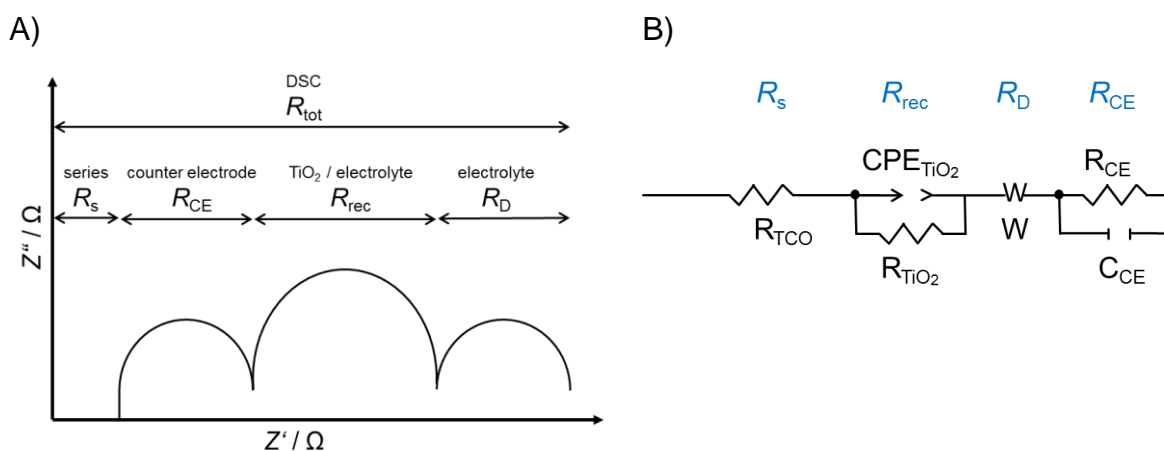


Fig. 3.2 – A) Schematic Nyquist plot of a DSC with different resistance contributions and B) equivalent circuit for a DSC adapted from Han *et al.*<sup>[126]</sup> with the modification that in this circuit instead of a capacitor a CPE is used to describe the  $\text{TiO}_2$ .

In the following, the description of the equivalent circuit for a DSC is presented. The sheet resistance of the TCO is described by a resistor ( $R_{\text{TCO}}$ ),  $R_{\text{rec}}$  is described by a CPE and a resistor in parallel,  $R_D$  is described by a Warburg element  $W$  and  $R_{\text{CE}}$  is described by a resistor and a capacitor in parallel. It is preferential to have a high  $R_{\text{rec}}$  which implies a high resistance of electrons in  $\text{TiO}_2$  moving back from the CB of  $\text{TiO}_2$  towards the oxidized redox mediator species (rec1 in Fig. 2.5) or the oxidized dye molecules (2 in Fig. 2.5) depending on the experimental conditions.

**Intensity-Modulated Photovoltage Spectroscopy.** IMVS is a technique to determine the periodic response of the photovoltage measured at open-circuit by means of a modulated light source. With this technique it is possible to obtain data about the recombination process under open-circuit conditions.<sup>[127]</sup> It is possible to measure the electron lifetime  $\tau_e$  be-

fore said electrons recombine with the oxidized species in the system (dye and redox mediator). Since no external current is flowing, all electrons stay within the cell. This setup allows the measurement of the recombination time with the oxidized species in the system.

**Intensity-Modulated Photocurrent Spectroscopy.** IMPS follows a similar approach as IMVS. At short-circuit, the periodic photocurrent response to a sinusoidal perturbation is measured to obtain information about the charge collection and the recombination under short-circuit conditions.<sup>[127]</sup>

Because commonly applied characterization methods, such as current-voltage characteristics (*IV*-curves), IMVS (intensity-modulated photovoltage spectroscopy), IMPS (intensity-modulated photocurrent spectroscopy) and IPCE, comprise all kinetic processes in a DSC, it is necessary to highlight single processes as was done in this thesis. TAS, for example, was used to measure the reaction rate constant of rec2 in Fig. 2.5 and EIS to measure the reaction rate constant of rec1 in Fig. 2.5. The results were published by the author of this thesis along with a cooperation partner from Uppsala University, Sweden, and are presented in chapter 7.4. SECM was employed to determine the reaction rate constant of reg in Fig. 2.5. Recently, Ardo and Meyer<sup>[128]</sup> published a critical review on DSC electron transfer kinetics, concluding that tremendous progress has been made towards understanding the charge-transfer processes at sensitized TiO<sub>2</sub> interfaces. However, the charge recombination process is still far away from being understood fully.

## 3.2 Microelectrodes

Microelectrodes (ME) play a vital role in SECM measurements since its quality and symmetry shape the foundation for high quality and precise images as well as approach curves and their good agreement with simulations. Several publications<sup>[129, 130]</sup> about MEs are available. There are different types of MEs, such as spherical electrodes, band electrodes and the commonly applied disk electrode. In this thesis, metal wires sealed in glass as insulating sheath were used. The disk-shaped cross-section of the metal wire forms the electrode surface. Electrodes exist in different sizes and shapes ranging from electrodes in the range of square meters to very small electrodes in the sub-micrometer range called nano-electrodes or nanodes. The latter ones are used for topographical investigations of electro-

active surfaces by SF-SECM, for example.<sup>[131]</sup> In between those superlatives, different electrode sizes exist which can either be bought or prepared by oneself. The latter option offers the possibility to adjust the electrode size and  $RG$  value (ratio of radius of the insulating material and radius of the active electrode material) to the experimental requirements. A detailed preparation is given in chapter 4.4.1.

MEs show some specific properties which make them highly suitable for analytical investigations.<sup>[132]</sup> By decreasing the electroactive surface area and thus altering the ratio of the electrode area and the electrolyte volume, the diffusion layer thickness  $\delta_N$  exceeds the radius of the electrode. As a consequence, more electroactive species reach the electrode surface per units of time and area by hemispherical diffusion to the ME in contrast to the planar diffusion prevailing at the macroelectrode (Fig. 3.3).

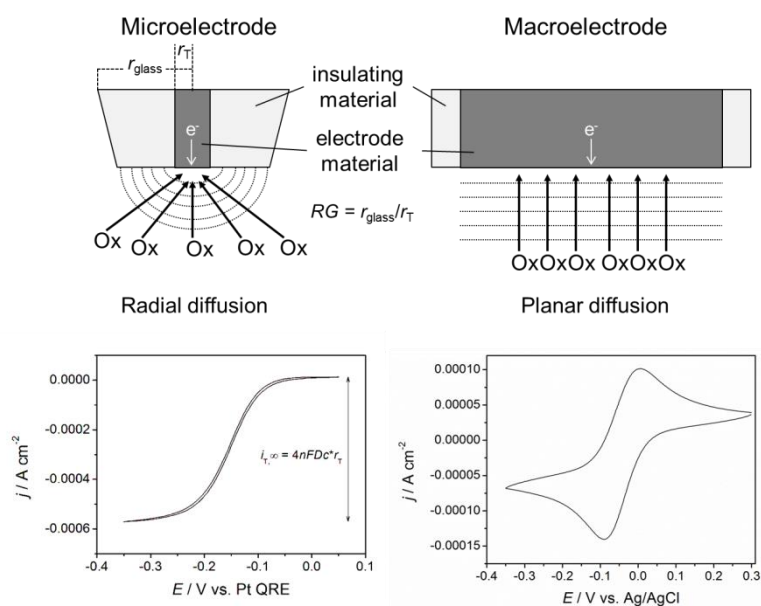


Fig. 3.3 – Top row: Diffusion behavior (arrows) and diffusion layer formation (hatched area) at a ME (left) and at a macroelectrode (right) with an oxidized redox species Ox diffusing towards the electrode. Bottom row: CV at  $v = 0.05 \text{ V s}^{-1}$  of 1 mM  $[\text{Co}(\text{bpy})_3](\text{PF}_6)_3$  in MeCN with 0.1 M TBAPF<sub>6</sub> at a Au ME ( $r_T = 12.3 \mu\text{m}$ ) with a typical sigmoidal shape (left) and at a 3 mm diameter glassy carbon macroelectrode (right).

In a spherical diffusion field, the mass transport coefficient  $m$ , which describes the speed of the molecules within a stationary diffusion layer, increases inversely proportional with the electrode radius ( $r_T$ ), leading to very high diffusion rates at very small electrode radii. The mass transport coefficient depends on the electrode shape and is  $m = \frac{4D}{\pi r_T}$  for a disk

ME.<sup>[132]</sup> Although the absolute currents are smaller at MEs than at macroelectrodes, the higher mass transport leads to higher current densities at MEs compared to macroelectrodes as shown by cyclic voltammetry (CV). This behavior directly leads to a better ratio of faradaic to capacitive current. Another special feature of MEs is the exceptionally small area (A)/volume (V) conditions. Due to the small electrode area and the relatively large surrounding electrolyte volume, the concentration of the electroactive species is not altered when current flows through the solution. Also, due to very small currents, the  $iR$ -drop ( $\Delta E$ ) is negligible<sup>[132]</sup> allowing investigation in highly resistive media without significant distortions of voltammetric signals. MEs are also suitable to determine kinetics because the reaction at the ME and thus the ME current  $i_T$  solely depends on the kinetics, and compared to a macroelectrode far less on the diffusion of the species towards the electrode.

### 3.3 Scanning Electrochemical Microscopy

#### 3.3.1 Setup and Techniques

Scanning electrochemical microscopy (SECM) is a versatile scanning probe technique to probe both electrochemical activity and/or topography of different types of substrates or of interfaces between different phases. SECM is derived from scanning tunneling microscopy (STM) whose principle relies on a tunnel current, whereas SECM is based on a faradaic current. The central element of a SECM is a ME operated as working electrode (WE) which is connected to a (bi-)potentiostat. The ME can be moved laterally and vertically with respect to a substrate. An auxiliary electrode (Aux) and a reference electrode (RE) complete the usually applied three- or four-electrode electrochemical cell (Fig. 3.4).

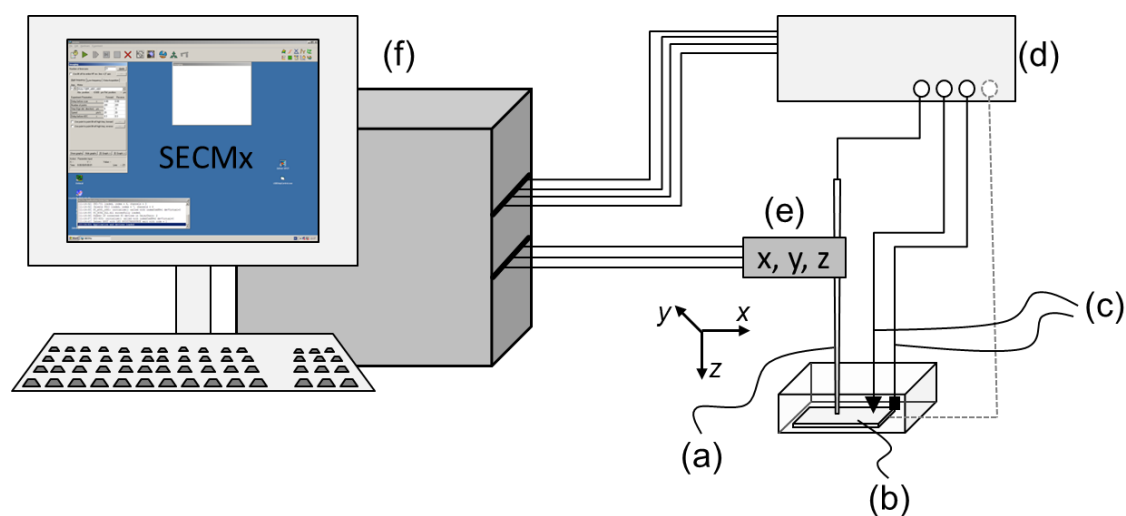


Fig. 3.4 – Schematic setup of an SECM adapted from Pust *et al.*<sup>[133]</sup> (a) ME, (b) substrate, (c) RE and Aux, (d) (bi-)potentiostat, (e) positioning system, (f) control PC.

SECM has a high spatial resolution so that differences down to the sub-micron length scale can be resolved.<sup>[13]</sup> SECM was first used by Bard *et al.*<sup>[134]</sup> who examined solid electrodes in solution. During further years, SECM was developed in different aspects and new research fields were established. SECM offers plenty of interesting applications in different research fields such as catalysis,<sup>[135, 136]</sup> for the analysis of beat fluctuations and oxygen consumption in cardiomyocytes as a medical research topic,<sup>[137]</sup> the investigation of cell membranes<sup>[138]</sup> or corrosion processes.<sup>[139]</sup> Informative reviews and a whole volume have been attributed to SECM recently.<sup>[133, 140-142]</sup> Also, an overview over 25 years of SECM applications was published in 2016.<sup>[143]</sup> Recently, SECM was used to image heterogeneous processes<sup>[144, 145]</sup> and determine redox processes on semiconductors.<sup>[146, 147]</sup> In order to enhance and further optimize the properties of SECM, it has been successfully combined with SFM<sup>[148]</sup> and scanning ion-conductance microscopy (SICM),<sup>[149]</sup> the latter offering the advantage of smaller probes, smaller  $RG$  and a very small or even no time constant until steady state conditions are established. Different measurement techniques enable SECM to be a versatile tool to study interfaces. The different techniques are:

**Approach Curves.** An approach curve is the measure of the ME current  $i_T$  as a function of the  $z$  position of the ME relative to the sample surface. Using a motor, a ME is approached towards a surface with a certain speed, generally  $1 \mu\text{m s}^{-1}$ , while  $i_T$  is recorded permanently. To compare approach curves from different experiments they are normalized by plot-

ting the normalized current  $I_T$  ( $I_T = i_T / i_{T,\infty}$ ) as a function of the normalized ME-to-substrate distance  $L$  ( $L = d / r_T$ ). The current at the ME at quasi-infinite distance ( $d > 20r_T$ ) is described by

$$i_{T,\infty} = gnFDc^*r_T \quad (3.4)$$

with  $g$  being a geometry-dependent factor related to the ME shape,  $n$  being the number of transferred electrons,  $F$  being Faraday's constant,  $D$  being the diffusion coefficient of the redox species,  $c^*$  being the bulk concentration of the redox species and  $r_T$  being the ME radius. In case of an infinite large insulator as substrate,  $g$  equals 4, which results in

$$i_{T,\infty} = 4nFDc^*r_T \quad (3.5)$$

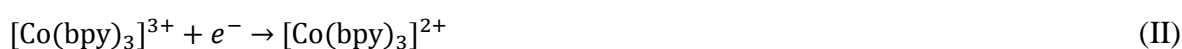
The shape of the approach curves contains kinetic information about the rate by which a mediator is regenerated at the sample surface. A least-square fitting of the approach curves to an analytical approximation by Cornut and Lefrou<sup>[150]</sup> (section 3.3.2) is influenced by mass transport of the mediator inside the porous electrode, interfacial electron transfer kinetics and recombination processes.

**Scanning Horizontal Lines.** To scan a sample surface horizontally, the ME is kept at a certain distance (for example 10  $\mu\text{m}$ ) above the substrate surface and is moved laterally in either  $x$ - or  $y$ -direction, simultaneously recording a current. A horizontal line scan is a useful tool for orientation at a substrate and hence finding a reasonable starting point for an image. This procedure was implemented for the SF distance regulation measurements on DSCs in chapter 8.

**Imaging.** The procedure of an image is analog to that of a horizontal line scan. During imaging, one of the two axes ( $x$  or  $y$ ) is set as high frequency axis, the other one as low frequency axis. The capability to display spatially resolved surface topographies and electrochemical surface performance is determined by the size of the substrate radius  $r_S$ , the ME radius  $r_T$  and the ME-to-substrate distance  $d$  relying on the relation  $r_S > r_T + 1.5 d$ . Imaging with SF distance regulation was performed on DSCs in this thesis and is presented in chapter 8.

## 3.3.2 Feedback Mode for Kinetic Investigations

SECM FB mode is a useful amperometric method to investigate electron transfer kinetics.<sup>[151]</sup> In a FB mode experiment, the ME is immersed in a solution in which the redox mediator is provided with only one oxidation state, such as  $[\text{Co}(\text{bpy})_3]^{3+}$ . The measurement principle is based on examining the steady-state current at a ME. When a sufficiently negative potential is applied to the ME, an oxidized species such as  $[\text{Co}(\text{bpy})_3]^{3+}$  is reduced at a diffusion controlled rate *via* reaction (II).



In FB mode, the ratio between the current in bulk  $i_{T,\infty}$  and  $i_T$  depends on the substrate kinetics.

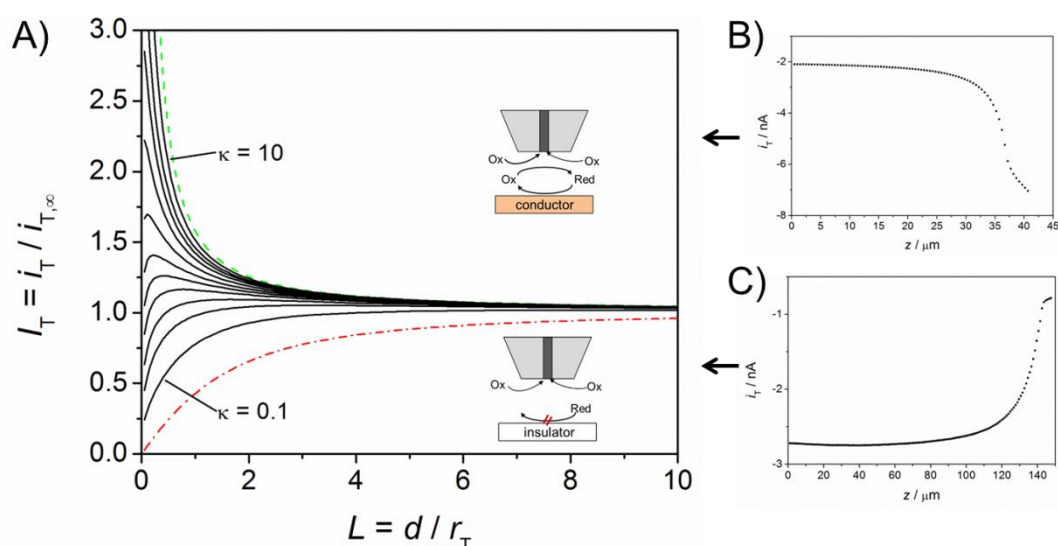


Fig. 3.5 – A) SECM FB mode approach curves under diffusion control (green dashed line) as an example of positive FB over a conductor and at hindered diffusion (red dash-dotted line) as an example of negative FB over an insulator. The solid black lines show the theoretical curves with a dimensionless normalized heterogeneous rate constant  $\kappa = 0.1$  (bottom solid line) to  $\kappa = 10$  (upper solid line). The  $\kappa$  values in between are in increasing order of 0.3, 0.5, 0.75, 1, 1.3, 1.8, 2.6, 3.6 and 5. All curves were calculated based on an analytical approximation of FB approach curves with a micro disk SECM tip and at the irreversible substrate kinetic reaction published by Cornut and Lefrou.<sup>[150]</sup> B) Approach curve recorded with a Pt ME ( $r_T = 5.11 \mu\text{m}$ ,  $\text{RG} = 48.52$ ) over a conducting gold substrate and C) approach curve recorded with a Au ME ( $r_T = 12.25 \mu\text{m}$ ,  $\text{RG} = 12.92$ ) over a non-illuminated DSC acting as an insulating substrate. Redox mediator for both B) and C) was 1 mM  $[\text{Co}(\text{bpy})_3]^{3+}$  in 0.1 M TBAPF<sub>6</sub>.

Depending on the substrate properties,  $i_T$  differs which results in different curve shapes of the normalized approach curves. If the substrate is an electronic insulator, for example a non-illuminated photoanode, and the ME is within a few  $r_T$  of this substrate surface, oxidized species Ox can diffuse to the ME, are reduced to Red but cannot be re-oxidized to Ox. If the ME is in very close proximity to the surface, the flux of Ox is hindered (“hindered diffusion”) and no net current is detected at the ME (Fig. 3.5C). This behavior is known as “negative FB” (red dash-dotted line in Fig. 3.5). If the substrate behaves like a perfect conductor, the mediator is recycled at the substrate by a heterogeneous diffusion controlled reaction from species Red to species Ox (Fig. 3.5B). This way, the flux of species Ox to the ME increases compared to the bulk solution and results in a current at the ME (“positive FB”, green dashed line in Fig. 3.5). The ME current during the approach towards a substrate depends on the substrate kinetics. A normalized heterogeneous rate constant  $\kappa$  is obtained by fitting normalized approach curves to an analytical approximation developed by Cornut and Lefrou.<sup>[150]</sup> It describes the finite kinetics of first order with respect to the local mediator concentration and results in the dimensionless normalized first order rate constant  $\kappa$ . With  $r_T$  of the ME and  $D$  of the redox mediator species, the rate constant of the reaction at the sample  $k_{\text{eff}}$  can be calculated according to:

$$k_{\text{eff}} = \frac{D \cdot \kappa}{r_T} \quad (3.6)$$

**Model of Finite Kinetics.** As a new modelling approach compared to formerly used models,<sup>[152]</sup> Cornut and Lefrou<sup>[150]</sup> developed analytical approximations for FB approach curves for irreversible kinetics at the substrate for  $L$  and  $RG$  values of commonly used MEs. For this model, only diffusional mass transfer is considered, while convection and migrational effects are neglected. Note that the symbols for parameters such as the normalized tip current  $I_T$ , the dimensionless reaction rate constant  $\kappa$  and the ratio of the glass radius to the electrode radius  $RG$  used in this thesis differ from the ones used by Cornut and Lefrou. In this thesis, the symbols were chosen in the style of the publications of Shen<sup>[18, 153]</sup> and Tefashe.<sup>[19, 21]</sup> For the sake of brevity, the development of Cornut and Lefrou’s analytical expression<sup>[150]</sup> is only presented in a shortened form. The reaction at the ME is considered fast and diffusion- controlled, the reaction at the substrate is considered

irreversible with a kinetic constant  $k_{\text{eff}}$ . In a first step, a dimensionless heterogeneous rate constant is defined as

$$\kappa = \frac{k_{\text{eff}} \times r_{\text{T}}}{D} \quad (3.7)$$

As a next step, the normalized tip current  $I_{\text{T}}$  is defined as

$$I_{\text{T}} = \frac{i_{\text{T}}}{i_{\text{T},\infty}} \quad (3.8)$$

with  $i_{\text{T}}$  being the tip current and  $i_{\text{T},\infty}$  being the tip current at infinite distance from the substrate („in the bulk“). An equation needed to be found that meets both limiting behaviors, i.e. a large  $\kappa$  for the infinite  $\kappa$  limit (diffusion control) and small  $\kappa$  as negative FB for null  $\kappa$  limit (hindered diffusion). For large  $\kappa$  values, the following relation was obtained

$$I_{\text{T}}(L, \text{large } \kappa, RG) \approx I_{\text{T,cond}}\left(L + \frac{1}{\kappa}, RG\right) \xrightarrow{\kappa \rightarrow \infty} I_{\text{T,cond}}(L, RG) \quad (3.9)$$

Considering the following small  $\kappa$  limit of (3.9)

$$\lim_{\kappa \rightarrow 0} I_{\text{T,cond}}\left(L + \frac{1}{\kappa}, RG\right) = \lim_{L \rightarrow \infty} I_{\text{T,cond}}(L, RG) = 1 \quad (3.10)$$

the searched equation is formed to:

$$I_{\text{T}}(L, \kappa, RG) = I_{\text{T,cond}}\left(L + \frac{1}{\kappa}, RG\right) + (I_{\text{T,ins}}(L, RG) - 1)f(L, \kappa, RG) \quad (3.11)$$

The following constraints on the function  $f$  for all  $L$  and  $RG$  values were made:

$$f(L, \kappa, RG) \xrightarrow{\kappa \rightarrow 0} 1 \text{ and } f(L, \kappa, RG) \xrightarrow{\kappa \rightarrow \infty} 0 \quad (3.12)$$

In the next step, an approximate analytical expression of  $f(L, \kappa, RG)$  was to be found. First,  $L$  and  $RG$  were held constant. This led to many functions with three adjustable parameters which all fit  $f$  on the whole  $\kappa$  range. In order to obtain an expression of  $f$  with  $L$  and  $\kappa$  as analytical variables at fixed  $RG$ , the dependency between each fitting parameter and  $L$  was analytically expressed. For each given  $RG$  value, this expression resulted in:

$$f(L, \kappa) = \frac{1}{(1 + a1L\kappa)(1 + L^2\kappa^3)} \quad (3.13)$$

To proof this new expression in terms of error susceptibility, it was initially used with  $RG = 10$  to be able to compare it with literature results.<sup>[154]</sup> Since the aim of the work of Cornut and Lefrou<sup>[150]</sup> was to find an expression that is true for every  $RG$  value, only expressions with  $RG$  as a variable in the positive ( $I_{T,cond}$ ) as well as in the negative FB current ( $I_{T,ins}$ ) have been selected:<sup>[155, 156]</sup>

$$I_{T,cond}(L, RG) = \alpha(RG) + \frac{\pi}{4\beta(RG)\arctan(L)} + \left(1 - \alpha(RG) - \frac{1}{2\beta(RG)}\right) \frac{2}{\pi} \arctan(L) \quad (3.14)$$

$$\alpha(RG) = \ln 2 + \ln 2 \left(1 - \frac{2}{\pi} \arccos\left(\frac{1}{RG}\right)\right) - \ln 2 \left(1 - \left(\frac{2}{\pi} \arccos\left(\frac{1}{RG}\right)\right)^2\right) \quad (3.15)$$

$$\beta(RG) = 1 + 0.639 \left(1 - \frac{2}{\pi} \arccos\left(\frac{1}{RG}\right)\right) - 0.186 \left(1 - \left(\frac{2}{\pi} \arccos\left(\frac{1}{RG}\right)\right)^2\right) \quad (3.16)$$

$$I_{T,ins}(L, RG) = \frac{\frac{2.08}{RG^{0.358}} \left(L - \frac{0.145}{RG}\right) + 1.585}{\frac{2.08}{RG^{0.358}} (L + 0.0023RG) + 1.57 + \frac{\ln RG}{L} + \frac{2}{\pi RG} \ln\left(1 + \frac{\pi RG}{2L}\right)} \quad (3.17)$$

In further steps, an expression for  $RG = 10$  was formed which showed very low errors of  $\pm 0.014$  at  $L \geq 0.01$ . A combination of equations (3.11), (3.13), (3.14) and (3.17) obtained (3.18).

$$I_T(L, \kappa) = I_{T,cond}\left(L + \frac{1}{\kappa}, RG\right) + \frac{I_{T,ins}(L, RG) - 1}{(1 + a1L\kappa)(1 + L^{a2}\kappa^{a3})} \quad (3.18)$$

The three adjustable parameters  $a1$ ,  $a2$  and  $a3$  were recalculated for each  $RG$ . The last step was to study the dependency of  $RG$  on  $a1$ ,  $a2$  and  $a3$ . This finally led to:

$$I_T(L, \kappa, RG) = I_{T,cond}\left(L + \frac{1}{\kappa}, RG\right) + \frac{I_{T,ins}(L, RG) - 1}{(1 + 2.47RG^{0.31}L\kappa)(1 + L^{0.006RG+0.113}\kappa^{-0.0236RG+0.91})} \quad (3.19)$$

Validity: For any  $\kappa$ , at  $L \geq 0.1$  and for  $RG \leq 20$  with an error below  $\pm 0.025$

The approach curves in this thesis were fitted to this analytical approximation using a least-square method. This was done with the solver function of Microsoft Excel, which seems to be an appropriate tool as a recent study by Cornut and Lefrou<sup>[157]</sup> showed.

### 3.3.3 Shear Force SECM and Spatially Resolving Techniques

In order to control the ME-to-sample distance accurately, a SF-based detection setup was applied. This technique offers great advantages in contrast to “conventional” imaging where the sample tilt is not corrected and large relatively working distances are necessary in order to avoid a collision of the ME with the sample (Fig. 3.6C). The principle of the distance control relies on the detection of shear forces between the oscillating ME and the sample. The oscillation is excited by a piezo plate fed with an AC voltage and detected by a second piezo plate attached to a ME. The vibration amplitude of the ME is damped in close proximity to the sample surface. This damping is registered by a lock-in amplifier to which the piezo electric plate is connected (see setup in Fig. 4.2B). This SF detection type is non-optical and was introduced by Schuhmann and co-workers.<sup>[158, 159]</sup> Tefashe<sup>[160]</sup> applied this technique in constant distance mode to resolve lateral structures with a 300 nm electrode and probed samples with lateral structures with valley-to-valley distances of 50  $\mu\text{m}$ . In contrast to usual SECM imaging using constant height mode (Fig. 3.6A), SF distance control allows for scanning rough surfaces at constant distances (Fig. 3.6B) as the ME registers by the principle described above when surfaces are in close proximity. By employing SF distance control, it is also possible to compensate a sample tilt (Fig. 3.6D). In SF-based experiments, a low working distance of about 500 – 700 nm between the ME and the sample surface is achieved.<sup>[160]</sup>

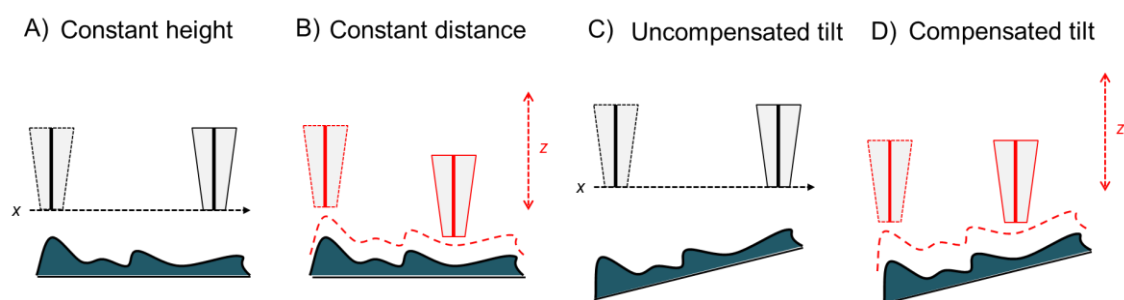


Fig. 3.6 – Scheme of A) a constant height mode in SECM imaging, B) constant distance mode in SF distance controlled SECM, C) uncompensated sample tilt in constant height mode SECM imaging and D) compensated sample tilt in SF distance controlled SECM by moving the ME along the vertical  $z$  axis.

#### 3.3.4 Further SECM Modes and Scanning Probe Techniques

Besides FB mode, several other SECM modes are known which are used for and tailored to certain applications. By biasing the ME ( $E_T$ ) or the substrate ( $E_S$ ), SECM measurements can be performed in different modes, important and widely used ones including FB,<sup>[161]</sup> substrate generation/tip collection (SG/TC),<sup>[162, 163]</sup> tip generation/substrate collection (TG/SC)<sup>[164]</sup> and redox competition (RC) modes.<sup>[165]</sup> For instance, the TG/SC mode is suitable for investigating the electrocatalytic activity of different catalysts on glassy carbon substrates for oxygen reduction in acidic media.<sup>[164]</sup> During SG/TC mode SECM, the species under consideration is generated on the substrate and detected at the ME. This mode was for example applied for the detection of the intermediate product  $H_2O_2$  during electrochemical oxygen reduction reactions.<sup>[162]</sup> RC mode involves a competition between the ME and the substrate which are both capable of reacting with the very same analyte. This mode is useful to visualize local catalytic activity.<sup>[165]</sup> A recent review<sup>[166]</sup> shows that alternating current SECM (AC-SECM), similar to SF-SECM, offers the possibility to determine topographical and electrochemical information simultaneously with the difference that during AC-SECM experiments no redox mediator is necessary. This way, AC-SECM is highly suitable for experiments in which a redox mediator could negatively influence the results. Horrocks *et al.*<sup>[167]</sup> were the first to conduct AC-SECM to position a biosensor that was then used to visualize  $H_2O_2$  diffusion over gold in SG/TC mode. Recently, SFM-SECM was applied to study the corrosion of copper in acidic chloride solution to correlate local passivation and pitting phenomena.<sup>[168]</sup> Another microscopic technique to investigate optical properties and topographies of surfaces in the sub-wavelength resolution is scanning near-field optical microscopy (SNOM).<sup>[169]</sup>

#### 3.4 Linear Sweep Voltammetry at a Rotating Disk Electrode

A rotating disk electrode (RDE) is particular suitable to determine kinetic parameters such as the diffusion coefficient  $D$  of redox mediators. An RDE consists of an active electrode material surrounded by a cylindrical mantle made from an insulating material such as polytetrafluoroethylene (PTFE). During the measurement, the potential is swept and a motor

rotates the electrode around its symmetry axis  $z$  with a defined rotation speed (Fig. 3.7A). The rotation causes a laminar flow of the electrolyte parallel to the electrode surface which leads to very high flow rates (Fig. 3.7B).

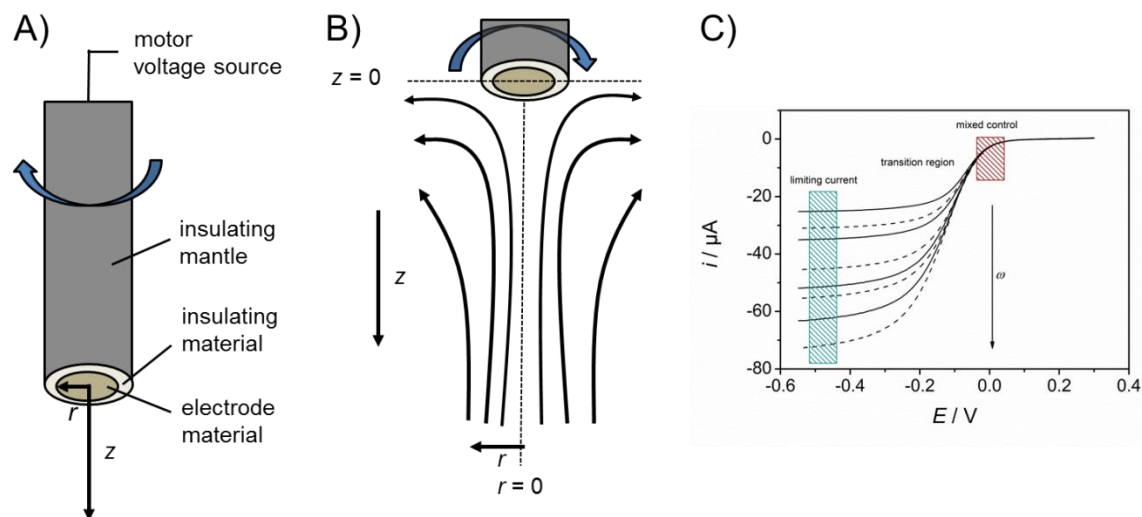


Fig. 3.7 – A) Schematic drawing of an RDE and B) scheme of the hydrodynamic mass transfer towards an RDE at lateral view and view from down below. Schemes adapted from Hamann and Vielstich<sup>[170]</sup> and Speiser.<sup>[171]</sup> C) Levich plot displaying the influence of the angular frequency  $\omega$  on the limiting current. The regions of limiting current (Levich current), the transition region and the region of mixed control where both the mass and the charge transfer influence the current are indicated. The redox electrolyte was 1 mM  $[\text{Co}(\text{bpy})_3](\text{PF}_6)_3$  in 0.1 M TBAPF<sub>6</sub> in MeCN.

By this rotation of the electrode, the redox species flow laminarly to the surface of the electrode (they are virtually drawn towards the electrode) and are radially slung away. Through this process, the Nernst diffusion layer  $\delta_N$  is obtained whose thickness can be calculated considering the differential equations for convective diffusion which is valid for mass transfer in stirred solutions. The equation was developed by Levich to

$$\delta_N = 1.61\omega^{-1/2}\nu^{1/6}D_{\text{Ox}}^{1/3} \quad (3.20)$$

with  $\omega$  being the angular velocity,  $\nu$  being the kinematic viscosity and  $D_{\text{Ox}}$  being the diffusion coefficient of the oxidized redox species. From equation (3.20) it becomes apparent, that the thickness of the diffusion layer in the case of an infinitely large electrode does not depend on the radius  $r$  of the electrode. This means that the mass transport occurs uniformly distributed all over the active electrode surface. The electrode is uniformly accessible

and the electrochemical current density  $j$  is location-independent. With Fick's first law,  $j$  is defined as

$$j = nFD \left( \frac{\partial c}{\partial x} \right)_{x=0} = nFD \frac{c^* - c^s}{\delta_N} \quad (3.21)$$

with  $n$  being the number of transferred electrons,  $c^*$  being the concentration of the redox species in the bulk and  $c^s$  on the electrode surface. At a temporally constant diffusion layer,  $j$  strives for a limiting value with a decreasing surface concentration  $c^s \rightarrow 0$  (equation (3.22)).

$$j_{\text{lim}} = nFD \frac{c^*}{\delta_N} \quad (3.22)$$

The limiting current density  $j_{\text{lim}}$  increases linearly with increasing  $c^*$  and decreasing  $\delta_N$ . For the determination of the diffusion coefficient, the electrode rotation speed is varied as a higher rotation speed leads to a thinner diffusion layer. This is due to the convective transport of redox species to the electrode which compresses the diffusion layer. Inserting equation (3.20) into (3.22) results in the Levich equation. It describes the dependence of the electrochemical limiting current density  $j_{\text{lim}}$  on the angular velocity in the region of limiting current

$$j_{\text{lim}} = 0.62nFD^{2/3}\nu^{-1/6}\omega^{1/2}c^* \quad (3.23)$$

$j_{\text{lim}}$  increases with an increasing square root of the angular frequency. The slope of a plot of  $j_{\text{lim}}$  over the square root of  $\omega$  could be applied to determine  $D$ , at known  $c^*$ .

If the electrode potential is swept while the electrode rotation speed is held constant, the current density follows the Butler-Volmer equation at very low overpotentials. In this region, the mass transport is very fast due to a high convection of the redox species. In the region of limiting current, the current density only depends on the mass transport (Fig. 3.7C). In the region in between, indicated as the transition region, the current density depends both on the convective diffusion and on the velocity of the charge transfer. In this thesis, the diffusion coefficients of  $[\text{Co}(\text{bpy})_3]^{3+}$  were determined using the method described above. Therefore, Levich's equation was solved for the diffusion coefficient to

$$D = \sqrt{\left(\frac{\nu^{1/6}m}{0.62nFc^*}\right)^3} \quad (3.24)$$

with  $m$  being the slope of the Levich plot. In this thesis,  $D$  [ $\text{cm}^2 \text{s}^{-1}$ ] was determined to use it for the calculation of  $k_{\text{eff}}$  [ $\text{cm s}^{-1}$ ] from  $\kappa$ .

## II Experimental Part

### 4 Material and Procedures

#### 4.1 Overview of Techniques Used

As presented in Fig. 4.1, various steps were necessary to obtain the overall results of this thesis: to determine the reaction rate constant of dye regeneration  $k_{\text{ox}}$  and to investigate the photoanode topography and correlate these results to the electrochemical activity of the photoanodes. A successful synthesis and succeeding oxidation of the Co complexes tris(2,2'-bipyridine)cobalt(II/III) hexafluorophosphate ( $[\text{Co}(\text{bpy})_3](\text{PF}_6)_{2/3}$ ) and tris(2,2'-bipyridine)cobalt(II/III) nitrate ( $[\text{Co}(\text{bpy})_3](\text{NO}_3)_{2/3}$ ) was confirmed by UV-Vis spectroscopy and nuclear magnetic resonance (NMR) spectroscopy. The spectroscopic characterization was followed by an electrochemical investigation during which CVs at a ME as well as LSVs at an RDE were performed in order to determine the diffusion coefficient  $D$  of  $[\text{Co}(\text{bpy})_3]^{2+}$  and  $[\text{Co}(\text{bpy})_3]^{3+}$ . The optimal ME material to be used for SECM experiments had to be found to obtain reliable results during SECM measurements. In order to determine the dye regeneration rate constant  $k_{\text{ox}}$ , the expression for the effective reaction rate constant  $k_{\text{eff}}$  had to be derived (chapter 6.1). For the spatially resolved analysis of screen-printed photoanodes the knowledge of the behavior of the redox mediator and the ME material was necessary.

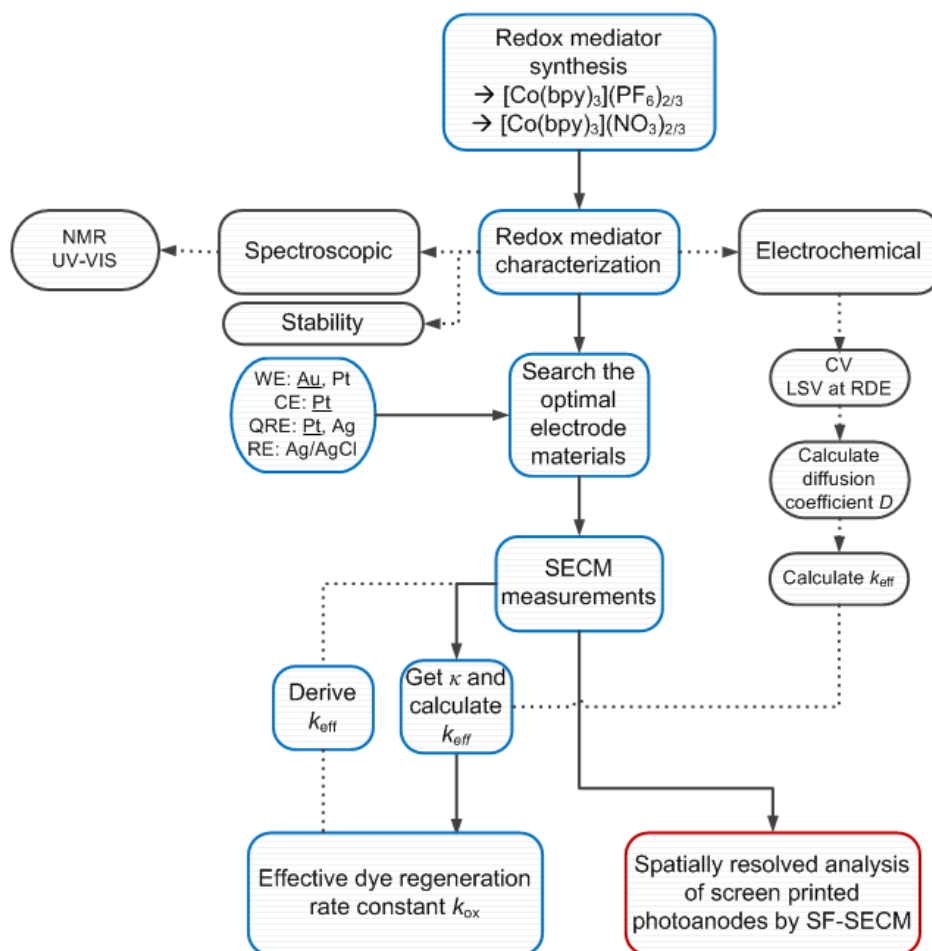


Fig. 4.1 – Flow chart of the steps: the procedure to obtain  $k_{ox}$  (blue), the redox mediator characterization along with additional necessary steps (black) and the imaging of photoanodes by SF-SECM (red).

## 4.2 Chemicals

The chemicals used for the synthesis of the cobalt complexes (Table 4.1), for the redox electrolyte preparation (Table 4.2), and for dye-sensitization, ME treatment and drying of solvents (Table 4.3) are given in this chapter. For each experiment, MeCN was dried under vacuum and stored under argon atmosphere over 3 Å molar sieve.

#### 4 Material and Procedures

Table 4.1 – Chemical name, sum formula, supplier and purity of all chemicals used for cobalt complex synthesis. Suppliers are from Germany unless noted otherwise.

<b>Chemical</b>	<b>Sum formula (abbreviation)</b>	<b>Supplier</b>	<b>Purity</b>
2,2'-bipyridine	$C_{10}H_8N_2$ (bpy)	Riedel-de-Haen	≥99.5 %
acetonitrile	$CH_3CN$ (MeCN)	VWR International, Darmstadt	HPLC grade
ammoniumhexafluorophosphate	$NH_4PF_6$	Fluka	≥98 %
cobalt(II) chloride hexahydrate	$CoCl_2 \cdot 6 H_2O$	Alfa Aesar	98 -102 %
cobalt(II) nitrate hexahydrate	$Co(NO_3)_2 \cdot 6 H_2O$	Sigma-Aldrich, Steinheim	99 %
diethylether	$(C_2H_5)_2O$	Roth	>99.0 %
dist. water	$H_2O$		$55 \mu S m^{-1}$
ethanol	$C_2H_5OH$	VWR International, Darmstadt	≥99.8 %
methanol	$CH_3OH$	Fluka	≥99.5 %
nitrosonium tetrafluoroborate	$NOBF_4$	Sigma-Aldrich, Steinheim	95 %
silver nitrate	$AgNO_3$	Baker	95 %
tetrabutylammonium hexafluorophosphate	$C_{16}H_{36}NPF_6$ (TBAPF <sub>6</sub> )	Sigma-Aldrich, Steinheim	≥99.0 %

## 4 Material and Procedures

---

Table 4.2 – Chemical name, sum formula, supplier and purity of all chemicals used for redox electrolyte preparation. Suppliers are from Germany unless noted otherwise.

<b>Chemical</b>	<b>Sum formula (abbreviation)</b>	<b>Supplier</b>	<b>Purity</b>
3-methoxypropionitrile	CH <sub>3</sub> OCH <sub>2</sub> CH <sub>2</sub> CN (MPN)	Sigma-Aldrich, Steinheim	≥98.0 %
acetonitrile	CH <sub>3</sub> CN (MeCN)	VWR International, Darmstadt	HPLC grade
dist. water	H <sub>2</sub> O		55 μS m <sup>-1</sup>
ferrocene	C <sub>10</sub> H <sub>10</sub> Fe	Alfa Aesar	99 %
ferrocenemethanol	C <sub>11</sub> H <sub>12</sub> FeO	Sigma-Aldrich, Steinheim	97 %
poly(ethylene glycol) 300	H(OCH <sub>2</sub> CH <sub>2</sub> ) <sub>n</sub> OH (PEG 300)	Fluka	-
potassium nitrate	KNO <sub>3</sub>	Fluka	-
tetrabutylammonium hexafluorophosphate	C <sub>16</sub> H <sub>36</sub> NPF <sub>6</sub> (TBAPF <sub>6</sub> )	Sigma-Aldrich, Steinheim	≥99.0 %

## 4 Material and Procedures

Table 4.3 – Chemical name, sum formula, supplier and purity of all chemicals used for dye-sensitization, ME treatment, drying of solvents. Suppliers are from Germany unless noted otherwise.

Chemical	Sum formula	Supplier	Purity
aluminum(III) oxide (MicroPolish II, 0.05 and 0.3 $\mu\text{m}$ ) (deagglomerated)	$\gamma\text{-Al}_2\text{O}_3$	Buehler, USA	-
D35: (E)-3-(5-(4-(Bis(2',4'-dibutoxy-[1,1'-biphenyl]-4-yl)amino)phenyl)-thiophene-2-yl)-2-cyanoacrylic acid	$\text{C}_{54}\text{H}_{58}\text{N}_2\text{O}_6\text{S}$	Dyename AB, Täby, Sweden	-
D45: (E)-3-(5-(4-(Bis(2',4'-dimethoxy [1,1'-biphenyl]-4-yl)amino)phenyl)-thiophene-2-yl)-2-cyanoacrylic acid	$\text{C}_{42}\text{H}_{34}\text{N}_2\text{O}_6\text{S}$	Dyename AB, Täby, Sweden	-
molar sieve (3 Å)		ACROS ORGANICS	-
sulfuric acid (Rotipuran)	$\text{H}_2\text{SO}_4$	Roth	96 %, p.a.
V35	$\text{C}_{58}\text{H}_{66}\text{N}_2\text{O}_{14}\text{S}$	Dyename AB, Täby, Sweden	-
Z-907: <i>cis</i> -Bis(isothiocyanato)(2,2'-bipyridyl-4,4'-dicarboxylato)(4,4'-dinonyl-2'-bipyridyl)ruthenium(II)	$\text{C}_{42}\text{H}_{52}\text{N}_6\text{O}_4\text{RuS}_2$	Cooperation partner, Huazhong University of Science and Technology, China	-

## 4.3 Instruments

### 4.3.1 Potentiostats

Potentiostats were used for electrochemical experiments as well as to power light emitting diodes (LED). The determination of the diffusion coefficients was performed with an Autolab PGSTAT128N (Metrohm Autolab B.V., Utrecht, Netherlands) with the associated software NOVA (version 1.9.16). The electrochemical characterization of Co complexes at MEs as well as the determination of  $r_T$  by calculation from the limiting current were performed in a Faraday cage with a CHI660 potentiostat (CH Instruments, Austin, Texas, USA). Major SECM measurements were performed with a custom-made potentiostat  $\mu$ -P3 (M. Schramm, Heinrich Heine Universität, Düsseldorf, Germany). A few other SECM experiments were conducted with another bipotentiostat (JAISSE BI POT. PG 10, Jaissle

Elektronik, Waiblingen, Germany). The long-term stability of  $[\text{Co}(\text{bpy})_3]^{2+}$  was determined using an OrigaStat e 100 (Orignalys, Rillieux-la-Pape, France).

The LED integrated into the SECM setup, was controlled by an XPot potentiostat (Zahner-Elektrik, Kronach, Germany). The intensities were validated with the help of an independent LED setup (see appendix 10.2) in order to obtain reliable light intensities. The independent LED setup was controlled by an Autolab PGSTAT128N (Metrohm Autolab B.V., Utrecht, Netherlands) with the associated software NOVA (version 1.8.17).

### 4.3.2 Rotating Disk Electrode Setup

A three-electrode setup controlled by a potentiostat (Autolab PGSTAT128N, Metrohm Autolab B.V., Utrecht, Netherlands) was used to determine diffusion coefficients. The WE was a 0.3 cm diameter glassy carbon macroelectrode (CHI104, CH Instruments, Austin, TX, USA). A Pt wire served as Aux in each experiment whereas the RE was adapted to the conditions of each experiment (see Table 4.9 in Chapter 4.9.4). A specially designed adapter between the WE and the rotation speed control (Jaissle Ring-Scheibe Drehzahlregler, Jaissle Elektronik, Waiblingen, Germany) with a tight hold ensured a precise rotation. With this setup, the rotation was adjusted to a rotation speed with an accuracy of 1 rpm. A contact thermometer (IKA ETS-D5, IKA, Staufen, Germany) was inserted into the electrochemical cell to determine the temperature of the solution.

### 4.3.3 Confocal Laser Scanning Microscope / Optical Microscope

The confocal laser scanning microscope (CLSM) Leica TCS SP2 AOBS (Leica Confocal Software 2.62) (Leica Microsystems GmbH, Heidelberg, Germany) using the 633 nm HeNe laser was used for the determination of the radius of the glass sheath ( $r_{\text{glass}}$ ) of each ME. An optical microscope was used to confirm the centered position of the Au or Pt wire, respectively, within the glass sheath during the ME preparation.

### 4.3.4 UV-Vis Spectrometer

A SPEKOL® 2000 dual beam photometer (Analytik Jena AG, Germany) with a spectral slit width (optical resolution) of 2 nm, a deuterium lamp for the UV range and a halogen

light source for the visible (Vis) range was used for every UV-Vis spectrophotometrical measurement. Both the sample and the reference solution were measured in precision cuvettes made from quartz SUPRASIL<sup>®</sup> 300 (Hellma Analytics, Müllheim, Germany). These cuvettes are appropriate for the UV range down to 200 nm and have a path length of 10 mm. UV-Vis measurements of the dyes D35, D45, V35 and Z-907 were conducted in a quartz cell (Hellma Analytics, Müllheim, Germany) with a path length of 1 mm. MeCN was used as reference solution for the measurements of the dyes.

$[\text{Co}(\text{bpy})_3]^{2+}$  and  $[\text{Co}(\text{bpy})_3]^{3+}$  were investigated UV-spectroscopically in the same type of cuvettes that were used for the dye solutions. The synthesized complex  $[\text{Co}(\text{bpy})_3](\text{PF}_6)_2$  and its oxidized analogue  $[\text{Co}(\text{bpy})_3](\text{PF}_6)_3$  were dissolved in dried MeCN each. 0.1 M TBAPF<sub>6</sub> were added to provide the same conditions as later during SECM experiments. The reference solution consisted of 0.1 M TBAPF<sub>6</sub> in dried MeCN.  $[\text{Co}(\text{bpy})_3](\text{NO}_3)_2$  and  $[\text{Co}(\text{bpy})_3](\text{NO}_3)_3$  were dissolved each in dist. water with 0.1 M KNO<sub>3</sub> as supporting electrolyte. Accordingly, the reference solution for these two complexes was 0.1 M KNO<sub>3</sub> in dist. water. 2,2'-bipyridine was dissolved in MeCN and the latter was also used as the reference solution. The spectrometer was operated by the software WinASPECT (version 2.3.1.0, Analytik Jena AG, Germany).

### 4.3.5 Nuclear Magnetic Resonance Spectroscopy

Nuclear magnetic resonance (NMR) spectra were recorded with a Fourier 300 resp. Bruker 500 AVANCE III spectrometer (measuring rate: <sup>1</sup>H-NMR: 300.1 MHz, <sup>13</sup>C-NMR: 499.9 MHz, <sup>31</sup>P-NMR: 499.9 MHz). The chemical shifts are given with respect to tetramethylsilane (TMS) ( $\delta = 0$  ppm). Signal multiplicities are denoted with (s) for singlet, (d) for doublet, (t) for triplet, (sept) for septet and (m) for multiplet. Signals of remaining protons of the deuterated solvents or the signals belonging to the carbon atoms of the solvents were drawn from literature.<sup>[172]</sup> MestRec (version 4.8.1.1) was used for the analysis of the NMR spectra.

### 4.4 Preparation and Characterization of Gold and Platinum Microelectrodes

#### 4.4.1 Preparation

Depending on the experimental requirements, MEs with  $r_T$  ranging from 12  $\mu\text{m}$  to 15  $\mu\text{m}$  or smaller MEs with  $r_T$  ranging from 1  $\mu\text{m}$  to 5  $\mu\text{m}$  were prepared. The preparation procedure is described below.

**Microelectrodes used for Kinetic Determination.** The Au and Pt MEs were prepared according to a published procedure with slight changes.<sup>[161]</sup> Borosilicate capillaries (length: 100 mm, outer diameter: 1.5 mm, wall thickness: 0.375 mm; Hilgenberg GmbH, Malsfeld, Germany) were cleaned with ethanol and pulled out with a capillary puller (Model PP-830, Narishige, Japan; mode: “Number 2”, heater level “70”) to obtain a narrow opening. The pointed end was held into the flame of a Bunsen burner for a few seconds. A 1 cm piece of Au respectively Pt wire (from now on referred to as “metal wire”; thickness: 25  $\mu\text{m}$ ; purity of Au: 99.99 %, purity of Pt: 99.99 %, Goodfellow GmbH, Bad Nauheim, Germany) was also cleaned with ethanol, left to dry and inserted into the borosilicate capillary by tapping the latter onto a table. The centered position of the metal wire within the glass capillary was confirmed by light microscopy. Only then the metal wire was bound to the glass capillary by melting. During this step, it is crucial to center the metal wire containing capillary within the heating coil of the capillary puller. Finally, the glass capillary was heated gradually at the device-specific heating level “45”, “60” and “75” for 1 to 3 min each. To prevent air bubbles from melting into the glass capillary, a vacuum pump was connected to the end of the capillary. The capillary was moved up and down throughout the melting process for a homogeneous temperature distribution.

Afterwards, the absence of bubbles was confirmed by light microscopy. The metal wire was exposed from the covering glass by polishing the electrode on sand paper with a home-built grinder. The successful exposure of the metal wire was checked by light microscopy. Further polishing steps on sandpaper with 15, 9, 3, 1 and 0.05  $\mu\text{m}$  particles, 10 min on each grain, were performed. A positive result was characterized by a smooth

electrode surface, no slit between the metal wire and the surrounding glass sheath as well as a good visibility of the metal wire.

The final step of the electrode preparation was to create an electrical contact to connect the electrode to any device *via* a crocodile clip. The insulation of both ends of a 15 cm piece of copper wire (conductor diameter: 0.5 mm, insulator thickness: 0.06 mm, insulation: polyimide, Goodfellow GmbH, Bad Nauheim, Germany) was removed by holding it into the flame of a Bunsen burner. To ensure the complete removal of the insulator, the ends were also polished with coarse sandpaper. A conducting two-component silver adhesive (Epoxy Kit Part A + B, Typ H2410Z, Epoxy Technology, Massachusetts, USA) ensured an electrical contact between the stripped copper wire and the metal wire. Two parts by volume of Epoxy Kit Part A and one part of Epoxy Kit Part B were mixed and applied to one end of the stripped copper wire. The latter was inserted repeatedly into the glass capillary with the metal wire. After the glass capillary and the sharp end were completely filled with glue, the copper wire was left inside the capillary. The electrodes were stored at 60 °C in a drying cabinet in order to harden the silver adhesive. Especially for the Au electrodes it was important not to increase the temperature above 60 °C in order to avoid a slit between the glass and the Au. This behavior was observed every other time and was most likely attributable to the different expansion coefficients of these two materials.

**Microelectrodes Used for Imaging with Shear Force-SECM.** For SF-SECM measurements (chapter 8), smaller Au MEs were prepared by Inka Plettenberg at Carl von Ossietzky University in Oldenburg. The preparation is given in the corresponding publication.<sup>[163]</sup>

### 4.4.2 Characterization

The MEs were characterized by two techniques. They were evaluated qualitatively by recording a CV and checking the obtained shape and quantitatively by calculating the tip radius  $r_T$  using the limiting current  $i_{T,\text{lim}}$  of a ferrocenemethanol solution of known concentration *via* relation (3.5). The radius of the insulating glass sheath of the ME  $r_{\text{glass}}$  was determined by CLSM. An important parameter for fitting approach curves to a kinetic model is the so-called *RG* value. *RG* is the ratio of  $r_{\text{glass}}$  to  $r_T$  and is listed in Table 10.1 for every ME used.

Despite the polishing step during the ME preparation, it is recommendable to polish the MEs only when absolutely necessary, i.e. as long as the electrochemical behavior in terms of the shape of a CV is good, the ME should not be polished. In general, polishing on polishing felts should be avoided. If really necessary they should be polished carefully with a grinder machine with almost no contact between the electrode and the sandpaper in order to avoid electrode contamination or damage of any kind. Also, an electrochemical cleaning in 2 M sulfuric acid is suitable where the potential of the ME is cycled fifty times. Usually, Pt MEs were polished on 0.3  $\mu\text{m}$  and 0.05  $\mu\text{m}$  alumina dispersion on polishing felts for 3 min each.

### 4.5 Scanning Electrochemical Microscope with Controlled Illumination

SECM was used in FB mode with two different setups: A photoelectrochemical setup was used to perform approach curves on dye-sensitized  $\text{TiO}_2$  electrodes (Fig. 4.2A) and was complemented by a shear-force unit which allows distance-controlled scanning of surfaces to probe dye-sensitized  $\text{TiO}_2$  substrates in terms of their topography and electrochemical activity both in the dark and under illumination (Fig. 4.2B). The measurements were performed with a home-built SECM consisting of a custom-made potentiostat  $\mu\text{-P3}$ , a data acquisition board (CIO-DAS 1602/16) and two positioning systems placed in a dark and grounded Faraday cage. Positioning system I (by SPI Robot) moved the ME relative to the light beam. Compared to the already published setup,<sup>[173, 174]</sup> a second positioning system II (by Physik Instrumente) was integrated which moved the sample laterally with respect to the focal point of the light source. It consisted of two piezo stepping linear actuators (N-661.21 A, resolution in the nm range) which were screwed on top of each other (rotated by 90°). The setup was controlled by the in-house software SECMx.<sup>[175]</sup> The data evaluation and profile analysis were performed with the program MIRA.<sup>[176]</sup>



redox mediator. The temperature increase of the redox mediator solution within two hours remained below 1 K. This was measured using a digital thermometer (Model E514, SUNARTIS, Willich, Germany) to exclude an increase in temperature which would lead to a higher solvent evaporation.

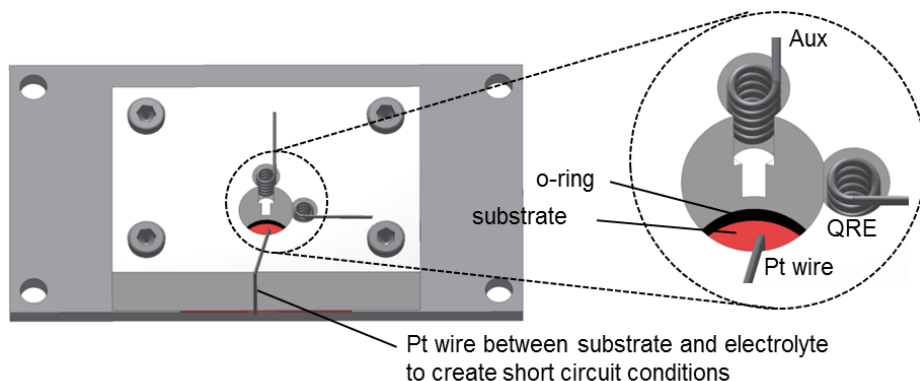


Fig. 4.3 – Left: Scheme of the Teflon® SECM cell with the DSC on the bottom (red) screwed onto an aluminum base plate. Right: Close-up of the coiled Pt Aux and QRE in the additional openings of the cell and the connection between the electrolyte and the photoanode to create short-circuit conditions.

**Shear Force Unit.** Based on the work of Tefashe,<sup>[160]</sup> the SF setup was developed further and integrated into the photoelectrochemical SECM (Fig. 4.2B). An independent personnel computer PC-II controlled the DSL4 SF control unit (including the internal lock-in amplifier LIA-II, operated by the SXM software, version 0.19f, Anfatec Instrument AG, Oelsnitz, Germany). Excitation and detection of vibrations for SF distance control was achieved by piezo electric plates (Piezomechanik Pickelmann GmbH, Munich, Germany) glued to home-made brass holders,<sup>[177]</sup> which were attached to the ME as depicted in Fig. 4.2B. The  $z$ -positional output of the DSL4 was connected to the input of the piezo controller E-665.CR<sup>[160]</sup> which moved the ME vertically along the  $z$ -axis. Simultaneously, this signal was monitored by a 16 bit analog-digital/digital-analog (AD/DA) board ((h) in Fig. 4.2B) connected to PC-I to generate a topography map. The SF control unit DS4L was operated with the following settings:  $K_i = 250$ ,  $K_p = 0$ , bias 409 mV, input gain 1, time constant = 1 ms, drive = 1 V. All components of the setup are given in the following Table 4.4.

Table 4.4 – Instrumental components of the photoelectrochemical SECM.

<b>Component</b>	<b>Distributor</b>	<b>Designation as in Fig. 4.2</b>
potentiostat $\mu$ -P3	M. Schramm, Heinrich Heine University, Düsseldorf, Germany	(c)
PC-I		(a)
PC-II		(g)
data acquisition board CIO-DAS 1602/16	Plug-in Electronic GmbH, Eichenau, Germany	(b)
data acquisition board CIO-DAC 02/16	Plug-in Electronic GmbH, Eichenau, Germany	(h)
positioning system I	SPI Robot, Oppenheim, Germany	(d)
positioning system II	N-661.21 A with controller E-861.1A1, Physik Instrumente, Karlsruhe, Germany	(e)
piezo motor P780.20 with E-665 LVPZT amplifier servo	Physik Instrumente, Karlsruhe, Germany	(i)
SF control unit DS4L	Anfatec Instrument AG, Oelsnitz, Germany (software version 0.19f)	(k)
LED	Zahner-Elektrik, Kronach, Germany	(f)
software SECMx	in-house	

In contrast to the TAS and EIS measurements performed by Hanna Ellis at Uppsala University, for which complete DSCs were used (Fig. 4.4B), only the photoanode with a redox electrolyte was used for SECM experiments (“pseudo-DSC” environment) (Fig. 4.4A).

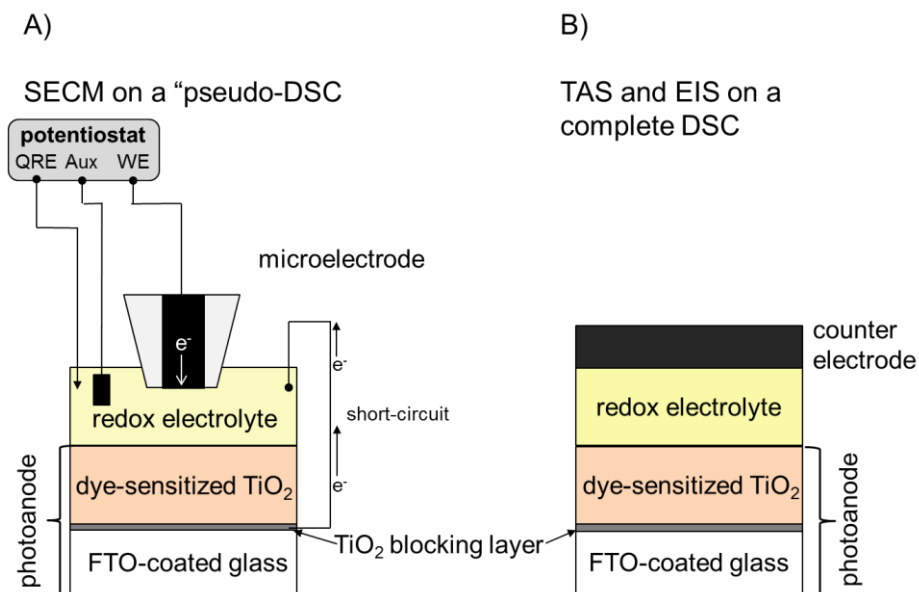


Fig. 4.4 – Scheme of the sample setup of A) a "pseudo-DSC" environment for SECM measurements without the counter electrode and B) a completely assembled DSC for TAS and EIS measurements.

In this thesis, the counter electrode is denoted as CE in a two-electrode setup, such as a DSC, and as Aux in a three-electrode setup as in SECM experiments. All SECM experiments were conducted at the Carl von Ossietzky University in Oldenburg by the author of this thesis.

## 4.6 Light Emitting Diodes

### 4.6.1 Setup of the LED Light Source

All experiments required a homogeneous light distribution, so the original LED setup<sup>[21]</sup> had to be extended. A condenser lens, a diffuser plate and an objective lens (10x) were inserted into the existing setup consisting of a potentiostat to power the LED, the actual LED and the photosensor which measured the light intensity and was connected to the potentiostat in a feedback loop (Fig. 4.5).

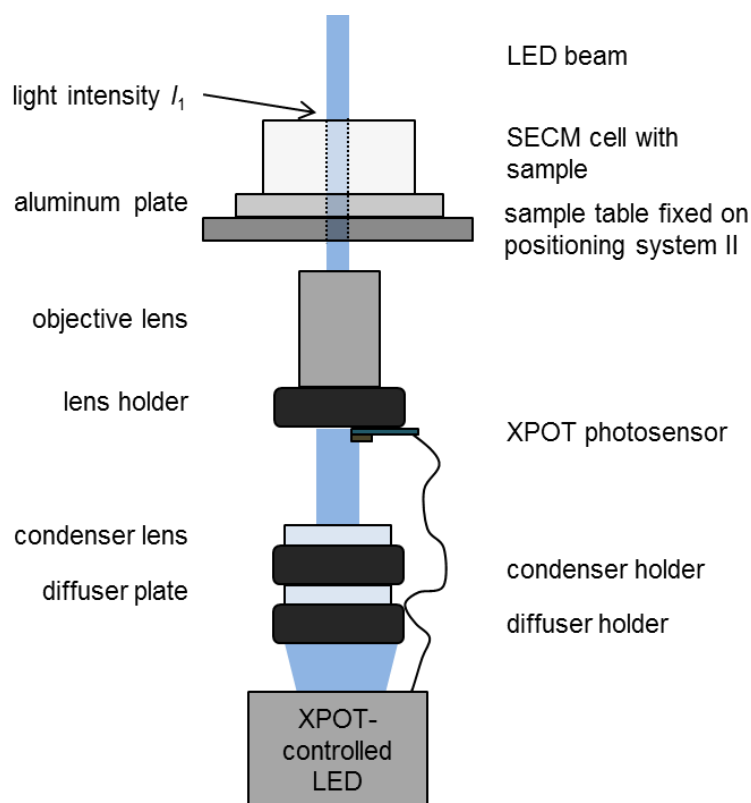


Fig. 4.5 – LED light source powered by XPOT potentiostat and necessary optics to ensure a homogeneous illumination of the sample integrated into the SECM setup.

These modifications ensured a homogeneous illumination of the sample. The size of the illuminated area ( $0.53 \text{ cm}^2$ ) is defined by the hole in the aluminum plate onto which the SECM cell is mounted. The SECM cell with the sample was placed 12.5 cm above the LED and illuminated from the backside. The illumination of the sample from the bottom simulates the situation of an actual DSC when the sunlight hits the FTO-coated carrier glass before it reaches the dye-sensitized semiconductor material (photoanode). The setup was designed in a way that ensured a stable light intensity  $I_1$  versus the applied voltage in the XPOT software which operated the potentiostat. The reproducibility of the intensity was checked monthly. All components of the illumination setup are summarized in Table 4.5.

Table 4.5 – Components of the illumination setup.

Component	Distributor
LED	Zahner-Elektrik, Kronach, Germany
Zahner XPOT software	Zahner-Elektrik, Kronach, Germany
condenser lens (focal length: 30 mm)	Thorlabs, Munich, Germany
diffuser plate (milk glass pane)	LOMO, St. Petersburg, Russia
objective lens Ultrafluar 10/0.2	Carl Zeiss, Jena, Germany
portable power meter	X9 <sub>3</sub> Laserpower, Gigahertz-Optik
potentiostat PGSTAT128N for Autolab LED Driver	Metrohm Autolab B.V., Germany
NOVA software (version 1.8.17)	Metrohm Autolab B.V., Germany

**Determination of Light Intensity.** A blue LED with a wavelength of 455 nm and a spectral half-width of 11 nm was used for the experiments in this thesis because the wavelength meets the excitation wavelength of the dyes D35, D45 and V35. Besides the blue LED, the photoelectrochemical SECM setup offers the possibility to use three more LEDs of different wavelengths (Fig. 4.6B). The spectra were recorded with a UV-Vis spectrometer (getSpec 2048, getAMO, Sofia, Bulgaria) using the software getSpec 7 (getAMO, Sofia, Bulgaria). One end of a 2 m long fiber optic cable (getSpec-LOH (Vis-NIR 350-2500 nm), getAMO, Sofia, Bulgaria) was connected to the spectrometer. The other end was fixed to the SECM aluminum ground plate where the SECM cell with the sample was placed during the measurements. The light intensity at the position of the sample,  $I_1$ , (see Fig. 4.5) was determined with the portable laser power meter X9<sub>3</sub> and plotted as a function of the applied voltage in the XPOT software (Fig. 4.6A).  $I_1$  was further corrected by a calibrated photodiode in an independent setup (see appendix 10.2) to obtain the actual light intensity  $I_3$ .

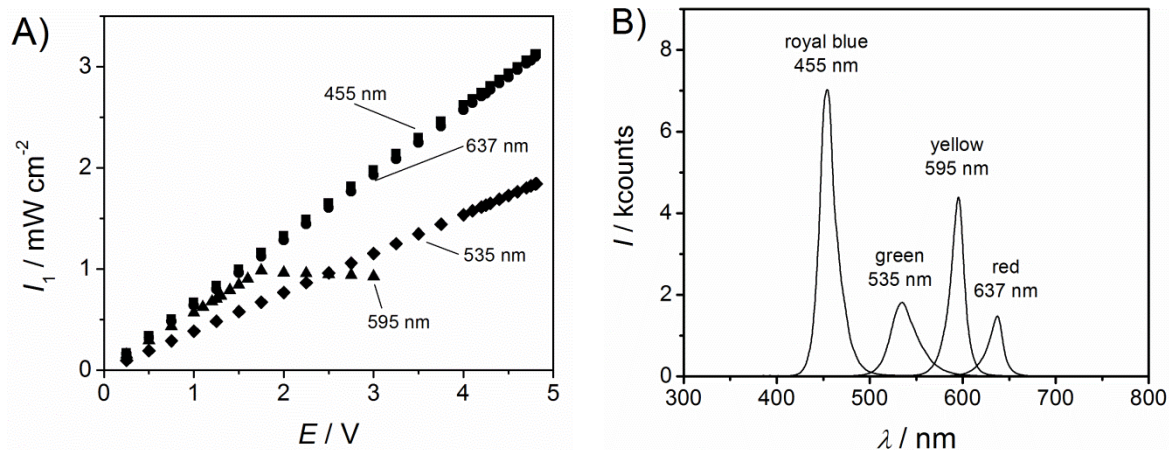


Fig. 4.6 – A) Light intensity  $I_1$  of four different LEDs (Zahner Elektronik) in dependence of the applied potential  $E$  in the Zahner XPOT software; 455 nm (royal blue, squares), 535 nm (green, diamonds), 595 nm (yellow, triangles), 637 nm (red, circles). B) Emission spectra of LEDs of Zahner Elektrik with maximum emission intensities at royal blue (455 nm), green (535 nm), yellow (595 nm) and red (637 nm).

The blue, green and red LED each give a linear function of the intensity when the applied voltage is increased. In contrast, the yellow LED shows saturation or even a slight decrease starting at an applied potential of about 1.7 V. Fig. 4.6B shows the emission maxima of the different LEDs with the intensity given in device specific units.

#### 4.6.2 Calculating the Photon Flux Density

To fit the dye regeneration rate constant  $k_{\text{ox}}$  according to equation (6.26), the light intensities need to be converted into a photon flux density,  $J_{h\nu}$ , which gives the number of photons per second and per square centimeter. In the first step, the photon energy  $E_{h\nu}$  is calculated *via*

$$E_{h\nu} = \frac{hc}{\lambda} \quad (4.1)$$

for the according wavelengths of the LEDs (Table 4.6).

Table 4.6 – Photon energies  $E_{hv}$  of LEDs of different wavelengths.

$\lambda_{LED} / \text{nm}$	455	535	595	637
$E_{hv} / 10^{-9} \text{ J}$	4.37	3.71	3.34	3.12

In a subsequent step, the number of photons per second,  $N_{hv}$ , was calculated using

$$N_{hv} = \frac{P}{E_{hv}} \quad (4.2)$$

where  $P$  denotes the power that was obtained by multiplying the light intensity  $I_3$  with the illuminated area,  $P = I_3 \times A$ .  $I_3$  was determined independently as the actual light intensity at the position of the photoanode in the SECM setup see equation (10.3) in appendix 10.2. For an exemplary light intensity of  $4.85 \text{ mW cm}^{-2}$  and an illuminated area of  $0.53 \text{ cm}^2$ ,  $P$  results in  $0.009159 \text{ W}$ .  $P$  divided by the photon energy,  $E_{hv}$ , obtained from equation (4.1) for  $\lambda = 455 \text{ nm}$  give the number of photons per second  $N_{hv}$ :

$$N_{hv} = \frac{0.009159 \text{ W}}{4.366 \times 10^{-19} \text{ W s}} = 2.098 \times 10^{16} \text{ s}^{-1} \quad (4.3)$$

As the last step, the photon flux density,  $J_{hv}$ , which is necessary for the analysis of the kinetic SECM experiments, can be calculated *via* the relation

$$J_{hv} = \frac{N_{hv}}{A \cdot N_A} \quad (4.4)$$

Considering the exemplary values, the illuminated area  $A$  and Avogadro's number,  $N_A$ ,  $J_{hv}$  results in:

$$J_{hv} = \frac{2.098 \times 10^{16} \text{ s}^{-1}}{0.53 \text{ cm}^2 \cdot 6.022 \times 10^{23} \text{ mol}^{-1}} = 6.57 \times 10^{-8} \text{ mol cm}^{-2} \text{ s}^{-1} \quad (4.5)$$

During the SECM experiments, special attention must be paid to keep the illumination conditions constant since  $J_{hv}$  varies with light intensity, wavelength and illuminated area.

## 4.7 Redox Electrolyte Preparation

### 4.7.1 Electrolyte for Experiments with Different Concentrations

The redox mediator concentrations used were significantly (by a factor 10 to 100) lower compared to regular DSCs in order to work under diffusion-controlled conditions. To obtain different concentrations of the redox mediator, a stock solution of 2 mM  $[\text{Co}(\text{bpy})_3](\text{PF}_6)_3$  + 0.1 M TBAPF<sub>6</sub> in MeCN was prepared and diluted with supporting electrolyte to the required concentrations (Table 4.7). The supporting electrolyte was 0.1 M TBAPF<sub>6</sub> in MeCN and was prepared by dissolving 0.7748 mg TBAPF<sub>6</sub> in 20 ml dried MeCN. The redox mediator stock solution and the supporting electrolyte were mixed with an Eppendorf pipette in an appropriate ratio to obtain the desired concentrations.

Table 4.7 – Desired  $[\text{Co}(\text{bpy})_3]^{3+}$  concentration and volumes of the 2 mM  $[\text{Co}(\text{bpy})_3]^{3+}$  stock solution and 0.1 M TBAPF<sub>6</sub> supporting electrolyte solution in dried MeCN each.

$c^* ([\text{Co}(\text{bpy})_3]^{3+})$ / mM	$V_{\text{stock}}$ / ml	$V_{\text{supporting electrolyte}}$ / ml
0.05	0.05	1.95
0.1	0.1	1.90
0.2	0.2	1.80
0.4	0.4	1.60
0.8	0.8	1.20
1	1.0	1.0
2	0	2.0

The solutions were stored in glass caps. Prior to each experiment, the solutions were bubbled with argon for 20 min, while the glass caps were closed with PARAFILM® to avoid solvent evaporation and thus a change in concentration as well as the diffusion of oxygen into the glass caps. The solution was removed from the glass cap using an Eppendorf pipette which was rinsed in the argon atmosphere of the glass cap five times. Afterwards, 500  $\mu\text{l}$  of the solution were removed from the glass cap and rapidly transferred to the SECM cell which had been filled with argon before. A CV was recorded to first check the

ME quality, second, check the mediator quality, third, determine the reduction potential of the redox mediator and fourth, determine the steady state current of the CV and calculate the actual concentration of the redox mediator using  $r_T$  and equation (3.5).

### 4.7.2 Electrolyte for Experiments with Different Light Intensities and Shear Force Imaging

MeCN, a solvent commonly employed in DSCs due to its high dielectric constant and its electrochemically inert behavior over a wide potential range, was dried over 3 Å molar sieve and stored under vacuum. Anhydrous TBAPF<sub>6</sub> was stored at 60 °C for at least 24 h prior to the experiment and then used as supporting electrolyte without further purification. TBAPF<sub>6</sub> was used in a 100fold concentration compared to the redox species to decrease the internal resistance of the solution to a minimum. TBAPF<sub>6</sub> was chosen since it dissociates in aprotic solvents like all tetraalkyl ammonium salts (cation: NR<sub>4</sub><sup>+</sup>, R = ethyl or butyl; anion: ClO<sub>4</sub><sup>-</sup>, PF<sub>6</sub><sup>-</sup>, BF<sub>4</sub><sup>-</sup>) and has a wide potential range which makes it suitable as supporting electrolyte in organic solvents.<sup>[178]</sup> The redox mediator [Co(bpy)<sub>3</sub>](PF<sub>6</sub>)<sub>3</sub> was synthesized according to published procedures (chapter 4.9.1).<sup>[10, 179]</sup> Depending on the experiment, different concentrations of redox mediator were used in 0.1 M TBAPF<sub>6</sub> as supporting electrolyte in dried MeCN. A 2 mM stock solution was prepared and diluted to the appropriate concentration using Eppendorf pipettes (see Table 4.7). The redox mediator solution was bubbled with argon for 30 min prior to each measurement. During SF-SECM measurements, a CV was recorded prior to and after each image to check the ME and to allow for the estimation of the redox mediator concentrations. This was necessary since the solvent evaporated to a small extent during imaging.

## 4.8 Titanium Dioxide Electrodes

### 4.8.1 Preparation of Titanium Dioxide Electrodes

For the experiments in this thesis, different kinds of TiO<sub>2</sub> electrodes were used. The TiO<sub>2</sub> electrodes were tailored to the dimensions of the [Co(bpy)<sub>3</sub>]<sup>2+/3+</sup> molecule in terms of pore size and further developed for the SECM measurements in cooperation with the Uppsala University in Sweden. One type of electrode, type C in Fig. 4.7, was manufactured by a

working group at the Huazhong University of Science and Technology in China. Five different types of TiO<sub>2</sub> electrodes were used for the SECM measurements (Fig. 4.7) which differ slightly in their structure because electrodes were prepared according to the latest scientific discoveries at the time of preparation. The thickness of the TiO<sub>2</sub> layer will be important in chapter 8 where the reliability of the SF distance control is tested.

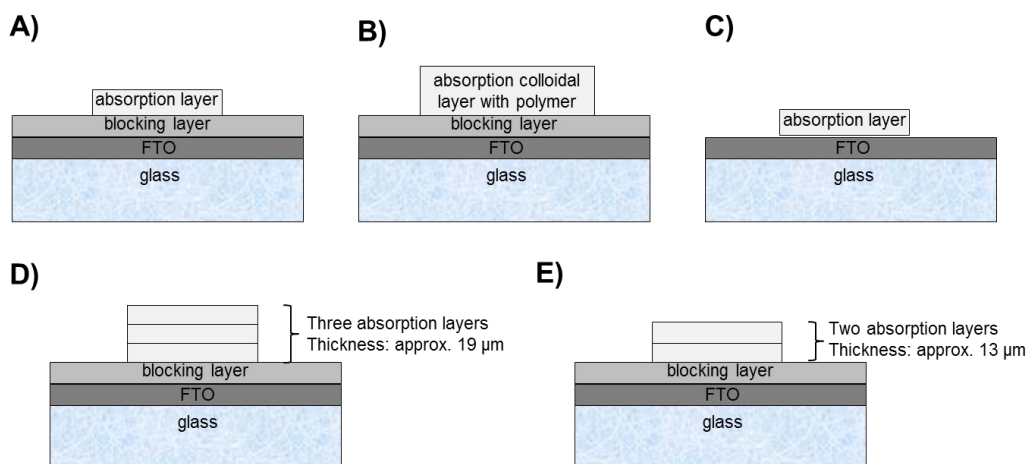


Fig. 4.7 – Scheme of structurally different TiO<sub>2</sub> electrodes used in this thesis. Dimensions are not true to scale.

Below, the preparation procedures of each type of TiO<sub>2</sub> electrode are described. Except for the formation of the blocking layer, the procedure for the substrates A, B, D and E is identical. FTO glass substrates with a conductivity of 15 Ω/sq were used (TEC15, Pilkington, Tokyo, Japan) and washed in an ultrasonic bath for 1 h in detergent, deionized water and ethanol, successively. Afterwards the electrodes were treated with a 40 mM aqueous titanium(IV) chloride (TiCl<sub>4</sub>) solution at 70 °C for 90 min to obtain a compact TiO<sub>2</sub> layer by thermal hydrolysis according to:



A blocking layer was applied to the FTO substrate to prevent a short-circuit and thus to minimize dark current<sup>[9]</sup> and to reduce charge recombination.<sup>[10]</sup> This step was followed by washing the electrodes with deionized water and ethanol. Depending on the electrode type (A, B, D or E), different TiO<sub>2</sub> pastes were used.

**Sample Type A.** One layer of Dyesol DSL 18NT-R (average nanoparticle size: 20 nm) was screen printed on an active area of  $5 \times 5 \text{ mm}^2$  ( $0.25 \text{ cm}^2$ ). The thickness of the films was about  $4.5 \text{ }\mu\text{m}$ .

**Sample Type B.** One layer of a mixture consisting of a  $\text{TiO}_2$  paste and a polymer was screen printed as a colloidal absorption layer that was tailored to the molecule size of  $[\text{Co}(\text{bpy})_3]^{2+/3+}$ . 60 wt% of the absorption paste DSL 18NR-T (average nanoparticle size: 20 nm) were diluted with 40 wt% of a mixture consisting of 90 wt% terpineol and 10 wt% ethylcellulose and screen printed on an area of  $5 \times 5 \text{ mm}^2$  ( $0.25 \text{ cm}^2$ ).

**Sample Type D.** Three layers of the  $\text{TiO}_2$  paste Dyesol DSL 30NR-D (nanoparticle size: 30 nm) were screen printed with a T53 mesh with 53 treads per centimeter. The screen printed area of the film was  $6 \times 8 \text{ mm}^2$  ( $0.42 \text{ cm}^2$ ) and the thickness about  $19 \text{ }\mu\text{m}$ .

**Sample Type E.** Two layers of the  $\text{TiO}_2$  paste Dyesol DSL 30NR-D (nanoparticle size: 30 nm) were screen printed with a T53 mesh, i.e. it has 53 treads per centimeter. The screen printed area of the film was  $6 \times 8 \text{ mm}^2$  ( $0.42 \text{ cm}^2$ ) and the thickness about  $13 \text{ }\mu\text{m}$ .

Types A, B, D and E were dried by heating them in an oven (Nabertherm Controller P320) for 10 min at  $125 \text{ }^\circ\text{C}$  in air. Each applied layer was dried before the next one was screen printed on top of it. As a last preparation step, the electrodes were sintered at a stepwise temperature program ( $180 \text{ }^\circ\text{C}$  for 10 min,  $320 \text{ }^\circ\text{C}$  for 10 min,  $390 \text{ }^\circ\text{C}$  for 10 min and  $500 \text{ }^\circ\text{C}$  for 60 min) in order to obtain electronic conductivity. It was important to screen print the  $\text{TiO}_2$  film in the center of the glass substrate which usually had a size of  $2 \times 3 \text{ cm}^2$ . Thus it was much more convenient to fix the substrate to the SECM Teflon<sup>®</sup> cell later on. A cooperation partner from Uppsala University determined the thickness of the  $\text{TiO}_2$  films (types A, D and E) on FTO by profilometry. In DSC research it is common to apply an additional compact layer on top of the absorption layer. However, this was not done in these experiments because it was assumed that this treatment might alter the pore size of the  $\text{TiO}_2$ , leaving pores of undefined size.

**Sample Type C.** The preparation of electrode type C was slightly different. FTO coated glass was washed and screen printed with a paste of 20 nm anatase particulates to obtain a film thickness of 5  $\mu\text{m}$ . The pore size of the  $\text{TiO}_2$  layer was also adjusted to the molecule size of the  $[\text{Co}(\text{bpy})_3]^{2+/3+}$  complex.

### 4.8.2 Dye-sensitization of the Titanium Dioxide Electrodes

The dye-sensitization of the  $\text{TiO}_2$  electrodes is described below. During the first SECM experiments, dye desorption was observed during the measurements. This problem was mitigated by changing the solvent of the dye solution from ethanol to MeCN. Ethanol was inappropriate because, similar to water, it can adsorb on  $\text{TiO}_2$  through hydrogen bonding and may have occupied the  $\text{TiO}_2$  sites with the effect that the dye molecules were bound loosely and desorbed as soon as the electrode was dipped into MeCN containing redox electrolyte. In order to proof the electrolyte to be free from dye, a few drops of the redox electrolyte was removed from the SECM cell during a measurement and investigated by UV-Vis. No bands which could be related to the respective dye under investigation were observed. MeCN is known to enhance the restructuring of the dye layer which was another argument to use it as solvent.

**Completely Sensitized  $\text{TiO}_2$  Electrodes.** In order to investigate dye-sensitized  $\text{TiO}_2$  photoanodes with SECM, they had to be prepared in a particular way. Different techniques were initially attempted but the following description based on Fig. 4.8 was the most suitable. The  $\text{TiO}_2$  electrode was cleaned carefully but thoroughly with MeCN to remove any pollution from the sample (Fig. 4.8, step 1). Afterwards, the  $\text{TiO}_2$  electrode was heated in a chamber furnace (K 1150-2, Heraeus, Germany; PID temperature controller 810, Eurotherm, Germany) to 350  $^\circ\text{C}$  within 20 min to desorb organic adsorbates and water from the  $\text{TiO}_2$  layer. To prevent the  $\text{TiO}_2$  pores from being burst by the fast evaporation of water at high temperatures, the furnace was heated up slowly. The final temperature was held for 15 min. Afterwards, the oven was cooled down to about 230  $^\circ\text{C}$ , the sample was removed and put on a heat-resistant glass plate. A funnel, whose opening was clogged with cotton wool, was placed upside down onto the sample to protect it from humidity and dirt. In the following step, the electrode was cooled to approx. 80  $^\circ\text{C}$  and stored in a 0.2 mM dye (D35 or D45) in MeCN bath for 12-16 h.

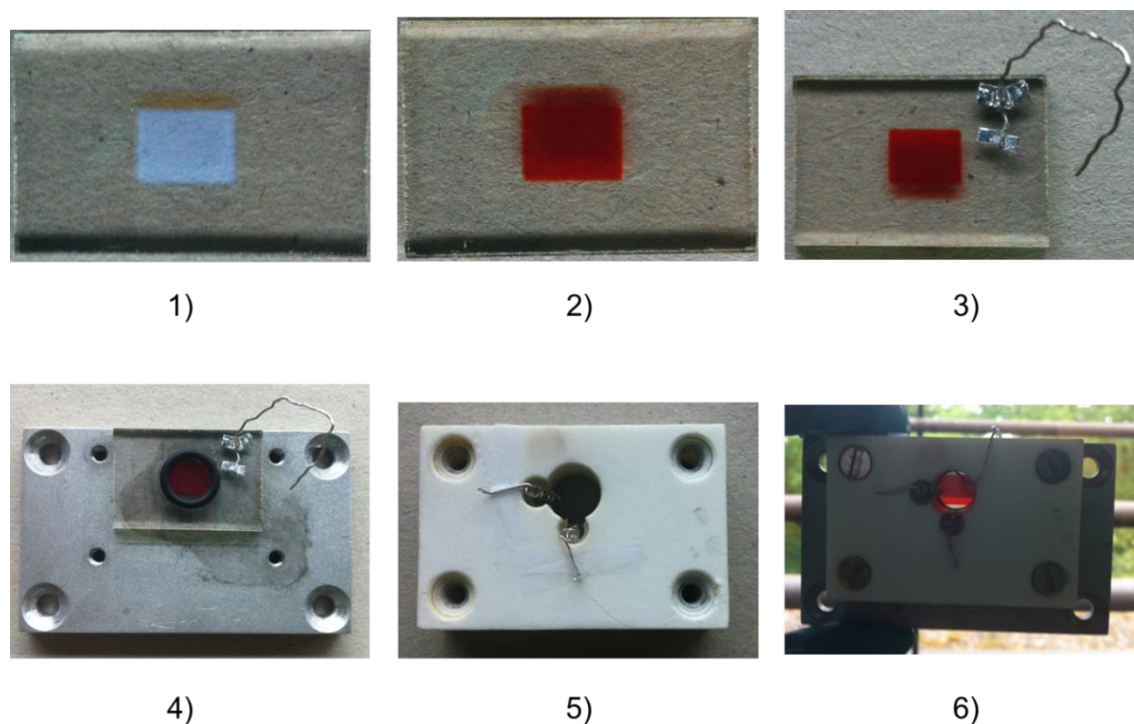


Fig. 4.8 – Photographic images of the preparation steps of a dye-sensitized TiO<sub>2</sub> electrode for the investigation with SECM.

It was necessary to dip the hot electrode into the dye solution to avoid capillary condensation of water. After removing the sample from the dye bath, it was rinsed with MeCN in order to eliminate the excess dye. The dyed sample was stored in MeCN for 1 h prior to each experiment (Fig. 4.8, step 2). Immediately before an experiment, the sample was rinsed with MeCN once more. The procedure for the hydrophilic dye V35 was slightly different. After the heating and cooling process, the electrodes were also inserted into 0.2 mM V35 in MeCN. They were left there for 12-16 h, removed, rinsed thoroughly with MeCN and put into an oven at 65 °C for 30 min to remove the MeCN completely. During the heating process, a funnel, whose opening was clogged with cotton wool, was placed upside down on the sample. Before the experiment, the sample was dipped into bidist. water in order to fill the pores.

Pt wires, an o-ring and the Teflon<sup>®</sup> cell were ultrasonicated in MeCN for 10 min and left to dry on a Kimtech cloth. To realize short-circuit conditions and hence avoid charging of the DSC during illumination and reduce recombination processes,<sup>[153, 180]</sup> a Pt wire was glued to the photoanode surface of the sample with silver adhesive tape (Fig. 4.8, step 3). The other end of the Pt wire was inserted into the electrolyte of the SECM cell

prior to a measurement. The connectivity between the photoanode and the Pt wire was confirmed with a multimeter. To define the region to be investigated, an o-ring was placed on the photoanode. Afterwards, the prepared photoanode was placed on the aluminum base plate of the SECM cell (Fig. 4.8, step 4). Coiled Pt wires as Aux and QRE were placed in the openings of the Teflon<sup>®</sup> SECM cell and fixed with scotch tape (Fig. 4.8, step 5). As a last step, the SECM cell was screwed onto the alumina base plate. By tightening the screws, the sample was fixed between the o-ring and the base plate to prevent leakage of the electrolyte (Fig. 4.8, step 6).

**Samples with Two Dyes Attached.** For experiments with two dyes attached to one TiO<sub>2</sub> substrate, the hot substrate was immersed into dye bath 1 with a low liquid level to obtain a small stripe of dye 1. After 12 h, the sample was removed from dye bath 1, rinsed with MeCN, turned by 180 degree and immersed into dye bath 2 to obtain a stripe of dye 2 (see Fig. 7.1A). A drawback of this procedure is that one dye was sensitized hot while the other was sensitized cold. In chapter 7.1 the consequences of this procedure are discussed.

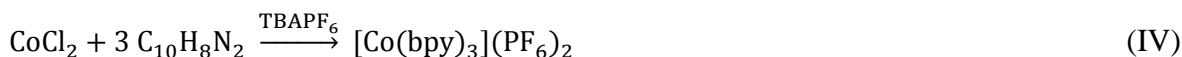
**Partly Sensitized TiO<sub>2</sub> Electrodes.** For the imaging experiments with SF-SECM, a sharp border between pristine TiO<sub>2</sub> and dye-sensitized TiO<sub>2</sub> was necessary. Therefore, the electrode was put into a small glass cap and the dye solution was inserted very carefully with a pipette until the level of the solution would lead to the desired thickness of the dye-sensitized area. The electrodes were left in the dye bath for 12 to 16 h.

## 4.9 Cobalt Complexes

### 4.9.1 Synthesis

**Tris(2,2'- bipyridine)cobalt(II/III) hexafluorophosphate.** The Co complexes [Co(bpy)<sub>3</sub>](PF<sub>6</sub>)<sub>2</sub> and [Co(bpy)<sub>3</sub>](PF<sub>6</sub>)<sub>3</sub> were synthesized with slight changes according to procedures known in literature.<sup>[10, 179]</sup> Briefly, 0.32 g (1.34 mmol) cobalt(II)-chloride hexahydrate dissolved in 10 ml methanol were added to a solution of 0.7 g (4.48 mmol) 2,2'-bipyridine dissolved in 30 ml methanol. The resulting brown solution was stirred for 2.5 h. Afterwards, an excess of TBAPF<sub>6</sub> (2.5 g) was added. The result was a light ochre precipi-

tate which was filtered and washed with 10 ml of ethanol, methanol and diethylether each. The color of the compound changed to a lighter shade after it was washed with diethylether. The compound was dried under vacuum for 5 h (decomposition point: 202 °C).



To oxidize the  $\text{Co}^{2+}$  complex, 0.19 g (0.23 mmol) of the synthesized compound was dissolved in 12 ml MeCN. An excess of the oxidation agent nitrosonium tetrafluoroborate ( $\text{NOBF}_4$ ) was added to the solution and stirred for 10 min.

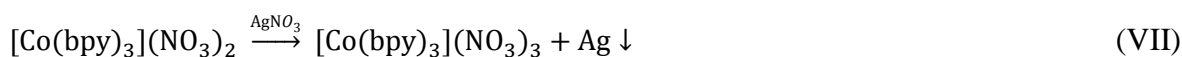


MeCN was removed carefully by cold distillation. The complex was redissolved in MeCN and a surplus amount of  $\text{TBAPF}_6$  was added. The addition of 15 ml diethyl ether precipitated the final  $\text{Co}^{3+}$  complex. It was filtered and washed with 10 ml methanol and ethanol each and dried under slightly reduced pressure (decomposition point: 285 °C). Recently, a research group from Uppsala, Sweden, successfully used hydrogen peroxide (30%) in MeCN to oxidize the  $\text{Co}^{2+}$  complex.<sup>[83]</sup>

**Tris(2,2'-bipyridine)cobalt(II/III) nitrate.**  $[\text{Co}(\text{bpy})_3](\text{NO}_3)_2$  and  $[\text{Co}(\text{bpy})_3](\text{NO}_3)_3$  were synthesized according to a known procedure.<sup>[22]</sup> First, 4.3 g (27.5 mmol) 2,2'-bipyridine were dissolved in 20 ml methanol and added dropwise to a solution of 2.7 g (9.28 mmol) cobalt(II) nitrate hexahydrate dissolved in 10 ml dist. water. This led to a gradual color change from pink to dark pink and finally to a dark reddish brown. After stirring the mixture for 18 h at room temperature, the solvent was removed carefully by cold distillation. The isolated product was washed consecutively with 15 ml of methanol and diethylether each and dried in a desiccator (melting point: 150 °C).



For the oxidation of the  $\text{Co}^{2+}$  complex, 1.9 g (2.92 mmol) of the dried  $[\text{Co}(\text{bpy})_3](\text{NO}_3)_2$  were dissolved in 120 ml MeCN and 0.5 g (2.94 mmol) silver(I) nitrate were added.



The mixture was stirred for 24 h. After the end of the reaction time, the silver particles were removed with a Büchner funnel. The mother liquor was left in a rotary evaporator to obtain a yellow-brown solid. It was washed twice with 5 ml methanol each and dried in a desiccator.

### 4.9.2 UV Spectroscopic Characterization

UV spectroscopy was used in this thesis to follow the synthesis of the Co complexes in three respects: first, to verify that all 2,2'-bipyridine coordinated to Co to build  $[\text{Co}(\text{bpy})_3]^{2+}$ , second, whether this complex has been completely oxidized to  $[\text{Co}(\text{bpy})_3]^{3+}$  and third, to compare the absorption range of both the reduced and oxidized complexes to literature.<sup>[181, 182]</sup> UV spectroscopy was chosen since it allows the determination of electron transitions and permits conclusions on the charge of central atoms in complexes.<sup>[181]</sup> Although the solvent influences the absorption wavelength, this influence is not considered here since the reduced and oxidized complexes were dissolved in the same solvent. MeCN as well as water are suitable to work within the UV range of the electromagnetic spectrum down to a wavelength of 195 nm at a sample thickness of 10 mm.<sup>[183]</sup> The four Co complexes investigated appear slight yellow in color and absorb electromagnetic radiation in the UV range. Compared to the lone ligand 2,2'-bipyridine (Fig. 4.9B, dashed blue line), the absorption bands of the  $\pi$ - $\pi^*$ -electron transitions of the four investigated  $[\text{Co}(\text{bpy})_3]^{2+/3+}$  complexes are shifted to longer wavelengths. The absorption bands of the oxidized complexes (red lines in Fig. 4.9B) are shifted to higher wavelengths in comparison to the reduced complexes (black lines in Fig. 4.9B). This bathochromic effect is attributed to the electrostatic interactions between the ligands and the central Co atom and is known for other transition metal complexes of rhodium and iridium.<sup>[181, 184]</sup>

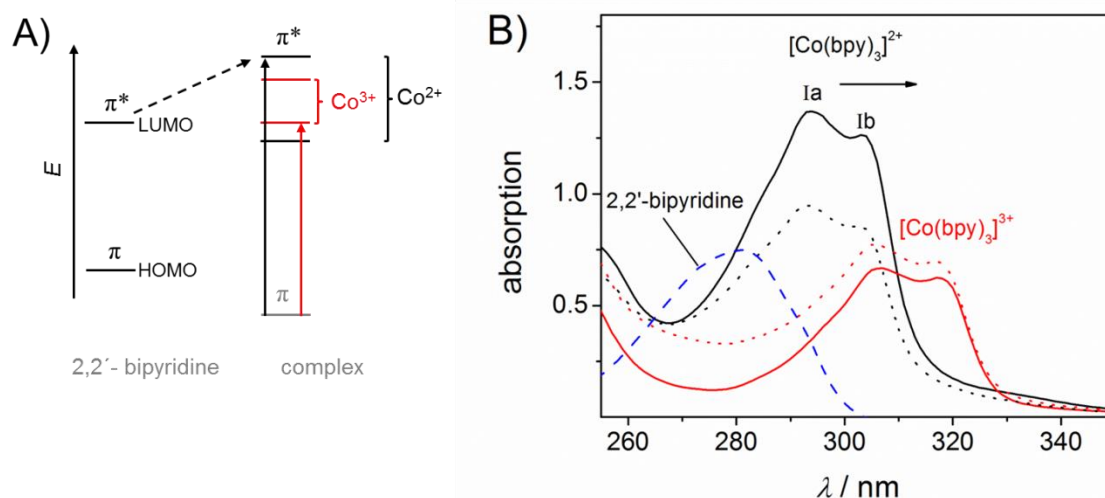


Fig. 4.9 – A) Energy levels of free 2,2'-bipyridine and of  $[\text{Co}(\text{bpy})_3]^{2+}$  and  $[\text{Co}(\text{bpy})_3]^{3+}$  with decreased energy levels due to shifted electron densities. B) UV spectra of a 2,2'-bipyridine solution (dashed blue line) and the used  $\text{Co}^{2+}$  complexes  $[\text{Co}(\text{bpy})_3](\text{PF}_6)_2$  (solid black line) and  $[\text{Co}(\text{bpy})_3](\text{NO}_3)_2$  (dotted black line) with absorption maxima at  $\lambda_{\text{max}} = 294$  und  $303$  nm as well as the  $\text{Co}^{3+}$  complexes, shifted to higher wavelengths,  $[\text{Co}(\text{bpy})_3](\text{PF}_6)_3$  (solid red line) and  $[\text{Co}(\text{bpy})_3](\text{NO}_3)_3$  (dotted red line) with absorption maxima at  $\lambda_{\text{max}} = 307$  and  $317$  nm. Different intensities result from different concentrations.

By complexation of 2,2'-bipyridine ligands with Co to  $[\text{Co}(\text{bpy})_3]^{2+}$ , electron density is shifted from the n orbital of the Co atom so that the  $\pi$  and  $\pi^*$  orbitals of the 2,2'-bipyridine move closer together. During oxidation of the reduced complex to  $[\text{Co}(\text{bpy})_3]^{3+}$ , even more electron density is removed from the n orbital and the distance between the  $\pi$  and  $\pi^*$  orbitals gets smaller and less energy is necessary to excite the electron (Fig. 4.9A). Thus, the absorption of the oxidized complex  $[\text{Co}(\text{bpy})_3]^{3+}$  is shifted to higher wavelengths (Fig. 4.9B). The wavelength maxima  $\lambda_{\text{max}}$  of the absorption bands Ia and Ib are equal for both  $\text{Co}^{2+}$  complexes  $[\text{Co}(\text{bpy})_3](\text{PF}_6)_2$  and  $[\text{Co}(\text{bpy})_3](\text{NO}_3)_2$ . The same is true for both  $\text{Co}^{3+}$  complexes  $[\text{Co}(\text{bpy})_3](\text{PF}_6)_3$  and  $[\text{Co}(\text{bpy})_3](\text{NO}_3)_3$ . In 2,2'-bipyridine, the pyridine rings rotate freely along the bonding axis between them and exhibit a  $\pi$ - $\pi^*$  transition at around 280 nm (dashed blue line). Complexed in  $[\text{Co}(\text{bpy})_3]^{2+/3+}$ , the pyridine rings of the 2,2'-bipyridine are fixed by bidentate coordination over the nitrogen atoms to the Co atom and do not rotate anymore. This results in a well-resolved vibronic structure with a peak-to-peak distance from Ia and Ib of approximately  $1020 \text{ cm}^{-1}$  ( $\tilde{\nu}_{\text{valence}}$  (pyridine)), a value that can also be extracted from table 3 of a study on 2,2'-bipyridyl complexes of Co, Rh and

Ir<sup>[181]</sup> and from figure S1 of a study on kinetics of tris(2,2'-bipyridine)cobalt(II/III).<sup>[182]</sup> All wavelength maxima are in good agreement with literature (Table 4.8, values in brackets) where perchlorate was the anion in the tris(2,2'-bipyridine)cobalt(II/III) complexes.

Table 4.8 – Position of the absorption bands of the  $\pi - \pi^*$ -electron transition of tris(2,2'-bipyridine) ligands in dependence of the charge on the central Co atom.

Charge on the central Co atom	$\lambda_{\max}$ Ia / nm (literature <sup>[181]</sup> )	$\lambda_{\max}$ Ib / nm (literature <sup>[181]</sup> )
+2	294 (289-298)	303 (298-306)
+3	307 (305-308)	317 (315-317)

The UV spectroscopic analysis of the four synthesized Co complexes and the comparison with the literature confirmed a change in oxidation state from +2 to +3 during the oxidation of the synthesized Co complexes. It also verified the coordination of the 2,2'-bipyridine ligands in *tris* configuration to the central Co atom as indicated by the splitting of the bands in Ia and Ib.<sup>[181, 184]</sup>

#### 4.9.3 Nuclear Magnetic Resonance Spectroscopy

The different magneticity of the Co complexes enabled the characterization by resonance techniques. The Co<sup>3+</sup> complexes used are diamagnetic *low-spin* complexes and can thus be characterized by NMR spectroscopy. On the contrary, Co<sup>2+</sup> complexes are *high-spin* complexes. Therefore they are paramagnetic and give no signal in NMR spectroscopy but are sensitive to electron paramagnetic resonance (EPR). NMR spectra of both Co<sup>2+</sup> complexes gave signals of the residual protons and carbon atoms of the solvent in <sup>1</sup>H-NMR and <sup>13</sup>C-NMR, respectively. The <sup>31</sup>P-NMR of [Co(bpy)<sub>3</sub>](PF<sub>6</sub>)<sub>2</sub> gave a septet with its maximum at -144.4 ppm. This behavior is known for a phosphorus atom which is sixfold coordinated by a halogen, in this case fluorine, dissolved in MeCN.<sup>[185, 186]</sup> <sup>31</sup>P-NMR (202 MHz, CD<sub>3</sub>CN, 305 K) [ppm]:  $\delta = -144.4$  (sept, 1P). Both Co<sup>3+</sup> complexes gave reasonable NMR spectra:

**[Co(bpy)<sub>3</sub>](PF<sub>6</sub>)<sub>3</sub>.** <sup>1</sup>H-NMR (500 MHz, CD<sub>3</sub>CN, 305 K) [ppm]:  $\delta = 7.32$  (d, 6H, bpy), 7.77 (t, 6H, bpy), 8.51 (t, 6H, bpy), 8.73 (d, 6H, bpy). The <sup>1</sup>H-NMR spectrum is in agreement with literature.<sup>[83]</sup>

<sup>13</sup>C-NMR (125.7 MHz, CD<sub>3</sub>CN, 305 K) [ppm]:  $\delta = 128.2$  (C1), 132.6 (C2), 144.9 (C3), 152.5 (C4), 156.7 (C5).

For checking purposes, a DEPT 135 spectrum was recorded which showed no quaternary C atoms. The signal of the carbon atom C5 was shifted upfield to the biggest extent compared to all other C atoms within the molecule ( $\delta = 156.7$ ). Due to its quaternary nature it gave no signal in the DEPT 135 spectrum.

<sup>31</sup>P-NMR (202 MHz, CD<sub>3</sub>CN, 305 K) [ppm]:  $\delta = -144.4$  (sept, 1P).

Comparable to [Co(bpy)<sub>3</sub>](PF<sub>6</sub>)<sub>2</sub>, the P atom of the hexafluorophosphate anion gave a septet at  $\delta = -144.4$  ppm.

**[Co(bpy)<sub>3</sub>](NO<sub>3</sub>)<sub>3</sub>.** <sup>1</sup>H-NMR (500 MHz, D<sub>2</sub>O, 305 K) [ppm]:  $\delta = 7.45$  (d, 6H, bpy), 7.77 (t, 6H, bpy), 8.53 (t, 6H, bpy), 8.81 (d, 6H, bpy).

<sup>13</sup>C-NMR (125.7 MHz, D<sub>2</sub>O, 305 K) [ppm]:  $\delta = 127.2$  (C1), 131.2 (C2), 144.1 (C3), 150.9 (C4), 155.9 (C5).

For checking purposes, a DEPT 135 spectrum was recorded which showed no quaternary C atoms. The signal of the carbon atom C5 was shifted upfield to the biggest extent compared to all other C atoms within the molecule ( $\delta = 155.9$ ). Due to its quaternary nature it gave no signal in the DEPT 135 spectrum. EPR spectra of both Co<sup>2+</sup> complexes were recorded with a Miniscope Control 6.51 spectrometer (Magnettech GmbH, Berlin, Germany) but no reliable data were obtained at room temperature.

### 4.9.4 Electrochemical Characterization

**Linear Sweep Voltammetry at a Rotating Disk Electrode.** LSV were recorded at an RDE in order to determine the diffusion coefficient  $D$  of [Co(bpy)<sub>3</sub>]<sup>2+/3+</sup> in different media (Table 4.9).

Table 4.9 – Reference electrodes employed for the electrochemical characterization of Co complexes.

Investigated system	Reference electrode	$E_{RE}$ / V vs. SHE
[Co(bpy) <sub>3</sub> ](PF <sub>6</sub> ) <sub>3</sub> in 0.1 M TBAPF <sub>6</sub> in MeCN	Ag/AgCl in 1-butyl-1-methylpyrrolidinium	0.197
[Co(bpy) <sub>3</sub> ](PF <sub>6</sub> ) <sub>3</sub> in 0.1 M TBAPF <sub>6</sub> in MPN	Ag/0.01 M AgNO <sub>3</sub> in 0.1 M TBAP in MeCN (CH Instruments)	approx. 0.36
[Co(bpy) <sub>3</sub> ](NO <sub>3</sub> ) <sub>3</sub> in 0.1 M KNO <sub>3</sub> in dist. water; with and without 1% PEG300	Ag/AgCl in 3 M KCl in dist. water	0.210 <sup>[187]</sup>

In order to work with a solution volume as small as possible, a pear-shaped flask was used as an electrochemical cell. The WE was a 3 mm diameter glassy carbon macroelectrode of which is known that no adsorption of Co species occurs thereon.<sup>[108]</sup> For each experiment, a Pt Aux was used and the RE was adjusted to the solvent of the investigated system (Table 4.9 gives the potential  $E$  with regard to the standard hydrogen electrode (SHE)). The solutions had a temperature of  $T = 23$  °. Rotation speeds were increased from 500 to 4000 rpm at a constant scan rate of  $\nu = 0.05$  V s<sup>-1</sup>. The start potential was set to a value at which no reaction occurred and was swept in cathodic direction to the reduction potential of the Co complex. 5 ml of 1 mM solutions of [Co(bpy)<sub>3</sub>](PF<sub>6</sub>)<sub>3</sub> in MeCN and MPN, respectively, were prepared with 0.1 M TBAPF<sub>6</sub> as supporting electrolyte. Also, a 1 mM solution of [Co(bpy)<sub>3</sub>](NO<sub>3</sub>)<sub>3</sub> in dist. water with 0.1 M KNO<sub>3</sub> as supporting electrolyte was prepared and heated to 70 °C to dissolve the Co complex.<sup>[22]</sup>

**Determination of Diffusion Coefficients at a ME.** CVs of 1 mM [Co(bpy)<sub>3</sub>](PF<sub>6</sub>)<sub>2</sub> and 1 mM [Co(bpy)<sub>3</sub>](PF<sub>6</sub>)<sub>3</sub> with 0.1 M TBAPF<sub>6</sub> as supporting electrolyte in MeCN were recorded at different scan rates  $\nu$ . All solutions were bubbled with argon for 10 min prior to the measurements. A three-electrode setup with a Au ME as WE ( $r_T = 12.26$  μm,  $RG = 12.9$ ), a 1 cm<sup>2</sup> Pt sheet as Aux and a Haber-Luggin RE ( $E^0_{Ag/Ag^+} = 0.23$  V vs. SHE) was controlled by a CH Instruments 660 workstation.

## III Results

### 5 Characterization of Cobalt Complexes

#### 5.1 Electrochemical Characterization

##### 5.1.1 Linear Sweep Voltammetry at a Rotating Disk Electrode

Linear sweep voltammograms (LSV) at different rotation speeds of the WE were recorded to determine  $D_{[\text{Co}(\text{bpy})_3]^{3+}}$  using Levich's equation (3.24). Four differently composed redox electrolytes (Table 5.1) were investigated by LSV.

Table 5.1 – Redox electrolytes employed.

Number	Redox mediator	Supporting electrolyte	Solvent	Additives
1	1 mM $[\text{Co}(\text{bpy})_3](\text{PF}_6)_3$	0.1 M TBAPF <sub>6</sub>	MeCN	-
2	1 mM $[\text{Co}(\text{bpy})_3](\text{PF}_6)_3$	0.1 M TBAPF <sub>6</sub>	MPN	-
3	1 mM $[\text{Co}(\text{bpy})_3](\text{NO}_3)_3$	0.1 M KNO <sub>3</sub>	dist. water	-
4	1 mM $[\text{Co}(\text{bpy})_3](\text{NO}_3)_3$	0.1 M KNO <sub>3</sub>	dist. water	1 % PEG300

Graph A in Fig. 5.1 shows LSVs of different rotation rates of  $[\text{Co}(\text{bpy})_3](\text{PF}_6)_3$  in MeCN (system 1) which was the most frequently used redox mediator system for the investigations in this thesis. 3-Methoxypropionitrile (MPN) offers several preferable properties such as lower flammability, lower volatility and a lower health risk than MeCN, the current state-of-the-art solvent in DSCs. MPN is therefore an interesting candidate to work as a DSC solvent (Fig. 5.1B) which worked well in combination with Co mediators.<sup>[108]</sup> Although MPN was not used in this thesis for further experiments, the diffusion coefficient of the Co redox species was nevertheless determined in this solvent. In order to use an aqueous redox mediator,  $D$  of  $[\text{Co}(\text{bpy})_3](\text{NO}_3)_3$  was determined in 0.1 M KNO<sub>3</sub> in dist. water (Fig. 5.1C) and in the same supporting electrolyte with 1 % of PEG300 being added (Fig. 5.1D), respectively. The cyan-colored shaded area indicates the region of limiting current

for which Levich's equation (3.24) is applicable.  $i_{lim}$  increased with an increasing rotation speed because a faster rotation enables more species to reach the active electrode surface. All LSVs show a steady-state region at the respective reduction potential of the Co redox system.

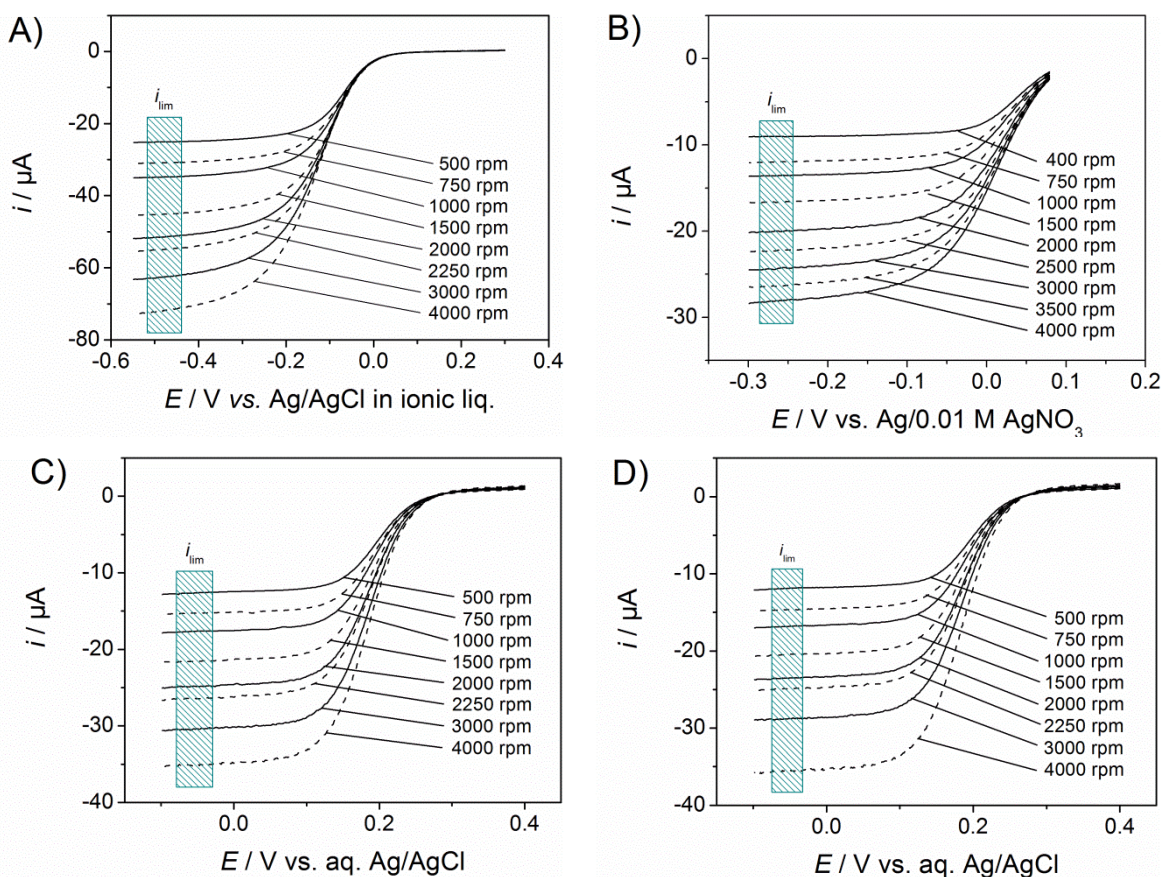


Fig. 5.1 – LSVs at a rotating glassy carbon electrode at varying rotation speeds of different redox mediators A) 1 mM  $[\text{Co}(\text{bpy})_3](\text{PF}_6)_3$  in 0.1 M TBAPF<sub>6</sub> in MeCN, B) 1 mM  $[\text{Co}(\text{bpy})_3](\text{PF}_6)_3$  in 0.1 M TBAPF<sub>6</sub> in MPN, C) 1 mM  $[\text{Co}(\text{bpy})_3](\text{NO}_3)_3$  in 0.1 M KNO<sub>3</sub> in dist. water, D) 1 mM  $[\text{Co}(\text{bpy})_3](\text{NO}_3)_3$  in 0.1 M KNO<sub>3</sub> in dist. water with 1% PEG300.

Since the square root of the angular frequency  $\omega$  was necessary for the Levich plot, it was calculated from the rotation speed ( $\omega = 2\pi f$ , with  $f$  being the rotation speed). As a further step, the limiting current  $i_{lim}$  had to be converted into the limiting current density  $j_{lim}$ , as the current per geometric electrode area. With an electrode radius  $r = 0.3$  cm, the active electrode area ( $A = \pi r^2$ ) was calculated to 0.071 cm<sup>2</sup> and the limiting current density  $j_{lim}$  could be calculated (Table 5.2).

## 5 Characterization of Cobalt Complexes

Table 5.2 – Limiting current densities  $j_{lim}$  resulting from the reduction of  $[\text{Co}(\text{bpy})_3]^{3+}$  in different redox electrolytes with regard to the square root of the angular frequency  $\omega$ .

$\omega$ /rpm	$\omega^{1/2}$ / $\text{s}^{-1/2}$	$j_{lim, \text{system 1}}^a$ / ( $10^{-3} \text{ A cm}^{-2}$ )	$j_{lim, \text{system 2}}^b$ / ( $10^{-3} \text{ A cm}^{-2}$ )	$j_{lim, \text{system 3}}^c$ / ( $10^{-3} \text{ A cm}^{-2}$ )	$j_{lim, \text{system 4}}^c$ / ( $10^{-3} \text{ A cm}^{-2}$ )
400	6.47	-	-0.128	-	-
500	7.23	-0.355	-	-0.181	-0.171
750	8.86	-0.437	-0.170	-0.217	-0.209
1000	10.23	-0.494	-0.192	-0.252	-0.240
1500	12.53	-0.640	-0.235	-0.305	-0.292
2000	14.47	-0.731	-0.285	-0.353	-0.334
2250	15.35	-0.780	-	-0.376	-0.354
2500	16.18	-	-0.316	-	-
3000	17.72	-0.891	-0.345	-0.431	-0.408
3500	19.14	-	-0.373	-	-
4000	20.47	-1.02	-0.400	-0.497	-0.504

a. at  $E = -0.55 \text{ V}$  vs. Ag/AgCl in 1-butyl-1-methylpyrrolidinium

b. at  $E = -0.3 \text{ V}$  vs. Ag/AgCl in 0.01 M  $\text{AgNO}_3$ , 0.1 M TBAP in MeCN

c. at  $E = -0.1 \text{ V}$  vs. Ag/AgCl in 3 M KCl

$j_{lim}$  was plotted as a function of the square root of  $\omega$  to obtain a Levich plot. If a Levich plot is a line passing through the origin, the current solely depends on the mass transport.<sup>[132]</sup> In this case, it is justified to apply the Levich equation to calculate the diffusion coefficient. All Levich plots shown in Fig. 5.2 display this behavior.

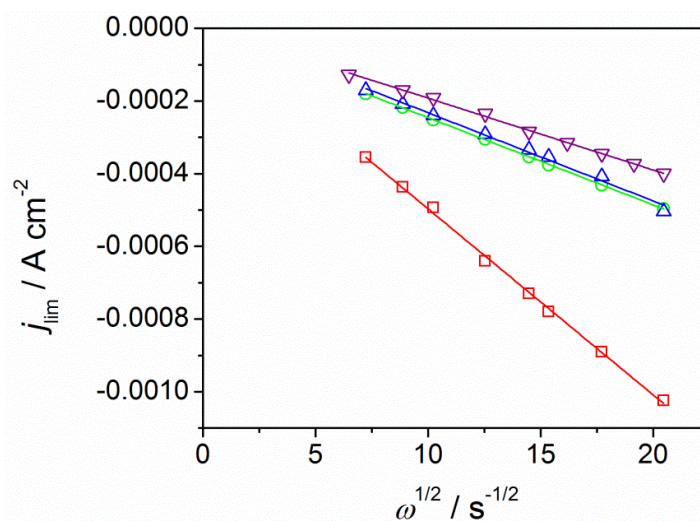


Fig. 5.2 – Levich plots of 1 mM  $[\text{Co}(\text{bpy})_3](\text{PF}_6)_3$  in MeCN (squares), 1 mM  $[\text{Co}(\text{bpy})_3](\text{PF}_6)_3$  in MPN (downward triangle), 1 mM  $[\text{Co}(\text{bpy})_3](\text{NO}_3)_3$  in dist. water (circle) and in dist. water with 1 % PEG300 (triangle).

The kinematic viscosity  $\nu$  of the solvent is, amongst others, a necessary parameter for the calculation of  $D$ . The kinematic viscosity of water at  $T = 25\text{ }^\circ\text{C}$  is  $\nu = 8.93 \times 10^{-3} \text{ cm}^2 \text{ s}^{-1}$ , obtained from the *Dortmund Data Bank*. For MeCN, the kinematic viscosity at  $T = 22.5\text{ }^\circ\text{C}$  was retrieved from the *Dortmund Data Bank* by data from references.<sup>[188, 189]</sup> They were interpolated to a value of  $\nu = 4.89 \times 10^{-3} \text{ cm}^2 \text{ s}^{-1}$ . No kinematic viscosity for MPN was available, hence it was calculated from the dynamic viscosity ( $\eta = 1.03 \text{ mPa s}$  at  $T = 25\text{ }^\circ\text{C}$ )<sup>[190]</sup> to  $\nu = 11.03 \times 10^{-3} \text{ cm}^2 \text{ s}^{-1}$  by  $\nu = \eta / \rho$  with  $\rho$  being the density ( $0.9341 \text{ g cm}^{-3}$  at  $T = 25\text{ }^\circ\text{C}$ ).<sup>[190]</sup> For all these measurements it has been assumed that the respective supporting electrolyte with a concentration of 0.1 M does not influence the viscosity of the solvent.  $D$  of  $[\text{Co}(\text{bpy})_3]^{3+}$  was calculated for different redox electrolytes (Table 5.3).

Table 5.3 – Diffusion coefficients of  $[\text{Co}(\text{bpy})_3]^{3+}$  calculated for different redox electrolytes.

Redox electrolytes	Levich slope / $\text{A s}^{1/2} \text{cm}^{-2}$	Kinematic viscosity $\nu$ / $\text{cm}^2 \text{s}^{-1}$	Diffusion coefficient $D$ / $\text{cm}^2 \text{s}^{-1}$
1	$-5.29 \times 10^{-5}$	$4.89 \times 10^{-3}$	<b><math>6.96 \times 10^{-6}</math></b>
2	$-1.96 \times 10^{-5}$	$11.03 \times 10^{-3}$	<b><math>1.92 \times 10^{-6}</math></b>
3	$-2.40 \times 10^{-5}$	$8.93 \times 10^{-3}$	<b><math>2.47 \times 10^{-6}</math></b>
4	$-2.26 \times 10^{-5}$	$8.93 \times 10^{-3}$	<b><math>2.26 \times 10^{-6}</math></b>

$D_{[\text{Co}(\text{bpy})_3]^{3+}}$  of  $6.96 \times 10^{-6} \text{ cm}^2 \text{ s}^{-1}$  obtained in MeCN (Table 5.3, system 1) is reasonable and in accordance with literature values which have been determined from diffusion-limited current of a CV at a Pt ME with a radius of  $r_T = 10 \mu\text{m}$  at  $\nu = 0.01 \text{ V s}^{-1}$  to  $D = 9.1 \times 10^{-6} \text{ cm}^2 \text{ s}^{-1}$  and by the same method at a glassy carbon microfiber disk ME with  $r_T = 5.5 \pm 1 \mu\text{m}$  to  $D = 4.3 \times 10^{-6} \text{ cm}^2 \text{ s}^{-1}$ , respectively.<sup>[10, 62]</sup> In the latter publication, the diffusion coefficient of the reduced compound  $[\text{Co}(\text{bpy})_3]^{2+}$  was determined to  $D = 4.6 \times 10^{-6} \text{ cm}^2 \text{ s}^{-1}$  and was hence slightly higher than that of the oxidized compound. The same trend was observed in chapter 5.1.2 where the reduced species showed a slightly higher diffusion coefficient than the oxidized form of the Co complex. The diffusion coefficient of  $[\text{Co}(\text{bpy})_3]^{3+}$  in MeCN obtained by CV at a ME in chapter 5.1.2 differed only by 10 % from the result obtained by LSV at an RDE in this chapter. This small difference can be attributed to slight changes in concentration, temperature and certain measurement inaccuracies.  $D$  of  $[\text{Co}(\text{bpy})_3]^{3+}$  in  $\text{H}_2\text{O}$  (redox electrolyte no. 3, Table 5.1),  $\text{H}_2\text{O}$  with 1% PEG 300 (redox electrolyte no. 4, Table 5.1) and MPN (redox electrolyte no. 2, Table 5.1) as solvent were slightly lower compared to the diffusion coefficient in MeCN as solvent. This can be attributed to the slightly higher viscosity of  $\text{H}_2\text{O}$  and MPN in comparison with MeCN.  $D$  was necessary to calculate the effective reaction rate constant  $k_{\text{eff}}$  from the experimentally determined normalized rate constant  $\kappa$  which interdepend by equation (3.7).

### 5.1.2 Determination of Diffusion Coefficients at a ME

Diffusion coefficients of  $[\text{Co}(\text{bpy})_3]^{2+}$  and  $[\text{Co}(\text{bpy})_3]^{3+}$  were also determined by recording CVs at a ME and compared to those obtained from RDE measurements. Limiting currents

$i_{\text{lim}}$  were taken from the steady-state regions of CVs of  $[\text{Co}(\text{bpy})_3]^{2+}$  (oxidation) and  $[\text{Co}(\text{bpy})_3]^{3+}$  (reduction) and diffusion coefficients were calculated from  $i_{\text{lim}}$  using equation (3.5). At every scan rate  $\nu$  ranging from 0.01 to 0.1  $\text{V s}^{-1}$ , the oxidized complex (filled symbols), have lower diffusion coefficients than the reduced complexes (empty symbols, Fig. 5.3).

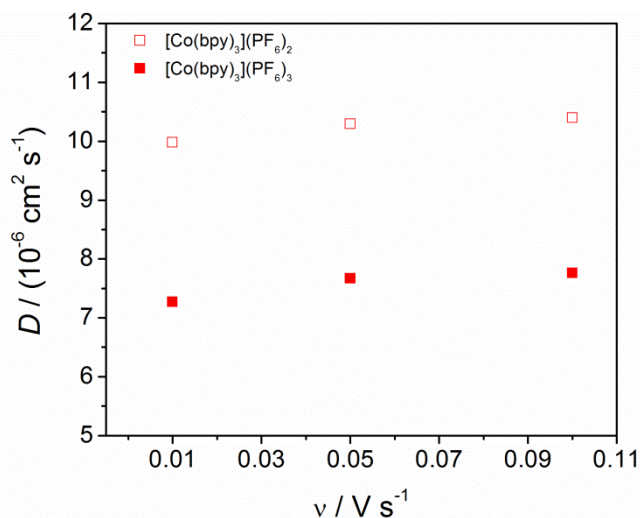


Fig. 5.3 – Determination of diffusion coefficients  $D$  of 1 mM  $[\text{Co}(\text{bpy})_3]^{2+}$  (empty symbols) and  $[\text{Co}(\text{bpy})_3]^{3+}$  (filled symbols) in 0.1 M TBAPF<sub>6</sub> in MeCN obtained by CV at a Au ME ( $r_T = 12.3 \mu\text{m}$ ) at different scan rates  $\nu = 0.01, 0.05$  and  $0.1 \text{ V s}^{-1}$ .

The diffusion coefficients of the reduced complex  $[\text{Co}(\text{bpy})_3]^{2+}$  in MeCN are in good agreement with literature values determined by Feldt *et al.*<sup>[10]</sup> from diffusion-limiting current to be  $9.1 \times 10^{-6} \text{ cm}^2 \text{ s}^{-1}$  as well as with values obtained in this thesis by LSV at an RDE for the oxidized complex ( $6.96 \times 10^{-6} \text{ cm}^2 \text{ s}^{-1}$ ). Ellis *et al.*<sup>[62]</sup> obtained a diffusion coefficient for  $[\text{Co}(\text{bpy})_3]^{2+}$  of  $D = 4.6 \times 10^{-6} \text{ cm}^2 \text{ s}^{-1}$  and for  $[\text{Co}(\text{bpy})_3]^{3+}$  of  $4.3 \times 10^{-6} \text{ cm}^2 \text{ s}^{-1}$  in an electrolyte consisting of 0.22 M  $\text{Co}(\text{bpy})_3(\text{PF}_6)_2$ , 0.05 M  $\text{Co}(\text{bpy})_3(\text{PF}_6)_3$ , 0.2 M TBP and 0.1 M  $\text{LiClO}_4$  in MeCN. The latter group also obtained higher  $D$  for the reduced species compared to the oxidized species. The diffusion coefficients obtained at different  $\nu$  do not deviate much when only one form of redox species is considered (Table 5.4). The diffusion coefficients are in good agreement with those obtained by LSV at a RDE (chapter 5.1.1).

Table 5.4 – Diffusion coefficients of  $[\text{Co}(\text{bpy})_3]^{2+}$  and  $[\text{Co}(\text{bpy})_3]^{3+}$  obtained from a 1 mM solution in 0.1 M TBAPF<sub>6</sub> in MeCN. Diffusion coefficients were obtained by CV at a ME with different scan rates  $\nu$  and calculated using equation (3.5).

Redox mediator	$\nu / \text{V s}^{-1}$	$D / (10^{-6} \text{ cm}^2 \text{ s}^{-1})$
$[\text{Co}(\text{bpy})_3]^{2+}$	0.01	9.98
	0.05	10.3
	0.10	10.4
$[\text{Co}(\text{bpy})_3]^{3+}$	0.01	7.27
	0.05	7.67
	0.10	7.76

## 5.2 Redox Mediator Stability

### 5.2.1 Stability towards Light

It was necessary to rule out that an illuminated Co complex contributes to the current at the ME by light-induced processes other than mediator regeneration, for example by light-induced decomposition. Therefore, approach curves with  $[\text{Co}(\text{bpy})_3](\text{PF}_6)_3$  (Fig. 5.4A) and  $[\text{Co}(\text{bpy})_3](\text{NO}_3)_3$  (Fig. 5.4B) were performed over thoroughly cleaned glass as substrate, both in the dark and under illumination. A 455 nm LED was set to different light intensities to illuminate the substrate. Each graph shows the experimental values (symbols) and fits (lines) to an analytical approximation.<sup>[150]</sup> In order to evaluate the experimentally obtained curves, an approach curve which corresponds to a slow reaction at the sample ( $\kappa = 0.1$ ), is plotted complementary.

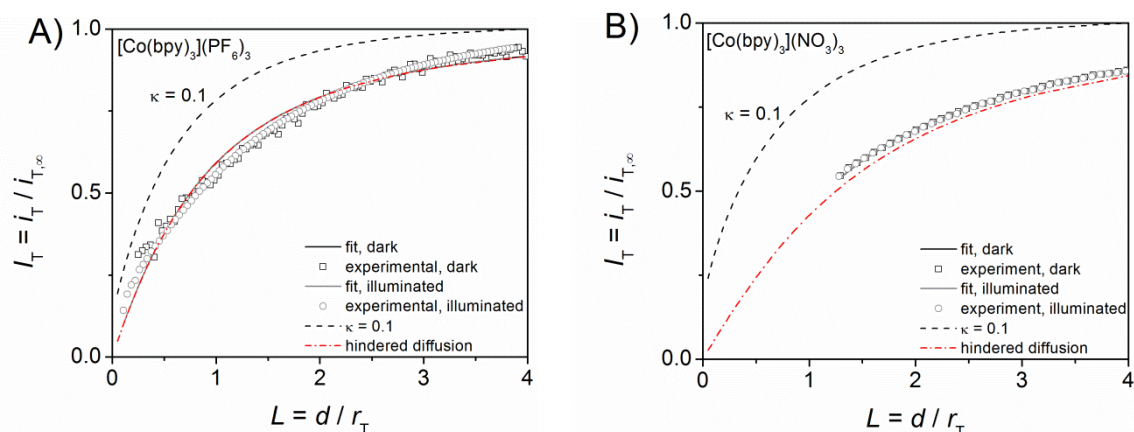


Fig. 5.4 – SECM approach curves above an insulating glass substrate with A) 1 mM  $[\text{Co}(\text{bpy})_3](\text{PF}_6)_3$  in dried MeCN with 0.1 M  $\text{TBAPF}_6$  at a Pt ME ( $r_T = 12.6 \mu\text{m}$ ,  $RG = 32.9$ ),  $E_T = -0.13 \text{ V}$  vs. Ag QRE in the dark and at  $3.8 \text{ mW cm}^{-2}$  455 nm LED and B) 1 mM  $[\text{Co}(\text{bpy})_3](\text{NO}_3)_3$  in dist. water with 0.1 M  $\text{KNO}_3$  and 1 % PEG300 at a Pt ME ( $r_T = 14.2 \mu\text{m}$ ,  $RG = 19.3$ ),  $E_T = -0.23 \text{ V}$  vs. Ag QRE in the dark and at  $4.9 \text{ mW cm}^{-2}$  455 nm LED. The three-electrode setup was completed by a Pt Aux and controlled by a potentiostat ( $\mu\text{-P3}$ , M. Schramm, Heinrich Heine Universität, Düsseldorf, Germany).

The normalized approach curves of both redox mediators overlap in the dark and under illumination. They are nearly congruent with hindered diffusion. This confirms that the redox mediators under illumination do not contribute to the current at the ME. It can thus be concluded that the electrochemical reactions in the dye regeneration experiments in the following chapters can be attributed to the reaction between the redox mediator and the dye rather than to a photoreaction of the redox mediator.

Another method was chosen to rule out a contribution from the  $[\text{Co}(\text{bpy})_3](\text{NO}_3)_3$  to the current at the ME during illumination. CVs were recorded at a ME-to-substrate distance of  $d = 12 \mu\text{m}$ . First, a CV was recorded in the dark, the intensity of the LED was set to  $1.2 \text{ mW cm}^{-2}$  and another CV was recorded. The light was switched off, a CV was recorded, the intensity of the LED was doubled ( $2.4 \text{ mW cm}^{-2}$ ) and another CV was recorded (Fig. 5.5B).

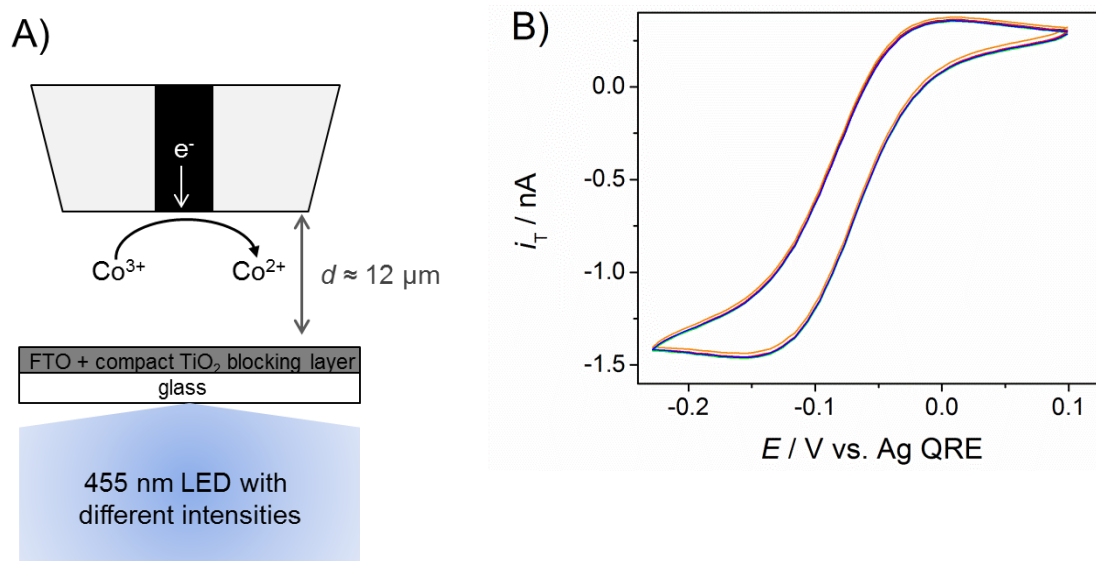


Fig. 5.5 – A) Experimental setup to record CVs at different light intensities and B) CVs at  $v = 0.05 \text{ V s}^{-1}$  of  $1 \text{ mM } [\text{Co}(\text{bpy})_3](\text{NO}_3)_3$  in the dark (black) and while illuminated with four different light intensities of a 455 nm emitting LED in  $\text{mW cm}^{-2}$ : 1.2 (orange), 2.4 (red), 3.7 (green), 4.9 (blue) at a Pt ME ( $r_T = 14.2 \text{ } \mu\text{m}$ ).

The CVs recorded at different light intensities do not deviate from the CV taken in the dark. It can be concluded that no light-induced decomposition of the redox mediator occurred. As a consequence, the current detected at the ME during recording of approach curves over an illuminated dye-sensitized electrode originated from the substrate-generated  $\text{Co}^{3+}$  species which are recycled at the ME. Thus, a contribution of the redox mediator to the current detected at the ME during SECM measurements can be excluded.

### 5.2.2 Long-Term Stability

The long-term stability of three differently aged  $0.1 \text{ mM } [\text{Co}(\text{bpy})_3](\text{NO}_3)_2$  solutions in  $0.1 \text{ M KNO}_3$  in dist. water was determined by CV. Therefore, the potential of a glassy carbon macroelectrode ( $\varnothing = 3 \text{ mm}$ ) was scanned in anodic direction. The current was detected at the electrode, calculated into a current density  $j$  and is plotted as a function of the potential  $E$  versus a saturated calomel electrode (SCE, Fig. 5.6). A Pt wire was used as Aux and an SCE (X10 OGL REF921, Orignalys, France) as RE. The electrochemical cell was controlled by an Origastat e 100 potentiostat.

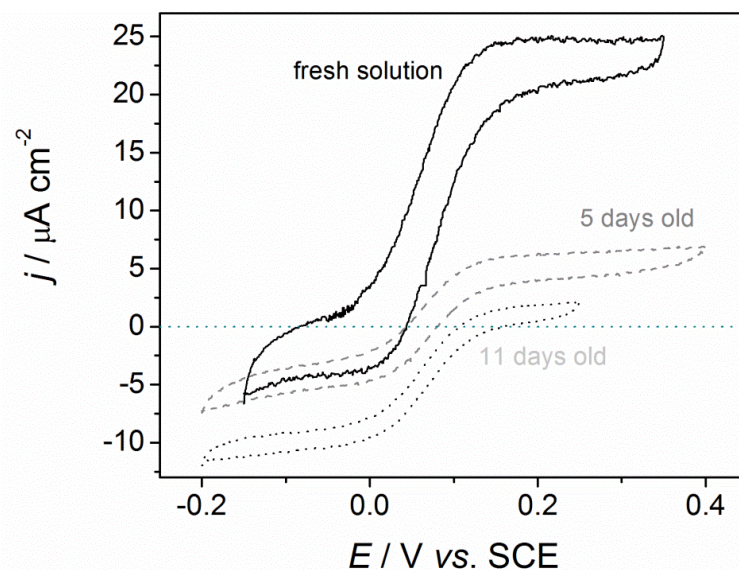


Fig. 5.6 – Comparison of  $[\text{Co}(\text{bpy})_3](\text{NO}_3)_2$  solutions in 0.1 M  $\text{KNO}_3$  in dist. water of different age: a freshly prepared (solid, black), a five days old (dashed, grey) and an eleven days old solution (dotted, black). The CVs have been recorded at a scan rate of  $0.05 \text{ V s}^{-1}$  and a rotation speed of 1500 rpm at a 3 mm glassy carbon macroelectrode. The solutions investigated had different concentrations which led to small deviations in the resulting current density and should be neglected.

Differences in current density of the three solutions investigated can be attributed to different concentrations that have been applied unintentionally. The CV of the freshly prepared solution (solid line in Fig. 5.6) showed an oxidation current and almost no reduction current as was expected for a complex that undergoes a change from oxidation state +2 to +3. After the solution was left exposed to air for five days, about half of the amount of  $[\text{Co}(\text{bpy})_3]^{2+}$  seemed to have been oxidized by oxygen in air. This led to a reduction current from  $[\text{Co}(\text{bpy})_3]^{3+}$  to  $[\text{Co}(\text{bpy})_3]^{2+}$  (dashed line in Fig. 5.6). An exposition of the solution to air for eleven days resulted in a complete oxidation of  $[\text{Co}(\text{bpy})_3]^{2+}$  to the oxidation state of +3. As a result, only the reduction current resulting from the electron transfer from  $\text{Co}^{3+}$  to  $\text{Co}^{2+}$  was observed (dotted line in Fig. 5.6). It is common practice to synthesize  $\text{Co}^{2+}$  complexes by bubbling air through a  $\text{Co}^{3+}$  complex solution.<sup>[96]</sup>

An explanation for the above observation is the stability of the different oxidation states of Co.  $\text{Co}^{3+}$  is more stable in a complex, whereas  $\text{Co}^{2+}$  shows a higher stability in salts and binary compounds which was described in more detail in chapter 2.5.2. The experiments conducted here led to the conclusion that only freshly prepared solution must be used for the experiments in this thesis such as the determination of diffusion coefficients.

### 5.3 Choice of Microelectrode Material

Pt is a common electrode material for SECM experiments. However, persistent adsorption phenomena observed during preliminary experiments in this thesis (Fig. 5.7A) have led to changing the electrode material. A ME was placed 150  $\mu\text{m}$  above a D35-sensitized  $\text{TiO}_2$  photoanode ( $z = 0 \mu\text{m}$ ) in order to perform approach curves in the dark and at different light intensities ranging from 0.73 to 4.8  $\text{mW cm}^{-2}$ . Within less than ten minutes, the bulk current detected at the ME at  $z = 0 \mu\text{m}$  decreased from  $-3 \text{ nA}$  to  $-0.5 \text{ nA}$  (Fig. 5.7A), most likely caused by adsorption of  $[\text{Co}(\text{bpy})_3]^{3+}$  on Pt. When Au instead of Pt was used as electrode material, the bulk current remained nearly constant and even increased slightly from  $-3.5 \text{ nA}$  to  $-4 \text{ nA}$  after the light intensity was increased (Fig. 5.7B).

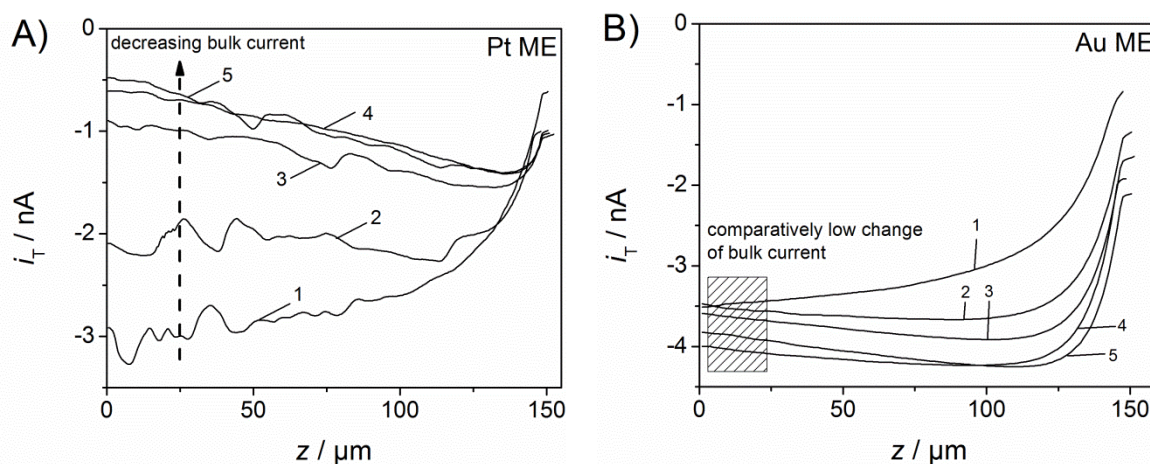


Fig. 5.7 – Approach curves with 600  $\mu\text{l}$  1 mM  $[\text{Co}(\text{bpy})_3](\text{PF}_6)_3$  mediator over a 4.5  $\mu\text{m}$  thick D35-sensitized  $\text{TiO}_2$  electrode (sample type A) with A) a Pt ME ( $r_T = 12.3 \mu\text{m}$ ,  $RG = 5.93$ ),  $E_T = -0.10 \text{ V}$ , and B) a Au ME ( $r_T = 13.5 \mu\text{m}$ ,  $RG = 17.8$ ),  $E_T = -0.20 \text{ V}$ . Approach curves were recorded with a translation speed of  $0.5 \mu\text{m s}^{-1}$  (A) and  $1 \mu\text{m s}^{-1}$  (B) at different light intensities (455 nm LED) in  $\text{mW cm}^{-2}$ : A) dark (curve 1), 1.2 (curve 2), 2.4 (curve 3), 3.8 (curve 4), 4.8 (curve 5); B) dark (curve 1), 0.73 (curve 2), 1.5 (curve 3), 2.3 (curve 4), 3.0 (curve 5).

The current increase mentioned can be attributed to a higher amount of substrate-generated oxidized redox species at increased light intensity which diffuse to and are detected at the ME. Sapp *et al.*<sup>[108]</sup> stated that Au and carbon outperform Pt as electrode material in terms of efficiency in DSCs with Co redox mediators, but they did not report on any adsorption on Pt and neither did Nusbaumer *et al.*<sup>[9]</sup>

The adsorption behavior of  $[\text{Co}(\text{bpy})_3](\text{PF}_6)_3$  was furthermore tested by recording the current in dependence of elapsed time ( $i$ - $t$ -curves). A small glass jar sealed with PAR-AFILM® served as an electrochemical cell with either a Pt or a Au ME as WE, a Pt wire as Aux and a Ag wire as QRE. Prior to each measurement, the solution was bubbled thoroughly with argon. During each measurement, argon flowed gently above the solution surface. First, in order to determine the steady state potential, CVs were recorded by scanning in cathodic direction to the range where the reduction from  $\text{Co}^{3+}$  to  $\text{Co}^{2+}$  proceeds (Fig. 5.8A). In the next step, the determined potential  $E_T = -0.10$  V for Pt ME and  $E_T = -0.05$  V for Au ME was applied to the WE and  $i$ - $t$ -curves were recorded (Fig. 5.8B).

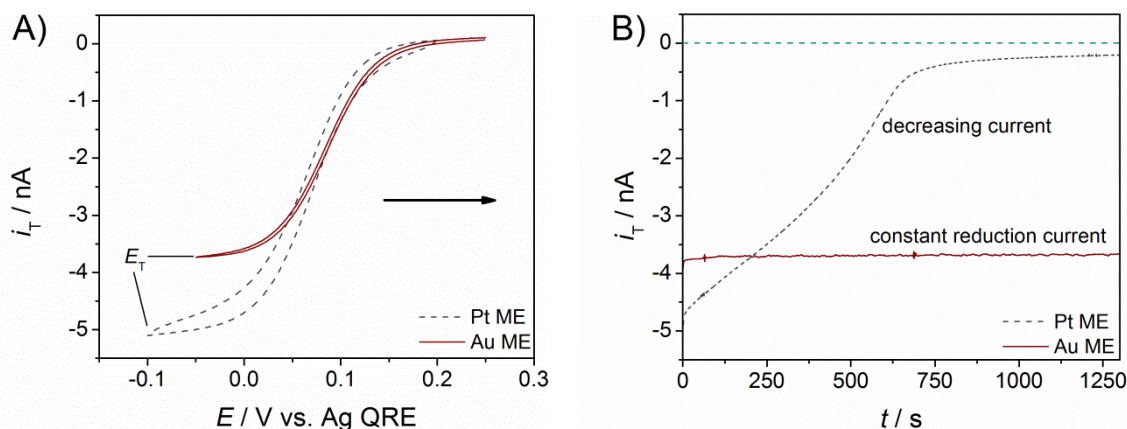


Fig. 5.8 – A) CVs of a 1 mM  $[\text{Co}(\text{bpy})_3](\text{PF}_6)_3$  solution with 0.1 M TBAPF<sub>6</sub> in dried MeCN at a Pt ME ( $r_T = 14.2$   $\mu\text{m}$ ,  $RG = 19.3$ ) (grey dashed line),  $\nu = 0.05$   $\text{V s}^{-1}$  and a Au ME ( $r_T = 13.5$   $\mu\text{m}$ ,  $RG = 17.8$ ) (red solid line),  $\nu = 0.01$   $\text{V s}^{-1}$ . B)  $i$ - $t$ -curves of the same solution with the applied potential  $E_T = -0.10$  V at a Pt ME (grey dashed line) and  $E_T = -0.05$  V at a Au ME (red solid line).

The reduction current at the Au ME remained constant over a time range of 1300 s. Afterwards, the measurement was terminated because a straight line was obtained with no tendency to lower currents. The behavior at the Pt ME was different and the current decreased within approximately 600 s from  $-4.7$  to  $-0.5$  nA presumably due to absorption of species to the metal surface of the ME. Not only tris-bipyridine ligands, but also  $\text{NO}_3^-$  is known to adsorb on Pt,<sup>[191, 192]</sup> thus no  $i$ - $t$ -curve was recorded with  $[\text{Co}(\text{bpy})_3](\text{NO}_3)_3$  on Pt, since it was considered more important to proof the suitability of Au as ME material than to demonstrate that Pt is not suitable to be applied in  $[\text{Co}(\text{bpy})_3](\text{NO}_3)_3$  solutions. Although Au MEs are suitable to work with Co complexes, they need to be handled specially and carefully in some aspects which are discussed in chapter 4.4.2.

## 6 Establishing DSC One-Electron Redox Mediators for use in SECM

### 6.1 SECM Model for Dye Regeneration by a One-Electron Redox Mediator

In this thesis, the one-electron redox mediator  $[\text{Co}(\text{bpy})_3]^{3+}$  was used for the first time in SECM kinetic experiments taking a correct stoichiometry as a basis (see chapter 7.3 and the corresponding publication by the author of this thesis and co-authors<sup>[122]</sup>) to determine the dye regeneration constant  $k_{\text{ox}}$ . Previous SECM studies have already used  $[\text{Co}(\text{bpy})_3]^{3+}$  for the investigation of dye regeneration but with a formula based on the stoichiometry of the  $\text{I}/\text{I}_3^-$  mediator.<sup>[16, 17]</sup> In order to obtain  $k_{\text{ox}}$ , it was necessary to derive a suitable equation of  $k_{\text{eff}}$  - which amongst others comprises  $k_{\text{ox}}$  - based on the work of Shen *et al.*<sup>[153]</sup> and Tefashe *et al.*<sup>[21]</sup> who derived kinetic information from SECM experiments employing the established redox mediator  $\text{I}/\text{I}_3^-$ . SECM has been proven suitable before to determine rate constants in a DSC with an  $\text{I}/\text{I}_3^-$  mediator.<sup>[18-21, 153]</sup>

In the following, the reaction at the one-electron redox mediator / dye-sensitized  $\text{TiO}_2$  interface is explained and the derivation of the overall effective reaction rate constant  $k_{\text{eff}}$  is presented. In order to use a redox mediator in an SECM FB experiment, it is essential to supply only the oxidized form of the redox mediator ( $\text{Co}^{3+}$ ) in the working solution. The reduced form ( $\text{Co}^{2+}$ ) is generated locally at the ME (Fig. 6.1). The ME-generated  $[\text{Co}(\text{bpy})_3]^{2+}$  species diffuses from the Au ME to the  $\text{TiO}_2$ /dye interface, reduces the photooxidized dye  $\text{D}^+$  while being oxidized itself to  $[\text{Co}(\text{bpy})_3]^{3+}$ . During the approach of the ME towards the illuminated photoanode, the current detected at the ME depends more and more on the regeneration of the  $[\text{Co}(\text{bpy})_3]^{3+}$  induced by the dye regeneration reaction on the substrate (and thus on the kinetic limitations of the reduction of  $\text{D}^+$ ) and less on the  $[\text{Co}(\text{bpy})_3]^{3+}$  diffusing from the surrounding working solution towards the ME.

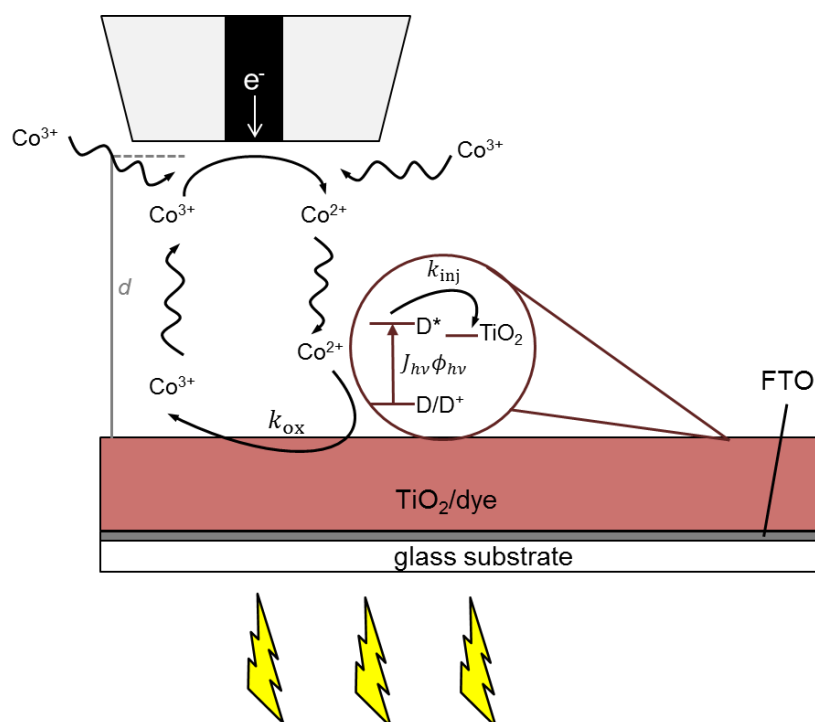


Fig. 6.1 – Scheme of the SECM FB mode investigation of the dye regeneration with the one-electron redox mediator  $[\text{Co}(\text{bpy})_3]^{2+}$  and  $[\text{Co}(\text{bpy})_3]^{3+}$ , for the sake of clarity denoted as  $\text{Co}^{2+}$  and  $\text{Co}^{3+}$ . Reprinted with permission from *J. Phys. Chem. C*, 2015, 119, 21775-21783 Copyright © 2015 American Chemical Society.<sup>[122]</sup>

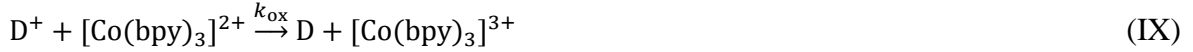
From SECM measurements, an overall effective rate constant  $k_{\text{eff}}$  was determined which comprises light absorption, electron injection, dye regeneration processes, and various recombination processes (see also Fig. 7.7 in chapter 7.2). Values of  $k_{\text{eff}}$  can be attributed to individual steps of the reaction sequence as long as photon flux  $J_{\text{hv}}$  and dye loading  $\Gamma_{\text{D}}$  of the  $\text{TiO}_2$  film are known. In particular, an oxidation rate constant  $k_{\text{ox}}$  of the oxidation of the reduced redox mediator species can be determined as a fitting parameter.

FB approach curves were fitted to an analytical approximation for irreversible kinetic reactions on a substrate (equation (3.19)), to obtain the normalized, dimensionless, first-order rate constant  $\kappa$ . Afterwards,  $k_{\text{eff}}$  ( $\kappa = k_{\text{eff}} \times r_{\text{T}}/D$ ) was related to the microscopic processes in the dye-sensitized  $\text{TiO}_2$  electrodes. The model described below assumes uniform accessibility of the dye molecules with respect to illumination and the  $\text{Co}^{2+}$  diffusion. Furthermore, the measurements were performed under short-circuit conditions, in order to reduce recombination reactions to a minimum. At the excitation wavelength of 455 nm, D35/ $\text{TiO}_2$  electrodes in combination with the  $[\text{Co}(\text{bpy})_3]^{2+/3+}$  mediator show an IPCE of

approximately 81 %.<sup>[83]</sup> That means that under short-circuit conditions there is almost no loss caused by recombination processes at the wavelength used in this thesis. At the interface between TiO<sub>2</sub> and the dye D, the following reactions occur under illumination



with D being the dye molecule in its uncharged state,  $h\nu$  being the photon energy,  $\phi_{hv}$  being the excitation cross-section in cm<sup>2</sup> mol<sup>-1</sup>, D\* being the excited dye molecule,  $k_{inj}$  being the rate constant of the electron injection into TiO<sub>2</sub> and D<sup>+</sup> being the photooxidized dye molecule. The overall reaction of the reduced redox mediator species with the photooxidized dye molecule and the dye regeneration rate  $k_{ox}$  is given as:



In the following, for the sake of clarity, the oxidized redox species  $[Co(bpy)_3]^{3+}$  is written as Co<sup>3+</sup> and the reduced redox species  $[Co(bpy)_3]^{2+}$  is written as Co<sup>2+</sup>. The dye loading of the TiO<sub>2</sub> film is given as

$$\Gamma_D = c_D \cdot l \quad (6.1)$$

with  $c_D$  being the dye concentration within the TiO<sub>2</sub> film in mol cm<sup>-3</sup> and  $l$  being the thickness of the dye layer in cm. The diffusion-limited ME current for a one-electron redox mediator such as the Co complex (Co<sup>3+</sup> + e<sup>-</sup> → Co<sup>2+</sup>) is given as

$$i_{T,\infty} = 4nFD[Co^{3+}]^* r_T \quad (6.2)$$

with  $n = 1$  being the number of electrons,  $F$  being Faraday's constant in A s mol<sup>-1</sup>,  $D$  being the diffusion coefficient of  $[Co^{3+}]^*$  in cm<sup>2</sup> s<sup>-1</sup>,  $[Co^{3+}]^*$  being the concentration of the oxidized redox species in the bulk in mol cm<sup>-3</sup> and  $r_T$  being the radius of the ME in cm. Equation (6.2) is exact for an infinite large value of  $RG$  ( $RG \rightarrow \infty$ ).<sup>[193]</sup> It is still a good approximation for  $RG = 10$ , which is used in a large number of SECM experiments.<sup>[194]</sup> The limiting current at the ME under SECM FB conditions is:

$$i_{T,lim} = 4nFD[Co^{3+}]^* r_T \cdot I_{T,cond}(L) \quad (6.3)$$

where  $I_{T,cond}(L)$  is the current resulting from the diffusion-controlled mediator recycling at the sample. The light absorption and charge injection are expressed by



and



With the known reaction on the sample (equation (IX)), expressions for  $\Gamma_{D^*}$  (equations (6.4) and (6.5)) and  $\Gamma_{D^+}$  (equations (6.6) and (6.7)) can be derived using the Bodenstein principle of steady state.

$$\frac{d\Gamma_{D^*}}{dt} = 0 = \phi_{hv} \cdot J_{hv} \cdot \Gamma_D - k_{inj} \cdot \Gamma_{D^*} \quad (6.4)$$

Herein,  $J_{hv}$  is the photon flux density in  $\text{mol cm}^{-2} \text{s}^{-1}$ .

$$\frac{\Gamma_D}{\Gamma_{D^*}} = \frac{k_{inj}}{\phi_{hv} \cdot J_{hv}} \quad (6.5)$$

$$\frac{d\Gamma_{D^+}}{dt} = 0 = k_{inj} \cdot \Gamma_{D^*} - k_{ox} \cdot \Gamma_{D^+} \cdot [\text{Co}^{2+}]_S \quad (6.6)$$

The index S denotes the concentration of  $\text{Co}^{2+}$  at the substrate surface.

$$\frac{\Gamma_{D^+}}{\Gamma_{D^*}} = \frac{k_{inj}}{k_{ox} \cdot [\text{Co}^{2+}]_S} \quad (6.7)$$

Considering the law of mass conservation (equation (6.8))

$$\Gamma_{D^0} = \Gamma_D + \Gamma_{D^+} + \Gamma_{D^*} \quad (6.8)$$

and the flux of  $[\text{Co}^{2+}]$  coming from the sample (equation (6.9))

$$\frac{1}{A} \frac{dn}{dt} = r = k_{ox} \Gamma_{D^+} [\text{Co}^{2+}]_S \quad (6.9)$$

the steady state expressions for the ratio of  $\Gamma_D$  from (6.5) and (6.7) are inserted into (6.9) to yield an expression for  $\Gamma_{D^*}$  (equation (6.10))

$$\frac{\Gamma_{D^0}}{\Gamma_{D^*}} = \left[ \frac{k_{inj}}{\phi_{hv} \cdot J_{hv}} + \frac{k_{inj}}{k_{ox} \cdot [\text{Co}^{2+}]_S} + 1 \right] \quad (6.10)$$

$$\Gamma_{D^*} = \frac{\Gamma_{D^0}}{\frac{k_{inj}}{\phi_{hv} \cdot J_{hv}} + \frac{k_{inj}}{k_{ox} \cdot [\text{Co}^{2+}]_S} + 1} \quad (6.11)$$

By substituting equation (6.11) into equation (6.12)

$$i_{k,\text{lim}} = nFAk_{\text{ox}} \cdot \Gamma_{\text{D}^+} \cdot [\text{Co}^{2+}]_{\text{S}} \quad (6.12)$$

and by replacing  $\Gamma_{\text{D}^+}$  with the expression of  $\Gamma_{\text{D}^*}$  from the Bodenstein principle, by replacing  $\Gamma_{\text{D}^*}$  with the mass balance, solving the fractional expression as well as expanding the denominator simplified for  $n = 1$ , the limiting substrate current can be written as:

$$i_{k,\text{lim}} = nFAk_{\text{inj}} \cdot \frac{\Gamma_{\text{D}^0}}{\frac{k_{\text{inj}}}{\phi_{h\nu} \cdot J_{h\nu}} + \frac{k_{\text{inj}}}{k_{\text{ox}} \cdot [\text{Co}^{2+}]_{\text{S}}} + 1} \quad (6.13)$$

$$i_{k,\text{lim}} = F\Gamma_{\text{D}^0} \frac{k_{\text{inj}}}{\frac{k_{\text{inj}} \cdot k_{\text{ox}} \cdot [\text{Co}^{2+}]_{\text{S}} + k_{\text{inj}} \cdot \phi_{h\nu} \cdot J_{h\nu} + \phi_{h\nu} \cdot J_{h\nu} \cdot k_{\text{ox}} \cdot [\text{Co}^{2+}]_{\text{S}}}{\phi_{h\nu} \cdot J_{h\nu} \cdot k_{\text{ox}} \cdot [\text{Co}^{2+}]_{\text{S}}}} \quad (6.14)$$

$$i_{k,\text{lim}} = F\Gamma_{\text{D}^0} \cdot \frac{k_{\text{inj}} \cdot \phi_{h\nu} \cdot J_{h\nu} \cdot k_{\text{ox}} \cdot [\text{Co}^{2+}]_{\text{S}}}{k_{\text{inj}} \cdot k_{\text{ox}} \cdot [\text{Co}^{2+}]_{\text{S}} + k_{\text{inj}} \cdot \phi_{h\nu} \cdot J_{h\nu} + \phi_{h\nu} \cdot J_{h\nu} \cdot k_{\text{ox}} \cdot [\text{Co}^{2+}]_{\text{S}}} \quad (6.15)$$

Now, the reciprocal value is formed and divided into the three core processes which contribute to the limiting substrate current: light absorption, dye regeneration and electron injection (equation (6.16)).

$$\frac{1}{i_{k,\text{lim}}} = \frac{1}{F\Gamma_{\text{D}^0} \cdot \phi_{h\nu} \cdot J_{h\nu}} + \frac{1}{F\Gamma_{\text{D}^0} \cdot k_{\text{ox}} \cdot [\text{Co}^{2+}]_{\text{S}}} + \frac{1}{F\Gamma_{\text{D}^0} \cdot k_{\text{inj}}} \quad (6.16)$$

### light absorption    dye regeneration    electron injection

Since the electron injection process was found to occur in the femtosecond to picosecond time regime,<sup>[65]</sup> the effective rate constant  $k_{h\nu,\text{eff}}$  is considered to be essentially equal to the overall rate of light absorption  $\phi_{h\nu}J_{h\nu}$ .<sup>[195]</sup>

$$\frac{1}{k_{h\nu,\text{eff}}} = \frac{1}{k_{\text{inj}}} + \frac{1}{\phi_{h\nu} \cdot J_{h\nu}} \approx \frac{1}{\phi_{h\nu} \cdot J_{h\nu}} \quad (6.17)$$

The limiting condition with respect to the concentration of  $\text{Co}^{2+}$  species on the sample,  $[\text{Co}^{2+}]_{\text{S}}$ , occurs if  $[\text{Co}^{2+}]_{\text{S}} = [\text{Co}^{3+}]^*$  where \* indicates the concentration in the bulk solution. Thus, the limiting current could be written as equation (6.18).

$$\frac{1}{i_{k,\text{lim}}} = \frac{1}{F\Gamma_{\text{D}^0} \cdot \phi_{h\nu} \cdot J_{h\nu}} + \frac{1}{F\Gamma_{\text{D}^0} \cdot k_{\text{ox}} \cdot [\text{Co}^{3+}]^*} \quad (6.18)$$

By dividing equation (6.18) by the ME current in bulk solution  $i_{T,\infty}$  from equation (6.2), we obtain the normalized limiting substrate current  $I_{k,\text{lim}}$

$$I_{k,\text{lim}} = \frac{i_{k,\text{lim}}}{i_{T,\infty}} = \frac{i_{k,\text{lim}}}{4nFD[\text{Co}^{3+}]^*r_T} \quad (6.19)$$

where  $n$  equals unity for the electron transfer from  $\text{Co}^{2+}$  to  $\text{Co}^{3+}$ . For the following, the sample surface that participates in the electron transfer is approximated to  $A \approx \pi r_T^2$ . The diffusion coefficient of both the reduced and the oxidized species is considered approximately equal:  $D_{\text{Co}^{2+}} \approx D_{\text{Co}^{3+}} = 6.96 \times 10^{-6} \text{ cm}^2 \text{ s}^{-1}$  (see chapters 5.1.1 and 5.1.2). The reciprocal substrate current consists of limiting currents of individual contributions. Those are the reciprocal electron migration through the semiconductor  $I_{\text{el,lim}}$  at a given working distance  $L$ , the reciprocal current for diffusion-controlled mediator recycling at the sample (“positive FB”)  $I_{T,\text{cond}}$  and the reciprocal limiting substrate current  $I_{k,\text{lim}} = i_{k,\text{lim}} / i_{T,\infty}$  that would flow if all other processes are more facile.

$$\frac{1}{I_S} = \frac{i_{T,\infty}}{i_{k,\text{lim}}} + \frac{1}{I_{T,\text{cond}}} + \frac{1}{I_{\text{el,lim}}} \quad (6.20)$$

The term  $1/I_{\text{el,lim}}$  is the electron migration through the semiconductor layer which is not limited at low mediator concentrations and therefore neglected.<sup>[153]</sup>

$$\frac{1}{I_{k,\text{lim}}} = \frac{i_{T,\infty}}{i_{k,\text{lim}}} \quad (6.21)$$

$$\frac{i_{T,\infty}}{i_{k,\text{lim}}} = \frac{4 \cdot F \cdot D \cdot [\text{Co}^{3+}]^* r_T}{F \cdot \pi \cdot r_T^2 \cdot \Gamma_{D^0} \cdot \phi_{h\nu} \cdot J_{h\nu}} + \frac{4 \cdot F \cdot D \cdot [\text{Co}^{3+}]^* r_T}{F \cdot \pi \cdot r_T^2 \cdot \Gamma_{D^0} \cdot k_{\text{ox}} \cdot [\text{Co}^{3+}]} \quad (6.22)$$

$$= \frac{4 \cdot D \cdot [\text{Co}^{3+}]^*}{\pi \cdot r_T \cdot \Gamma_{D^0} \cdot \phi_{h\nu} \cdot J_{h\nu}} + \frac{4 \cdot D}{\pi \cdot r_T \cdot k_{\text{ox}} \cdot \Gamma_{D^0}} \quad (6.23)$$

The term for  $1/I_S$  must be compared with the expression

$$\frac{1}{I_S} = \frac{1}{I_{T,\text{cond}}} + \frac{4}{\pi} \cdot \frac{1}{\kappa} \quad (6.24)$$

for the uncomplicated first order irreversible process at the surface for which analytical expressions of SECM approach curves are available ( $\kappa = k_{\text{eff}}^*(r_T/D)$ ). The reciprocal limiting substrate current  $I_{k,\text{lim}} = i_{k,\text{lim}} / i_{T,\infty}$  can be expressed as:

$$\frac{i_{T,\infty}}{i_{k,\text{lim}}} = \frac{1}{I_{T,\text{cond}}} + \frac{4}{\pi} \cdot \frac{D}{r_T \cdot k_{\text{eff}}} \quad (6.25)$$

Considering (6.23), the overall rate constant  $k_{\text{eff}}$  was derived to (6.26).

$$k_{\text{eff}} = \frac{\Gamma_{D^0} \cdot \phi_{h\nu} \cdot J_{h\nu} \cdot k_{\text{ox}}}{[\text{Co}^{3+}]^* k_{\text{ox}} + \phi_{h\nu} \cdot J_{h\nu}} \quad (6.26)$$

Herein,  $\Gamma_{D^0}$  denotes the dye loading which was obtained from absorption and desorption measurements of sensitized  $\text{TiO}_2$  electrodes by a cooperation partner from Uppsala University.  $\phi_{h\nu}$  denotes the excitation cross-section,  $J_{h\nu}$  is the photon flux density,  $k_{\text{ox}}$  is the regeneration rate constant and  $[\text{Co}^{3+}]^*$  stands for the bulk concentration of  $[\text{Co}(\text{bpy})_3]^{3+}$ . Three limiting cases must be considered when working under extreme conditions. First, if  $J_{h\nu}$  approaches infinity, meaning that the light intensity is infinitely high (6.27) second, if an infinite large number of oxidized redox species are in the bulk solution (6.28) and third, if no oxidized redox species are available (6.29):

$$\lim(k_{\text{eff}})_{J_{h\nu} \rightarrow \infty} = \Gamma_{D^0} \cdot k_{\text{ox}}, \quad [\text{Co}^{3+}]^* \cdot k_{\text{ox}} \ll \phi_{h\nu} \cdot J_{h\nu} \quad (6.27)$$

$$\lim(k_{\text{eff}})_{[\text{Co}^{3+}]^* \rightarrow \infty} = \frac{\Gamma_{D^0} \cdot \phi_{h\nu} \cdot J_{h\nu}}{[\text{Co}^{3+}]^*} = 0, \quad [\text{Co}^{3+}]^* \cdot k_{\text{ox}} \gg \phi_{h\nu} \cdot J_{h\nu} \quad (6.28)$$

$$\lim(k_{\text{eff}})_{[\text{Co}^{3+}]^* \rightarrow 0} = \Gamma_{D^0} \cdot k_{\text{ox}}, \quad [\text{Co}^{3+}]^* \cdot k_{\text{ox}} \ll \phi_{h\nu} \cdot J_{h\nu} \quad (6.29)$$

**Simpler Stoichiometry of  $\text{Co}^{2+/3+}$  Compared with  $\Gamma/\text{I}_3^-$ .** In order to see in which way the simpler stoichiometry of the applied one-electron Co mediator (Fig. 6.2A) influences  $k_{\text{eff}}$ , this development is compared to previously applied models for the  $\Gamma/\text{I}_3^-$  mediator by Tefashe *et al.*<sup>[21]</sup> and Shen *et al.*<sup>[153]</sup> Based on the findings of Anderson *et al.*,<sup>[196]</sup> Tefashe *et al.* assumed a reaction order of one with respect to  $[\Gamma]$  in a  $\Gamma/\text{I}_3^-$  mediator system (Fig. 6.2B).

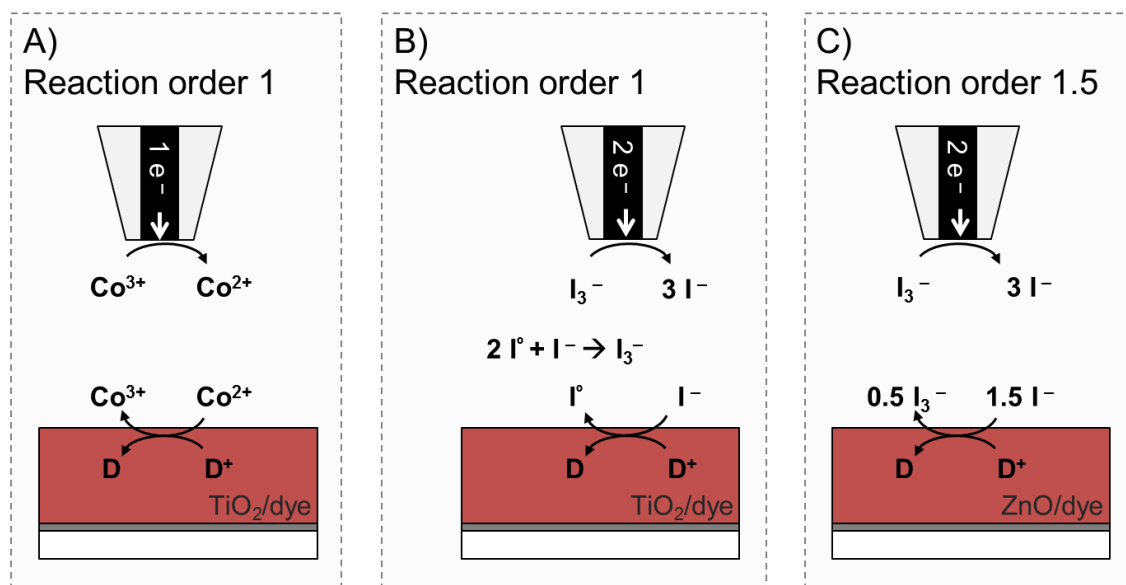


Fig. 6.2 – Comparison of the one-electron cobalt redox mediator with A) reaction order of one<sup>[122]</sup> used in this thesis and the  $\text{I}^-/\text{I}_3^-$  with B) reaction order of one but with a more complicated stoichiometry<sup>[21]</sup> and C) with a reaction order 1.5.<sup>[153]</sup>

For details of the kinetic discussion, see the publication of Tefashe *et al.*<sup>[21]</sup> Here, only the important and according to several studies most likely reactions between the redox mediator and the photooxidized dye considered by Tefashe *et al.* are described. First, iodide reacts with the adsorbed photooxidized dye to an intermediate surface complex during which the dye is neutralized expressed by a certain reaction rate constant  $k_1$ .



In a next step, the iodide of the dye/iodide surface complex  $[\text{D} \cdots \text{I}]_{\text{ads}}$  reacts with another iodide ion to a diiodide radical anion (reaction (XIII)). In a consecutive step, two diiodide radical anions disproportionate to iodide and triiodide.



In Tefashe's study from 2012,<sup>[21]</sup> it was assumed that the dye is uniformly accessible to light and redox mediator and that all dye molecules have the same excitation cross-section  $\phi_{hv}$  (which means that they have the same probability of absorbing a photon entering the film from the back) so that an effective rate constant  $k_{hv,\text{eff}}$  can be obtained from the ab-

sorption cross section  $\phi_{hv}$ , the photon flux  $J_{hv}$  and the rate of electron injection  $k_{inj}$ . The same assumptions were made in this thesis (see equation (6.17)). They also assumed that only the oxidized redox species triiodide and no iodine or iodide was present in the bulk phase.

Shen *et al.*<sup>[153]</sup> also employed the  $\Gamma/I_3^-$  mediator in their study about photoelectrochemical kinetics at Eosin Y sensitized ZnO films and they made the same assumptions as Tefashe with regard to dye accessibility to light and redox mediator molecules. In 2006, the formation of the dye/iodide surface complex was not known and hence not considered. Thus, Shen *et al.*<sup>[153]</sup> assumed the reaction of the redox mediator with the photooxidized dye (Fig. 6.2C) to be



To conclude, compared to the  $\Gamma/I_3^-$  mediator, the equation for the overall rate constant  $k_{eff}$  for a one-electron redox mediator is simpler in terms of the less complex stoichiometry of the Co mediator (Table 6.1) and also regarding the rate constant  $k_{ox}$ . While the term  $k_{ox}$  consists of  $k_1$  and  $k_2$  in the case of the  $\Gamma/I_3^-$  mediator (equations (XII) to (XIV)), it is expressed as only one term ( $k_{ox}$ ) in the case of the Co mediator (equation (IX)).

Table 6.1 – Comparison of the reaction rate constant  $k_{eff}$  for different redox mediators, the reaction of the redox mediator at the dye-sensitized photoanode and the assumed reaction orders  $n$  with respect to the reduced species.

Redox system	Surface reaction	$n$	$k_{eff}$
$Co^{2+/3+}$	$Co^{2+} + D^+ \rightarrow Co^{3+} + D$	1	$\frac{1}{k_{eff}} = \frac{[Co^{3+}]^* k_{ox} + \phi_{hv} J_{hv}}{\Gamma_{D^0} \phi_{hv} J_{hv} k_{ox}}$ [122]
$\Gamma/I_3^-$	Formation of $[D \cdots I]_{ads}$ (eq. (XII) to (XIV))	1	$\frac{1}{k_{eff}} = \frac{1[I_3^-]^*}{l[D^0]\phi_{hv}J_{hv}} + \frac{2}{3l[D^0]k'_{ox}}$ [21]
$\Gamma/I_3^-$	$1.5 \Gamma + D^+ \rightarrow 0.5 I_3^- + D$	1.5	$\frac{1}{k_{eff}} = \frac{2}{3\sqrt{3}\Gamma_{D^0} k_{ox} \sqrt{[I_3^-]^*}} + \frac{2[I_3^-]^*}{\Gamma_{D^0} \phi_{hv} J_{hv}} + \frac{2[I_3^-]^*}{\Gamma_{D^0} k_{inj}}$ [153]

During the development from the model considering a reaction order of 1.5 to the model considering a reaction order of one, the term  $3^{1/2} k_{ox} [I_3^-]^{3/2}$  was replaced by  $k'_{ox} [I_3^-]$  (Table 6.1) with  $1/k'_{ox} = 1/k_1 + 1/k_2$ . For correlating the experimentally obtained  $k_{eff}$  values to the kinetics of dye regeneration, the model used in this thesis, was simplified in terms of less

complex kinetics of the Co complex. Although the presented model is based on preliminary works,<sup>[21, 153]</sup> and some assumptions were necessary for its development, it constitutes a first approximation. However, the results obtained with this model are reasonable and in good agreement with the results obtained by other techniques used to determine kinetics (see chapter 7).

**Fitting Approach Curves to an Analytical Approximation.** One aim of this thesis was to determine the dye regeneration reaction rate constant  $k_{\text{ox}}$  of different dyes.  $k_{\text{ox}}$  contributes to  $k_{\text{eff}}$  which is derived in chapter 6.1 (equation (6.26)) and cannot be determined directly. The following steps were necessary to determine  $k_{\text{ox}}$  (Fig. 6.3).

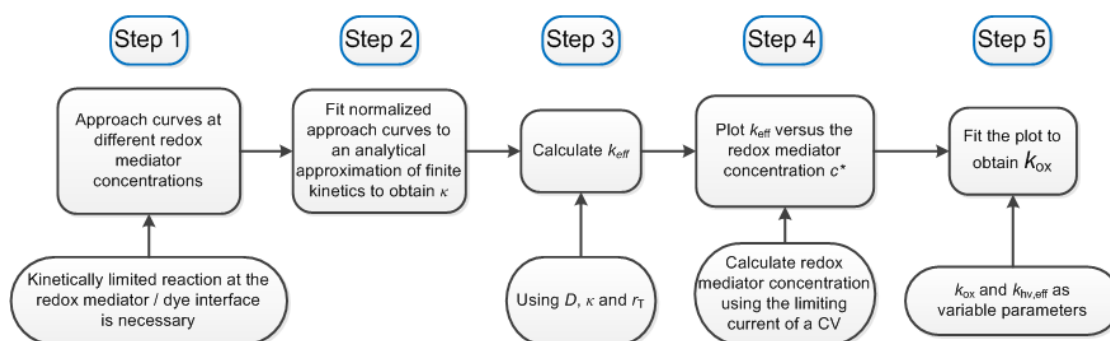


Fig. 6.3 – Procedure of the fitting of approach curves and necessary comprehensive steps.

- Step 1: Approach curves in FB mode were recorded at different redox mediator concentrations in the bulk  $c^*$ . It was necessary to choose  $c^*$ ,  $J_{\text{hv}}$  and  $r_{\text{T}}$  in a way that the reaction occurs kinetically limited.
- Step 2: The experimentally obtained approach curves were fitted to an analytical approximation of finite kinetics by Cornut and Lefrou<sup>[150]</sup> to obtain  $\kappa$ .
- Step 3: Using equation (3.6), the pseudo first order<sup>[154]</sup> reaction rate constant  $k_{\text{eff}}$  of the reaction at the interface between an electrolyte and the dye-sensitized  $\text{TiO}_2$  interface can be calculated for known  $D$  (in this thesis determined by RDE measurements),  $r_{\text{T}}$  (in this thesis determined by CV at ME, calculated *via* equation (3.5)) and  $\kappa$ . Doing so, a  $k_{\text{eff}}$  value for each  $c^*$  was obtained.
- Step 4:  $k_{\text{eff}}$  was plotted versus  $c^*$  as experimentally varied parameter.  $c^*$  was initially obtained by carefully mixing a 2 mM  $[\text{Co}(\text{bpy})_3]^{3+}$  stock solution with an appropriate amount of  $\text{TBAPF}_6$  as supporting electrolyte in MeCN.  $c^*$  was verified by calculation over the

steady state current at known  $r_T$  which is possible since the current is proportional to the concentration of the electrochemically active species.

- Step 5: The plot obtained in step 4 was fitted to  $k_{\text{eff}}$  (equation (6.26), derived in chapter 6.1) where  $k_{\text{ox}}$  can then be obtained as a fitting parameter (see chapter 7.3). The second variable parameter is the effective rate constant  $k_{h\nu,\text{eff}}$  ( $k_{h\nu,\text{eff}} = J_{h\nu} \times \phi_{h\nu}$ ) with  $\phi_{h\nu}$  being the absorption cross-section.

## 6.2 Probing the Reliability of the New Redox Mediator

### 6.2.1 Effect of Increasing Redox Mediator Concentration

[Co(bpy)<sub>3</sub>](PF<sub>6</sub>)<sub>2/3</sub> is an established redox mediator in DSCs<sup>[10]</sup> but was used for the first time as a one-electron SECM redox mediator in this thesis taking into account a correct stoichiometry.<sup>[122]</sup> Thus, the first step was to obtain the same trends in results which have been obtained with the I<sup>-</sup>/I<sub>3</sub><sup>-</sup> redox mediator before. The applicability of SECM has been established in the working group of Prof. Wittstock at the University of Oldenburg by Shen<sup>[18, 153]</sup> and Tefashe<sup>[19-21]</sup> both of whom varied the redox mediator concentration and the light intensity. An increase of the redox mediator concentration is supposed to lead to a decrease of the effective first order rate constant  $k_{\text{eff}}$  due to the growing influence of the redox species diffusing from the bulk to the ME at higher concentrations. For this reason, the first experiments done with [Co(bpy)<sub>3</sub>]<sup>3+</sup> as redox mediator were performed with different redox mediator concentrations over a standard Ru dye Z-907 which is known to give efficiencies of 10% and more in DSCs which employ the I<sup>-</sup>/I<sub>3</sub><sup>-</sup> mediator.<sup>[197]</sup> However, Z-907 without coadsorbents in combination with a Co mediator reached an efficiency of only 1.9%, which could be increased to 5.7% by the addition of the coadsorbent chenodeoxycholic acid (CHENO) that blocks recombination reactions.<sup>[198]</sup> In another study, Z-907 endowed with nonyl chains outperformed another ruthenium dye N-719 endowed with carboxylic groups, by an efficiency increase of 4.5 % in combination with a Co mediator.<sup>[197]</sup> This better efficiency of Z-907 was attributed to a surface-blocking effect induced by the nonyl chains forming a compact layer of Z-907 molecules on the semiconductor surface.<sup>[197]</sup> Thus, Z-907 was used for preliminary experiments.

Solutions of 0.06, 0.12, 0.25, 0.50, 1.0 and 2.0 mM  $[\text{Co}(\text{bpy})_3](\text{PF}_6)_3$  with 0.1 M TBAPF<sub>6</sub> in MeCN were prepared by diluting a 2 mM  $[\text{Co}(\text{bpy})_3](\text{PF}_6)_3$  stock solution with the supporting electrolyte (see Table 4.7 in chapter 4.7.1) The 0.06 mM solution was filled into the SECM cell, a CV was recorded and the determined reduction potential of  $[\text{Co}(\text{bpy})_3]^{3+}$  was applied to the ME. An approach curve was recorded in the dark. The ME was pulled back by 200  $\mu\text{m}$ , the 455 nm LED was switched on with an intensity of 4  $\text{mW cm}^{-2}$  and another approach curve was recorded under illumination. The ME was again retracted by 200  $\mu\text{m}$ , the mediator solution was removed from the cell and the 1 mM solution was inserted. This procedure was repeated for each mediator concentration. To show the different behavior of approach curves at both low and high redox mediator concentrations, those of  $c^* = 0.06$  and  $c^* = 1.0$  mM are shown exemplary. The dye regeneration and thus the surface reactivity of the substrate depends on the amount of redox species in the solution as is evident from raw, not yet normalized approach curves ( $c^* = 0.06$  mM in Fig. 6.4A and  $c^* = 1.0$  mM in Fig. 6.4B).

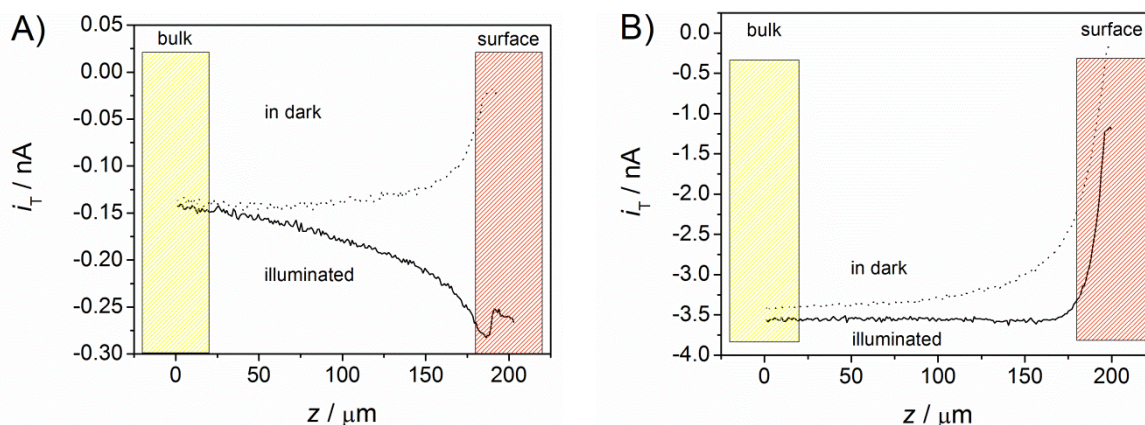


Fig. 6.4 – Approach curves with the absolute ME current  $i_T$  as a function of the vertical movement of the ME ( $E_T = -0.10$  V vs. Ag QRE) over a Z-907-sensitized  $\text{TiO}_2$  electrode (sample type C) (“surface”) with a Pt ME ( $r_T = 12.6$   $\mu\text{m}$ ,  $RG = 8.6$ ) under illumination (solid line) and in the dark (dotted line) with  $c^*$  ( $[\text{Co}(\text{bpy})_3]^{3+}$ ) of A) 0.06 mM and B) 1.0 mM.

As the biased ME was approached towards a photoanode in the dark, it acted as an insulator and the current at the ME decreased due to hindered diffusion, i.e. the redox species were not able to reach the active electrode area. This is shown by the dotted graphs in Fig. 6.4A and B with the current approaching zero when the ME is close to the surface of the photoanode. Under illumination, the approach curves with both redox mediator concentra-

tions differed significantly. At a lower concentration (0.06 mM), the absolute current almost doubled during approach to the sample. At a higher concentration (1.0 mM), the absolute current at the ME stayed constant until the distance between the ME and the substrate was only about 15  $\mu\text{m}$ . After that point was passed, the current decreased rapidly until the current reached a value to that of the current recorded in the bulk. The approach curves under illumination in Fig. 6.4 and from further concentrations mentioned above performed during the same experiment were normalized by dividing the actual ME current,  $i_T$ , by the current in the bulk,  $i_{T,\infty}$ , and by dividing the distance between the ME and the substrate surface,  $d$ , by the ME radius,  $r_T$ , fitted to equation (3.20) determined as an analytical approximation by Cornut and Lefrou<sup>[150]</sup> (Fig. 6.5).

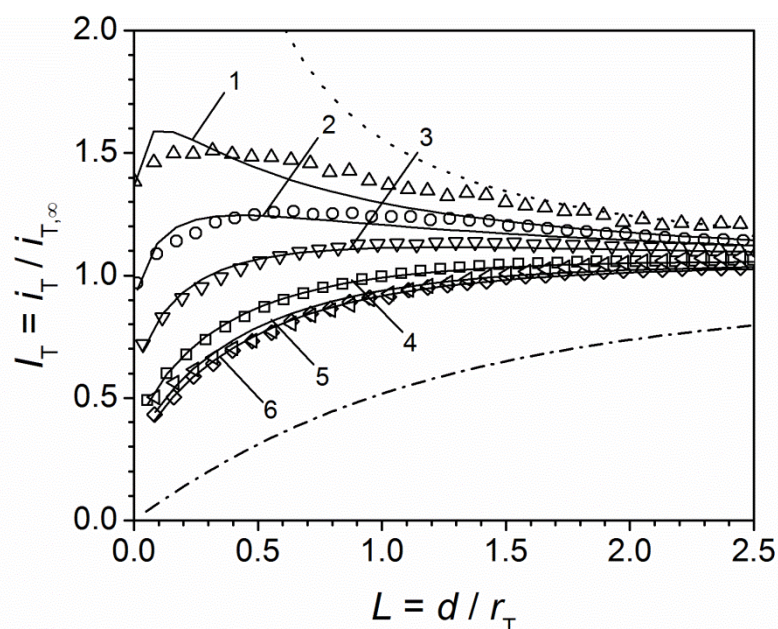


Fig. 6.5 – Normalized SECM approach curves with  $[\text{Co}(\text{bpy})_3](\text{PF}_6)_3$  as redox mediator and 0.1 M TBAPF<sub>6</sub> as inert supporting electrolyte in MeCN over Z-907-sensitized 5  $\mu\text{m}$  thick TiO<sub>2</sub> electrodes (sample type C) at a Pt ME ( $E_T = -0.10$  V vs. Ag QRE), ( $r_T = 12.6$   $\mu\text{m}$ ,  $RG = 8.6$ ). The redox mediator concentration was changed whereas the illumination intensity of a blue LED with 455 nm was held constant at 4  $\text{mW cm}^{-2}$ . According to the mediator concentrations, the corresponding values of ( $\kappa$ ) were obtained: 0.06 mM (1.67) (triangles, curve 1), 0.12 mM (1.019) (circles, curve 2), 0.25 mM (0.629) (downward triangles, curve 3), 0.50 mM (0.345) (squares, curve 4), 1.0 mM (0.236) (diamonds, curve 5) and 2.0 mM (0.263) (left pointing triangles, curve 6). Symbols refer to experimental data; lines are fits to an analytical approximation. The dash-dotted line refers to hindered diffusion and the dotted line to diffusion control.

Although the approach curves did not reflect the analytical approximation perfectly, the trend of  $\kappa$ , and consequently  $k_{\text{eff}}$ , which decreased with increasing redox mediator concentration  $c^*$  (Table 6.2) is evident.

Table 6.2 – Concentration in the bulk  $c^*$ , dimensionless first order rate constant  $\kappa$  and the first order reaction rate constant  $k_{\text{eff}}$  (calculated by  $k_{\text{eff}} = \kappa D / r_T$  with  $D = 6.95 \times 10^{-6} \text{ cm}^2 \text{ s}^{-1}$  and  $r_T = 12.6 \text{ }\mu\text{m}$ ).

$c^* [\text{Co}(\text{bpy})_3]^{3+} / \text{mM}$	$\kappa$	$k_{\text{eff}} / (10^{-3} \text{ cm s}^{-1})$
0.06	1.67	9.23
0.12	1.02	5.64
0.25	0.629	3.48
0.50	0.345	1.91
1.0	0.236	1.31
2.0	0.263	1.46

**Dependency of the Redox Mediator Concentration on the Photocurrent.** To determine whether the photocurrent  $i_{\text{T,photo}}$  depends linearly on the redox mediator concentration, CVs were performed when the ME was approximately  $5 \text{ }\mu\text{m}$  above the substrate.  $i_{\text{T,photo}}$  is the current difference detected at the ME coming from either an illuminated or a non-illuminated photoanode. A CV was recorded in the dark, light of  $455 \text{ nm}$  was switched on and another CV was recorded immediately. This procedure was carried out for five different  $[\text{Co}(\text{bpy})_3](\text{PF}_6)_3$  concentrations ranging from  $0.06$  to  $1.0 \text{ mM}$  (Fig. 6.6A to E).

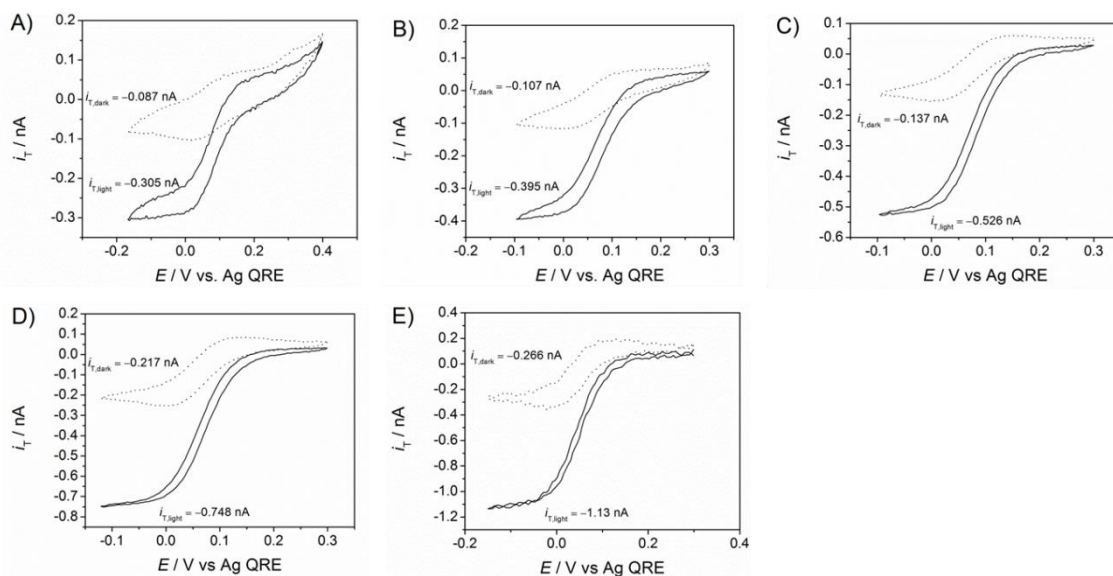


Fig. 6.6 – CVs of a  $[\text{Co}(\text{bpy})_3](\text{PF}_6)_3$  solution at a Pt ME about  $5 \mu\text{m}$  above a Z-907-sensitized  $\text{TiO}_2$  electrode (sample type C) in the dark (dotted line) and under  $4 \text{ mW cm}^{-2}$  455 nm LED (solid line) at different redox mediator concentrations in mM: A) 0.06, B) 0.12, C) 0.25, D) 0.50 and E) 1.0.

$i_{\text{T,photo}}$  was calculated as differences between the ME current generated at an illuminated sample surface,  $i_{\text{T,illu}}$ , and at a non-illuminated sample surface,  $i_{\text{T,dark}}$ , (Table 6.3).

Table 6.3 – Currents detected at the ME in the dark,  $i_{\text{T,dark}}$ , and under illumination,  $i_{\text{T,illu}}$ , as well as  $i_{\text{T,photo}}$  in dependence of the redox mediator concentration in the bulk  $c^*$ .

$c^* [\text{Co}(\text{bpy})_3]^{3+} / \text{mM}$	$i_{\text{T,dark}} / \text{nA}$	$i_{\text{T,illu}} / \text{nA}$	$i_{\text{T,photo}} / \text{nA}$
0.06	-0.087	-0.305	-0.218
0.12	-0.107	-0.395	-0.288
0.25	-0.137	-0.526	-0.389
0.50	-0.217	-0.748	-0.531
1.0	-0.266	-1.13	-0.864

$i_{\text{T,photo}}$  stemming from the Z-907-sensitized  $\text{TiO}_2$  electrode was plotted as a function of the redox mediator concentration which showed a nearly linear dependence of the redox mediator concentration ( $R^2 = 0.99461$ , Fig. 6.7).

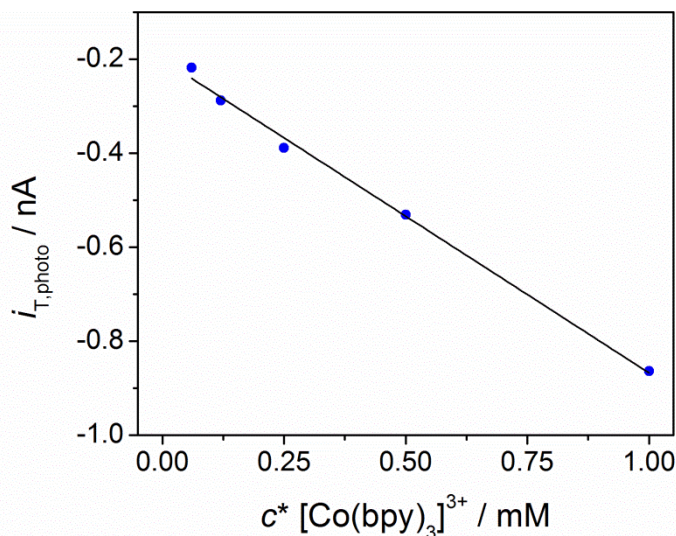


Fig. 6.7 – Photocurrent,  $i_{\text{T,photo}}$ , as a function of the redox mediator concentration,  $c^*$ .

To conclude the results in this chapter, a Z-907-sensitized  $\text{TiO}_2$  substrate in combination with  $[\text{Co}(\text{bpy})_3]^{3+}$  as redox mediator, the latter one new with regard to the application in SECM, was successfully tested in SECM measurements with two respects: First, the trend of decreasing  $k_{\text{eff}}$  with increasing redox mediator concentration was the same as in the study of Tefashe *et al.*<sup>[21]</sup> Second, approach curves recorded over glass as well as over non-illuminated photoanodes fit the analytical approximation of hindered diffusion. This shows that the redox mediator system consisting of  $[\text{Co}(\text{bpy})_3]^{3+}$  and the supporting electrolyte  $\text{TBAPF}_6$  in MeCN is suitable for further experiments. Since this redox electrolyte was applied successfully with the high performance dye Z-907 it was the next step to switch to dye D35 as the main research object in this thesis.

### 6.2.2 Effect of Different Light Intensities

To investigate a D35-sensitized  $\text{TiO}_2$  electrode with  $[\text{Co}(\text{bpy})_3]^{3+}$  in terms of its behavior towards the influence of light intensity, an experiment comparable to the one employing different concentrations (see chapter 6.2.1) was performed in order to proof the applicability of the Co mediator and to confirm the trends published by Tefashe.<sup>[21]</sup> In his study, the regeneration of an N-719-sensitized  $\text{TiO}_2$  electrode by an  $\text{I}/\text{I}_3^-$  mediator was investigated in MeCN as well as in the ionic liquid EMimTFS at different light intensities of a green LED. In both solvents, the regeneration rate constant increased with increasing light intensity whereby the regeneration was higher in MeCN compared to EMimTFS due to the lower

viscosity and hence a higher diffusion coefficient of the redox species. Here, the regeneration of a D35-sensitized TiO<sub>2</sub> electrode was investigated with [Co(bpy)<sub>3</sub>]<sup>3+</sup> by recording approach curves at different light intensities of a 455 nm LED. The approach curves were normalized and plotted (Fig. 6.8).

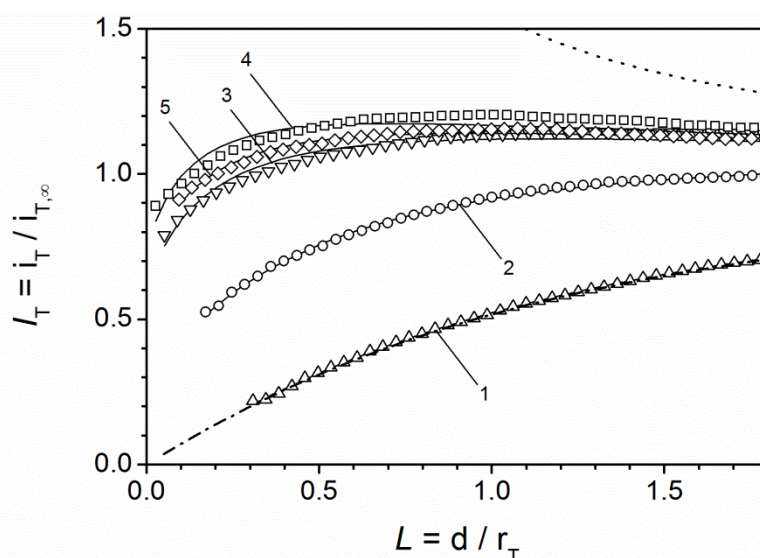


Fig. 6.8 – Normalized SECM approach curves recorded with a Pt ME ( $E_T = -0.12$  V vs. Ag QRE) ( $r_T = 12.3$   $\mu\text{m}$ ,  $RG = 5.93$ ) with 1 mM [Co(bpy)<sub>3</sub>](PF<sub>6</sub>)<sub>3</sub> as redox mediator and 0.1 M TBAPF<sub>6</sub> as inert supporting electrolyte in MeCN. The redox mediator concentration was held constant whereas the illumination intensity of a blue LED with 455 nm was varied. In regard to the light intensities, the corresponding values of ( $\kappa$ ) were obtained: dark (0.0001) (triangles, curve 1), 0.79  $\text{mW cm}^{-2}$  (0.2332) (circles, curve 2), 1.6  $\text{mW cm}^{-2}$  (0.6545) (downward triangles, curve 3), 2.5  $\text{mW cm}^{-2}$  (0.7248) (squares, curve 4), 3.2  $\text{mW cm}^{-2}$  (0.8334) (diamonds, curve 5). Aux: Pt, QRE: Ag; connection between photoanode (30  $\Omega$ , determined by multimeter) and the electrolyte: Pt; substrate: TiO<sub>2</sub> (sample type A), adsorbed: D35. Symbols refer to experimental data; lines are fits to an analytical approximation. The dash-dotted line refers to hindered diffusion and the dotted line to diffusion control.

With increasing light intensity, the reaction rate constant also increased until saturation was reached at a light intensity between 2.5  $\text{mW cm}^{-2}$  and 3.2  $\text{mW cm}^{-2}$ . The results of the experiments performed in this thesis were in good agreement with those in literature.<sup>[18-21,</sup>

<sup>153]</sup> Based on these findings, it was assumed that the system could be reliably applied for further experiments which demand illumination at different light intensities.

## 6.3 Influence of DSC Components of Different Polarity

### 6.3.1 Aqueous Redox Mediator

Aqueous systems offer an attractive alternative compared to systems based on organic solvents, because the latter one has a negative impact on the environment and most often a high vapor pressure. Besides the research on hole conducting polymers,<sup>[199]</sup> ionic liquids<sup>[200]</sup> and polymer gel electrolytes,<sup>[201]</sup> aqueous redox electrolyte systems are interesting because they may also prevent the leakage of the solar cells, which is a constant problem with solar cells based on organic solvents. One way to develop such a system is to combine a water-soluble redox mediator with a hydrophilic dye. Xiang *et al.*<sup>[22]</sup> reported in 2013 on the aqueous redox mediator  $[\text{Co}(\text{bpy})_3](\text{NO}_3)_{2/3}$  which achieved a PCE of over 5 % with 1% PEG300 added as a wetting agent for the hydrophobic, metal-free, carbazole-based dye MK-2 and the aqueous electrolyte. They used different concentrations of PEG300 and achieved the highest efficiency with an amount of 1%. To follow up on this research,  $[\text{Co}(\text{bpy})_3](\text{NO}_3)_{2/3}$  was synthesized and characterized in this thesis (see chapter 4.9), and tested for its applicability for kinetic SECM measurements.

### 6.3.2 Reactions over Pristine Titanium Dioxide Electrodes

The procedure of the experiment was as follows: a Pt ME was used as WE, a coiled Pt wire as Aux and a coiled Ag wire as QRE. A 1 mM solution of  $[\text{Co}(\text{bpy})_3](\text{NO}_3)_3$  in dist. water with 0.1 M  $\text{KNO}_3$  as supporting electrolyte was prepared and heated to 70 °C to dissolve the Co complex. The same solution with additional 1 % PEG300, which supports the wettability of the hydrophobic dye by the aqueous redox electrolyte, was prepared analogously. First, approach curves were recorded over blocking layer-coated FTO and over unsensitized porous  $\text{TiO}_2$  (sample type B) in the dark as well as under illumination of 4.9  $\text{mW cm}^{-2}$  at 455 nm (Fig. 6.9). The aim of this approach was to rule out reactions of the unsensitized  $\text{TiO}_2$  and hence confirm that only a dye-sensitization of  $\text{TiO}_2$  leads to a photo-active surface by electron injection into the semiconducting material. The Pt ME was fixed within a holder and positioned above the substrate region with the compact  $\text{TiO}_2$  layer. Afterwards, a CV was recorded to determine the reduction potential of the redox mediator.

After the approach curve with  $E_T = -0.23$  V vs. Ag QRE over blocking layer-coated FTO was performed, the ME was positioned above the region of porous  $\text{TiO}_2$ .

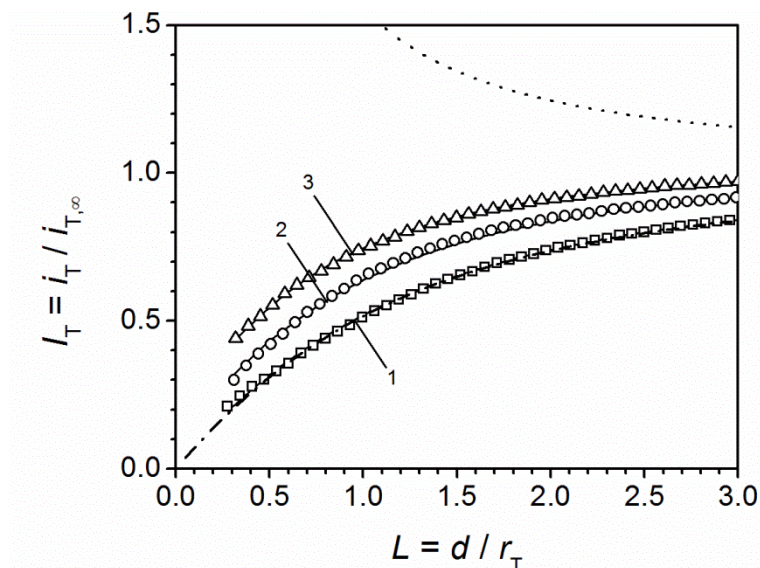


Fig. 6.9 – Normalized SECM approach curves with 1 mM  $[\text{Co}(\text{bpy})_3](\text{NO}_3)_3$  as redox mediator in 0.1 M  $\text{KNO}_3$  and 1% PEG 300 in dist. water at a Pt ME ( $E_T = -0.23$  V vs. Ag QRE,  $r_T = 15.2$   $\mu\text{m}$ ,  $RG = 9.85$ ). The  $\kappa$  values given in brackets depended on the  $\text{TiO}_2$  surface (sample type B) and the illumination conditions: above compact  $\text{TiO}_2$  blocking layer in the dark (0.0033, squares, curve 1), above porous  $\text{TiO}_2$  in the dark (0.0383, circles, curve 2) and above  $\text{TiO}_2$  under illumination with  $4.9$   $\text{mW cm}^{-2}$  at  $455$  nm (0.0894, triangles, curve 3). Symbols refer to experimental data; lines are fits to an analytical approximation. The dash-dotted line refers to hindered diffusion and the dotted line to diffusion control.

Over the insulating compact  $\text{TiO}_2$  blocking layer a first order reaction rate constant  $k_{\text{eff}}$  of  $0.0049 \times 10^{-3}$   $\text{cm s}^{-1}$  (squares) was obtained, so no reaction took place. It was assumed that the reaction on non-illuminated porous  $\text{TiO}_2$  would also be very slow as well since it should act as an insulator. However, the Co mediator can diffuse through the porous  $\text{TiO}_2$  network (see Fig. 8.2C), a behavior that was also observed during imaging of DSCs (see chapter 8). Thus, the diffusion is hindered to a certain extent but not completely blocked. As a result, a reaction takes place at the surface with a  $k_{\text{eff}}$  of  $0.057 \times 10^{-3}$   $\text{cm s}^{-1}$ . Under illumination,  $k_{\text{eff}}$  has doubled to  $0.13 \times 10^{-3}$   $\text{cm s}^{-1}$  compared to dark conditions (Table 6.4).

Table 6.4 – Substrate, illumination condition, dimensionless first order rate constant  $\kappa$ , first order reaction rate constant  $k_{\text{eff}}$  (calculated by  $k_{\text{eff}} = \kappa D / r_T$  with  $D = 2.26 \times 10^{-6} \text{ cm}^2 \text{ s}^{-1}$  and  $r_T = 15.2 \text{ }\mu\text{m}$ ) and the closest ME-to-substrate distance  $d_0$ .

Substrate	Illumination <sup>a</sup> / $\text{mW cm}^{-2}$	$\kappa$	$k_{\text{eff}} / (10^{-3} \text{ cm s}^{-1})$	$d_0 / \mu\text{m}$
blocking layer-coated FTO	no	0.0033	0.00492	4.18
TiO <sub>2</sub>	no	0.0383	0.057	4.71
TiO <sub>2</sub>	4.9	0.0894	0.133	4.85

<sup>a</sup> with a 455 nm LED

An explanation of the positive FB of the supposedly unsensitized TiO<sub>2</sub> electrode might be the sensitization of TiO<sub>2</sub> by the redox mediator itself. This was evident by TiO<sub>2</sub> appearing yellow after the substrate was removed from the SECM cell. Even after rinsing the sample with ethanol and MeCN, the yellow color did not vanish. Co complexes with organic ligands are known as sensitizers, however, the used [Co(bpy)<sub>3</sub>](NO<sub>3</sub>)<sub>3</sub> absorbs light in the region between 305 and 320 nm (see Fig. 4.9B). Another explanation is that after some time has elapsed during which the substrate is in contact with the electrolyte, the pores of the TiO<sub>2</sub> were completely filled which could have facilitated the diffusion of the redox species through the pores. During this experiment, since this was one of the first experiments for this thesis, an eye was kept on the closest distance between the ME and the substrate  $d_0$  (Table 6.4).  $d_0$  depends on the position of the ME within the ME holder and whether or not the substrate is tilted and it should not differ by more than 1  $\mu\text{m}$  within a certain experimental setup. The largest deviation of  $d_0$  during this experiment was 0.67  $\mu\text{m}$ , which is tolerable.

### 6.3.3 Comparison of Redox Mediators of Different Polarity

In a sequential experiment, both [Co(bpy)<sub>3</sub>](NO<sub>3</sub>)<sub>3</sub> in a water-based electrolyte and [Co(bpy)<sub>3</sub>](PF<sub>6</sub>)<sub>3</sub> in organic-based electrolyte were probed in combination with the hydrophobic dye D35 which was adsorbed on a TiO<sub>2</sub> substrate (sample type D). For measurements with [Co(bpy)<sub>3</sub>](NO<sub>3</sub>)<sub>3</sub> in aqueous media, 500  $\mu\text{l}$  mediator solution were inserted into the SECM cell. A tube with a slight argon flow was placed on top of the SECM cell to guarantee nearly oxygen-free conditions during the measurements. A CV was recorded by

scanning in cathodic direction from 0.4 to  $-0.05$  V and the potential at which a steady conversion from  $\text{Co}^{3+}$  to  $\text{Co}^{2+}$  occurred was applied to the ME. An  $i$ - $t$ -curve was recorded over 350 s until a constant reduction current was obtained. An approach curve was recorded in the dark. Afterwards, the ME was retracted by  $150 \mu\text{m}$  from the substrate into the bulk. The light (455 nm LED) was switched on with  $1 \text{ mW cm}^{-2}$  and after 1 min an approach curve was recorded. Again, the ME was retracted by  $150 \mu\text{m}$ , the LED was set to the next higher light intensity, the system was left to equilibrate and after 1 min another approach curve was recorded. This procedure was repeated at different light intensities and the approach curves were normalized (Fig. 6.10A).

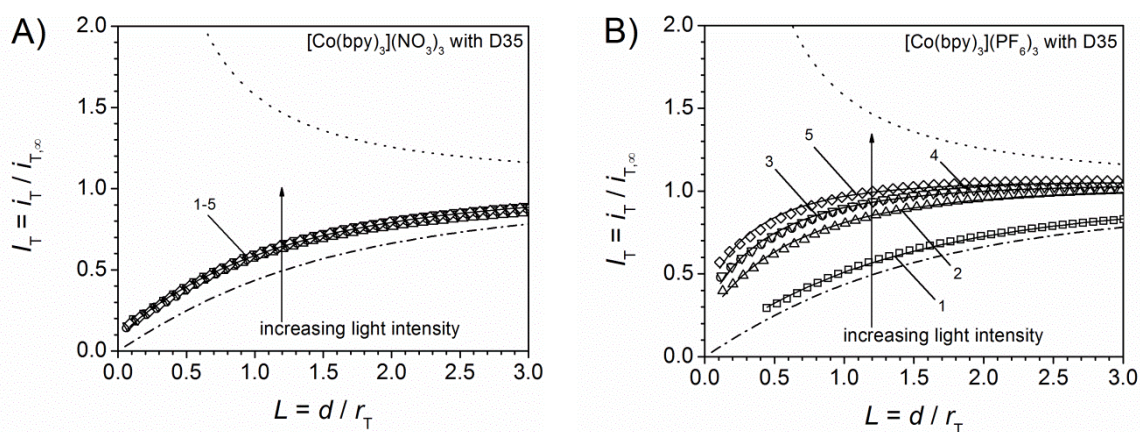


Fig. 6.10 – A) Normalized approach curves of a 2.4 mM  $[\text{Co}(\text{bpy})_3](\text{NO}_3)_3$  at a Au ME ( $E_T = -0.05$  V vs. Pt QRE,  $r_T = 13.5 \mu\text{m}$ ) over a D35-sensitized  $\text{TiO}_2$  electrode (sample type D) illuminated with different light intensities in  $\text{mW cm}^{-2}$  ( $J_{hv} / (10^{-9} \text{ mol cm}^{-2} \text{ s}^{-1})$ ) of a 455 nm LED: dark (squares, curve 1), 1.0 (13.5) (triangles, curve 2), 2.0 (27.2) (circles, curve 3), 3.0 (40.6) (downward triangles, curve 4) and 4.0 (54.0) (diamonds, curve 5). For the sake of clarity, every second approach curve was omitted (compared to Table 6.5). B) Normalized approach curves of a 2.6 mM  $[\text{Co}(\text{bpy})_3](\text{PF}_6)_3$  at a Au ME ( $E_T = -0.20$  V vs. Pt QRE,  $r_T = 13.5 \mu\text{m}$ ) over a D35-sensitized  $\text{TiO}_2$  electrode (sample type B) illuminated with different light intensities in  $\text{mW cm}^{-2}$  ( $J_{hv} / (10^{-9} \text{ mol cm}^{-2} \text{ s}^{-1})$ ) of a 455 nm LED: dark (squares, curve 1), 0.73 (9.83) (triangles, curve 2), 1.47 (19.9) (circles, curve 3), 2.22 (30.7) (downward triangles, curve 4) and 2.95 (41.0) (diamonds, curve 5). Symbols refer to experimental data; lines are fits to an analytical approximation. The dash-dotted lines refer to hindered diffusion and the dotted lines to diffusion control.

The procedure for the measurements with  $[\text{Co}(\text{bpy})_3](\text{PF}_6)_3$  was similar to the one described above with the exception that the waiting time between the approach curves at different light intensities was 5 s instead of 1 min. This experiment was performed earlier in

the thesis, but the development of the method showed a better comparability of the  $k_{\text{eff}}$  values after applying a longer waiting time. Also, a slightly thinner  $\text{TiO}_2$  electrode with  $4.9 \mu\text{m}$  thickness (sample type B) was used in contrast to  $19 \mu\text{m}$  thick electrodes used during the experiments with  $[\text{Co}(\text{bpy})_3](\text{NO}_3)_3$ . The normalized approach curves showed significant differences for the water-based (Fig. 6.10A) and the organic-based redox electrolyte (Fig. 6.10B). An increase in light intensity had no effect on the substrate reaction of the water-based redox electrolyte with  $[\text{Co}(\text{bpy})_3](\text{NO}_3)_3$  and the hydrophobic dye D35 (Fig. 6.10A), whereas the organic redox mediator  $[\text{Co}(\text{bpy})_3](\text{PF}_6)_3$  showed a faster reaction of the substrate with increasing light intensity (Fig. 6.10B). For better illustration, the reaction rate constant  $k_{\text{eff}}$  was plotted versus the light intensity to elucidate the clear difference between the aqueous and the organic redox electrolyte in combination with a hydrophobic dye (Fig. 6.11).

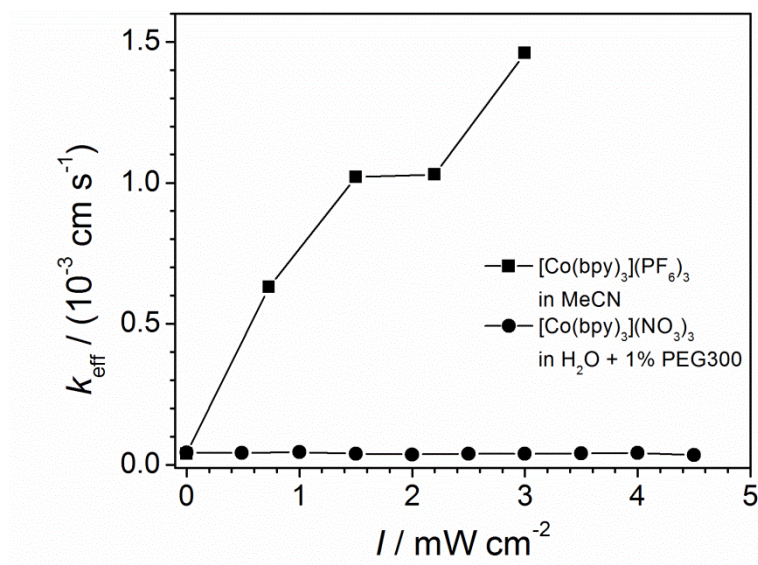


Fig. 6.11 – First order reaction rate constants  $k_{\text{eff}}$  of  $[\text{Co}(\text{bpy})_3](\text{PF}_6)_3$  (squares) and  $[\text{Co}(\text{bpy})_3](\text{NO}_3)_3 + 1\% \text{ PEG300}$  (circles) obtained by fitting approach curves which were recorded above D35-sensitized  $\text{TiO}_2$  photoanodes. Lines are guide to the eyes.

Table 6.5 gives the first order reaction rate constant  $k_{\text{eff}}$  as well as the closest ME-to-substrate distance  $d_0$  in dependence of the light intensity. The values of  $d_0$  do not deviate significantly which is required for reliable results. Using  $[\text{Co}(\text{bpy})_3](\text{PF}_6)_3$ , the reaction rate constant  $k_{\text{eff}}$  increases with increasing light intensity while no reaction occurred using the aqueous redox mediator  $[\text{Co}(\text{bpy})_3](\text{NO}_3)_3$ . This observation is expected and reasonable

due to the poor wetting at the interface of the hydrophobic dye D35 and the aqueous redox mediator although 1% PEG300 was added to increase the surface wetting within the pores.

Table 6.5 Light intensity  $I$ , photon flux density  $J_{hv}$ , dimensionless first order rate constant  $\kappa$ , the first order reaction rate constant  $k_{eff}$  (calculated by  $k_{eff} = \kappa D / r_T$  with  $D = 2.26 \times 10^{-6} \text{ cm}^2 \text{ s}^{-1}$  ( $[\text{Co}(\text{bpy})_3](\text{NO}_3)_3$ ) and  $D = 6.95 \times 10^{-6} \text{ cm}^2 \text{ s}^{-1}$  ( $[\text{Co}(\text{bpy})_3](\text{PF}_6)_3$ ) as well as  $r_T = 13.5 \text{ }\mu\text{m}$ ) and the closest ME-to-substrate distance  $d_0$ .

$I / \text{mW cm}^{-2}$ ( $J_{hv} / (10^{-9} \text{ mol cm}^{-2} \text{ s}^{-1})$ )	$\kappa$	$k_{eff} / (10^{-3} \text{ cm s}^{-1})$	$d_0 / \mu\text{m}$
<b><math>[\text{Co}(\text{bpy})_3](\text{NO}_3)_3</math></b>			
dark	0.0266	0.044	1.5
0.49 (6.65)	0.0251	0.042	1.2
1.0 (13.5)	0.0275	0.046	1.5
1.5 (20.3)	0.0235	0.039	1.3
2.0 (27.2)	0.0221	0.037	0.83
2.5 (33.8)	0.0241	0.040	0.93
3.0 (40.6)	0.0240	0.040	0.96
3.5 (47.1)	0.0246	0.041	1.1
4.0 (54.0)	0.0249	0.042	1.2
4.5 (60.5)	0.0212	0.035	0.64
<b><math>[\text{Co}(\text{bpy})_3](\text{PF}_6)_3</math></b>			
dark	0.0078	0.040	6.03
0.73 (9.83)	0.1229	0.631	1.74
1.47 (19.9)	0.1988	1.02	1.52
2.22 (30.7)	0.2002	1.03	1.67
2.95 (41.0)	0.2850	1.46	1.45

The rate constants obtained with the organic-based electrolyte with  $[\text{Co}(\text{bpy})_3](\text{PF}_6)_3$  increased from  $0.040 \times 10^{-3} \text{ cm s}^{-1}$  in the dark to  $1.46 \times 10^{-3} \text{ cm s}^{-1}$  at a light intensity of  $2.95 \text{ mW cm}^{-2}$ . In comparison, the rate constant obtained using the water-based redox elec-

trolyte showed no significant differences between the behavior in the dark ( $k_{\text{eff}} = 0.044 \times 10^{-3} \text{ cm s}^{-1}$ ) and under  $4.95 \text{ mW cm}^{-2}$  illumination ( $k_{\text{eff}} = 0.035 \times 10^{-3} \text{ cm s}^{-1}$ ). This is probably due to the fact that the hydrophobic alkoxy chains of the D35 hinder the redox couple to reach the positive charge, located on the triphenylamine unit. To regenerate the oxidized dye, the amount of 1% PEG as wetting agent is apparently insufficient to achieve an efficient wetting of the substrate surface.

### 6.3.4 Comparison of a Hydrophilic to a Hydrophobic Dye

In order to check whether  $[\text{Co}(\text{bpy})_3](\text{NO}_3)_3$  in aqueous media shows dye regenerative properties at all, another dye, namely V35, was used. The basic structure of both dye molecules is equal. In contrast to D35 with *n*-butoxy chains, V35 has longer and more hydrophilic glycolic chains (see Fig. 2.7).

For this experiment, 1 mM  $[\text{Co}(\text{bpy})_3](\text{NO}_3)_3$  was used in dist. water with 0.1 M  $\text{KNO}_3$  as supporting electrolyte and either 1 or 10 % PEG300. Au MEs served as WEs, a coiled Pt wire as Aux and an aqueous Ag/AgCl served as RE. The procedure was the same as described for the water-based mediator in chapter 6.3.3. Approach curves were recorded with different combinations of dye and redox mediator at different light intensities of a 455 nm LED. The resulting first order reaction rate constant  $k_{\text{eff}}$  was plotted as a function of the light intensity  $I$  (Fig. 6.12).

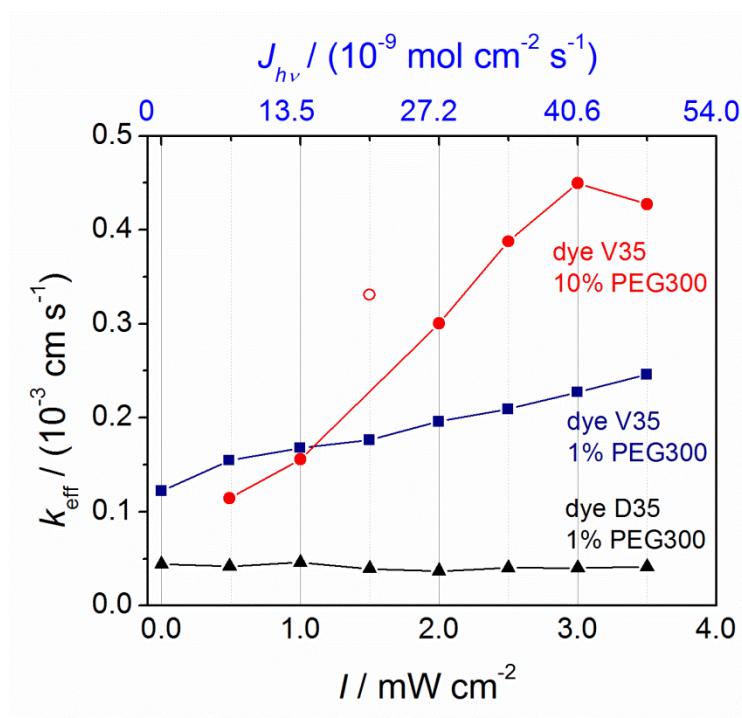


Fig. 6.12 – Comparison of first order reaction rate constants  $k_{\text{eff}}$  of the reaction between different combinations of redox electrolytes and dyes as a function of the light intensity  $I$  in  $\text{mW cm}^{-2}$ :  $[\text{Co}(\text{bpy})_3](\text{NO}_3)_3$  + 1% PEG300 and the hydrophobic dye D35 (triangles) as well as for the mediator  $[\text{Co}(\text{bpy})_3](\text{NO}_3)_3$  + 1% PEG300 and the hydrophilic dye V35 (squares) (Au ME,  $r_T = 13.5 \mu\text{m}$ ,  $RG = 17.8$ ) and  $[\text{Co}(\text{bpy})_3](\text{NO}_3)_3$  + 10% PEG300 and the hydrophilic dye V35 (circles) (Au ME,  $r_T = 14.2 \mu\text{m}$ ,  $RG = 8.02$ ). The open red circle corresponds to an outlier.

While Xiang *et al.*<sup>[22]</sup> described the best performance of a DSC consisting of the hydrophobic dye MK2 attached to  $\text{TiO}_2$  and the aqueous redox mediator  $[\text{Co}(\text{bpy})_3](\text{NO}_3)_3$  with an additional 1% PEG300, the results obtained during the experiments in this thesis were different. The hydrophobic dye D35 in combination with  $[\text{Co}(\text{bpy})_3](\text{NO}_3)_3$  in aqueous media showed no substrate reaction. Regardless of the illumination intensity, the substrate seemed to act as an insulator since the mediator could not reach the photooxidized dye, probably due to poor wetting of the surface within the pores. A  $\text{TiO}_2$  substrate sensitized with the more hydrophilic dye V35, a substrate reaction was observed, indicated by an increasing  $k_{\text{eff}}$  with increasing light intensity. This effect could even be enhanced by increasing the amount of PEG300 from 1 to 10% (Table 6.6).

Table 6.6 Light intensity  $I$ , photon flux density  $J_{hv}$ , dimensionless first order rate constant  $\kappa$  and first order reaction rate constant  $k_{\text{eff}}$  (calculated by  $k_{\text{eff}} = \kappa D / r_T$  with  $D = 2.26 \times 10^{-6} \text{ cm}^2 \text{ s}^{-1}$  and  $r_T = 13.5 \text{ }\mu\text{m}$  (for 1% PEG), resp.  $14.2 \text{ }\mu\text{m}$  (for 10% PEG)).

$I / \text{mW cm}^{-2}$ ( $J_{hv} / (10^{-9} \text{ mol cm}^{-2} \text{ s}^{-1})$ )	$k_{\text{eff}} / (10^{-3} \text{ cm s}^{-1})$ [Co(bpy) <sub>3</sub> ](NO <sub>3</sub> ) <sub>3</sub> 1% PEG300 D35	$k_{\text{eff}} / (10^{-3} \text{ cm s}^{-1})$ [Co(bpy) <sub>3</sub> ](NO <sub>3</sub> ) <sub>3</sub> 1% PEG300 V35	$k_{\text{eff}} / (10^{-3} \text{ cm s}^{-1})$ [Co(bpy) <sub>3</sub> ](NO <sub>3</sub> ) <sub>3</sub> 10% PEG300 V35
dark	0.044	0.122	fitting not possible
0.49 (6.65)	0.042	0.155	0.114
1.0 (13.5)	0.046	0.168	0.156
1.5 (20.3)	0.039	0.176	0.331
2.0 (27.2)	0.037	0.196	0.300
2.5 (33.8)	0.040	0.209	0.388
3.0 (40.6)	0.040	0.227	0.450
3.5 (47.1)	0.041	0.246	0.427

Except for the light intensities of 0.49 and 1  $\text{mW cm}^{-2}$ , where no increasing reaction rate constant  $k_{\text{eff}}$  could be observed with increasing amount of PEG300, the light intensity as well as the amount of PEG300 directly influenced the regeneration of the dye, i.e. the first order reaction rate constant  $k_{\text{eff}}$  increased with increasing light intensity. This is probably caused by the enhanced wetting of the dye-sensitized TiO<sub>2</sub> surface by the aqueous electrolyte when PEG is added. Xiang *et al.*<sup>[22]</sup> proved this wetting by contact angle measurements. Also, Ellis *et al.*<sup>[24]</sup> showed that the contact angle of V35 is significantly smaller (V35/H<sub>2</sub>O,  $\theta_c = 41^\circ$ ) than that of D35 (D35/H<sub>2</sub>O,  $\theta_c = 124^\circ$ ). For the calculation of  $k_{\text{eff}}$  determined in the solution containing 10% PEG300, the diffusion coefficient of the [Co(bpy)<sub>3</sub>]<sup>3+</sup> species was assumed to be the same as for the solution with 1% PEG300. To conclude, in terms of the environmentally friendlier behavior of water in contrast to organic solvents such as MeCN, it is worthwhile considering water-based redox electrolytes in a DSC.

## 7 Impact of Dye Architecture on Kinetics in Dye-Sensitized Solar Cells

### 7.1 Method Development

Prior to the study which is the topic of the following chapters 7.2 to 7.4 dealing with the influence of dye architecture on the dye regeneration, an appropriate SECM method in terms of duration of illumination time, the order of measurement of the dyes and the conditions under which the  $\text{TiO}_2$  electrodes were sensitized was to be developed. In a first attempt, two dyes were attached to one  $\text{TiO}_2$  electrode (Fig. 7.1A and B) to guarantee the exact same conditions during the SECM experiment. During the method development, every electrode was prepared in the same way, however with a different order of sensitizing the dyes. As a consequence of sensitizing one electrode with two different dyes consecutively, one dye was adsorbed to a hot  $\text{TiO}_2$  electrode (after removing it from the oven), while the second dye was attached 24 h later to the same, but cold  $\text{TiO}_2$  electrode.

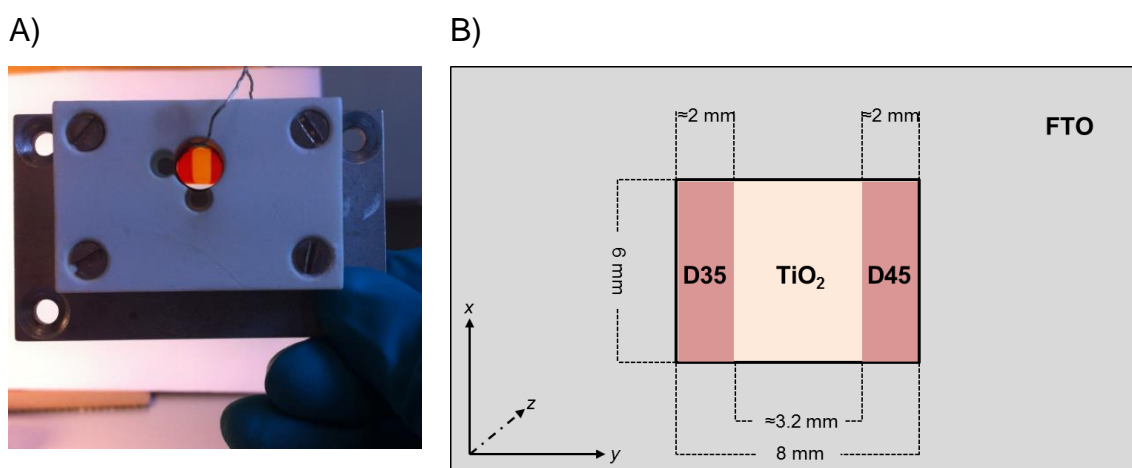


Fig. 7.1 – A) Sensitized  $\text{TiO}_2$  electrode in an SECM cell and B) Scheme of the screen printed  $\text{TiO}_2$  electrode adsorbed with the two orange colored dyes D35 and D45 on an FTO-coated glass substrate.

Approach curves were recorded over both dyes D35 and D45. Therefore, the ME was laterally placed above the D35-sensitized region of the substrate and manually placed very

close to the surface. For each concentration, a CV was taken to determine the steady-state region of reduction of  $[\text{Co}(\text{bpy})_3]^{3+}$  and to check the quality of the ME (see exemplary Fig. 7.4A). This reduction potential was determined individually prior to each experiment because it slightly differed from day to day due to the use of a QRE instead of a RE. However, the potential was stable over a time range of at least five hours which was checked by CV at the beginning and the end of each experimental day. Afterwards, the reduction potential was applied to the ME ( $E_T$ ) and an approach curve was recorded in the dark. The 455 nm LED was turned on and after waiting for 5 s, an approach curve was recorded over the D35-sensitized area. The ME was moved in positive  $y$ -direction to place it over the D45-sensitized area. Another approach curve was recorded. The LED was turned off, the ME was moved in negative  $y$ -direction and placed over D35 again, the redox mediator was carefully removed and a mediator solution of next higher concentration was inserted into the cell. With each mediator concentration, approach curves were recorded over D35 and D45 and rate constants  $k_{\text{eff}}$  were calculated from the fitting parameter  $\kappa$  received by fitting the normalized approach curves to an analytical approximation of finite sample kinetics.

The following figures show normalized approach curves and effective heterogeneous rate constants  $k_{\text{eff}}$  in dependence of the bulk concentration of the redox mediator  $[\text{Co}(\text{bpy})_3]^{3+}$ . During first experiments (Fig. 7.2 – Fig. 7.4), the illumination time was 5 s before the ME was placed above the region with the dye measured second. When D45 was sensitized first (hot  $\text{TiO}_2$  electrode) and measured second and D35 was sensitized second (cold  $\text{TiO}_2$  electrode) and measured first, D45 showed higher  $k_{\text{eff}}$  (black symbols in Fig. 7.2).

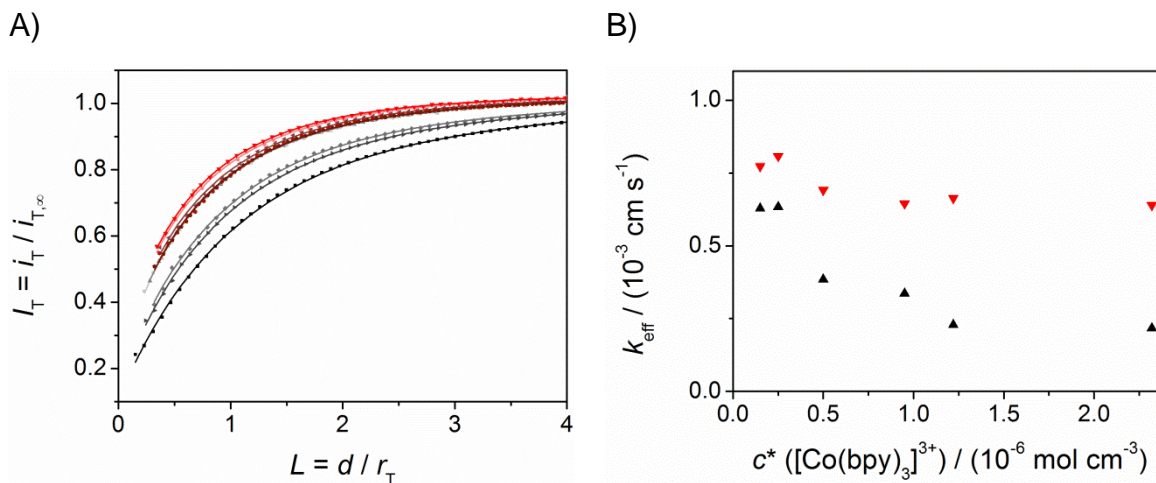


Fig. 7.2 – A) Normalized SECM FB approach curves for the approach of a Au disk ME ( $r_T = 13.5 \mu\text{m}$ ,  $RG = 17.8$ ) ( $E_T = -0.3 \text{ V}$  vs. Pt QRE) towards a D35-sensitized (grey shades, a darker shade corresponds to a higher concentration) and a D45-sensitized (red tones, a darker shade corresponds to a higher concentration)  $\text{TiO}_2$  film (sample type D) illuminated with a blue (455 nm) LED with a photon flux density of  $9.28 \times 10^{-8} \text{ mol cm}^{-2} \text{ s}^{-1}$  for the following  $c^*([\text{Co}(\text{bpy})_3]^{3+})$  given in ( $10^{-6} \text{ mol cm}^{-3}$ ) for both dyes: 2.3, 1.2, 0.95, 0.50, 0.25 and 0.15. Symbols indicate normalized experimental approach curves whereas lines are fits to an analytical approximation.<sup>[150]</sup> B) Effective heterogeneous first order rate constant  $k_{\text{eff}}$  as a function of the bulk redox mediator concentration  $c^*$ . D45 (red symbols) was sensitized 24 h, D35 (black symbols) was sensitized 48 h.

For the next experiment, the order of sensitization was switched in order to rule out the influence of the temperature of the electrode during sensitization and approach curves were recorded over the D45-sensitized area first and over D35-sensitized area second. As in the prior experiment, higher  $k_{\text{eff}}$  were obtained for the dye measured second, in this experiment D35 (Fig. 7.3).

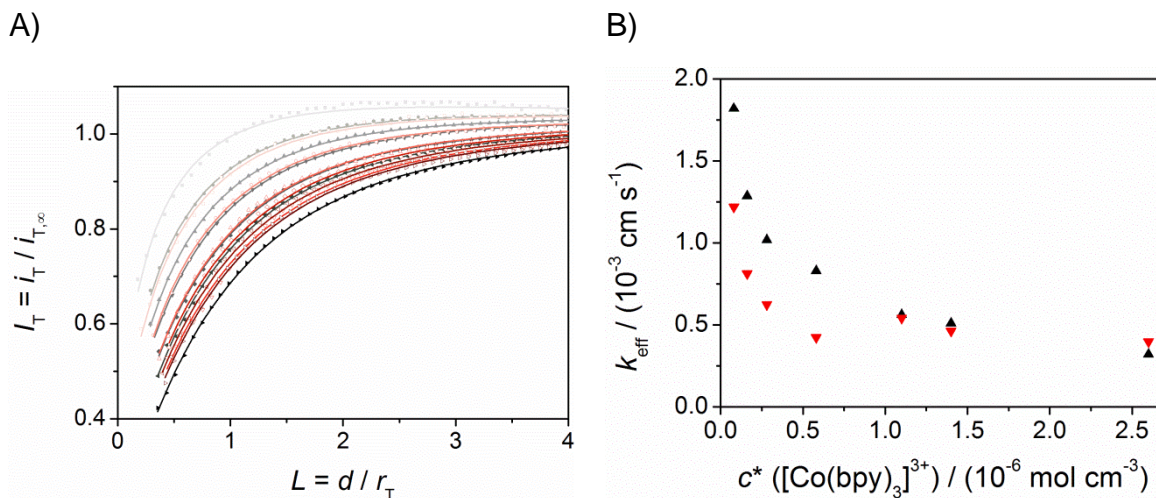


Fig. 7.3 – A) Normalized SECM FB approach curves for the approach of a Au disk ME ( $r_T = 13.5 \mu\text{m}$ ,  $RG = 17.8$ ) ( $E_T = -0.28 \text{ V}$  vs. Pt QRE) towards a D35-sensitized (grey shades, a darker shade corresponds to a higher concentration) and a D45-sensitized (red tones; a darker shade corresponds to a higher concentration)  $\text{TiO}_2$  film (sample type D) illuminated with a blue (455 nm) LED with a photon flux density of  $6.57 \times 10^{-8} \text{ mol cm}^{-2} \text{ s}^{-1}$  for the following  $c^*([\text{Co}(\text{bpy})_3]^{3+})$  given in ( $10^{-6} \text{ mol cm}^{-3}$ ) for both dyes: 2.6, 1.4, 1.1, 0.58, 0.28, 0.16 and 0.08. Symbols indicate normalized experimental approach curves whereas lines are fits to an analytical approximation.<sup>[150]</sup> B) Effective heterogeneous first order rate constants  $k_{\text{eff}}$  as a function of the bulk redox mediator concentration  $c^*$ . D35 (black symbols) was sensitized 24 h, D45 (red symbols) was sensitized 96 h.

In another experiment, D35 was sensitized first (hot) and D45 second (cold) and during the experiment an approach curve was recorded over D35 first and over D45 second. Here, also the dye measured second, D45, showed higher  $k_{\text{eff}}$  (red symbols in Fig. 7.4C).

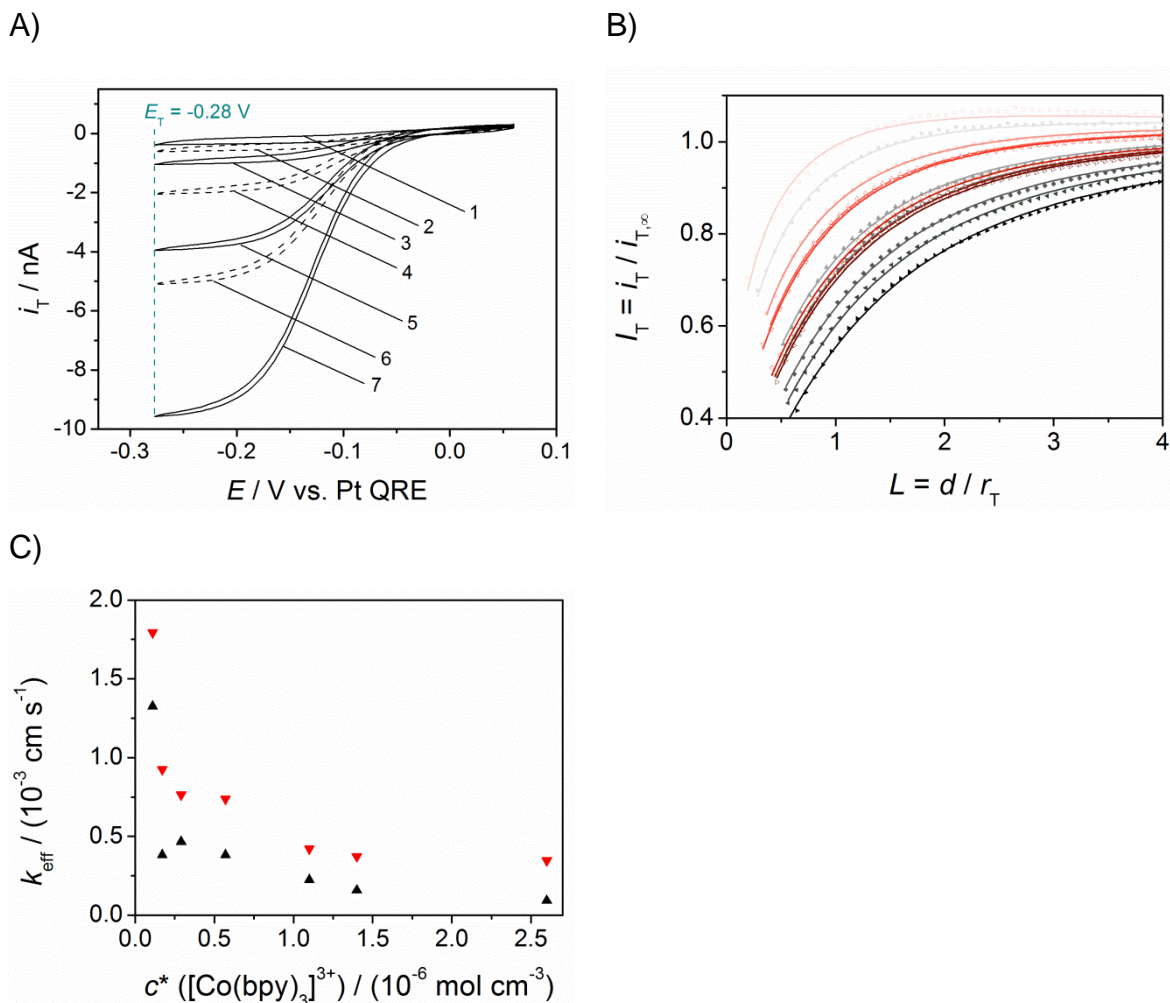


Fig. 7.4 – A) CVs of  $[\text{Co}(\text{bpy})_3]^{3+}$  for the following  $c^*([\text{Co}(\text{bpy})_3]^{3+})$  given in ( $10^{-6} \text{ mol cm}^{-3}$ ) 2.6 (7), 1.4 (6), 1.1 (5), 0.57 (4), 0.29 (3), 0.17 (2) and 0.11 (1); B) Normalized SECM FB approach curves for the approach of a Au disk ME ( $r_T = 13.5 \mu\text{m}$ ,  $RG = 17.8$ ) ( $E_T = -0.28 \text{ V vs. Pt QRE}$ ) towards a D35-sensitized (grey shades, a darker shade corresponds to a higher concentration) and a D45-sensitized (red tones, a darker shade corresponds to a higher concentration)  $\text{TiO}_2$  film (sample type D) illuminated with a blue (455 nm) LED with a photon flux density of  $6.99 \times 10^{-8} \text{ mol cm}^{-2} \text{ s}^{-1}$  at above given different  $c^*([\text{Co}(\text{bpy})_3]^{3+})$ . Symbols indicate normalized experimental approach curves whereas lines are fits to an analytical approximation.<sup>[150]</sup> C) Effective heterogeneous first order rate constants  $k_{\text{eff}}$  as a function of the bulk redox mediator concentration  $c^*([\text{Co}(\text{bpy})_3]^{3+})$ . D35 (black symbols) was sensitized for 24 h, D45 (red symbols) was sensitized for 96 h.

It was concluded that the order of sensitization did not matter and that the critical parameter was the illumination time. A higher illumination time leads to a higher amount of photooxidized dye molecules which could be reduced by the redox mediator giving a current at the ME. As a consequence from these results and to decrease the influence of the illumina-

tion time on the reaction rate for further experiments, the illumination time was prolonged from 5 s to 1 min aiming to minimize the relative difference of illumination time for both dyes. However, these results were difficult to interpret because  $k_{\text{eff}}$  showed no trend (Fig. 7.5B). Dye D45 was measured first and dye D35 second but the interpretation of  $k_{\text{eff}}$  is ambiguous. There is, however, a tendency of higher  $k_{\text{eff}}$  again for the dye measured second, in this case D35.

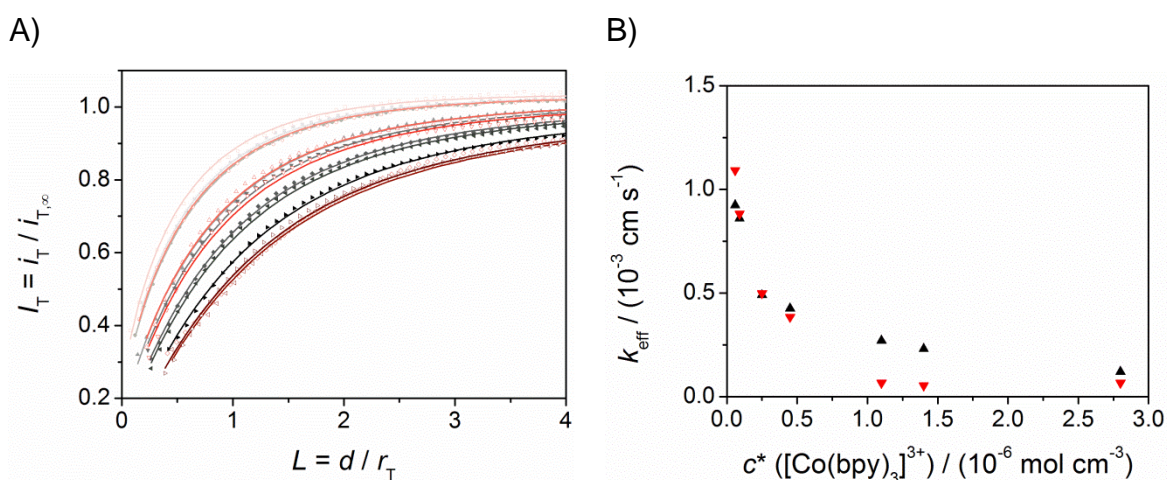


Fig. 7.5 – A) Normalized SECM FB approach curves for the approach of a Au disk ME ( $r_T = 12.3 \mu\text{m}$ ,  $RG = 12.9$ ) ( $E_T = -0.28 \text{ V}$  vs. Pt QRE) towards a D35-sensitized (grey shades, a darker shade corresponds to a higher concentration) and a D45-sensitized (red tones, a darker shade corresponds to a higher concentration)  $\text{TiO}_2$  film (sample type D) illuminated with a blue (455 nm) LED with a photon flux density of  $6.99 \times 10^{-8} \text{ mol cm}^{-2} \text{ s}^{-1}$  for the following  $c^*([\text{Co}(\text{bpy})_3]^{3+})$  given in ( $10^{-6} \text{ mol cm}^{-3}$ ) for both dyes: 2.8, 1.4, 1.1, 0.45, 0.25, 0.09 and 0.06. Symbols indicate normalized experimental approach curves whereas lines are fits to an analytical approximation.<sup>[150]</sup> B) Effective heterogeneous first order rate constants  $k_{\text{eff}}$  as a function of the bulk redox mediator concentration  $c^*$ . D35 (black triangles) was sensitized for 24 h, D45 (red downward triangles) was sensitized for 96 h.

In Table 7.1 the results of the experiments with a different order of measurement in dependence of the reaction rate constant  $k_{\text{eff}}$  are compiled.

Table 7.1 – Compilation of experimental conditions during the method development.

Dye measured first	Dye measured second	higher $k_{\text{eff}}$
D35	D45	D45
D45	D35	D35
D35	D45	D45
D45	D35	D35

On this account and to be sure to have equal conditions for both dyes, for the study in the next chapter, two samples with one dye, D35 or D45 each, were prepared in the exact same way to rule out uncontrollable variables. Therefore, twice the amount of redox electrolyte was prepared and divided in order to use one part for the first and the other part for the second sample. These solutions were bubbled with argon for exactly the same time. The photoanode preparation, the illumination and the WE, Aux and QRE were the same. So, as the best compromise derived from the method development, the procedure outlined in Fig. 7.6 was used for the following experiments.

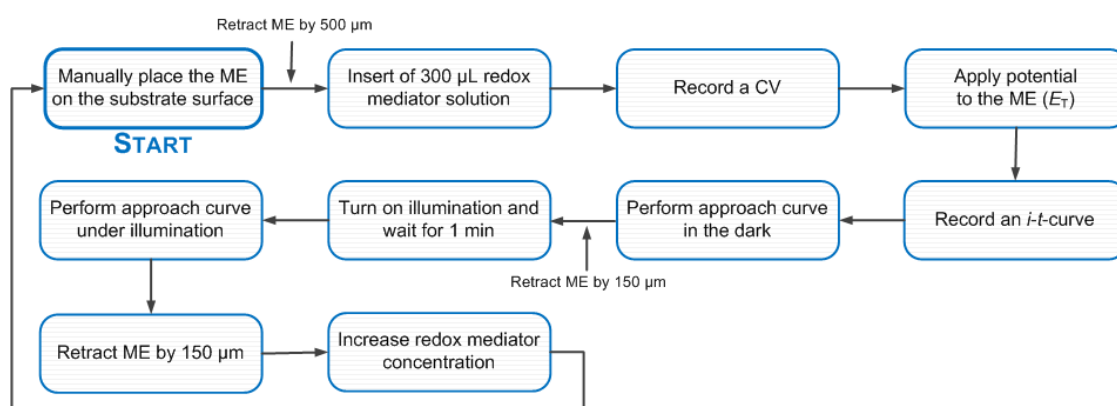


Fig. 7.6 – Procedure for the dye regeneration measurements using SECM in FB mode.

In retrospective, it was a good idea to use only one dye per electrode since dye migration on the  $\text{TiO}_2$  electrode was observed in experiments which lasted longer than 1 h (chapter 8.2). This observation can probably be attributed to desorption and adsorption if the dye-sensitized electrode is in contact with the redox electrolyte for a longer time.

## 7.2 SECM Feedback Mode Investigation of D35- and D45-sensitized TiO<sub>2</sub>

The answer to the question whether a small change in the molecular dye architecture could influence the regeneration (reduction) of a photooxidized dye D<sup>+</sup> by the one-electron redox mediator [Co(bpy)<sub>3</sub>]<sup>2+/3+</sup> is given in this chapter and was also published by the author of this thesis.<sup>[122]</sup> Two structurally similar organic dyes D35 and D45 were studied by SECM and compared to TAS and EIS measurements which were performed by the cooperation partner at Uppsala University, Sweden. The redox potential of both dyes is similar ( $E^0(D35/D35^+) = 1.08$  V and  $E^0(D45/D45^+) = 1.09$  V vs. NHE) (Fig. 7.7) suggesting that possible differences in regeneration could be attributed to architectural differences of the dye molecules (see Fig. 2.7) rather than differences in energy levels. In D45 with its shorter methoxy chains, the distance between the redox species and the positive charge on the triphenylamine unit is shorter which facilitates dye regeneration.

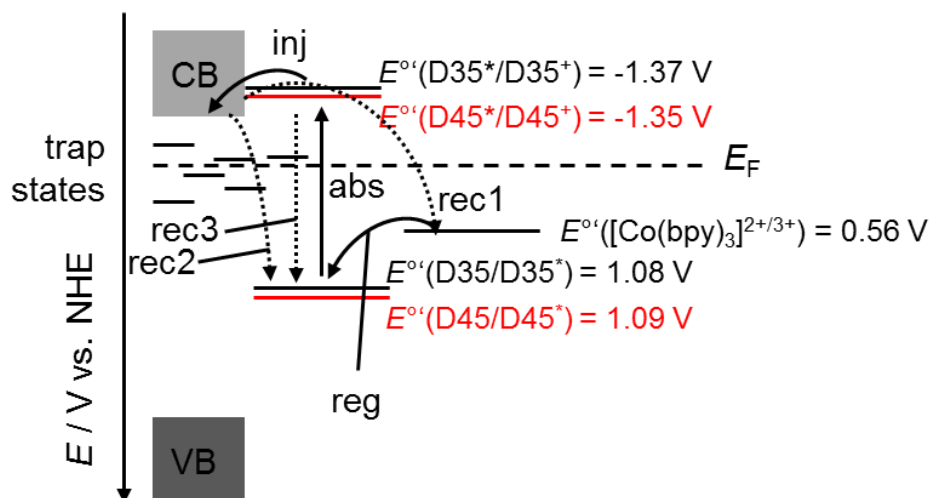


Fig. 7.7 – Energy levels of dyes D35 and D45 and the regeneration (solid arrows) and recombination (dotted arrows) processes present in a DSC. The energy levels and redox potentials were determined by absorption and fluorescence spectroscopy as well as by CV by Hanna Ellis at Uppsala University. Reprinted with permission from *J. Phys. Chem. C*, 2015, 119, 21775-21783 Copyright © 2015 American Chemical Society.<sup>[122]</sup>

The detailed description of the working principle of a DSC is given in Fig. 2.5. Here, only a brief comprehension of the reactions important for the study in this chapter is presented.

After being absorbed (abs), electrons are injected (inj) from the excited dye molecule  $D^*$  into the CB of the semiconductor  $TiO_2$ . There, the electrons are transported to the back contact of the photoanode causing a current in the external circuit. During the transport within the nanoporous  $TiO_2$  film, electrons undergo multiple trapping-detrapping mechanisms in so-called trap states. These appear to be exponentially distributed below the CB edge and have been intensively studied by Bisquert *et al.*<sup>[66]</sup> The current circuit is closed at the CE where the oxidized form of the redox mediator is reduced. At this point, the different recombination (rec1, rec2 and rec3) and regeneration (reg) reactions should be mentioned. The regeneration reaction reg was determined by SECM, whereas rec1 was determined by EIS and rec2 by TAS. Rec3 is a loss mechanism in a DSC during which  $D^*$  is deactivated to  $D$  without electron injection into CB of  $TiO_2$  and was not investigated within the scope of this thesis.

**Experimental Procedure.** A tube was placed above the SECM cell to ensure a slight argon flow during the measurements. All approach curves were recorded with a translation speed of  $1 \mu m s^{-1}$ . Prior to each experiment, a CV was recorded to confirm the cleanliness of the ME, to determine a steady-state current necessary to calculate the concentration of  $[Co(bpy)_3]^{3+}$  and to determine the potential at which a diffusion-controlled reduction occurs. After the ME was immersed into the electrolyte, a CV was recorded to determine the potential at which the  $[Co(bpy)_3]^{3+}$  complex is reduced to  $[Co(bpy)_3]^{2+}$  (Fig. 7.8A) and the ME was biased at  $E_T = -0.28 V$  vs. Pt QRE for subsequent measurements. While approach curves over D35- and D45-sensitized  $TiO_2$  films immersed into working solutions with different concentrations of  $[Co(bpy)_3]^{3+}$  were recorded, the samples were illuminated from the bottom with an LED at a fixed wavelength of 455 nm and a photon flux density of  $J_{hv} = 6.57 \times 10^{-8} mol cm^{-2} s^{-1}$  (at  $4.85 mW cm^{-2}$ ). D35 and D45 each dissolved in MeCN show a strong absorbance of 2 at 455 nm which corresponds to 99% of the photons being absorbed (see SI-8, Figure SI-10 in Ref.<sup>[122]</sup>). However, the photon energy of 2.72 eV ( $\lambda = 455 nm$ ) is too low to excite the semiconductor  $TiO_2$  ( $E_g = 3.2 eV$ ,  $\lambda = 387 nm$ ). Under these conditions, the photoelectrochemical reactions (VIII) (page 90) and (IX) (page 90) occur at the substrate. At the ME,  $[Co(bpy)_3]^{3+}$  is reduced under quasi-stationary conditions:



During the experiment, the concentration of  $[\text{Co}(\text{bpy})_3]^{3+}$  was varied from 0.153 to 2.56 mM (i.e.,  $0.153 \times 10^{-6}$  to  $2.56 \times 10^{-6}$  mol  $\text{cm}^{-3}$ ), starting with the lowest concentration. The normalized approach curves (Fig. 7.8B) are presented in dimensionless normalized coordinates with the normalized current  $I_T$  being the ratio between the distance-dependent current at the ME  $i_T(d)$  and the current in the bulk solution  $i_{T,\infty}$ . The normalized distance  $L$  is the ratio of the ME-to-substrate distance  $d$  and the ME radius  $r_T$ . To obtain these normalized approach curves, experimentally obtained approach curves were fitted by a least-squares method to an analytical approximation by Cornut and Lefrou.<sup>[150]</sup>

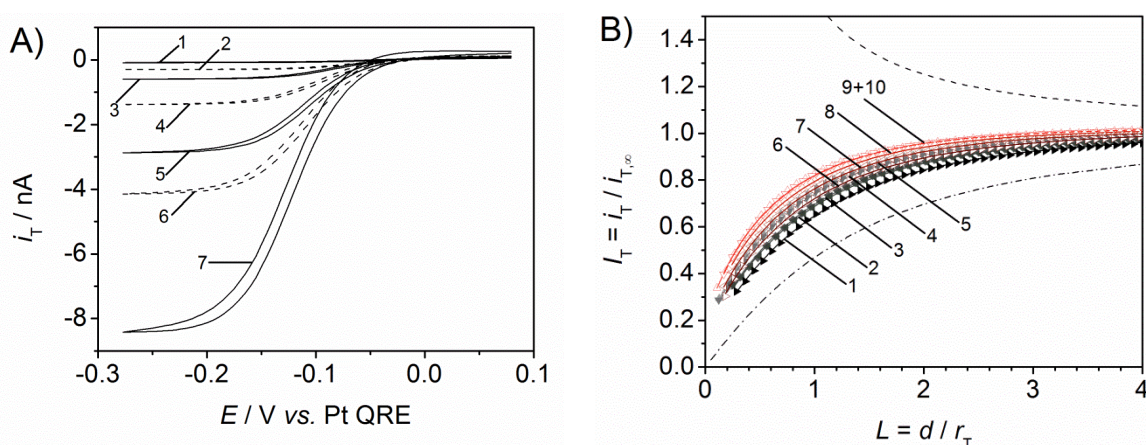


Fig. 7.8 – A) CVs of  $[\text{Co}(\text{bpy})_3]^{3+}$  at different concentrations recorded before each approach curve at a Au ME ( $r_T = 12.25 \mu\text{m}$ ,  $RG = 12.92$ ) with Pt wire as Aux and Pt wire as QRE. B) Normalized SECM FB approach curves for the approach of a Au disk ME towards a D35-sensitized (grey shades, curves 1–5) and a D45-sensitized (red tones, curves 6–10)  $\text{TiO}_2$  film (sample type D) illuminated with a blue (455 nm) LED with a photon flux density of  $6.57 \times 10^{-8}$  mol  $\text{cm}^{-2} \text{s}^{-1}$  for the following  $[\text{Co}(\text{bpy})_3]^{3+}$  given in ( $10^{-6}$  mol  $\text{cm}^{-3}$ ) above D35 (1) 1.78, (2) 1.14, (3) 0.707, (4) 0.333, (5) 0.153 and above D45 (6) 2.56, (7) 1.26, (8) 0.875, (9) 0.421 and (10) 0.182. Top and bottom dash-dotted lines correspond to diffusion-controlled FB and hindered diffusion, respectively. Symbols indicate normalized experimental approach curves whereas lines are fits to an analytical approximation.<sup>[150]</sup> Reprinted with permission from *J. Phys. Chem. C*, 2015, 119, 21775-21783 Copyright © 2015 American Chemical Society.<sup>[122]</sup>

The calculated approach curves in Cornut and Lefrou's publication<sup>[150]</sup> describe the irreversible first order kinetics with respect to the local mediator concentration. The experimentally obtained approach curves fit very well to these predictions (Fig. 7.8B) and resulted in the normalized heterogeneous rate constants  $\kappa$  shown in Table 7.2. The diffusion coefficient  $D$  of  $[\text{Co}(\text{bpy})_3]^{3+}$  necessary for the calculation of  $k_{\text{eff}}$  from  $\kappa$  was determined by

recording LSVs at an RDE (chapter 5.1.1). The diffusion coefficient of  $[\text{Co}(\text{bpy})_3]^{2+}$  is assumed not to deviate to a large extent to that of  $[\text{Co}(\text{bpy})_3]^{3+}$ ,<sup>[202]</sup> also shown by own experiments (chapter 5.1.2) which have shown a slightly higher diffusion coefficient of the reduced species.

Table 7.2 – Concentration in the bulk  $c^*$ , dimensionless first order rate constant  $\kappa$ , the first order reaction rate constant  $k_{\text{eff}}$  (calculated by  $k_{\text{eff}} = \kappa D / r_T$  with  $D = 6.95 \times 10^{-6} \text{ cm}^2 \text{ s}^{-1}$  and  $r_T = 12.26 \text{ }\mu\text{m}$ )

$c^*([\text{Co}(\text{bpy})_3]^{3+}) / 10^{-6} \text{ mol cm}^{-3}$	$\kappa$	$k_{\text{eff}} / (10^{-3} \text{ cm s}^{-1})$
<b>D35</b>		
0.153	0.094	0.532
0.333	0.086	0.488
0.707	0.064	0.365
1.14	0.061	0.345
1.78	0.045	0.252
<b>D45</b>		
0.182	0.139	0.785
0.421	0.137	0.778
0.875	0.119	0.676
1.26	0.099	0.561
2.56	0.076	0.433

### 7.3 Determination of Regeneration Rate Constant from SECM Experiments

In a next step, the obtained  $k_{\text{eff}}$  values (Table 7.2) which summarize the influence of absorption, electron injection, recombination, and regeneration (Fig. 7.7) were fitted. Fig. 7.9 shows the experimentally determined  $k_{\text{eff}}$  values (symbols) and the best least-square fit (performed with MS Excel) to equation (6.26) (lines) for different  $[\text{Co}(\text{bpy})_3]^{3+}$  concentrations with  $k_{\text{ox}}$  and  $\phi_{h\nu}$  as fitting parameters.  $i_{T,\infty}$  and  $r_T$  were adjusted within reasonable range during the fitting procedure. The photon flux density  $J_{h\nu}$  was obtained from the

wavelength of the LED (455 nm) and the measured light intensity ( $4.85 \text{ mW cm}^{-2}$ ). For the calculation of the photon flux density see chapter 4.6.2. This fitting was performed here for a one-electron redox mediator to a tailored equation (chapter 6.1).

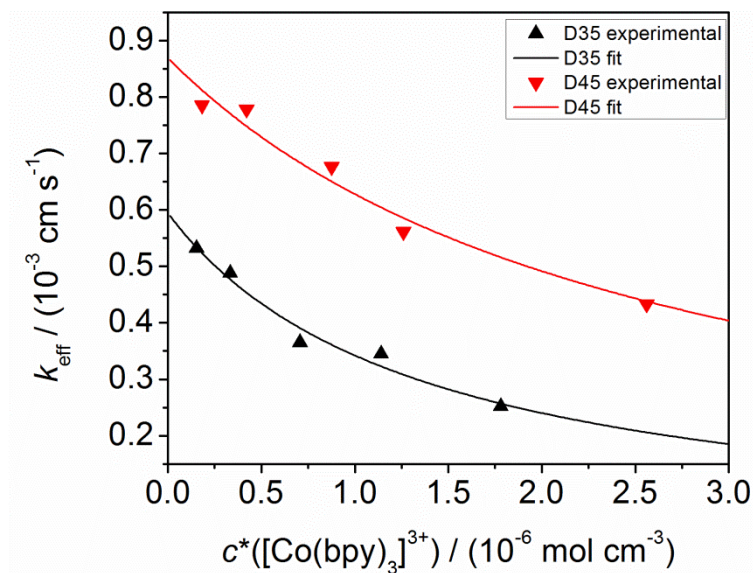


Fig. 7.9 – Effective heterogeneous first order rate constants  $k_{\text{eff}}$  as a function of the bulk redox mediator concentration  $c^*$ . Symbols correspond to experimentally determined values and lines are least-square fits to equation (6.26) with  $k_{\text{ox}} = 2.40 \times 10^3 \text{ cm}^3 \text{ mol}^{-1} \text{ s}^{-1}$  and  $\phi_{\text{hv}} = 4.95 \times 10^4 \text{ cm}^2 \text{ mol}^{-1}$  ( $\phi_{\text{hv}} = 8.22 \times 10^{-20} \text{ cm}^2 \text{ molecule}^{-1}$ ) for D35 (triangles) and  $k_{\text{ox}} = 3.50 \times 10^3 \text{ cm}^3 \text{ mol}^{-1} \text{ s}^{-1}$  and  $\phi_{\text{hv}} = 1.39 \times 10^5 \text{ cm}^2 \text{ mol}^{-1}$  ( $\phi_{\text{hv}} = 2.30 \times 10^{-19} \text{ cm}^2 \text{ molecule}^{-1}$ ) for D45 (downward triangles). Reprinted with permission from *J. Phys. Chem. C*, 2015, 119, 21775-21783 Copyright © 2015 American Chemical Society.<sup>[122]</sup>

The best fit of the experimental data to equation (6.26) was obtained with values of  $k_{\text{ox}} = 2.40 \times 10^3 \text{ cm}^3 \text{ mol}^{-1} \text{ s}^{-1}$  for D35 and  $k_{\text{ox}} = 3.50 \times 10^3 \text{ cm}^3 \text{ mol}^{-1} \text{ s}^{-1}$  for D45 and excitation cross sections,  $\phi_{\text{hv}}$ , of  $4.95 \times 10^4 \text{ cm}^2 \text{ mol}^{-1}$  (D35) and  $1.39 \times 10^5 \text{ cm}^2 \text{ mol}^{-1}$  (D45) with comparable dye loadings.

Table 7.3 – Reaction rate constant of dye regeneration  $k_{ox}$  obtained using the dye regeneration reaction rate law of order 1.

Dye	$k_{ox} / \text{cm}^3 \text{mol}^{-1} \text{s}^{-1}$
D35	$2.40 \times 10^3$
D45	$3.50 \times 10^3$

Since  $k_{ox}$  can also depend on internal mass transport conditions,<sup>[20]</sup> comparable thickness, porosity, and dye loading of the photoanodes are important to provide equivalent conditions for the internal mass transport of the mediator. These conditions were met due to the identical preparation of the D35-sensitized and the D45-sensitized photoanodes.

## 7.4 Comparison with TAS and EIS Measurements

The finding of D35 with its longer *n*-alkoxy chains showing a slower regeneration reaction compared to D45 was confirmed by TAS measurements by a cooperation partner from Uppsala University. The detailed procedure is described in a publication.<sup>[122]</sup> Only a brief description is provided here. In TAS measurements, the dye attached to the TiO<sub>2</sub> is pumped to an excited state from which electrons are injected into the CB of the TiO<sub>2</sub>. Laser pulses measure the absorption of D<sup>+</sup> which is formed after electron injection. The study revealed that the use of different concentrations of the [Co(bpy)<sub>3</sub>]<sup>2+/3+</sup> redox couple led to shorter time constants and thus lower regeneration rates (reg in Fig. 7.7) for D45 with its shorter *n*-methoxy chains compared to D35 with its bulkier *n*-butoxy chains (Table 3 in Ref<sup>[122]</sup>). Furthermore, the recombination rate of electrons from TiO<sub>2</sub> to D<sup>+</sup> (rec2 in Fig. 7.7A) was studied for D35 and D45. Therefore, the measured signals were fitted to biexponential decay functions which have proven to be reliable and relatively straightforward in their application.<sup>[203]</sup> Surprisingly, the measurements showed a recombination which was 7-fold faster for D45 than for D35. This observation might be explained by differences in reorganization energy which is due to the differences in the *n*-alkoxy chains and the dye loading. This could lead to different ways of interaction between the Li<sup>+</sup> cation provided in the stock solution (for the preparation of the stock solution see the corresponding publication<sup>[122]</sup>) and the TiO<sub>2</sub> surface possibly affecting the electron transfer kinetics. A good ex-

planation of this observation is lacking at present. Additionally to the TAS measurements, EIS measurements were performed on completely assembled DSCs.<sup>[122]</sup> Briefly, for each dye, two DSCs were prepared and measured at the same applied potential in the dark as well as at 1 sun ( $1000 \text{ mW cm}^{-2}$ ). The results of the IS measurements agree with those of the TAS measurements: D35 shows slower recombination compared to D45.

In conclusion, the two structurally similar triphenylamine dyes D35 and D45 with similar energy levels as well as HOMO–LUMO differences (Fig. 7.7) were investigated in terms of their regeneration and recombination behavior. Because they show no energetic differences, differences in kinetics should not stem from different driving forces but rather from different distances between the redox species and the positive charge on the triphenylamine unit.<sup>[204, 205]</sup> The regeneration rate constants obtained by SECM are in the same order as those obtained by TAS measurements. The EIS measurements revealed that the longer *n*-butoxy chains seem to prevent recombination both to  $\text{D}^+$  as well as to the oxidized form of the Co redox couple.

## 8 Spatially Resolved Analysis of Screen Printed Photoanodes by SF-SECM

### 8.1 Methodology

Chapter 8, except for chapter 8.4, is based on the recent study by the author of this thesis jointly published with co-workers.<sup>[163]</sup> Among the photovoltaic devices, DSCs are photoelectrochemical devices whose performance depends critically on the design of the semiconductor/electrolyte interface. The efficiency of whole DSCs is commonly characterized by *j*-*V* characteristics, IPCE and absorbed photon-to-current conversion efficiency (APCE) measurements. CV and EIS are usually used to characterize photoanodes<sup>[59]</sup> and particular electron transfer processes have been analyzed by TAS<sup>[83]</sup> and SECM.<sup>[122, 153]</sup> Except for SECM, these techniques are integral techniques which provide signals averaged over macroscopic regions of a DSC or a photoanode. Since the photoanode is a nanostructured material, it seems logical to apply techniques of spatial resolution to analyze its local performance. While a number of local techniques have been applied or even developed for ana-

lyzing the performance of all solid state solar cells, such as SFM-based techniques,<sup>[206-208]</sup> lock-in-thermography<sup>[209, 210]</sup> and solar cell local characterization (CELLO),<sup>[211, 212]</sup> scanning probe microscopies (SPM) have found limited application in the characterization of DSCs. Among other reasons, a DSC is an encapsulated device. When opened, it may easily lose the functional connection between the electrodes and the liquid electrolyte. Our group of Prof. Wittstock at Carl von Ossietzky University of Oldenburg, Germany<sup>[18-21, 153]</sup> and others<sup>[16, 17, 213-216]</sup> have extensively applied SECM to characterize dye regeneration kinetics by different redox electrolytes. However, this methodology relies entirely on recording approach curves. Related approaches to the field have been provided by Figgemeier *et al.*<sup>[12]</sup> who used the SG/TC mode to observe the generation of the oxidized form of the redox electrolyte above illuminated photoanodes. Two-dimensional imaging was much less often reported. Tefashe *et al.*<sup>[19]</sup> could visualize the locally enhanced electrochemical activity of a partially illuminated D149-sensitized ZnO electrode by an SG/TC SECM experiment at constant height applying an  $\Gamma/I_3^-$  mediator.

Zhang *et al.*<sup>[217]</sup> used SECM to screen for efficient dye mixtures for DSCs. They microspotted different dye solutions locally on TiO<sub>2</sub> films and compared the SECM FB currents above the different spots. Aaronson *et al.*<sup>[218]</sup> applied scanning electrochemical cell microscopy (SECCM) with photo illumination to achieve a submicrometer spatial resolution with an ionic liquid electrolyte at a thin film of TiO<sub>2</sub> aggregates. This technique achieves high lateral resolution by wetting only areas of submicrometer diameter with a liquid suspended from a capillary. By placing the meniscus on different locations of the surfaces, lateral inhomogeneities of the response upon illumination were clearly demonstrated. Chen and co-workers combined SECCM with CV to obtain much more information compared to traditional fixed potential imaging.<sup>[219]</sup>

In the present chapter, the options for demonstrating local variations of DSC performance with various approaches to SECM imaging are explored systematically. The measurements in this chapter were performed in cooperation with Inka Plettenberg at Carl von Ossietzky University of Oldenburg. Current and topography images of D35-sensitized TiO<sub>2</sub> electrodes were obtained by SF distance control SECM in the FB mode (Fig. 8.1A) where [Co(bpy)<sub>3</sub>]<sup>3+</sup> was used as oxidized species, Ox, as part of the redox electrolyte. The ME was moved laterally along the *x*- and *y*-axis over the nanostructured substrate surface of which it constantly detected the current,  $i_T$ , and the amplitude in positive or negative

$z$ -direction as the ME retracts at elevations on the surface or follows a deepening in substrate topography, respectively. Exemplary, a CV of an approximately 0.5 mM  $[\text{Co}(\text{bpy})_3]^{3+}$  solution at a small Au ME ( $r_T \approx 1 \mu\text{m}$ ) is shown with a wide steady state region where the reduction from  $[\text{Co}(\text{bpy})_3]^{3+}$  to  $[\text{Co}(\text{bpy})_3]^{2+}$  occurs at  $E_T = -0.25$  to  $-0.35$  V vs. Pt QRE (Fig. 8.1B). Prior to each imaging experiment, the ME potential  $E_T$  was determined by CV as diffusion-controlled  $[\text{Co}(\text{bpy})_3]^{3+}$  reduction reaction.

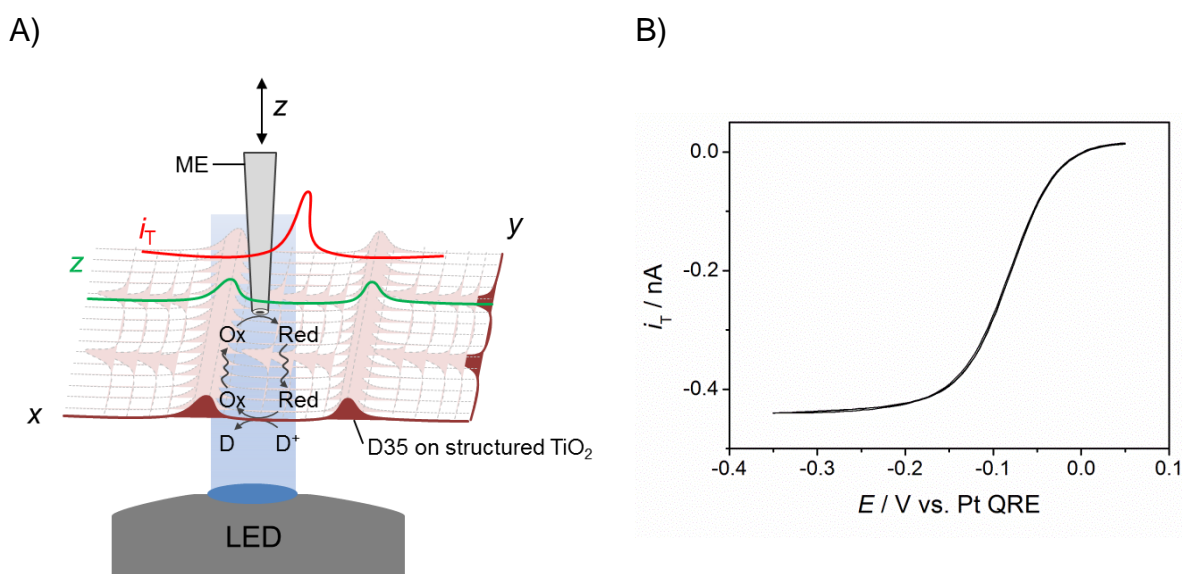


Fig. 8.1 – A) SF-SECM in FB mode used for the investigation of dye-sensitized  $\text{TiO}_2$  photoanodes to correlate the current detected at the ME ( $i_T$ ) and the retraction of the ME in  $z$  direction which corresponds to the topography of the substrate in order to achieve a submicrometer resolution of the structure. B) CV at  $v = 50 \text{ mV s}^{-1}$  of approx. 0.5 mM  $[\text{Co}(\text{bpy})_3]^{3+}$  in 0.1 M TBAPF<sub>6</sub> in MeCN at a Au ME ( $r_T \approx 1 \mu\text{m}$ ) showing the reduction regime of  $[\text{Co}(\text{bpy})_3]^{3+}$  to  $[\text{Co}(\text{bpy})_3]^{2+}$ .

One can think of three scenarios of the redox mediator reduction reactions at the ME and a substrate with three different regions (Fig. 8.2): a compact  $\text{TiO}_2$  blocking layer (A), D35-sensitized porous  $\text{TiO}_2$  (B) and porous but pristine  $\text{TiO}_2$  (C). In the dark, all three regions are insulating giving a negative FB in SECM experiments. However, being illuminated with light of 455 nm corresponding to the excitation wavelength of D35, the D35-sensitized region gives a positive FB due to the formation of the oxidized species  $[\text{Co}(\text{bpy})_3]^{3+}$  at the substrate. This oxidized species diffuses to the ME and results in a higher current detected at the ME. At very close proximity to the surface, a higher amount

of oxidized redox species diffuses to the ME and is reduced to  $[\text{Co}(\text{bpy})_3]^{2+}$ . The pristine and porous  $\text{TiO}_2$  also gives a, however significantly lower, positive feedback because the porous structure allows the redox species to move within. However, the reduced redox species are not oxidized at the sample surface hence no species are generated that can diffuse to the ME and be reduced thereon to contribute to a positive feedback.

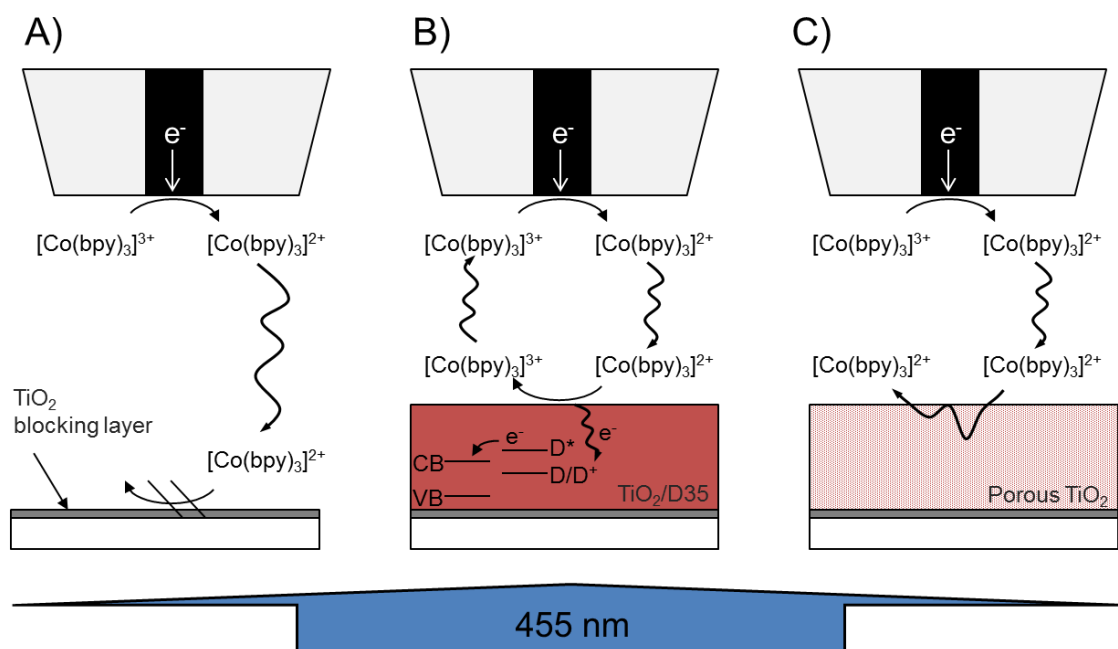


Fig. 8.2 – Scheme of ME-generated  $[\text{Co}(\text{bpy})_3]^{2+}$  regeneration at A) compact  $\text{TiO}_2$  blocking layer, B) D35-sensitized porous  $\text{TiO}_2$  and C) porous but pristine  $\text{TiO}_2$  illuminated with a 455 nm LED.

## 8.2 Dye Migration

Partly sensitized electrodes have been used in screening approaches before.<sup>[217]</sup> Herein, the potential of identifying areas of different dye loading by SECM is explored. Nanoporous  $\text{TiO}_2$  electrodes were prepared on blocking layer-coated FTO and immersed 1 mm into a D35 dye solution. This generated a strip of 1 mm sensitized  $\text{TiO}_2$  (Fig. 8.4A, right side, top image). The image frame was selected to include  $\text{TiO}_2$  blocking layer, D35-sensitized  $\text{TiO}_2$  and as-prepared porous  $\text{TiO}_2$  on  $\text{TiO}_2$  blocking layer.

The appropriate concentration of  $[\text{Co}(\text{bpy})_3]^{3+}$  was determined by approach curves at different redox mediator concentrations. Finally, a concentration of 0.8 mM was chosen because it showed sufficiently high sample kinetics. Constant distance SECM FB image of a region containing D35-sensitized  $\text{TiO}_2$  at  $x < 1100 \mu\text{m}$  and bare  $\text{TiO}_2$  at  $x > 1100 \mu\text{m}$

under illumination is shown in Fig. 8.4A. The associate topography maps (Fig. 8.3) do not show any significant variations in morphology over the entire image frame.

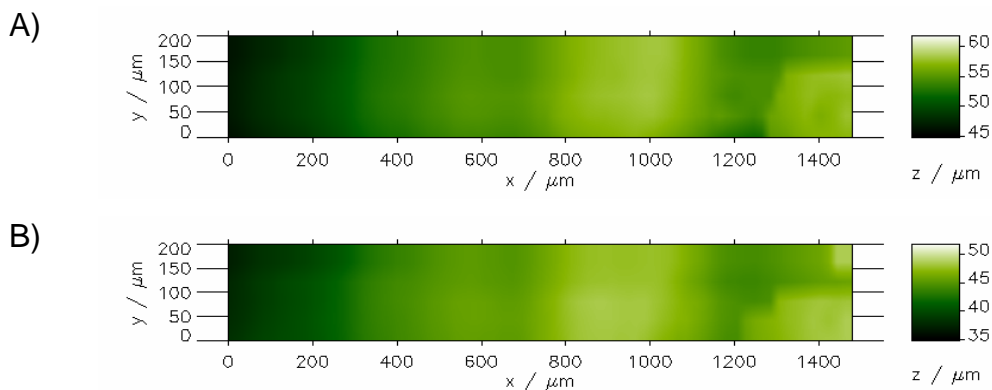


Fig. 8.3 – Topographic images of D35-sensitized  $\text{TiO}_2$  (sample type D, thickness  $19\ \mu\text{m}$ ) showing the topography of A) at the start of the measurement and B) after one hour.  $E_T = -0.3\ \text{V}$  (vs. Pt QRE),  $v = 20\ \mu\text{m s}^{-1}$ ;  $\Delta y = \Delta x = 20\ \mu\text{m}$ ; redox electrolyte:  $0.8\ \text{mM} [\text{Co}(\text{bpy})_3](\text{PF}_6)_3$  in  $0.1\ \text{M TBAPF}_6$  in MeCN; Au ME  $r_T = 4.5\ \mu\text{m}$ , RG = 12.2; CE: Pt, QRE: Pt, positioning system I, SF parameter: reference 83%, frequency: 408652 Hz.

The topography and the current data were recorded both at the forward and a retracing backward scan in order to directly verify the result. In this thesis, only the data obtained during the forward scan are presented since they were equal to those obtained during the backward scan. The originally dyed regions are indicated above the SECM image by a color bar (in Fig. 8.4). The current response corresponds very well to the local sensitization. However, a repetition of the experiment over the identical region after 1 h only showed a blurred transition between areas of high FB current on the left side and the regions of initially low currents on the right side of Fig. 8.4B. The initially unsensitized areas on the right side of Fig. 8.4B show substantially enhanced FB currents. Please note the identical color scale in Fig. 8.4A and B as well as the constant working distance controlled by the SF apparatus to fractions of a micrometer.<sup>[160]</sup> The increase of the FB current above the initially bare  $\text{TiO}_2$  regions is due to spreading of the dye by multiple desorption/re-adsorption events, similar to thin layer chromatography. In this case, the effect can be clearly seen in the photographic images taken before (Fig. 8.4A, right side) and after (Fig. 8.4B, right side) the imaging experiments. After the dye incubation, the border between the dyes is sharp whereas after complete immersion in the electrolyte during SECM imaging,

the region became blurred. The current data were set to a range from  $-0.35$  to  $-2.45$  nA to compare both images.

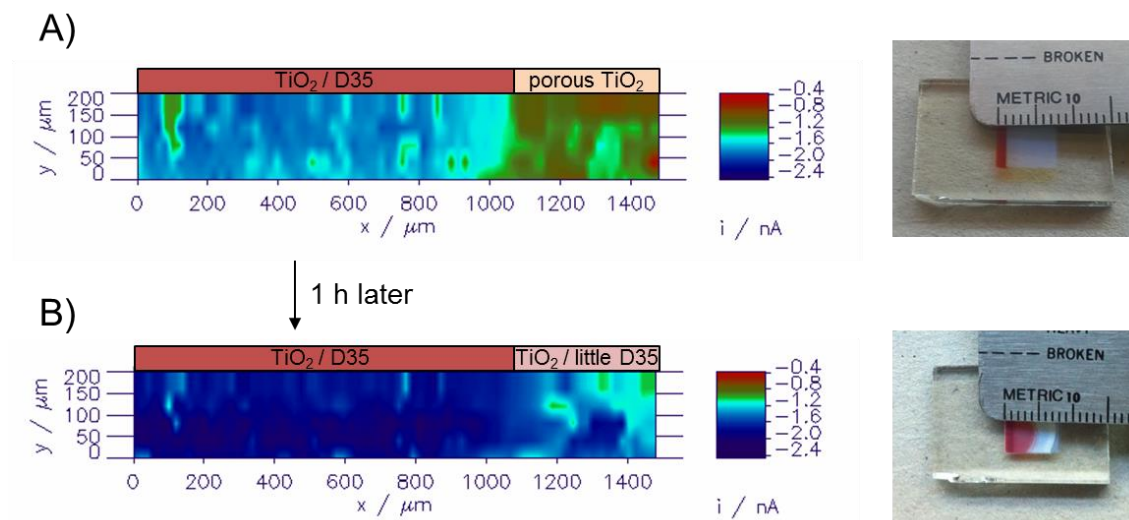


Fig. 8.4 – SF-SECM image of the transition from D35-sensitized  $\text{TiO}_2$  to pristine  $\text{TiO}_2$  (sample type D, thickness  $19\ \mu\text{m}$ ) A) immediately after positioning and B) after 1 h. Photographic images of  $\text{TiO}_2$  on FTO substrate partly sensitized with the dark orange colored D35 before (A) and after (B) the measurements are shown next to the data.  $E_T = -0.3\ \text{V}$  (vs. Pt QRE);  $v_T = 20\ \mu\text{m}\ \text{s}^{-1}$ ;  $\Delta y = \Delta x = 20\ \mu\text{m}$ ; total imaging time = 43 min; redox electrolyte:  $0.8\ \text{mM}\ [\text{Co}(\text{bpy})_3](\text{PF}_6)_3$  in  $0.1\ \text{M}\ \text{TBAPF}_6$  in MeCN; Au ME  $r_T = 4.5\ \mu\text{m}$ ,  $RG = 12.2$ ; positioning system I. A spike was removed at position  $x = 1200$  and  $y = 50\ \mu\text{m}$ . Reprinted with permission from *Electrochim. Acta* 2016, 222, 735-746 Copyright © 2016 Elsevier Ltd.<sup>[163]</sup>

### 8.3 SF-SECM Imaging of the Transition between Illuminated and Non-illuminated Areas of D35-Sensitized $\text{TiO}_2$ Electrodes

In a further step, differences between the response under illumination and in the dark were compared. For this experiment, the image frame was placed above the border between D35-sensitized  $\text{TiO}_2$  and transparent  $\text{TiO}_2$  blocking layer at  $x = 500\ \mu\text{m}$  (Fig. 8.5). During image acquisition, an image was constructed from all forward line scans and another image was constructed from all reverse line scans that retrace the forward scans. During the forward scans, the LED was switched on to illuminate the sample (Fig. 8.5A) while the LED

was switched off during reverse scans (Fig. 8.5B). A waiting time of 5 s was applied before each line scan to allow the sample to equilibrate to the new illumination condition.

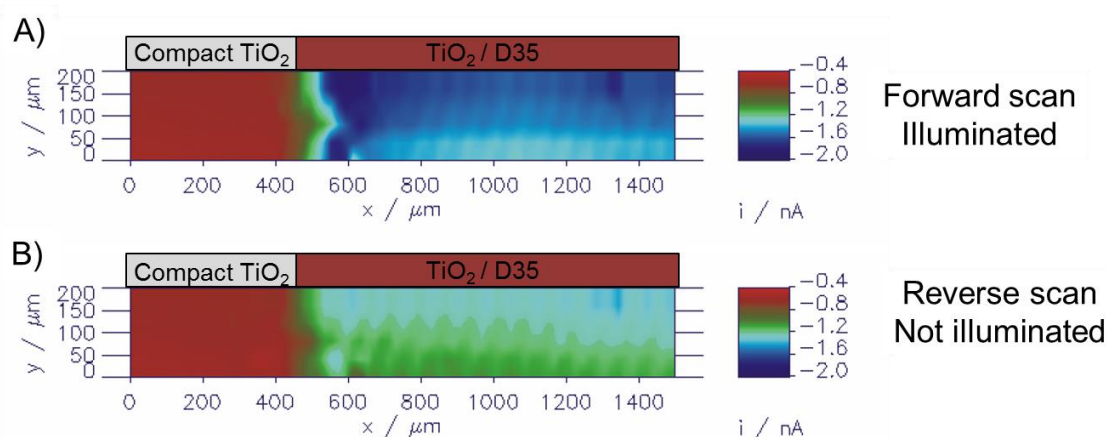


Fig. 8.5 – SF-SECM current image of the transition from blocking layer-coated FTO to sensitized  $\text{TiO}_2$  (sample type D, thickness  $19 \mu\text{m}$ ) A) under illumination (forward scan) and B) without illumination (reverse scan).  $E_T = -0.2 \text{ V}$  (vs. Pt QRE);  $v_T = 20 \mu\text{m s}^{-1}$ ;  $\Delta y = \Delta x = 20 \mu\text{m}$ ; total imaging time = 46 min; redox electrolyte:  $0.7 \text{ mM } [\text{Co}(\text{bpy})_3](\text{PF}_6)_3$  in  $0.1 \text{ M TBAPF}_6$  in MeCN; Au ME  $r_T = 5.2 \mu\text{m}$ ; positioning system II. Reprinted with permission from *Electrochim. Acta* 2016, 222, 735-746 Copyright © 2016 Elsevier Ltd.<sup>[163]</sup>

The texture in the images visible in particular above the  $\text{TiO}_2$  layers is an artefact caused by the positioning system. However, it was found that the electrodes are indeed structured as a consequence of the  $\text{TiO}_2$  screen printing process. The image measurements that revealed the pattern are discussed in chapter 8.5. The topography image shows the thickness of the  $\text{TiO}_2$  film of about  $20 \mu\text{m}$  taken as the height difference between the blocking layer-coated FTO and the porous screen-printed  $\text{TiO}_2$  (Fig. 8.6). This is in good agreement with the layer thickness of  $19 \mu\text{m}$  determined independently by profilometry by cooperation partners at Uppsala University, Sweden. It is stressed that a lower amplitude corresponds to an elevation in topography because the motor retracts the ME in negative  $z$ -direction. Over a sample deepening, the motor moves into positive  $z$ -direction as it “follows” the ME (Fig. 8.6C).

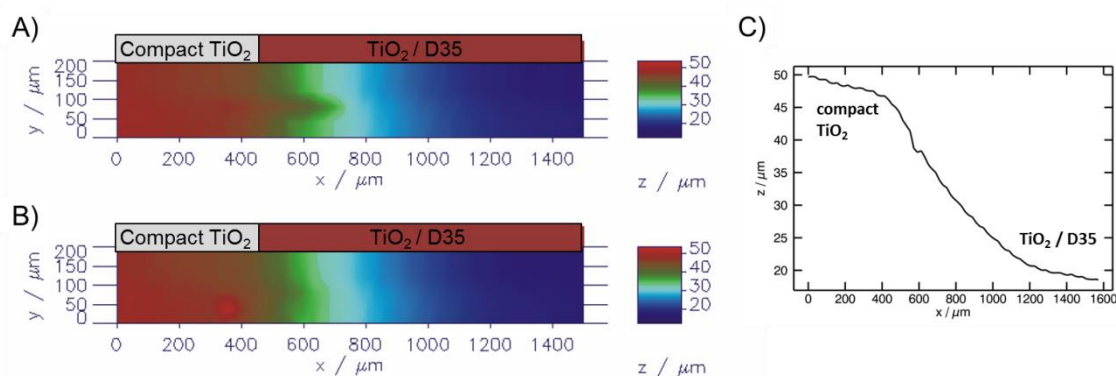


Fig. 8.6 – SF-SECM topographical map of the transition from blocking layer-coated FTO to sensitized  $\text{TiO}_2$  (sample type D, thickness  $19\ \mu\text{m}$ ) A) under illumination (forward scan), B) without illumination (reverse scan) and C) a profile scan showing the height difference.  $E_T = -0.2\ \text{V}$  (vs. Pt QRE);  $v_T = 20\ \mu\text{m s}^{-1}$ ;  $\Delta y = 20\ \mu\text{m}$ ,  $\Delta x = 20\ \mu\text{m}$ ; total imaging time = 46 min; redox electrolyte:  $0.7\ \text{mM} [\text{Co}(\text{bpy})_3](\text{PF}_6)_3$  in  $0.1\ \text{M TBAPF}_6$  in MeCN; Au ME  $r_T = 5.2\ \mu\text{m}$ ; positioning system II. Reprinted with permission from *Electrochim. Acta* 2016, 222, 735-746 Copyright © 2016 Elsevier Ltd.<sup>[163]</sup>

During imaging, the sample had a slight tilt which was compensated by the SF apparatus. The response over blocking layer-coated FTO does not depend on illumination and is comparable to that in Fig. 8.5A and B. The signal is larger above the porous  $\text{TiO}_2$  layer than above the insulating blocking layer, even in the dark. This is reasonable since the porous structure of the electrode allows the mediator to diffuse through the nanoporous network (Fig. 8.2C). Therefore, the current decrease measured by the SF control is smaller over nanoporous  $\text{TiO}_2$  than above a smooth impermeable surface if measured at the same distance to the outer surface.<sup>[220, 221]</sup> However, under illumination the ME currents above D35-sensitized  $\text{TiO}_2$  (Fig. 8.5A) are enlarged by about  $0.4\ \text{nA}$  compared to the situation in the dark (Fig. 8.5B). Both images show an increase of the detected current during the imaging process (from  $y = 0\ \mu\text{m}$  to  $y = 200\ \mu\text{m}$ ) which can be explained by gradual evaporation of the solvent MeCN resulting in a growing concentration of the mediator.

## 8.4 Consideration of Positioning Systems

The photoelectrochemical SECM applied in this thesis had two positioning systems. Positioning system I (by SPI Robot) moved the ME in  $x$ -,  $y$ - and  $z$ -direction and positioning system II (by Physik Instrumente) moved the sample in  $x$ - and  $y$ -direction (see Fig. 4.2 on page 55).

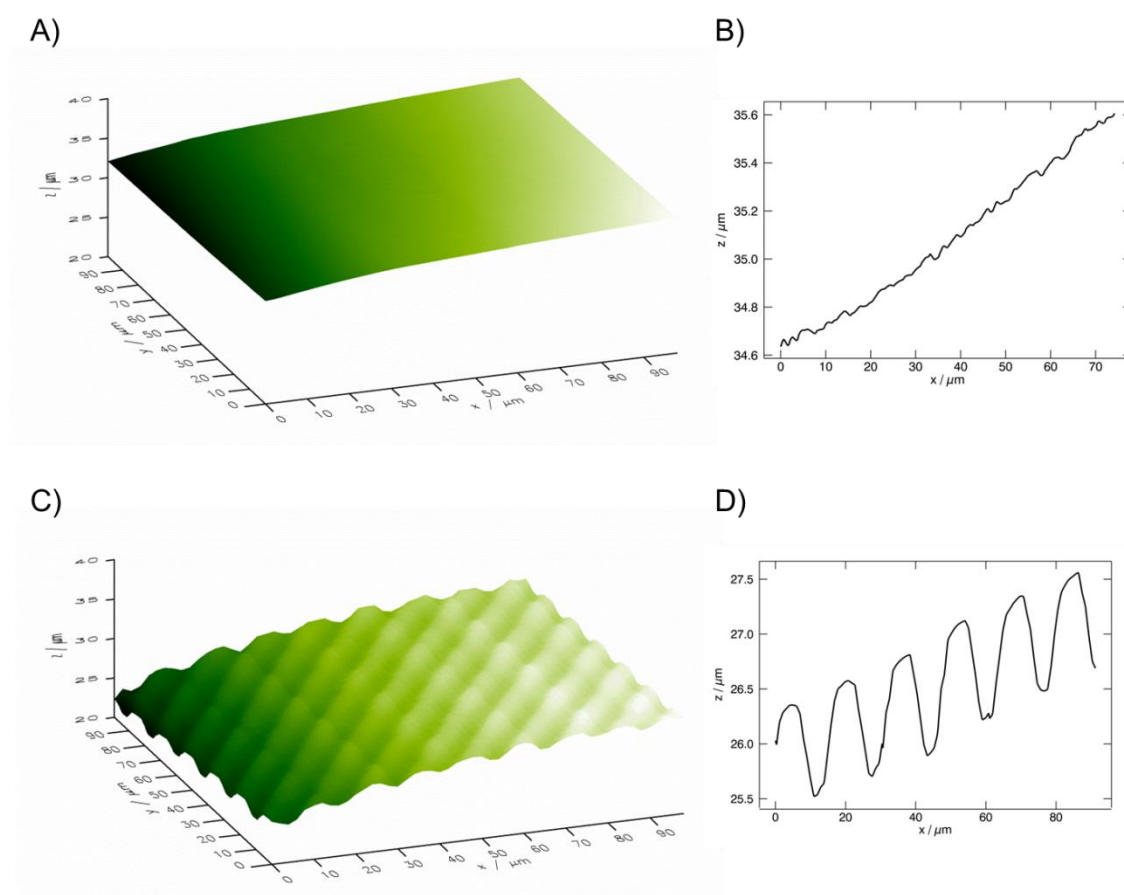


Fig. 8.7 – SF-SECM topography images of a glass substrate recorded using A) positioning system I (movement of the ME), reference: 87 %, frequency: 306287 Hz, with B) the corresponding height profile and C) positioning system II (movement of the substrate), reference: 77 %, frequency: 307564 Hz) with D) the corresponding height profile;  $v_T = 3 \mu\text{m s}^{-1}$ ;  $\Delta y = 2 \mu\text{m}$  (low frequency axis (LFA)),  $\Delta x = 1 \mu\text{m}$  (high frequency axis (HFA)); working solution: dist. water; Au ME  $r_T = 2.5 \mu\text{m}$ .

Before high resolution images of the photoanodes were recorded, it was necessary to verify a proper functioning of the positioning systems. According to the manufacturer's specification, the piezo stepping linear motors (N-661, PI) provide sub-nanometer resolution with a

travel range of up to 20 mm. This resolution is sufficient for probing the photoanodes. A glass substrate was used as a sample to check whether the actuators cause artefacts seen before with other micropositioning systems.

Depending on the positioning system, the topography images of the glass substrate deviate from each other. The glass substrate showed a diagonal structure with an amplitude of about 1  $\mu\text{m}$  using positioning system II (Fig. 8.7C and D) while a smooth surface with a height variation of  $<0.1 \mu\text{m}$  was obtained with positioning system I (Fig. 8.7A and B) which is negligible in further experiments. As a consequence of these measurements, positioning system I was chosen for the following high resolution SF-SECM images because it did not cause any artefacts during scanning the surface of a glass substrate.

## 8.5 Visualization of Defects Using High Resolution SF-SECM FB Imaging

SECM with conventional ME is not able to provide images with the resolution of the individual nanostructures occurring in typical  $\text{TiO}_2$  electrodes produced from  $\text{TiO}_2$  nanoparticles with average diameters of 30 nm. However, local heterogeneities in DSC performance may also result from various processing steps such as paste production, screen printing and gradients across the electrodes during subsequent thermal processing. Therefore, an SF-SECM image in the FB mode of a  $980 \mu\text{m} \times 840 \mu\text{m}$  sized region images was recorded from presumably homogeneous D35-sensitized  $\text{TiO}_2$  photoanodes (Fig. 8.8).<sup>[163]</sup> The ME current in Fig. 8.8A shows a grid structure running diagonally across the image frame. It has a periodicity slightly below 200  $\mu\text{m}$  (Fig. 8.8C). The FB current at those features is enhanced by about 0.6 nA compared to the average current in the image. The grid structure in the current image correlates with a periodic structure in the topography image in Fig. 8.8B showing a height variation of  $<0.2 \mu\text{m}$  with the grid structure elevated against the intermediate spaces. This is most probably a result of the screen printing process for which a T53 mesh (53 lines on a length of 1 cm, periodicity of 189  $\mu\text{m}$ ) was used. The effect of an increased current at the grid structure can on the one hand be explained by the enlarged surface area in these regions related to the horizontal plane. Thereby, additional pores are superficial and facilitate diffusion of the mediator. Furthermore, the gap between the electroactive tip area and the substrate is slightly enhanced when the ME follows the height

profile in the regions close to the height maximum as the SF signal of disk electrodes will mainly depend on the interaction of the comparatively large surrounding insulating layer determining the overall tip dimensions. If the edge of the tip reaches the grid structure, the SF distance control will already lift the probe although the electroactive area did not yet reach the respective structure. The enhanced gap between tip and substrate facilitates mediator diffusion and leads to a current increase. A closer view into the current map reveals that the current is notably high at the edge of the grid structure (Fig. 8.8A), which supports this explanation. Besides the grid structure, the current and topography data both show a defect of 100  $\mu\text{m}$  diameter with center coordinates  $(x/\mu\text{m}, y/\mu\text{m}) = (300, 700)$  where the FB current is reduced while the region is elevated against the surrounding area. Presumably, the effect is caused by material such as the  $\text{TiO}_2$  paste being dropped during the production process. The observed grid structure has been confirmed by contact mode SFM imaging in air by Julia Witt and also by phase contrast microscopy by Carsten Dosche at Carl von Ossietzky University in Oldenburg.<sup>[163]</sup> An area as large as 1500  $\mu\text{m} \times 1500 \mu\text{m}$  was investigated. The phase contrast image shows the same periodicity found in the SECM current and SF topography image supporting its origin from the screen printing process. The enhanced area is located up to 200 nm above the level of the plain regions between the wires and displays a width of approximately 50  $\mu\text{m}$ . The wires of the screen printing mesh had a thickness of 55  $\mu\text{m}$ .

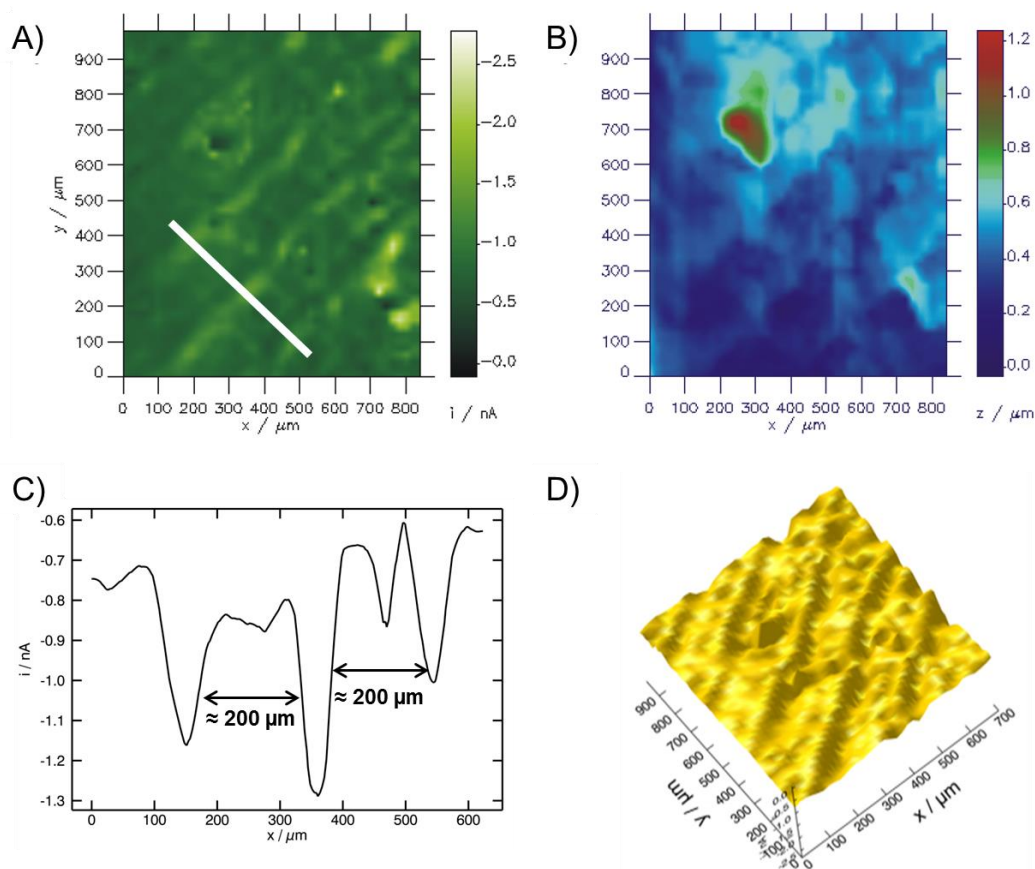


Fig. 8.8 – SF-SECM image of D35-sensitized  $\text{TiO}_2$  (sample type E, thickness  $13 \mu\text{m}$ ) showing A) the FB current image, B) the topography image, C) the profile of the current along the white line in A) and D) the current image plotted in 3D.  $E_T = -0.3 \text{ V}$  (vs. Pt QRE);  $v_T = 20 \mu\text{m s}^{-1}$ ;  $\Delta y = \Delta x = 20 \mu\text{m}$ ; total imaging time = 105 min; redox electrolyte: 1 mM  $[\text{Co}(\text{bpy})_3](\text{PF}_6)_3$  in 0.1 M TBAPF<sub>6</sub> in MeCN; Au ME,  $r_T = 5.2 \mu\text{m}$ ; positioning system I, SF parameter: reference: 67%, frequency: 330978 Hz. Line-by-line-flattening was applied to topography data. The topographic scale was normalized. Reprinted with permission from *Electrochim. Acta* 2016, 222, 735-746 Copyright © 2016 Elsevier Ltd.<sup>[163]</sup>

Summarizing the SF-SECM, SFM and phase contrast microscopy data, it is apparent that the screen printing process leads to the formation of periodic thickness variations of the  $\text{TiO}_2$  layer. Although SF-SECM measurements of the samples show uneven mediator regeneration kinetics in the SECM FB mode, it cannot be concluded how this affects the overall performance of the DSCs. Aforementioned processes studied by FB SECM measurements are not necessarily the performance limiting processes of a complete DSC but rather one out of several performance determining factors. Nevertheless, the detection of

occasional, non-periodic defect structures underlines that such structures may indeed influence device performance.

## 8.6 High Resolution Imaging by SF-SECM

In order to gain a better understanding of the role of such defects, an equally prepared D35-sensitized TiO<sub>2</sub> sample was imaged using a smaller ME ( $r_T = 2.3 \mu\text{m}$ ,  $RG \approx 15$ ) to enhance the lateral resolution (Fig. 8.9). The mediator concentration was selected low in order to stay in the regime where the ME response is sensitive to the sample kinetics (the "kinetic window"<sup>[160]</sup>). For this measurement, the ME was placed close to the sample surface using the SF control. Within an image frame of  $100 \mu\text{m} \times 100 \mu\text{m}$ , several areas are visible that show a deviation of  $i_T$  by 3 pA (Fig. 8.9A) whereas the topography map shows variations of about  $0.5 \mu\text{m}$  (Fig. 8.9B) which very certainly can be attributed to a defect. In general, both images correspond rather well to each other. A small area with notably lower regeneration kinetics is visible at  $x \approx 40 \mu\text{m}$ ,  $y \approx 25 \mu\text{m}$  in the current image (Fig. 8.9A). There is no equally accentuated structure in the topography image (Fig. 8.9B) illustrating that it is not just a mere finite size effect that often occurs in combined high resolution SECM images.<sup>[148]</sup> The topography image (Fig. 8.9B) contains deepened regions between (40, 20) to (90, 15) that do not show up in the current image. The independence of particular features in the current and topography images of photoanodes indicates that besides the general trend that layer thickness is coupled to dye loading, i.e. amount of adsorbed dye per geometric area of the photoanode, there are also defects which alter the dye regeneration kinetics in this specific situation compared to the average material properties. These could be electrically isolated particles, micro-fissures in the nanoporous material, or regions with particular high light fluxes due to scattering effects in the surrounding nanoporous layer. The glass slides used have a height variation of 4 nm which should not influence the experiments performed.

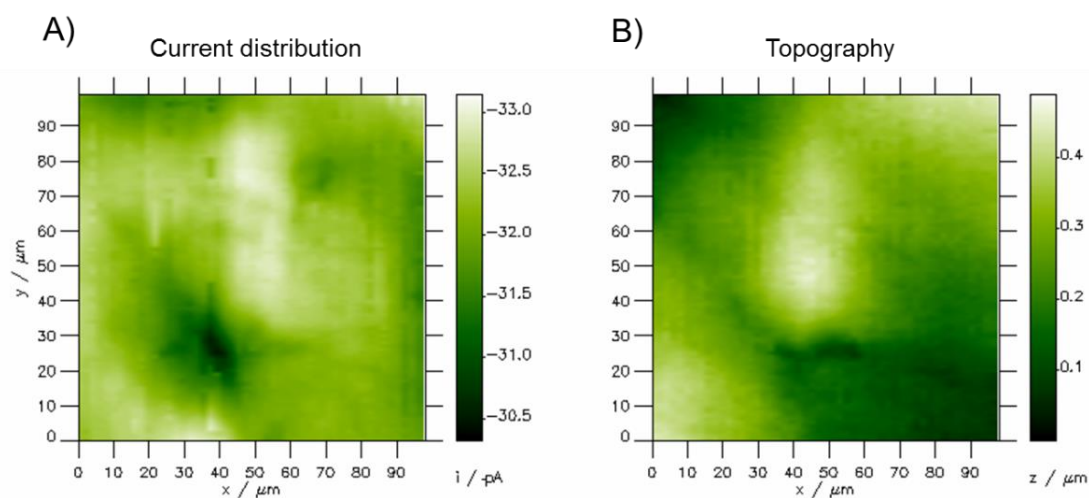


Fig. 8.9 – SF-SECM image of D35-sensitized  $\text{TiO}_2$  (sample type D, thickness  $19 \mu\text{m}$ ) showing A) the FB current and B) the topography.  $E_T = -0.25 \text{ V}$  (vs. Pt QRE),  $v_T = 3 \mu\text{m s}^{-1}$ ;  $\Delta y = 1 \mu\text{m}$ ,  $\Delta x = 2 \mu\text{m}$ ; redox electrolyte:  $0.2 \text{ mM } [\text{Co}(\text{bpy})_3](\text{PF}_6)_3$  in  $0.1 \text{ M TBAPF}_6$  in MeCN; Au ME  $r_T = 2.3 \mu\text{m}$ ; positioning system I, SF parameter: reference 91%, frequency:  $374658 \text{ Hz}$ . Line-by-line-flattening and spike removal was applied to both images. The topographic scale was normalized. Reprinted with permission from *Electrochim. Acta* 2016, 222, 735-746 Copyright © 2016 Elsevier Ltd.<sup>[163]</sup>

To conclude the experiments conducted in this chapter, the difficulties and potential of SECM were evaluated for the spatially resolved functional analysis of D35-sensitized  $\text{TiO}_2$  photoanodes. Intermittent illumination bears the potential of  $\text{D}^+$  being still available in the dark phase when working in the FB mode where the reduced mediator is only generated at the ME probe. A further possible complication is the spreading of dyes by desorption and re-adsorption in inhomogeneously sensitized samples. SF-SECM was able to eliminate issues with sample tilt, in particular when scanning rather large areas. In such images, local kinetic differences were observed that correlated with periodic topographic features originating from the screen printing process of the  $\text{TiO}_2$  paste and was independently confirmed by SF topographical imaging in the SECM instrument, SFM and phase contrast microscopy. In most regions, thickness and function are correlated. Furthermore, SF-SECM with smaller MEs shows isolated features where topography data and local dye regeneration kinetics do not follow the same trend. This indicates that processing conditions may result in different local structures with slightly different functional properties. For the future, it would be extremely interesting to analyze photoanodes extracted from DSCs after prolonged operation, similar to the investigation of aged solid electrolyte interphase on graph-

ite negative electrodes from Li-ion batteries that revealed stark lateral reactivity differences.<sup>[222]</sup>

## 9 Summary and Perspective

**Summary.** A DSC is an attractive photovoltaic device and it is the only solar cell which mimics photosynthesis to convert sunlight into electric current and consists of abundant and mainly non-toxic materials. Due to the variation of components that can be used to design a DSC, it is possible to create attractive colors and structures. These can for example be employed as decorative elements in facades, windows, backpacks or bags. The characterization of DSCs is in general performed by current density – voltage curves, IPCE, TAS and EIS. A very important step in the working principle of a DSC is the regeneration of the photooxidized dye by the reduced form of a redox mediator. In this thesis, a model for the dye regeneration considering a rate law of order 1 with respect to the one-electron redox mediator  $[\text{Co}(\text{bpy})_3]^{2+/3+}$  was developed and successfully tested.

$[\text{Co}(\text{bpy})_3](\text{PF}_6)_{2/3}$  and  $[\text{Co}(\text{bpy})_3](\text{NO}_3)_{2/3}$  were synthesized as redox mediators and characterized in terms of their electrochemical and spectroscopic properties and tested towards their long-term and light stability. Furthermore, the diffusion coefficient of  $[\text{Co}(\text{bpy})_3]^{3+}$  was determined in different solvents using LSV at an RDE. Diffusion coefficients of both  $[\text{Co}(\text{bpy})_3]^{2+}$  and  $[\text{Co}(\text{bpy})_3]^{3+}$  were also determined by CV with different scan rates at a ME. The obtained diffusion coefficients were in good agreement with literature values. Furthermore, it was shown that Pt is an inappropriate electrode material to use with the cobalt mediator, but that Au is very well suited for the measurements performed in this thesis (chapter 5).

Chapter 6 presents the development and testing of a model for the dye regeneration rate law of order 1 with respect to the redox mediator  $[\text{Co}(\text{bpy})_3]^{2+}$ . The model was compared to earlier models which considered the stoichiometry of the  $\text{I}/\text{I}_3^-$  redox mediator. SECM in the FB mode was employed to probe the reliability of the cobalt redox mediator. This was done by increasing the redox mediator concentration and the light intensity (in independent experiments) and compare the results to those obtained by Tefashe *et al.*<sup>[19-21]</sup> using the  $\text{I}/\text{I}_3^-$  redox mediator. After these experiments were accomplished successfully, the cobalt redox mediator was used to compare the regenerative ability of  $[\text{Co}(\text{bpy})_3]^{3+}$  in

both aqueous and organic media with the organic dye D35. It could be shown, that no regeneration in aqueous media occurred unless PEG300 has been added as wetting agent. With  $[\text{Co}(\text{bpy})_3]^{3+}$  used in organic media, dye regeneration could be observed, indicated by an increased reaction rate constant  $k_{\text{eff}}$  at increasing light intensity. To check whether the, in terms of SECM, new redox mediator  $[\text{Co}(\text{bpy})_3](\text{NO}_3)_3$  dissolved in a water-based electrolyte is able to regenerate a dye at all, another dye, namely V35, was used. This dye has glycolic chains which creates a higher hydrophilicity than in D35. To achieve a higher wettability between the aqueous mediator and the dye, PEG300 was added as a wetting agent. It was shown that a higher concentration of PEG300 in the redox mediator solution led to a higher reaction rate constant  $k_{\text{eff}}$  and that  $[\text{Co}(\text{bpy})_3]^{3+}$  in aqueous media regenerates dye V35.

In chapter 7, the structurally similar dyes D35 and D45 were investigated in terms of dye regeneration by the redox mediator  $[\text{Co}(\text{bpy})_3](\text{PF}_6)_3$  in organic media by recording approach curves and fitting those to an analytical model. The FB mode SECM study revealed that although the energy levels of both dyes are similar, D45 shows a faster regeneration compared to D35 which is attributed to the difference in their architecture: D45 has *n*-methoxy chains whereas D35 has longer *n*-butoxy chains. The dye regeneration rate constant  $k_{\text{ox}}$  was determined to be  $2.40 \times 10^3 \text{ cm}^3 \text{ mol}^{-1} \text{ s}^{-1}$  for D35 and  $3.50 \times 10^3 \text{ cm}^3 \text{ mol}^{-1} \text{ s}^{-1}$  for D45, showing a higher regeneration rate for D45. These results are in the same order as the regeneration rate constants obtained from TAS measurements which were performed by cooperation partners from Uppsala University, Sweden.

In chapter 8, two-dimensional imaging with SF distance controlled SECM was performed on D35-sensitized nanoparticulate  $\text{TiO}_2$  electrodes. Therefore, a SF unit was integrated into the photoelectrochemical SECM setup. The FB mode was applied to probe partly and fully sensitized  $\text{TiO}_2$  electrodes and to show differences between illuminated and non-illuminated regions of a photoanode and to explore local variations that could have an influence on the functional properties of DSC photoanodes. As expected, the current was higher above illuminated dye-sensitized  $\text{TiO}_2$  photoanodes compared to non-illuminated regions because the redox mediator is only oxidized on the sample surface if the dye attached to the sample is oxidized. Topographical and current distribution maps of a  $980 \mu\text{m} \times 840 \mu\text{m}$  sized region of a D35-sensitized region shows a grid-like structure which was confirmed by SFM and phase contrast microscopy and can be attributed to the

screen printing process during fabrication. It was also shown that in partly sensitized electrodes, the dye spreads by desorption and re-adsorption processes, a fact that complicates the scanning of dye libraries, for example. Furthermore, SF-SECM with smaller MEs (down to  $r_T = 2$ ) revealed isolated behavior of topography and local dye regeneration kinetics. SF-SECM imaging strategies find application for assuring the most efficient DSC processing and could be interesting for analyzing photoanodes of DSCs after long-term operation. The SF control was stable on topographical height variations of at least up to 20  $\mu\text{m}$ .

**Perspective.** The successful application of the SF-coupled photoelectrochemical SECM paves way for further spatially resolved measurements. In this thesis, comparatively large Au MEs were employed. It would be interesting to find the smallest ME size possible without reaching kinetic limitations to investigate photoanodes with a higher spatial resolution. Also, a super continuum light source could be applied for scanning photoanodes much faster. With regard to imaging methods, it would be extremely interesting to analyze photoanodes extracted from DSCs after prolonged operation and to reveal possible deficiencies that could lead to an overall efficiency loss. In order to be able to scan a larger photoanode surface in less time, applying soft microelectrode arrays might be interesting, similar to the method used by Lesch *et al.*<sup>[223, 224]</sup>

In terms of kinetic experiments, it would be interesting to combine experimental data and simulations to investigate the redox mediator diffusion through the porous  $\text{TiO}_2$  electrodes or various other porous semiconductor electrodes. Therefore, the thickness of the semiconductor needs to be varied. Kim *et al.*<sup>[225]</sup> found optimized layer thicknesses of 600 nm for a  $\text{TiO}_2$  nanoparticle layer and 20  $\mu\text{m}$  for a  $\text{TiO}_2$  nanorod layer. Considering different electrolyte media than organic solvents, the redox couple  $[\text{Co}(\text{bpy})_3]^{2+/3+}$  used in aqueous media offers a variety of possible experiments. Its applicability should be extended since water-based electrolytes are environmentally more friendly and more easy to handle when long-term stable DSCs are manufactured compared to organic-based electrolytes which mainly due to their volatility easily corrode the sealing.

In general, despite a lot of research during the past years, the efficiency of DSCs did not increase significantly. The missing efficiency could be compensated by installing much larger devices since the material cost of a DSC is low compared to silicon solar cells.

Also, the variety of possible components and colors offers the opportunity to use DSCs in glass façade constructions or for mobile power generation in backpacks or bags.

## 10 Appendix

### 10.1 Microelectrodes Used

Table 10.1 – Electrode material, electrode radius  $r_T$  and the ratio of the radius of the insulating glass sheath  $r_{\text{glass}}$  to  $r_T$  ( $RG$ ) of each ME that has been used.

Number	ME material	$r_T / \mu\text{m}$	$RG$ value
1	Au	13.5	17.8
2	Pt	12.6	32.9
3	Pt	12.3	5.93
4	Pt	15.2	9.85
5	Pt	5.1	48.9
6	Au	12.3	12.9
7	Au	14.2	8.02
8	Au	14.6	9.24
9	Pt	12.6	8.6
10	Pt	12.7	10.4
11	Au	4.5	12.2
13	Au	5.2	13.5
14	Pt	14.2	19.3
15	Au	< 1	
16	Au	$\approx 1$	
17	Au	$\approx 2.5$	

## 10.2 Validation of the LED Light Intensity

Because the mobile laser power meter showed ageing behavior, it was necessary to verify the obtained light intensities by means of a recently calibrated photodiode. This was done with an independent setup. Three LEDs, blue (LDC470, 470 nm), green (LDC530, 530 nm) and red (LDC627, 627 nm, all three from Metrohm Autolab) were used and controlled by a potentiostat (*PGSTAT128N* with LED Driver, Metrohm Autolab BV, Germany). Two detectors were used to compare the light intensities: first, a portable X9<sub>3</sub> Laserpower, which was also used in the photoelectrochemical SECM setup, and second, a recently calibrated photodiode which belongs to the LED setup from Metrohm Autolab (Fig. 10.1). The distance between the LED and the detectors was 25 cm.

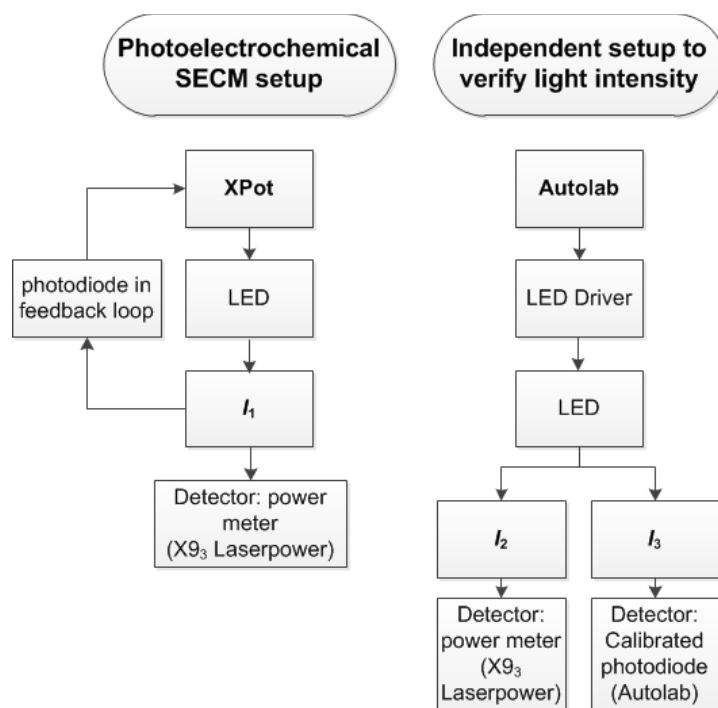


Fig. 10.1 – Flow chart of the procedure of the accurate light intensity determination of the LEDs.

For the validation, a program sequence was written in the operating software of the Autolab potentiostat *NOVA* (Version: 1.8.17 by Metrohm Autolab B.V.). As a first step, the output current of the Autolab LED Driver is entered. In a further step, the open-circuit potential is determined for a period of 20 s. Afterwards, an *i*-*V*-curve is recorded from  $-0.5$  to  $0$  V to obtain the short-circuit current  $i_{SC}$  (at  $0$  V). This procedure has been performed for an appropriate number of times until a reliable calibration curve was obtained (Fig. 10.2).

The light intensity  $I_3$  was calculated using the following equation (10.1) which was supplied by the manufacturer

$$I_3 = \frac{i_{SC}}{A \cdot \eta} \quad (10.1)$$

with  $i_{SC}$  being the short-circuit current [A],  $A$  the active surface of the photodiode ( $0.13 \text{ cm}^2$ ) and  $\eta$  a photon factor [ $\text{A W}^{-1}$ ] provided by the manufacturer Metrohm Autolab for LEDs of different wavelengths (Table 10.2). The X9<sub>3</sub> Laserpower displays the light intensity  $I_2$  in  $\text{mW cm}^{-2}$ .

Table 10.2 – Photon factors of three LEDs provided by the manufacturer.

$\lambda / \text{nm}$	$\eta / \text{A W}^{-1}$
470	0.138
530	0.210
630	0.330

The determined light intensities  $I_2$  obtained with the portable laser power meter and  $I_3$  obtained with the calibrated photodiode and calculated with equation (10.1) were plotted versus the output current of the LEDs (Fig. 10.2).

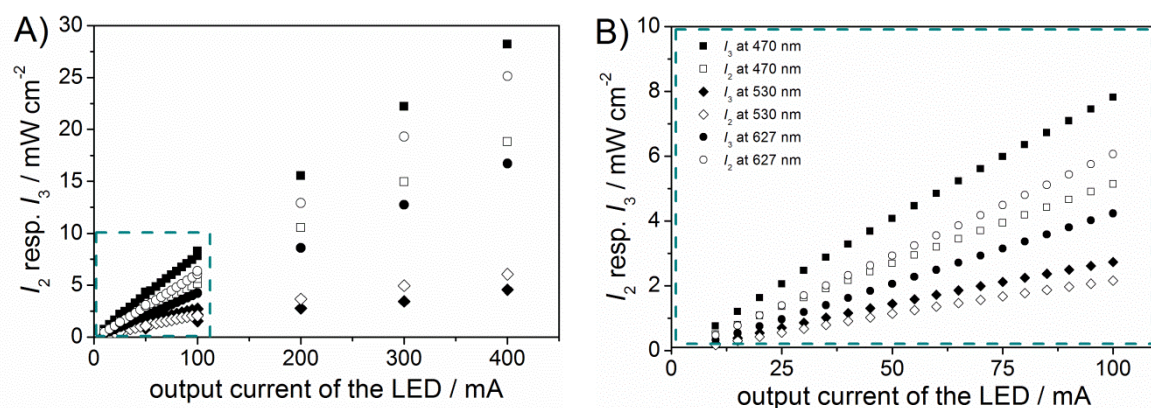


Fig. 10.2 – A) Light intensities of three LEDs: 470 nm (squares), 530 nm (diamonds) and 627 nm (circles) measured with the X9<sub>3</sub> Laserpower (blank symbols,  $I_2$ ) as well as a calibrated photodiode from Autolab (filled symbols,  $I_3$ ); B) Close-up of output currents of 0-100 mA which are relevant for the SECM measurements.

From Fig. 10.2 it is evident that the calibration of the blue (470 nm) and the red (627 nm) LED is approximately linear, while the calibration of the green (530 nm) is non-linear. Normally, the latter case would be expected since the light intensity of an LED does not depend linearly on the output current. However, since the blue LED was used in this thesis and shows a linear dependence on the output current, the linear equation was applied to calculate the actual light intensities.

Table 10.3 – Function of the calibration curves of a blue, red and yellow LED from the Autolab set-up resulting from the detection with the X9<sub>3</sub> Laserpower and the calibrated photodiode from Autolab.

$\lambda_{LED} / \text{nm}$	Function (X9 <sub>3</sub> Laserpower ( $I_2$ ))	Function (Autolab ( $I_3$ ))
470	$y = 0.0512x + 0.0857$	$y = 0.078x + 0.11$
530	$y = -0.0005x^2 + 0.0265x - 0.0857$	$y = -0.00005x^2 + 0.0338x - 0.1061$
627	$y = 0.0621x - 0.1611$	$y = 0.0435x - 0.1146$

In the following, the calculation of the actual light intensity of a blue LED is given. By merging both linear equations of the calibration line of  $I_2$  (X9<sub>3</sub> Laserpower) on the one hand and  $I_3$  (Autolab) on the other hand, equation (10.2) was obtained, in which the  $y$  value stands for the light intensity  $I$  and  $x$  stands for the output current of the LED:

$$y_{\text{Autolab}} = m_{\text{Autolab}} \cdot \frac{y_{\text{X9}_3 \text{ Laserpower}} - b_{\text{X9}_3 \text{ Laserpower}}}{m_{\text{X9}_3 \text{ Laserpower}}} + b_{\text{Autolab}} \quad (10.2)$$

If the parameters of the linear functions from Table 10.3 for the blue LED are inserted into equation (10.2), equation (10.3) is obtained which gives  $I_3$  in  $\text{mW cm}^{-2}$ :

$$I_3 = 0.078 \cdot \left( \frac{(I_2 - 0.0857)}{0.0512} \right) + 0.11 \quad (10.3)$$

Using this equation, all values obtained with the portable X9<sub>3</sub> Laserpower ( $y_{\text{X9}_3 \text{ Laserpower}} = I_2$ ) were converted into actual values ( $y_{\text{Autolab}} = I_3$ ) which are based on a recently calibrated photodiode. Those calculated values are in good agreement with the values that initially were entered in the XPOT software within the SECM setup to set the illumination intensity.

---

## 10.3 Abbreviations

---

<b>Abbreviation</b>	<b>Meaning</b>
$^1\text{H-NMR}$	nuclear magnetic resonance of $^1\text{H}$ nuclei
$^{13}\text{C-NMR}$	nuclear magnetic resonance of $^{13}\text{C}$ nuclei
$^{31}\text{P-NMR}$	nuclear magnetic resonance of $^{31}\text{P}$ nuclei
AC-SECM	alternating current SECM
AD/DA	analog-digital/digital-analog
APCE	absorbed photon-to-current conversion efficiency
Aux	auxiliary electrode
BIPV	building integrated photovoltaics
bpy	2,2'-bipyridine
CB	conduction band
CE	counter electrode
CELLO	solar cell local characterization
CIGS	copper-indium-gallium-selenide
CHENO	chenodeoxycholic acid
CLSM	confocal laser scanning microscopy / microscope
CPE	constant phase element
CT	charge transfer
CV	cyclic voltammetry / voltammogram
D	ground state dye
$\text{D}^*$	excited dye
$\text{D}^+$	oxidized dye
d	doublet (NMR)
D- $\pi$ -A	donor- $\pi$ -acceptor
DSC	dye-sensitized solar cell
EI	electron impact ionization
EIS	electrochemical impedance spectroscopy
EMimTFS	1-ethyl-3-methylimidazolium bis-(trifluoromethylsulfonyl)imide
EPR	electron paramagnetic resonance
FB mode	feedback mode
<i>FF</i>	fill factor
FTO	fluorine doped tin oxide (F:SnO <sub>2</sub> )
HFA	high frequency axis
HOMO	highest occupied molecular orbital
HS	high spin
HTM	hole transport material

IMPS	intensity-modulated photocurrent spectroscopy
IMVS	intensity-modulated photovoltage spectroscopy
IPCE	incident photon-to-current efficiency
IR	infrared
<i>i</i> - <i>V</i>	current-voltage
<i>j</i> - <i>V</i>	current density-voltage
LCCT	ligand-centered charge transfer
LED	light emitting diode
LFA	low frequency axis
LFSE	ligand field stabilization energy
LHE	light harvesting efficiency
LSV	linear sweep voltammogram / voltammetry
LUMO	lowest unoccupied molecular orbital
m	multiplet (NMR)
ME	microelectrode
MLCT	metal-ligand charge transfer
MS	mass spectrometry
NHE	normal hydrogen electrode
NIR	near infrared
NMBI	<i>n</i> -methylbutyl imidazole
NMR	nuclear magnetic resonance
OPA	octadecylphosphonic acid
PCE	power conversion efficiency
PEDOT	poly-3,4-ethylenedioxythiophene
PEG	poly-(ethylene glycol)
phen	phenanthroline
PIA	photo-induced absorption spectroscopy
PTFE	polytetrafluoroethylene
PV	photo voltaic
QRE	quasireference electrode
RC	redox competition
RDE	rotating disk electrode
RE	reference electrode
s	singlet (NMR)
SCE	saturated calomel electrode
SECM	scanning electrochemical microscopy / microscope
SECCM	scanning electrochemical cell microscopy / microscope
sept	septet (NMR)
SF	shear force

## 10 Appendix

---

SFM	scanning force microscopy / microscope
SF-SECM	shear force distance controlled SECM
SG/TC	substrate generation / tip collection
SICM	scanning ion-conductance microscopy / microscope
SNOM	scanning near-field optical microscopy / microscope
spiro-MeOTAD	2,2',7,7'-tetrakis-(N,N-di-4-methoxyphenylamino)-9,9'-spirobifluorene
SPM	scanning probe microscopy / microscope
sq	square
STM	scanning tunneling microscopy / microscope
t	triplet (NMR)
TAS	transient absorption spectroscopy
TBAP	tetrabutylammonium perchlorate
TBP	4- <i>tert</i> -butylpyridine
TCO	transparent conducting oxide
TG/SC	tip generation/substrate collection
TMS	tetramethylsilane
UV	ultraviolet
UV-Vis	ultraviolet-visible
VB	valence band
WE	working electrode

---

## 10.4 Symbols and Units

Symbol	Meaning	Unit/value
A	ampere	
$A$	area	$\text{cm}^2$
$c$	velocity of light	$299792458 \text{ m s}^{-1}$
$c^*$	bulk concentration	$\text{mol cm}^{-3}$
$c_D$	dye concentration in the semiconductor film	$\text{mol cm}^{-3}$
$c_{\text{ox}}$	concentration of oxidized species	$\text{mol cm}^{-3}$
$c_{\text{red}}$	concentration of reduced species	$\text{mol cm}^{-3}$
$d$	ME-to-substrate distance	$\mu\text{m}$
$D$	diffusion coefficient	$\text{cm}^2 \text{ s}^{-1}$
$d_0$	closest ME-to-substrate distance	$\mu\text{m}$
$e^-$	electron	
$E_C$	energy of the conduction band edge	eV
$E_F$	Fermi level	eV
$E_g$	band gap energy	eV
$E_{h\nu}$	photon energy	J
$E_{\text{redox}}$	electrochemical potential of a redox mediator on the energy scale	eV
$E_{\text{redox}}^0$	formal redox energy	eV
$E_S$	substrate potential	V
$E_T$	tip potential	V
$E_V$	energy of the valence band edge	eV
$f$	frequency	$\text{s}^{-1}$
$F$	Faraday's constant	$96485 \text{ As mol}^{-1}$
$g$	geometric factor	
$h$	Planck's constant	$6.626069 \cdot 10^{-34} \text{ J s}$
$h^+$	hole	
$h\nu$	photon	
$I$	intensity of light	$\text{mW cm}^{-2}$
$i_T$	normalized tip current ( $i_T / i_{T,\infty}$ )	
$i_{\text{el,lim}}$	electron migration through semiconductor	
$i_{k,\text{lim}}$	limiting substrate current	A
$I_{k,\text{lim}}$	normalized limiting substrate current	
$i_{\text{SC}}$	short-circuit current	A
$i_{T,\infty}$	bulk tip current	A
$i_{T,\infty}$	limiting tip current in the bulk	A

## 10 Appendix

---

$i_{T,cond}$	normalized current at a conducting sample	
$i_{T,dark}$	currents detected in the dark	A
$i_{T,illu}$	currents detected under illumination	A
$i_{T,lim}$	limiting tip current	A
$I_{T,lim}$	normalized limiting tip current	
$i_{T,photo}$	photocurrent	A
$j$	current density	A cm <sup>-2</sup>
$J_{hv}$	photon flux density	mol cm <sup>-2</sup> s <sup>-1</sup>
$J_{hv} \phi_{hv}$	overall rate of light absorption	s <sup>-1</sup>
$j_{lim}$	limiting current density	A cm <sup>-2</sup>
$j_{SC}$	short-circuit current density	A cm <sup>-2</sup>
$k_B$	Boltzmann constant	8.617×10 <sup>-5</sup> eV K <sup>-1</sup>
$k_{eff}$	efficient rate constant	cm s <sup>-1</sup>
$k_{hv,eff}$	effective rate constant	s <sup>-1</sup>
$k_{inj}$	rate constant of electron injection into the conducting band of the semiconductor	s
$k_{ox}$	regeneration constant of dye reduction	cm <sup>3</sup> mol <sup>-1</sup> s <sup>-1</sup>
$l$	thickness of the dye layer	cm
$L$	normalized distance ( $d/r_T$ )	
$n$	number of transferred electrons	
$n$	electron level	
$N_A$	Avogadro's number	6.02214129×10 <sup>23</sup> mol <sup>-1</sup>
$N_{hv}$	number of photons per second	s <sup>-1</sup>
$P$	power	J s <sup>-1</sup>
$r$	radius	cm
$r$	reaction rate	mol s <sup>-1</sup> cm <sup>-2</sup>
$R$	resistance	Ω
$R_{CE}$	counter electrode resistance	Ω
$R_D$	electrolyte diffusion resistance	Ω
$RG$	ratio of $r_{glass}$ to $r_T$	
$r_{glass}$	radius of the glass sheath of a ME	μm
$R_{rec}$	recombination resistance	Ω
$r_S$	substrate radius	cm
$R_S$	sheet resistance	Ω
$r_T$	radius of the electrode material	μm
$T$	temperature	°C
$V$	volts	
$V$	volume	cm <sup>3</sup>
$V_{OC}$	open-circuit potential	V

## 10 Appendix

---

$W$	Warburg element	
$\Gamma_D^*$	dye loading of the excited dye	$\text{mol cm}^{-2}$
$\Gamma_D^+$	dye loading of the oxidized dye	$\text{mol cm}^{-2}$
$\Gamma_D$	dye loading of the neutral dye	$\text{mol cm}^{-2}$
$\delta$	chemical shift	ppm
$\Delta E$	energy difference	eV
$\Delta x$	step size in $x$ -direction	$\mu\text{m}$
$\Delta y$	step size in $y$ -direction	$\mu\text{m}$
$\Delta\phi$	potential difference	eV
$\eta$	photon factor	$\text{A W}^{-1}$
$\eta$	dynamic viscosity	$\text{mPa s}$
$\kappa$	normalized heterogeneous rate constant	
$\lambda_{\text{max}}$	maximum wavelength	nm
$\tau_e$	electron lifetime	ps
$\nu$	frequency	$\text{s}^{-1}$
$\nu$	kinematic viscosity	$\text{cm}^2 \text{s}^{-1}$
$\nu$	scan rate (CV)	$\text{V s}^{-1}$
$\nu_T$	translation rate (SECM imaging)	$\mu\text{m s}^{-1}$
$\tilde{\nu}$	wave number	$\text{cm}^{-1}$
$\pi$	mathematical constant	3.14159
$\pi^*$	electron level	
$\rho$	density	$\text{g cm}^{-3}$
$\phi_{hv}$	excitation cross-section	$\text{cm}^2 \text{mol}^{-1}$
$\omega$	angular frequency	$\text{s}^{-1}$

---

---

## 11 References

- [1] G. Ciamician, *Science* **1912**, *36*, 385.
- [2] C. Le Quere, et al., *Earth Syst. Sci. Data* **2016**, *8*, 605.
- [3] <https://yearbook.enerdata.net/#wind-solar-share-electricity-production.html> accessed **April, 14th 2017**.
- [4] N. S. Lewis, D. G. Nocera, *Proc. Natl. Acad. Sci. U. S. A.* **2006**, *103*, 15729.
- [5] M. Tao, *Electrochem. Soc. Interface* **2008**, *17*, 30.
- [6] B. O'Regan, M. Graetzel, *Nature* **1991**, *353*, 737.
- [7] <https://www.nrel.gov/pv/assets/images/efficiency-chart.png>, accessed **January 2018**.
- [8] G. Boschloo, A. Hagfeldt, *Acc. Chem. Res.* **2009**, *42*, 1819.
- [9] H. Nusbaumer, J.-E. Moser, S. M. Zakeeruddin, M. K. Nazeeruddin, M. Graetzel, *J. Phys. Chem. B* **2001**, *105*, 10461.
- [10] S. M. Feldt, E. A. Gibson, E. Gabrielsson, L. Sun, G. Boschloo, A. Hagfeldt, *J. Am. Chem. Soc.* **2010**, *132*, 16714.
- [11] K. Kakiage, Y. Aoyama, T. Yano, K. Oya, J.-i. Fujisawa, M. Hanaya, *Chem. Commun.* **2015**, *51*, 15894.
- [12] B. Bozic, E. Figgemeier, *Chem. Commun.* **2006**, 2268.
- [13] P. Bertoncello, *Energy Environ. Sci.* **2010**, *3*, 1620.
- [14] A. Sumboja, U. M. Tefashe, G. Wittstock, P. S. Lee, *J. Power Sources* **2012**, *207*, 205.
- [15] P. Wang, S. M. Zakeeruddin, R. Humphry-baker, J. E. Moser, M. Graetzel, *Adv. Mater.* **2003**, *15*, 2101.
- [16] B. Zhang, X. Xu, X. Zhang, D. Huang, S. Li, Y. Zhang, F. Zhan, M. Deng, Y. He, W. Chen, Y. Shen, M. Wang, *ChemPhysChem* **2014**, *15*, 1182.
- [17] B. Zhang, H. Yuan, X. Zhang, D. Huang, S. Li, M. Wang, Y. Shen, *ACS Appl. Mater. Interfaces* **2014**, *6*, 20913.
- [18] Y. Shen, U. M. Tefashe, K. Nonomura, T. Loewenstein, D. Schlettwein, G. Wittstock, *Electrochim. Acta* **2009**, *55*, 458.
- [19] U. M. Tefashe, T. Loewenstein, H. Miura, D. Schlettwein, G. Wittstock, *J. Electroanal. Chem.* **2010**, *650*, 24.
- [20] U. M. Tefashe, M. Rudolph, H. Miura, D. Schlettwein, G. Wittstock, *Phys. Chem. Chem. Phys.* **2012**, *14*, 7533.
- [21] U. M. Tefashe, K. Nonomura, N. Vlachopoulos, A. Hagfeldt, G. Wittstock, *J. Phys. Chem. C* **2012**, *116*, 4316.
- [22] W. Xiang, F. Huang, Y.-B. Cheng, U. Bach, L. Spiccia, *Energy Environ. Sci.* **2013**, *6*, 121.
- [23] D. P. Hagberg, X. Jiang, E. Gabrielsson, M. Linder, T. Marinado, T. Brinck, A. Hagfeldt, L. Sun, *J. Mater. Chem.* **2009**, *19*, 7232.
- [24] V. Leandri, H. Ellis, E. Gabrielsson, L. Sun, G. Boschloo, A. Hagfeldt, *Phys. Chem. Chem. Phys.* **2014**, *16*, 19964.
- [25] L. Schlappbach, A. Zuetzel, *Nature* **2001**, *414*, 353.
- [26] Y. Demirel, in *Energy* Springer International Publishing, London, **2012**.
- [27] H. Gerischer, *J. Electroanal. Chem. Interfacial Electrochem.* **1975**, *58*, 263.
- [28] H. Gerischer, *J. Electroanal. Chem. Interfacial Electrochem.* **1977**, *82*, 133.
- [29] H. Gerischer, *Electrochim. Acta* **1990**, *35*, 1677.
- [30] A. Fujishima, K. Honda, *Nature* **1972**, *238*, 37.
- [31] A. Henglein, M. Graetzel, *Sol. Power Fuels, [Proc. Int. Conf.], 1st* **1977**, 53.
- [32] J. Kiwi, M. Graetzel, *Angew. Chem.* **1979**, *91*, 659.
- [33] J. Kiwi, E. Borgarello, E. Pelizzetti, M. Visca, M. Graetzel, *Angew. Chem.* **1980**, *92*, 663.
- [34] U. Koelle, M. Graetzel, *Angew. Chem.* **1987**, *99*, 572.
- [35] A. J. Bard, *Science* **1980**, *207*, 139.
- [36] C. Y. Liu, H. L. Pan, M. A. Fox, A. J. Bard, *Science* **1993**, *261*, 897.
- [37] P. A. Kohl, A. J. Bard, *J. Am. Chem. Soc.* **1977**, *99*, 7531.
- [38] A. J. Bard, *J. Electroanal. Chem. Interfacial Electrochem.* **1984**, *168*, 5.
- [39] A. J. Bard, *J. Photochem.* **1979**, *10*, 59.
- [40] H. Sakai, R. Baba, K. Hashimoto, A. Fujishima, *J. Electroanal. Chem.* **1994**, *379*, 199.

- [41] H. Maeda, K. Ikeda, K. Hashimoto, K. Ajito, M. Morita, A. Fujishima, *J. Phys. Chem. B* **1999**, *103*, 3213.
- [42] M. Grätzel, *Nature* **2001**, *414*, 338.
- [43] A. J. Nozik, *Annu. Rev. Phys. Chem.* **1978**, *29*, 189.
- [44] M. S. Wrighton, *Acc. Chem. Res.* **1979**, *12*, 303.
- [45] M. Law, L. E. Greene, J. C. Johnson, R. Saykally, P. Yang, *Nat. Mater.* **2005**, *4*, 455.
- [46] A. Listorti, B. O'Regan, J. R. Durrant, *Chem. Mater.* **2011**, *23*, 3381.
- [47] R. Memming, *Prog. Surf. Sci.* **1984**, *17*, 7.
- [48] T. Marinado, D. P. Hagberg, M. Hedlund, T. Edvinsson, E. M. J. Johansson, G. Boschloo, H. Rensmo, T. Brinck, L. Sun, A. Hagfeldt, *Phys. Chem. Chem. Phys.* **2009**, *11*, 133.
- [49] L. Kavan, M. Graetzel, S. E. Gilbert, C. Klemenz, H. J. Scheel, *J. Am. Chem. Soc.* **1996**, *118*, 6716.
- [50] W. Shockley, H. J. Queisser, *J. Appl. Phys.* **1961**, *32*, 510.
- [51] A. Chirila, S. Buecheler, F. Pianezzi, P. Bloesch, C. Gretener, A. R. Uhl, C. Fella, L. Kranz, J. Perrenoud, S. Seyrling, R. Verma, S. Nishiwaki, Y. E. Romanyuk, G. Bilger, A. N. Tiwari, *Nat. Mater.* **2011**, *10*, 857.
- [52] S. H. Moon, S. J. Park, S. H. Kim, M. W. Lee, J. Han, J. Y. Kim, H. Kim, Y. J. Hwang, D.-K. Lee, B. K. Min, *Sci. Rep.* **2015**, *5*, 8970.
- [53] A. De Vos, *J. Phys. D: Appl. Phys.* **1980**, *13*, 839.
- [54] P. Wuerfel, T. Trupke, *Phys. J.* **2003**, *2*, 45.
- [55] L. Kranz, A. Abate, T. Feurer, F. Fu, E. Avancini, J. Lockinger, P. Reinhard, S. M. Zakeeruddin, M. Graetzel, S. Buecheler, A. N. Tiwari, *J. Phys. Chem. Lett.* **2015**, *6*, 2676.
- [56] J.-Y. Kim, J. Yang, J. H. Yu, W. Baek, C.-H. Lee, H. J. Son, T. Hyeon, M. J. Ko, *ACS Nano* **2015**, *9*, 11286.
- [57] K. Zhao, Z. Pan, I. Mora-Sero, E. Canovas, H. Wang, Y. Song, X. Gong, J. Wang, M. Bonn, J. Bisquert, X. Zhong, *J. Am. Chem. Soc.* **2015**, *137*, 5602.
- [58] G. Conibeer, *Proc. SPIE* **2012**, *8256*, 82560Z/1.
- [59] A. Hagfeldt, G. Boschloo, L. Sun, L. Kloo, H. Pettersson, *Chem. Rev.* **2010**, *110*, 6595.
- [60] N. Vlachopoulos, P. Liska, J. Augustynski, M. Graetzel, *J. Am. Chem. Soc.* **1988**, *110*, 1216.
- [61] J. Desilvestro, M. Graetzel, L. Kavan, J. Moser, J. Augustynski, *J. Am. Chem. Soc.* **1985**, *107*, 2988.
- [62] H. Ellis, N. Vlachopoulos, L. Haeggman, C. Perruchot, M. Jouini, G. Boschloo, A. Hagfeldt, *Electrochim. Acta* **2013**, *107*, 45.
- [63] A. Burke, S. Ito, H. Snaith, U. Bach, J. Kwiakowski, M. Graetzel, *Nano Lett.* **2008**, *8*, 977.
- [64] K.-j. Jiang, S. Yanagida, in *Dye-Sensitized Solar Cells, Vol. 1* (Ed. H. H. Girault), CRC Press, Lausanne, **2010**.
- [65] J. Schnadt, P. A. Bruehwiler, L. Patthey, J. N. O'Shea, S. Soedergren, M. Odelius, R. Ahuja, O. Karis, M. Baessler, P. Persson, H. Siegbahn, S. Lunell, N. Martensson, *Nature* **2002**, *418*, 620.
- [66] J. Bisquert, F. Fabregat-Santiago, I. Mora-Sero, G. Garcia-Belmonte, S. Gimenez, *J. Phys. Chem. C* **2009**, *113*, 17278.
- [67] A. Ehret, L. Stuhl, M. T. Spitler, *J. Phys. Chem. B* **2001**, *105*, 9960.
- [68] R. Y. Ogura, S. Nakane, M. Morooka, M. Orihashi, Y. Suzuki, K. Noda, *Appl. Phys. Lett.* **2009**, *94*, 073308/1.
- [69] H. Zhou, Q. Chen, G. Li, S. Luo, T.-b. Song, H.-S. Duan, Z. Hong, J. You, Y. Liu, Y. Yang, *Science* **2014**, *345*, 542.
- [70] N. Robertson, *Angew. Chem., Int. Ed.* **2006**, *45*, 2338.
- [71] N. A. Ludin, A. M. Al-Alwani Mahmoud, A. B. Mohamad, A. A. H. Kadhum, K. Sopian, N. S. Abdul Karim, *Renew. Sust. Energ. Rev.* **2014**, *31*, 386.
- [72] S. A. Haque, E. Palomares, B. M. Cho, A. N. M. Green, N. Hirata, D. R. Klug, J. R. Durrant, *J. Am. Chem. Soc.* **2005**, *127*, 3456.
- [73] <http://rredc.nrel.gov/solar/spectra/>, accessed July 2017.
- [74] L. Yang, U. B. Cappel, E. L. Unger, M. Karlsson, K. M. Karlsson, E. Gabrielsson, L. Sun, G. Boschloo, A. Hagfeldt, E. M. J. Johansson, *Phys. Chem. Chem. Phys.* **2012**, *14*, 779.
- [75] Z. Yu, H. Tian, E. Gabrielsson, G. Boschloo, M. Gorlov, L. Sun, L. Kloo, *RSC Adv.* **2012**, *2*, 1083.

- [76] X. Jiang, T. Marinado, E. Gabrielsson, D. P. Hagberg, L. Sun, A. Hagfeldt, *J. Phys. Chem. C* **2010**, *114*, 2799.
- [77] A. Dualeh, J. H. Delcamp, M. K. Nazeeruddin, M. Graetzel, *Appl. Phys. Lett.* **2012**, *100*, 173512/1.
- [78] J.-H. Yum, T. W. Holcombe, Y. Kim, J. Yoon, K. Rakstys, M. K. Nazeeruddin, M. Graetzel, *Chem. Commun.* **2012**, *48*, 10727.
- [79] D. Kuang, S. Uchida, R. Humphry-Baker, S. M. Zakeeruddin, M. Graetzel, *Angew. Chem., Int. Ed.* **2008**, *47*, 1923.
- [80] H. Tian, E. Gabrielsson, P. W. Lohse, N. Vlachopoulos, L. Kloo, A. Hagfeldt, L. Sun, *Energy Environ. Sci.* **2012**, *5*, 9752.
- [81] Y. Liu, R. Jennings James, X. Wang, Q. Wang, *Phys. Chem. Chem. Phys.* **2013**, *15*, 6170.
- [82] E. Gabrielsson, H. Ellis, S. Feldt, H. Tian, G. Boschloo, A. Hagfeldt, L. Sun, *Adv. Energ. Mater.* **2013**, *3*, 1647.
- [83] H. Ellis, S. K. Eriksson, S. M. Feldt, E. Gabrielsson, P. W. Lohse, R. Lindblad, L. Sun, H. Rensmo, G. Boschloo, A. Hagfeldt, *J. Phys. Chem. C* **2013**, *117*, 21029.
- [84] M. K. Nazeeruddin, R. Humphry-Baker, M. Graetzel, D. Wohrle, G. Schnurpfeil, G. Schneider, A. Hirth, N. Trombach, *J. Porphyrins Phthalocyanines* **1999**, *3*, 230.
- [85] S. Mathew, A. Yella, P. Gao, R. Humphry-Baker, B. F. E. Curchod, N. Ashari-Astani, I. Tavernelli, U. Rothlisberger, M. K. Nazeeruddin, M. Graetzel, *Nat. Chem.* **2014**, *6*, 242.
- [86] K. Hara, M. Kurashige, Y. Dan-oh, C. Kasada, A. Shinpo, S. Suga, K. Sayama, H. Arakawa, *New J. Chem.* **2003**, *27*, 783.
- [87] T. Horiuchi, H. Miura, K. Sumioka, S. Uchida, *J. Am. Chem. Soc.* **2004**, *126*, 12218.
- [88] A. Burke, L. Schmidt-Mende, S. Ito, M. Graetzel, *Chem. Commun.* **2007**, 234.
- [89] A. Dualeh, R. Humphry-Baker, J. H. Delcamp, M. K. Nazeeruddin, M. Graetzel, *Adv. Energy Mater.* **2013**, *3*, 496.
- [90] J. E. Kroeze, N. Hirata, S. Koops, M. K. Nazeeruddin, L. Schmidt-Mende, M. Graetzel, J. R. Durrant, *J. Am. Chem. Soc.* **2006**, *128*, 16376.
- [91] A. Peddapuram, H. Cheema, R. E. Adams, R. H. Schmehl, J. H. Delcamp, *J. Phys. Chem. C* **2017**, *121*, 8770.
- [92] A. Hagfeldt, M. Graetzel, *Acc. Chem. Res.* **2000**, *33*, 269.
- [93] B. Xu, D. Bi, Y. Hua, P. Liu, M. Cheng, M. Graetzel, L. Kloo, A. Hagfeldt, L. Sun, *Energy Environ. Sci.* **2016**, *9*, 873.
- [94] B. A. Gregg, F. Pichot, S. Ferrere, C. L. Fields, *J. Phys. Chem. B* **2001**, *105*, 1422.
- [95] K.-j. Jiang, S. Yanagida, in *Dye-Sensitized Solar Cells* (Ed. K. Kalyanasundaram), EPFL Press, Lausanne, **2010**, p. 126.
- [96] E. Riedel, *Anorganische Chemie*, Walter de Gruyter GmbH & Co. KG, Berlin, **2004**.
- [97] I. Krivokapic, M. Zerara, M. L. Daku, A. Vargas, C. Enachescu, C. Ambrus, P. Tregenna-Piggott, N. Amstutz, E. Krausz, A. Hauser, *Coord. Chem. Rev.* **2007**, *251*, 364.
- [98] A. Vargas, M. Zerara, E. Krausz, A. Hauser, L. M. L. Daku, *J. Chem. Theory Comput.* **2006**, *2*, 1342.
- [99] E. Mosconi, J.-H. Yum, F. Kessler, C. J. Gomez Garcia, C. Zuccaccia, A. Cinti, M. K. Nazeeruddin, M. Graetzel, F. De Angelis, *J. Am. Chem. Soc.* **2012**, *134*, 19438.
- [100] J.-H. Yum, E. Baranoff, F. Kessler, T. Moehl, S. Ahmad, T. Bessho, A. Marchioro, E. Ghadiri, J.-E. Moser, C. Yi, M. K. Nazeeruddin, M. Graetzel, *Nat. Commun.* **2012**, *3*, 1655/1.
- [101] H. N. Tsao, C. Yi, T. Moehl, J.-H. Yum, S. M. Zakeeruddin, M. K. Nazeeruddin, M. Graetzel, *ChemSusChem* **2011**, *4*, 591.
- [102] S. M. Feldt, G. Wang, G. Boschloo, A. Hagfeldt, *J. Phys. Chem. C* **2011**, *115*, 21500.
- [103] A. Yella, H.-W. Lee, H. N. Tsao, C. Yi, A. K. Chandiran, M. K. Nazeeruddin, E. W.-G. Diau, C.-Y. Yeh, S. M. Zakeeruddin, M. Graetzel, *Science* **2011**, *334*, 629.
- [104] A. B. F. Martinson, T. W. Hamann, M. J. Pellin, J. T. Hupp, *Chem. - Eur. J.* **2008**, *14*, 4458.
- [105] S. Cazzanti, S. Caramori, R. Argazzi, C. M. Elliott, C. A. Bignozzi, *J. Am. Chem. Soc.* **2006**, *128*, 9996.
- [106] S. Yanagida, Y. Yu, K. Manseki, *Acc. Chem. Res.* **2009**, *42*, 1827.
- [107] L. M. Peter, *J. Phys. Chem. Lett.* **2011**, *2*, 1861.

- [108] S. A. Sapp, C. M. Elliott, C. Contado, S. Caramori, C. A. Bignozzi, *J. Am. Chem. Soc.* **2002**, *124*, 11215.
- [109] H.-S. Kim, S.-B. Ko, I.-H. Jang, N.-G. Park, *Chem. Commun. (Cambridge, U. K.)* **2011**, *47*, 12637.
- [110] B. V. Bergeron, A. Marton, G. Oskam, G. J. Meyer, *J. Phys. Chem. B* **2005**, *109*, 937.
- [111] J. Liu, J. Zhang, M. Xu, D. Zhou, X. Jing, P. Wang, *Energy Environ. Sci.* **2011**, *4*, 3021.
- [112] Y. Bai, J. Zhang, D. Zhou, Y. Wang, M. Zhang, P. Wang, *J. Am. Chem. Soc.* **2011**, *133*, 11442.
- [113] M. Wang, N. Chamberland, L. Breau, J.-E. Moser, R. Humphry-Baker, B. Marsan, S. M. Zakeeruddin, M. Graetzel, *Nat. Chem.* **2010**, *2*, 385.
- [114] H. Tian, X. Jiang, Z. Yu, L. Kloo, A. Hagfeldt, L. Sun, *Angew. Chem., Int. Ed.* **2010**, *49*, 7328.
- [115] I. R. Perera, A. Gupta, W. Xiang, T. Daeneke, U. Bach, R. A. Evans, C. A. Ohlin, L. Spiccia, *Phys. Chem. Chem. Phys.* **2014**, *16*, 12021.
- [116] G. Boschloo, L. Haeggman, A. Hagfeldt, *J. Phys. Chem. B* **2006**, *110*, 13144.
- [117] F. Fabregat-Santiago, J. Bisquert, G. Garcia-Belmonte, G. Boschloo, A. Hagfeldt, *Sol. Energy Mater. Sol. Cells* **2005**, *87*, 117.
- [118] G. Boschloo, A. Hagfeldt, *Inorg. Chim. Acta* **2008**, *361*, 729.
- [119] U. B. Cappel, S. Plogmaker, E. M. J. Johansson, A. Hagfeldt, G. Boschloo, H. Rensmo, *Phys. Chem. Chem. Phys.* **2011**, *13*, 14767.
- [120] T. W. Hamann, J. W. Ondersma, *Energy Environ. Sci.* **2011**, *4*, 370.
- [121] J. van de Lagemaat, N. G. Park, A. J. Frank, *J. Phys. Chem. B* **2000**, *104*, 2044.
- [122] H. Ellis, I. Schmidt, A. Hagfeldt, G. Wittstock, G. Boschloo, *J. Phys. Chem. C* **2015**, *119*, 21775.
- [123] J. Bisquert, F. Fabregat-Santiago, in *Dye-Sensitized Solar Cells, Vol. 1* (Ed. H. H. Girault), CRC Press, Lausanne, **2010**.
- [124] F. Fabregat-Santiago, J. Bisquert, L. Cevey, P. Chen, M. Wang, S. M. Zakeeruddin, M. Gratzel, *J. Am. Chem. Soc.* **2009**, *131*, 558.
- [125] L. Han, N. Koide, Y. Chiba, A. Islam, R. Komiya, N. Fuke, A. Fukui, R. Yamanaka, *Appl. Phys. Lett.* **2005**, *86*, 213501/1.
- [126] L. Han, N. Koide, Y. Chiba, T. Mitate, *Appl. Phys. Lett.* **2004**, *84*, 2433.
- [127] H. J. Snaith, in *Dye-Sensitized Solar Cells, Vol. 1* (Ed. H. H. Girault), CRC Press, Lausanne, **2010**.
- [128] S. Ardo, G. J. Meyer, *Chem. Soc. Rev.* **2009**, *38*, 115.
- [129] R. J. Forster, *Chem. Soc. Rev.* **1994**, *23*, 289.
- [130] J. Heinze, *Angew. Chem.* **1991**, *103*, 175.
- [131] L. Danis, M. E. Snowden, U. M. Tefashe, C. N. Heinemann, J. Mauzeroll, *Electrochim. Acta* **2014**, *136*, 121.
- [132] A. J. Bard, L. R. Faulkner, *Electrochemical Methods - Fundamentals and Applications*, John Wiley Sons Ltd., West Sussex, **2001**.
- [133] S. E. Pust, W. Maier, G. Wittstock, *Z. Phys. Chem.* **2008**, *222*, 1463.
- [134] H.-Y. Liu, F.-R. F. Fan, C. W. Lin, A. J. Bard, *J. Am. Chem. Soc.* **1986**, *108*, 3838.
- [135] J. H. Bae, Y. Yu, M. V. Mirkin, *J. Phys. Chem. C* **2016**, *120*, 20651.
- [136] T. J. Stockmann, J.-M. Noel, S. Ristori, C. Combellas, A. Abou-Hassan, F. Rossi, F. Kanoufi, *Anal. Chem.* **2015**, *87*, 9621.
- [137] Y. Hirano, M. Kodama, M. Shibuya, Y. Maki, Y. Komatsu, *Anal. Biochem.* **2014**, *447*, 39.
- [138] J. D. Henderson, F. P. Filice, M. S. M. Li, Z. Ding, *ChemElectroChem* **2017**, *4*, 749.
- [139] M. A. Malik, P. J. Kulesza, G. Pawlowska, *Electrochim. Acta* **2009**, *54*, 5537.
- [140] S. Amemiya, A. J. Bard, F.-R. F. Fan, M. V. Mirkin, P. R. Unwin, *Annu. Rev. Anal. Chem.* **2008**, *1*, 95.
- [141] G. Wittstock, M. Burchardt, S. E. Pust, Y. Shen, C. Zhao, *Angew. Chem. Int. Ed.* **2007**, *46*, 1584.
- [142] A. J. Bard, M. V. Mirkin, *Scanning Electrochemical Microscopy, Second Edition*, Taylor & Francis, Boca Raton, **2012**.
- [143] D. Polcari, P. Dauphin-Ducharme, J. Mauzeroll, *Chem. Rev.* **2016**, *116*, 13234.
- [144] M. V. Mirkin, B. R. Horrocks, *Anal. Chim. Acta* **2000**, *406*, 119.
- [145] M. V. Mirkin, *Mikrochim. Acta* **1999**, *130*, 127.

- [146] D. Mandler, A. J. Bard, *J. Electrochem. Soc.* **1990**, *137*, 2468.
- [147] B. R. Horrocks, M. V. Mirkin, A. J. Bard, *J. Phys. Chem.* **1994**, *98*, 9106.
- [148] S. E. Pust, M. Salomo, E. Oesterschulze, G. Wittstock, *Nanotechnology* **2010**, *21*, 105709/1.
- [149] M. A. O'Connell, A. J. Wain, *Anal. Chem.* **2014**, *86*, 12100.
- [150] R. Cornut, C. Lefrou, *J. Electroanal. Chem.* **2008**, *621*, 178.
- [151] B. Liu, A. J. Bard, M. V. Mirkin, S. E. Creager, *J. Am. Chem. Soc.* **2004**, *126*, 1485.
- [152] J. L. Amphlett, G. Denuault, *J. Phys. Chem. B* **1998**, *102*, 9946.
- [153] Y. Shen, K. Nonomura, D. Schlettwein, C. Zhao, G. Wittstock, *Chem. Eur. J.* **2006**, *12*, 5832.
- [154] C. Wei, A. J. Bard, M. V. Mirkin, *J. Phys. Chem.* **1995**, *99*, 16033.
- [155] C. Lefrou, *J. Electroanal. Chem.* **2007**, *601*, 94.
- [156] R. Cornut, C. Lefrou, *J. Electroanal. Chem.* **2007**, *608*, 59.
- [157] R. Cornut, S. Griveau, C. Lefrou, *J. Electroanal. Chem.* **2010**, *650*, 55.
- [158] M. Etienne, A. Schulte, S. Mann, G. Jordan, I. D. Dietzel, W. Schuhmann, *Anal. Chem.* **2004**, *76*, 3682.
- [159] B. B. Katemann, A. Schulte, W. Schuhmann, *Electroanalysis* **2004**, *16*, 60.
- [160] U. M. Tefashe, G. Wittstock, *C. R. Chim.* **2013**, *16*, 7.
- [161] B. Liu, A. J. Bard, *J. Phys. Chem. B* **2002**, *106*, 12801.
- [162] Y. Shen, M. Träuble, G. Wittstock, *Anal. Chem.* **2008**, *80*, 750.
- [163] I. Schmidt, I. Plettenberg, D. Kimmich, H. Ellis, J. Witt, C. Dosche, G. Wittstock, *Electrochim. Acta* **2016**, *222*, 735.
- [164] J. L. Fernandez, A. J. Bard, *Anal. Chem.* **2003**, *75*, 2967.
- [165] K. Eckhard, X. Chen, F. Turcu, W. Schuhmann, *Phys. Chem. Chem. Phys.* **2006**, *8*, 5359.
- [166] K. Eckhard, W. Schuhmann, *Analyst* **2008**, *133*, 1486.
- [167] B. R. Horrocks, D. Schmidtke, A. Heller, A. J. Bard, *Anal. Chem.* **1993**, *65*, 3605.
- [168] J. Izquierdo, A. Eifert, C. Kranz, R. M. Souto, *Electrochim. Acta* **2017**, *247*, 588.
- [169] S. Kurai, R. Mihara, G. Nobata, K. Okawa, N. Okada, K. Tadatomo, Y. Yano, T. Tabuchi, K. Matsumoto, Y. Yamada, *Phys. Status Solidi B* **2017**, Ahead of Print.
- [170] C. H. Hamann, W. Vielstich, *Elektrochemie*, WILEY-VCH Verlag GmbH & Co. KGaA, Weinheim, **2005**.
- [171] B. Speiser, *Chem. unserer Zeit* **1981**, *15*, 21.
- [172] H. E. Gottlieb, V. Kotlyar, A. Nudelman, *J. Org. Chem.* **1997**, *62*, 7512.
- [173] Y. Shen, U. M. Tefashe, K. Nonomura, T. Loewenstein, D. Schlettwein, G. Wittstock, *Electrochim. Acta* **2009**, *55*, 458.
- [174] U. M. Tefashe, T. Loewenstein, H. Miura, D. Schlettwein, G. Wittstock, *J. Electroanal. Chem.* **2010**, *650*, 24.
- [175] C. N. Kirchner, K. H. Hallmeier, R. Szargan, T. Raschke, C. Radehaus, G. Wittstock, *Electroanal.* **2007**, *19*, 1023.
- [176] G. Wittstock, T. Asmus, T. Wilhelm, *Fresenius J. Anal. Chem.* **2000**, *367*, 346.
- [177] B. B. Katemann, A. Schulte, W. Schuhmann, *Chem. - Eur. J.* **2003**, *9*, 2025.
- [178] K. Izutsu, *Electrochemistry in Nonaqueous Solutions*, Wiley-VCH GmbH & Co. KGaA, Matsumoto, Japan, **2002**.
- [179] T. W. Hamann, F. Gstrein, B. S. Brunschwig, N. S. Lewis, *J. Am. Chem. Soc.* **2005**, *127*, 13949.
- [180] P. J. Cameron, L. M. Peter, S. Hore, *J. Phys. Chem. B* **2005**, *109*, 930.
- [181] B. Martin, W. R. McWhinnie, G. M. Waing, *J. Inorg. Nucl. Chem.* **1961**, *23*, 207.
- [182] Y. Fu, A. S. Cole, T. W. Swaddle, *J. Am. Chem. Soc.* **1999**, *121*, 10410.
- [183] M. Hesse, H. Meier, B. Zeeh, *Spektroskopische Methoden in der organischen Chemie*, Thieme Verlag, Stuttgart, **2005**.
- [184] M. G. Simic, M. Z. Hoffman, R. P. Cheney, Q. G. Mulazzani, *J. Phys. Chem.* **1979**, *83*, 439.
- [185] Y. V. Kokunov, M. M. Ershova, G. A. Razgonyaeva, *Russ. J. Coord. Chem.* **2002**, *28*, 461.
- [186] L. Riesel, J. Pauli, A. Porzel, E. G. Il'in, *Z. Anorg. Allg. Chem.* **1989**, *571*, 127.
- [187] E. P. Friis, J. E. T. Andersen, L. L. Madsen, N. Bonander, P. Moller, J. Ulstrup, *Electrochim. Acta* **1998**, *43*, 1113.
- [188] B. Garcia, J. C. Ortega, *J. Chem. Eng. Data* **1988**, *33*, 200.

- [189] G. A. Alper, *Viniti* **1986**, 1.
- [190] D. S. Gill, U. Kamp, A. Doelle, M. D. Zeigler, *Ind. J. Chem.* **2001**, 40A, 693.
- [191] K. Nakata, Y. Kayama, K. Shimazu, A. Yamakata, S. Ye, M. Osawa, *Langmuir* **2008**, 24, 4358.
- [192] M. Hourani, B. Waleed, *J. Appl. Electrochem.* **2000**, 30, 859.
- [193] Y. Saito, *Rev. Polarogr.* **1968**, 15, 177.
- [194] C. G. Zoski, M. V. Mirkin, *Anal. Chem.* **2002**, 74, 1986.
- [195] U. M. Tefashe, K. Nonomura, N. Vlachopoulos, A. Hagfeldt, G. Wittstock, *J. Phys. Chem. C* **2012**, 116, 4316.
- [196] A. Y. Anderson, P. R. F. Barnes, J. R. Durrant, B. C. O'Regan, *J. Phys. Chem. C* **2011**, 115, 2439.
- [197] Y. Liu, J. R. Jennings, Y. Huang, Q. Wang, S. M. Zakeeruddin, M. Graetzel, *J. Phys. Chem. C* **2011**, 115, 18847.
- [198] M. Konstantakou, P. Falaras, T. Stergiopoulos, *Polyhedron* **2014**, 82, 109.
- [199] U. Bach, D. Lupo, P. Comte, J. E. Moser, F. Weissortel, J. Salbeck, H. Spreitzer, M. Graetzel, *Nature* **1998**, 395, 583.
- [200] N. Papageorgiou, Y. Athanassov, M. Armand, P. Bonhote, H. Pettersson, A. Azam, M. Graetzel, *J. Electrochem. Soc.* **1996**, 143, 3099.
- [201] Y. Shi, C. Zhan, L. Wang, B. Ma, R. Gao, Y. Zhu, Y. Qiu, *Phys. Chem. Chem. Phys.* **2009**, 11, 4230.
- [202] A. J. Bard, F.-R. F. Fan, J. Kwak, O. Lev, *Anal. Chem.* **1989**, 61, 132.
- [203] K. C. D. Robson, K. Hu, G. J. Meyer, C. P. Berlinguette, *J. Am. Chem. Soc.* **2013**, 135, 1961.
- [204] K. Westermark, S. Tingry, P. Persson, H. Rensmo, S. Lunell, A. Hagfeldt, H. Siegbahn, *J. Phys. Chem. B* **2001**, 105, 7182.
- [205] J. Nyhlen, G. Boschloo, A. Hagfeldt, L. Kloo, T. Privalov, *ChemPhysChem* **2010**, 11, 1858.
- [206] A. L. Lipson, M. C. Hersam, *J. Phys. Chem. C* **2013**, 117, 7953.
- [207] S. Watanabe, Y. Fukuchi, M. Fukasawa, T. Sassa, A. Kimoto, Y. Tajima, M. Uchiyama, T. Yamashita, M. Matsumoto, T. Aoyama, *ACS Appl. Mater. Interfaces* **2014**, 6, 1481.
- [208] C. Musumeci, A. Liscio, V. Palermo, P. Samori, *Mater. Today* **2014**, 17, 504.
- [209] J. Y. Liu, A. Melnikov, A. Mandelis, *Int. J. Thermophys.* **2015**, 36, 987.
- [210] O. Breitenstein, *Sol. Energy Mater. Sol. Cells* **2011**, 95, 2933.
- [211] J. Carstensen, A. Schutt, G. Popkirov, H. Foll, *Phys. Status Solidi C* **2011**, 8, 1342.
- [212] J. M. Wagner, J. Carstensen, A. Schuett, H. Foell, *J. Appl. Phys.* **2013**, 113, 064503/1.
- [213] G. Alemu, B. Zhang, J. Li, X. Xu, J. Cui, Y. Shen, M. Wang, *Nano* **2014**, 9, 1440008/1.
- [214] G. Alemu, J. Cui, K. Cao, J. Li, Y. Shen, M. Wang, *RSC Adv.* **2014**, 4, 51374.
- [215] C. J. Martin, B. Bozic-Weber, E. C. Constable, T. Glatzel, C. E. Housecroft, I. A. Wright, *Electrochim. Acta* **2014**, 119, 86.
- [216] G. Alemu, J. Li, J. Cui, X. Xu, B. Zhang, K. Cao, Y. Shen, Y. Cheng, M. Wang, *J. Mater. Chem. A: Mater. Energy Sustain.* **2015**, 3, 9216.
- [217] F. Zhang, V. Roznyatovskiy, F.-R. F. Fan, V. Lynch, J. L. Sessler, A. J. Bard, *J. Phys. Chem. C* **2011**, 115, 2592.
- [218] B. D. B. Aaronson, J. C. Byers, A. W. Colburn, K. McKelvey, P. R. Unwin, *Anal. Chem.* **2015**, 87, 4129.
- [219] C.-H. Chen, L. Jacobse, K. McKelvey, S. C. S. Lai, M. T. M. Koper, P. R. Unwin, *Anal. Chem.* **2015**, 87, 5782.
- [220] R. Cornut, C. Lefrou, *J. Electroanal. Chem.* **2008**, 623, 197.
- [221] L. C. P. M. de Smet, H. Zuilhof, E. J. R. Sudholter, G. Wittstock, M. S. Duerdin, L. H. Lie, A. Houlton, B. R. Horrocks, *Electrochim. Acta* **2002**, 47, 2653.
- [222] H. Bülter, F. Peters, J. Schwenzel, G. Wittstock, *Angew. Chem. Int. Ed.* **2014**, 53, 10531.
- [223] A. Lesch, B. Vaske, F. Meiners, D. Witte, D. Momotenko, F. Cortés-Salazar, I. Wirth, H. H. Girault, G. Wittstock, *Bunsen-Magazin* **2012**, 14, 203.
- [224] A. Lesch, D. Momotenko, F. Cortes-Salazar, I. Wirth, U. M. Tefashe, F. Meiners, B. Vaske, H. H. Girault, G. Wittstock, *J. Electroanal. Chem.* **2012**, 666, 52.
- [225] Y.-H. Kim, I.-K. Lee, Y.-S. Song, M.-H. Lee, B.-Y. Kim, N.-I. Cho, D. Y. Lee, *Electron. Mater. Lett.* **2014**, 10, 445.

## 12 Publications

### *Publications*

Ina Schmidt, Inka Plettenberg, Daniel Kimmich, Hanna Ellis, Julia Witt, Carsten Dosche, Gunther Wittstock; Spatially Resolved Analysis of Screen Printed Photoanodes of Dye-Sensitized Solar Cells by Scanning Electrochemical Microscopy, *Electrochim. Acta*, **2016**, *222*, 735-746.

Hanna Ellis,\* Ina Schmidt,\* Anders Hagfeldt, Gunther Wittstock, Gerrit Boschloo; Influence of Dye Architecture of Triphenylamine Based Organic Dyes on the Kinetics in Dye-Sensitized Solar Cells, *J. Phys. Chem. C*, **2015**, *119*, 21775-21783.

\*Authors share first authorship.

### *Poster presentations*

Ina Schmidt, Hanna Ellis, Gunther Wittstock; “*Determining kinetics of the dye regeneration of a D35-sensitized TiO<sub>2</sub> photoanode with different cobalt tris(2,2-bipyridine) redox mediators using scanning electrochemical microscopy (SECM)*”; “Electrochemistry” in Mainz, 22 – 24 September 2014.

Ushula Mengesha Tefashe, Ina Schmidt, Melanie Rudolph, Hidetoshi Miura, Derck Schlettwein, Gunther Wittstock; “*Correlation of kinetics of dye regeneration by SECM and macroscopic photovoltaic properties in electrodeposited D149-sensitized ZnO*”; “Electrochemistry” in Munich, 17 – 19 September 2012.

Ina Schmidt, Ushula Mengesha Tefashe, Melanie Rudolph, Derck Schlettwein, Gunther Wittstock; “*Photovoltaic characteristics and dye regeneration kinetics in D149-sensitized ZnO with varied dye loading and film thickness*”; “Bunsentagung” in Leipzig, 17 – 19 May 2012.

Ina Schmidt, Jens Tepe, Gunther Wittstock; „*Experimentalvorlesung – Photochemische Energiegewinnung*“; Kick-Off Event „FoL – Forschungsorientiertes Lernen“, 26 March 2012.

*Travel Grants for Conferences*

2014: 250 € from the GDCh for the “Electrochemistry 2014” in Mainz

2012: 250 € from the GDCh for the “Electrochemistry 2012” in Munich

## 13 Curriculum vitae

### Personal Data

Name	Ina Schmidt
Date of birth	11.11.1983
Place of birth	Nienburg / Weser, Germany
Languages	German (mother tongue), English (very good), Spanish (conversational), Swedish and French (basic knowledge)

### Background

07/2016 – today	Product & Sales Manager InProcess Instruments Gesellschaft für Prozessanalytik mbH, Bremen
10/2011 – today	Doctorate Physical chemistry, Carl von Ossietzky University Oldenburg
10/2011 – 03/2015	Teaching assistant Experiment planning and implementing those in lectures Supervision of students Physical chemistry, Carl von Ossietzky University Oldenburg
10/2006 – 10/2011	Bachelor of Science and Master of Science Industrial chemistry, Carl von Ossietzky University Oldenburg
09/2003 – 07/2006	Apprenticeship as a chemical laboratory assistant ACMOS Chemie, Bremen
06/2003	Abitur Albert-Schweitzer-Schule, Nienburg an der Weser

## Eigenständigkeitserklärung

Ich versichere hiermit, dass ich diese Arbeit selbstständig verfasst und nur die angegebenen Quellen und Hilfsmittel benutzt habe.

Während der Promotionszeit sind die unter „Publications“ genannten Veröffentlichungen entstanden.

Die Dissertation hat weder zu Teilen noch in Gänze einer anderen wissenschaftlichen Hochschule zur Begutachtung in einem Promotionsverfahren vorgelegen.

Oldenburg, den 07. März 2018

Ina Schmidt